Structural, Thermal, and Geomorphic Evolution of the Eastern Margin of the Tibetan Plateau

by

Eric Kirby

M.Sc. Geology
University of New Mexico, 1994

B.A. Geology
Hamilton College, 1992

SUBMITTED TO THE DEPARTMENT OF EARTH, ATMOSPHERIC, AND PLANETARY SCIENCES IN PARTIAL FULFILLMENT OF THE REQUIREMENTS FOR THE DEGREE OF

Undgrer

DOCTOR OF PHILOSOPHY
AT THE
MASSACHUSETTS INSTITUTE OF TECHNOLOGY

FEBRUARY, 2001

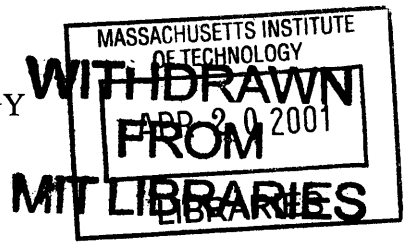

Signature of Author: _____
Department of Earth, Atmospheric, and Planetary Sciences
September, 2000

Certified by: _____
B. Clark Burchfiel
Thesis Co-supervisor

Certified by: _____
Kelin X. Whipple
Thesis Co-supervisor

Accepted by: _____
Ronald G. Prinn
Department Head

Structural, Thermal, and Geomorphic Evolution of the Eastern Margin of the Tibetan Plateau

by

Eric Kirby

Submitted to the Department of Earth, Atmospheric, and Planetary Sciences on October 13, 2000 in Partial Fulfillment of the Requirements for the Degree of Doctor of Philosophy in Geology

ABSTRACT

The eastern margin of the Tibetan Plateau adjacent to and north of the Sichuan Basin poses a fundamental geodynamic problem; the topography of eastern Tibet apparently developed in the absence of significant shortening of the upper crust. This study investigates the development and subsequent evolution of the topographic margin of the plateau in an effort to ascertain the controls on and geodynamic significance of present-day topography. The primary results from this study are threefold, and include: 1) an estimate of the inception of high relief along the plateau margin in the Late Miocene; 2) documentation of active deformation in the Min Shan range and estimates of the rates and pattern of Pleistocene-Recent rock uplift; 3) an assessment of the controls on the spatial distribution of bedrock channel gradients in this landscape.

Thermal histories of rocks along the margin inferred from $^{40}Ar/^{39}Ar$ and (U-Th)/He thermochronology provide constraints on the long-term rates and distribution of denudation across this margin of the plateau. Results indicate that 1) prior to the Late Miocene (ca. 11 Ma) regional denudation rates were low (< 0.1 mm/yr), and 2) rocks adjacent to the plateau margin were exhumed from depths of 8-10 km since that time. Active deformation and rock uplift in the Min Shan is documented by tilted Pleistocene basins along the western range flank. Geologic mapping and chronology demonstrate that rates of tilting are rapid (~10^8 rad/yr), and that rock uplift is highest near the range crest. However, mapped faults adjacent to the range do not appear to exert a direct control on the distribution of rock uplift. Analysis of bedrock river longitudinal profiles reveals a region of steep channels (normalized for drainage area) adjacent to the topographic front of the plateau margin. The spatial distribution of channel steepness appears to reflect active rock uplift focused along the plateau margin. Thus, the high topography along the plateau margin is argued to be a dynamic response to rock uplift in the absence of significant horizontal shortening and may reflect thickening in the lower crust.

Thesis co-supervisor: B. Clark Burchfiel
Thesis co-supervisor: Kelin X. Whipple

Acknowledgements

As I sit to write this, the proposition of properly thanking all those who have contributed to this dissertation and touched my life during its evolution seems daunting indeed. Let me begin by offering thanks to all not mentioned below and apologies for my oversight.

First, my advisors, Clark Burchfiel and Kelin Whipple. Clark for allowing me the freedom to pursue a problem of my choosing and for encouraging me to tackle it by whatever means I thought necessary. Kelin for introducing me to a world of rivers, for acting as a soundingboard for all manner of ideas, and for his seemingly endless suggestions for what to do next. In particular, I want to thank Kelin for suggesting that we pursue the question of whether climate can induce significant uplift of mountain peaks; that project lifted me out of the post-generals doldrums and provided the motivation for a good portion of this work.

The rest of my committee, Kip Hodges and Wiki Royden for reading the thesis and providing encouragement along the way. Thanks to Kip, in particular, for access to his laboratory and for advice on all manner of things, solicited or otherwise. Doug Burbank also deserves acknowledgement for taking time to participate in the defense and launch some tough questions. I look forward to working with him.

A number of people contributed scientifically to the work contained within this thesis. Thanks to Mike Krol for showing me the ropes in the noble gas lab and to Bill Oszewski for technical assistance with sample analysis. Thanks to Pete Reiners and Ken Farley of Caltech for providing the (U-Th)/He analyses and for advice on data interpretation. Glenn Berger of the Desert Research Institute performed the luminescence analyses. Although the data turned out to be of limited use, thanks to Yemane Asmerom and Steve Getty of the University of New Mexico for preliminary U-series analyses. Likewise, thanks to Darryl Granger of Purdue University for preliminary cosmogenic isotope measurements. Special thanks go to Doug Walker and Aaron Ferris of the University of Kansas for their generosity in teaching me some of the basics of producing a geologic map in Arcinfo and for sharing their software.

Colleagues in China, in particular Tang Wenqing, Chen Zhiliang, and Sun Zhiming, deserve special recognition, for without their multifacted roles as guides, scientists, translators, and logistic coordinators, much of this work would not have been possible. Special thanks to the drivers of the Chengdu Institute of Geology and Mineral Resources for safe travel.

Somewhat less tangible contributions to the ideas contained within are the result of discussions (often lively) with a number of individuals. In no particular order, these include: Greg Tucker, Noah Snyder, Marin Clark, Bob King, Peter Molnar, Erchie Wang (Academica Sinica), Charlie Rubin (Central Washington University), Mark Behn, Simon Brocklehurst, Jose Hurtado, Arthur White, Audrey Huerta, Anke Friedrich, Karl Karlstrom (University of New Mexico), Mousumi Roy (University of New Mexico), Frank Pazzaglia (Lehigh University), and Gene Humphreys (University of Oregon).

It has been said that one learns as much from one's fellow graduate students as from one's advisors. Whether or not this adage runs true, many thanks to all: CJ Northrop, Meg Coleman, Audrey Huerta, Anke Friedrich, Shane Pelechaty, Mousumi Roy, Jim Van Orman, Steve Parman, Kirstin Nicolaysen, Mark Schmitz, Noah Snyder,

Arthur White, Jose Hurtado, Sinan Ackiz, Simon Brocklehurst, Marin Clark, Julie Baldwin, Karen Viskupic, Firn Schoenbohm, John Thurmond, Steve DiBenedetto, Bill Lyons, Jenny Matzel, Mark Behn, and Fredrick Simons. Thanks also to Jeff Parsons, Mike Krol, Chris Marone, and Karen Mair.

Perhaps as significant are those who keep a graduate student life in perspective. Thanks to Noah, Biz, and Lydia for moments of recreation in a busy schedule. Elizabeth and her family, in particular, for three years of support and a haven in times of need. Many thanks to climbing/skiing/cycling buddies Jessica, Karen, Kerim, Veronique, Partick, and Daniel for keeping me healthy over the past year, and to Jessica for sharing thesis angst these past several months. Thanks to my brother Scott, sister Rebecca, and brother Matthew for unconditional love and support, even from thousands of miles away.

My decision to pursue a Ph.D. at MIT and a career in science has been the result of a long string of coincidence and happenstance. I want to acknowledge the early encouragement of Karen Kirby, who took me to the volcanoes of the Cascades at the ripe young age of 5 and fostered my budding fascination with mountains. Mark Jellinek suggested, nay, demanded, that I take an introductory geology class as a new student at Hamilton College. That class introduced me to Barb Tewksbury who, by example and by deed, instilled in me a deep sense of appreciation for the importance of creativity in science and in education. Barb also recommended that I talk to Karl Karlstrom, at the University of New Mexico when I was considering where to pursue graduate studies in geology. Karl served as advisor, mentor and friend for 3 short years in Albuquerque, and he continues to be a source of inspiration. I want to also thank Karl and Jane Selverstone for encouraging me to attend MIT, even as they hoped I would stay at UNM for a Ph.D.

Last, and certainly not least, thanks to my parents Gary and Margaret Kirby for instilling in me a deep and abiding sense of curiosity and wonder at the world and for patiently answering the resultant barrage of questions.

To Gary and Margaret Kirby

Table of Contents

Chapter 1

Introduction

Since the insightful proposition of Argand (1924) that the high topography and active deformation of Central Asia could be the result of collision between the continents of India and Eurasia, the region has emerged as one of the world's foremost laboratories for the study of intracontinental deformation. From it have emerged such fundamental advances as the concept of 'lateral escape' and the importance of translational motions during continental collision (Molnar and Tapponnier, 1975), the geodynamic role of extension in convergent orogens (Burchfiel et al., 1992), and potential linkages between the development of the Tibetan Plateau and global climate change (Raymo et al., 1988; Ruddiman and Kutzbach, 1989). Each of these problems is intimately tied to the development of high topography in Central Asia (indeed, the topography in the vicinity of the collision zone is arguably the most fundamental expression of the continuing convergence between India and Eurasia), and knowledge of the spatial and temporal evolution of topography within the collision zone would contribute to a refined understanding of a number of these processes. While the continued development of remote sensing technology allows us to quantify topography at greater resolution and in increasingly remote areas, ascertaining the evolution of topography over geologic time scales remains a notoriously difficult task (e.g., England and Molnar, 1990).

This thesis represents an effort to interpret the development and subsequent evolution of the topographic margin of the Tibetan Plateau adjacent to and north of the Sichuan Basin. As such, it is inherently a regional study, and bears the limitations imposed by a restricted geography. However, the study area presents a fundamental enigma, one that challenges conventional modes of mountain building – the topography of eastern Tibet apparently developed with little attendant shortening of the upper crust (Burchfiel et al., 1995; Royden et al., 1997). One of the keys to testing models of plateau formation is to understand both the mechanism of crustal deformation as well as its spatial and temporal distribution. Thus, the locale of the thesis was chosen to address two first-order problems in continental tectonics: the processes of continental

deformation during the formation of orogenic plateaux, and the role of surface processes in the development of the topographic margin of the plateau.

The structure of this introductory chapter reflects the dual nature of the thesis. Each chapter was written as a manuscript intended for publication in professional journals. As such, there is some unavoidable overlap between chapters. This chapter is intended to give the reader an brief introduction to the regional problems in eastern Tibet, provide a larger context from which to gauge the work, and function as a guide to the material contained in each chapter.

Processes of plateau formation

Deformation is typically distributed over a wider region in continental than in oceanic lithosphere due primarily to the ubiquitous presence of anisotropies and to the rheologic properties of silicic crust (Brace and Kohlstedt, 1980). Nowhere is this more evident than in Central Asia, were active deformation extends for ~1000km north and east of the Indian continent (Molnar and Tapponnier, 1975). Although most workers agree that the Tibetan crust nearly doubled in thickness (Chen and Molnar, 1981) as a result of the Indian collision, the manner in which it did so is the matter of some debate. Large-magnitude shortening structures in the Himalaya aside (Hodges, 2000; LeFort, 1975), there is limited evidence for shortening of the upper crust throughout much of Tibet; shortening appears to be limited to ~50% and heterogeneously distributed (Coward et al., 1988) across the high plateau. Fueled by these observations and by geophysical evidence for a fluid middle crust in southern Tibet (Nelson et al., 1996), a generation of geodynamic models now consider the development of a weak mid-lower crust as integral to the formation of flat-topped, steep-sided continental plateaux (Royden, 1996; Royden et al., 1997; Willett and Pope, 1999). For reasons described below, eastern Tibet provides a particularly important place to examine the processes of generating topography along the margins of continental plateaux.

Erosion at plateaux margins

One of the most exciting developments in the field of continental tectonics over the past decade has been the recognition of the profound influence that erosion and

surficial mass redistribution can have on orogenic evolution (e.g., Molnar and England, 1990). Ultimately, topography on the earth's surface is the result of a competition between rock uplift and erosion. Rock uplift fundamentally influences channel gradients and incision rates and thus dictates much of the relief structure of tectonically active landscapes (e.g., Whipple and Tucker, 1999). Rock uplift is itself, however, influenced by the rates and spatial distribution of erosion through the isostatic response to mass removal and through focusing of strain and mass flux in the orogen (e.g., Willett, 1999). This interplay has been proposed to account for much of the morphology of plateau margins (e.g., Masek et al., 1994; Montgomery, 1994). However, detailed investigations of the distribution of rock uplift and its relationship to topography along a plateau margin are extremely limited. The minor role of upper crustal shortening in eastern Tibet makes it an important region in which to assess the role of erosion in influencing the geodynamic and morphologic evolution of the plateau margin.

Tectonic and topographic setting of eastern Tibet

The eastern margin of the Tibetan Plateau in the vicinity of the Sichuan Basin is one of the world's great continental escarpments. Mean elevations rise from ~500m in the basin to ~4000m over a horizontal distance of less than 50km. Regional topographic gradients across this margin typically exceed 10% and rival any margin of the plateau. The margin is deeply dissected by steep bedrock channels that rise on the Tibetan Plateau and drain across the Sichuan Basin to join the Yangtze River. Peak elevations along the topographic front range up to 6500m and define a region of high mountains coincident with the dissected plateau edge. The controls on, and evolution of, this topographic front frame the subject matter of this thesis.

Although the topography in eastern Tibet is impressive, its evolution is enigmatic. Shortening of the upper crust in this region during the Cenozoic appears to have been relatively minor (Burchfiel et al., 1995) and limited to a few tens of kilometers. In addition, the Sichuan Basin contains only a thin veneer of Cenozoic terrestrial sediments and does not appear to have been flexurally loaded during development of the plateau (Royden et al., 1997). Finally, space geodetic campaigns are not able to resolve active

shortening across the margin during the past decade (Chen et al., 2000; King et al., 1997); the eastern plateau adjacent to the Sichuan Basin is effectively linked to south China.

These three observations imply that conventional notions of the processes by which topography is generated in most collisional orogens may not be readily extended to orogenic plateaux. They led Royden and others (1997) to consider the role that a depth-dependent rheology may play in influencing the style, rates, and distribution of crustal thickening during continental collision. The results of their modeling suggest that much of the topography in eastern Tibet could be a consequence of thickening driven by flow within a weak lower crust. This model predicts, in a general way, that topography along the eastern margin may be decoupled from shortening features in the upper crust and may instead reflect the isostatic and dynamic response to thickening in the lower crust.

Structure of the thesis

The overarching goal of the thesis is to interpret the rates and patterns of rock uplift and to ascertain their relationship to topography along this margin of the plateau. The interdisciplinary nature of the problem dictates an approach that spans a range of techniques.

Chapter 2 is an attempt to delineate the rates and distribution of active deformation and rock uplift in the Min Shan, a high-standing mountain range along the margin of the plateau north of the Sichuan Basin. Remnant Pleistocene basins preserved along the western flank of the range allow determination of tilting (and thus, differential rock uplift) rates between the range crest and the western plateau. In addition, we investigate the kinematics and rates of displacement on several fault zones that flank the range. We show that rates of tilting far exceed the maximum allowable shortening across the range (Chen et al., 2000) and that the flanking faults, while active, appear to have slow displacement and exert little control on rock uplift within the range. We further assess the potential role of a simple flexural isostatic response to erosion (i.e. no dynamic feedback) in driving rock uplift within the range and demonstrate that it is likely a small component of the observed rock uplift.

Chapter 3 is an investigation of the long-term denudation rates and their spatial distribution across the margin of the plateau. We utilize low-temperature thermal

histories inferred from $^{40}Ar/^{39}Ar$ thermochronology on biotite and alkali feldspar and (U-Th)/He thermochronology on apatite. We demonstrate that much of the region underwent extremely slow cooling following Mesozoic tectonism until the Late Miocene. In the Late Miocene (ca. 11 Ma), rocks along the margin experienced a rapid cooling that was apparently coincident with exhumation from ~8-10km depth. During the same time period, rocks on the plateau continued to cool slowly, and exhumation appears to be limited to a few kilometers. We argue that the onset of rapid cooling marks the initial development of significant topographic relief in this region and that subsequent denudation of the margin was focused in a narrow region along the topographic front.

Chapter 4 represents an effort to understand the controls on the distribution of stream gradients and bedrock river incision in this region. We utilize the topographic characteristics of drainage basins extracted from a digital elevation model (DEM) in conjunction with field observations to assess downstream changes in channel gradient. The results of this analysis demonstrate that channel gradients, normalized for drainage area, are highest adjacent to the topographic front. Channels flowing into this zone from the west display an increase in relative gradient, while those rising within the zone and flowing east show a decrease in relative gradient. We argue that this spatial distribution of high stream gradients is best explained by active rock uplift focused along the topographic front of the plateau margin. The implied spatial gradients in rock uplift rate have important implications for the present-day controls on topography along the margin of the plateau.

Chapter 5 is an attempt to assess the impact of spatial variations in rock uplift rate on bedrock channel profiles. Although the field site lies outside the region of the thesis, the work evolved in an effort to address issues raised in chapter 4, and is so included here. We develop a theory for the manner in which spatial variations in rock uplift will affect channel profile concavity within the context of the unit stream power incision model (e.g., Howard, 1994). We test the model in the Siwalik Hills of central Nepal, a region of known variation in Holocene rock uplift rates (Lave and Avouac, 2000). Analysis of channel profiles demonstrates that variations in concavity of profiles is dependent on the position and direction of channels relative to rock uplift gradients. We utilize the downstream changes in channel gradient along two of the largest channels to

calibrate parameters in the stream power incision model. Application of this calibrated model to other channels in the region yields estimates of erosion rate that mimic expected variations in rock uplift across a fault-bend fold (e.g., Lave and Avouac, 2000). Thus, the apparent sensitivity of channel gradients to rock uplift in this landscape allow us to extract quantitative information regarding the rates of active deformation directly from topography and lends further confidence to our interpretation of channel profiles in eastern Tibet (Chapter 4).

Chapter 2 was published in the *Geological Society of America Bulletin* in March of 2000 (Kirby et al., 2000) with co-authors Kelin Whipple, Clark Burchfiel, Glenn Berger, Tang Wenqing, Sun Zhiming, and Chen Zhiliang. Chapter 3 is currently in review at *Tectonics* with co-authors Pete Reiners, Mike Krol, Kip Hodges, Kelin Whipple, Ken Farley, Wenqing Tang, and Chen Zhiliang. Chapter 5 is currently in review for publication in *Geology* with co-author Kelin Whipple. Finally, chapter 4 will be submitted to the *Journal of Geophysical Research* with Kelin Whipple as co-author.

References Cited

Argand, E., 1924, La tectonique de l'Asia, Proceedings 13th Int. Geol. Congress, Volume 7: Brussels, p. 171-372.

Brace, W.B., and Kohlstedt, D.L., 1980, Limits on lithospheric stress imposed by laboratory experiments: Journal of Geophysical Research, v. 85, p. 6248-6252.

Burchfiel, B.C., Chen, Z., Hodges, K.V., Liu, Y., Royden, L.H., Deng, C., and Xu, J., 1992, The South Tibetan Detachment System, Himalayan Orogen: Extension Contemporaneous with and Parallel to Shortening in a Collisional Mountain Belt, 41 p.

Burchfiel, B.C., Chen, Z., Liu, Y., and Royden, L.H., 1995, Tectonics of the Longmen Shan and adjacent regions: International Geology Review, v. 37, p. 661-735.

Chen, W.P., and Molnar, P., 1981, Constraints on the seismic wave velocity structure beneath the Tibetan Plateau and their tectonic implications: Journal of Geophysical Research, v. 86, p. 5937-5962.

Chen, Z., Burchfiel, B.C., Liu, Y., King, R.W., Royden, L.H., Tang, W., Wang, E., Zhao, J., and Zhang, X., 2000, GPS measurements from eastern Tibet and their implications for India/Eurasia intracontinental deformation: Journal of Geophysical Research, v. 105, p. 16215-16227.

Coward, M.P., Kidd, W.S.F., Pan, Y., Shackelton, R.M., and Zhang, H., 1988, The structure of the 1985 Tibet Geotraverse, Lhasa to Golmud, *in* Chang, C., Shackleton, R.M., Dewey, J.F., and Yin, J., eds., The Geological Evolution of Tibet, Volume 327, Phil. Trans. Royal Soc. London, p. 307-336.

England, P., and Molnar, P., 1990, Surface uplift, uplift of rocks, and exhumation of rocks: Geology, v. 18, p. 1173-1177.

Hodges, K.V., 2000, Tectonics of the Himalaya and southern Tibet from two perspectives: Geological Society of America Bulletin, v. 112, p. 324-350.

King, R.W., Shen, F., Burchfiel, B.C., Royden, L.H., Wang, E., Chen, Z., Liu, Y., Zhang, X., Zhao, J., and Li, Y., 1997, Geodetic measurement of crustal motion in southwest China: Geology, v. 25, p. 179-182.

Kirby, E., Whipple, K.X., Burchfiel, B.C., Tang, W., Berger, G., Sun, Z., and Chen, Z., 2000, Neotectonics of the Min Shan, China: Implications for mechanisms driving Quaternary deformation along the eastern margin of the Tibetan Plateau: Geological Society of America Bulletin, v. 112, p. 375-393.

LeFort, P., 1975, Himalayas: The collided range. Present knowledge of the continental arc: American Journal of Science, v. 275-A, p. 1-44.

Masek, J.G., Isacks, B.L., Gubbels, T.L., and Fielding, E.J., 1994, Erosion and tectonics at the margins of continental plateaus: Journal of Geophysical Research, v. 99, p. 13,941-13,956.

Molnar, P., and England, P., 1990, Late Cenozoic uplift of mountain ranges and global climate change: chicken or egg?: Nature, v. 346, p. 29-34.

Molnar, P., and Tapponnier, P., 1975, Cenozoic tectonics of Asia: Effects of a continental collision: Science, v. 189, p. 419-426.

Montgomery, D.R., 1994, Valley incision and the uplift of mountain peaks: Journal of Geophysical Research, v. 99, p. 13,913-13,921.

Nelson, K.D., Zhao, W., Brown, L.D., Kuo, J., Che, J., Liu, X., Klemperer, S.L., Makovsky, Y., Meissner, R., Mechie, J., Kind, R., Wenzel, F., Ni, J., Nabelek, J.,

Leshou, C., Tan, H., Wei, W., Jones, A.G., Booker, J., Unsworth, M., Kidd, W.S.F., Hauck, M., Alsdorf, D., Ross, A., Cogan, M., Wu, C., Sandvol, E., and Edwards, M., 1996, Partially molten middle crust beneath southern Tibet: synthesis of project INDEPTH results: Science, v. 274, p. 1684-1688.

Raymo, M.E., Ruddiman, W.F., and Froelich, P.N., 1988, Influence of late Cenozoic mountain building on ocean geochemical cycles: Geology, v. 16, p. 649-653.

Royden, L., 1996, Coupling and decoupling of crust and mantle in convergent orogens: Implications for strain partitioning in the crust: Journal of Geophysical Research, v. 101, p. 17,679-17,705.

Royden, L.H., Burchfiel, B.C., King, R.W., Chen, Z., Shen, F., and Liu, Y., 1997, Surface deformation and lower crustal flow in Eastern Tibet: Science, v. 276, p. 788-790.

Ruddiman, W.F., and Kutzbach, J.E., 1989, Forcing of late Cenozoic northern hemisphere climate by plateau uplift in southern Asia and the American West: Journal of Geophysical Research, v. 94, p. 18409-18427.

Whipple, K.X., and Tucker, G.E., 1999, Dynamics of the stream-power river incision model: Implications for height limits of mountain ranges, landscape response timescales, and research needs: Journal of Geophysical Research, v. 104, p. 17,661-17,674.

Willett, S.D., 1999, Orogeny and orography: the effects of erosion on the structure of mountain belts: Journal of Geophysical Research, v. 104, p. 28,957-28,981.

Willett, S.D., and Pope, D.C., 1999, The mechanics of orogenic plateaus: A crustal problem: GSA Abstracts with Programs, v. 31, p. A-65.

Neotectonics of the Min Shan, China: Implications for mechanisms driving Quaternary deformation along the eastern margin of the Tibetan Plateau

Eric Kirby*
Kelin X. Whipple
B. Clark Burchfiel
Dpartment of Earth, Atmospheric, and Planetary Sciences, Massachusetts Institute of Technology, Cambridge, Massachusetts 02139

Wenqing Tang
Chengdu Institute of Geology and Mineral Resources, Chengdu, Sichuan Province, China

Glenn Berger
Desert Research Institute, 2215 Raggio Parkway, Reno, Nevada 89512

Zhiming Sun
Zhiliang Chen
Chengdu Institute of Geology and Mineral Resources, Chengdu, Sichuan Province, China

ABSTRACT

The Min Shan region, located along the eastern margin of the Tibetan Plateau north of the Sichuan Basin, provides an important natural laboratory in which to study the rates and patterns of deformation and their relationship to mountain building at the margin of the plateau. The topographic margin of the plateau is coincident with a north-trending mountain range, the Min Shan, that stands nearly 2 km above the mean elevation of the plateau (~3500 m in this region). We exploit the preservation of a series of variably deformed Quaternary sediments along the western flank of the range to investigate the Pleistocene-Holocene deformation field within the Min Shan region. Mapping and field observations of remnant alluvial fans of late Pleistocene age indicate that deformation within the Min Shan involved substantial (~10°), rapid, down-to-the-northwest tilting. The geometry of the deposits and the partial preservation of an erosion surface beneath the basin suggest that much of the modern relief of the Min Shan relative to the Tibetan Plateau is a consequence of this late Pleistocene tilting. Rates of tilting inferred from luminescence dating of interbedded loess have been remarkably rapid (~10^{-8} rad/yr). Similarly rapid rates of Holocene differential rock uplift are inferred from tilted lacustrine sediments in the southwestern part of the range. The range is bounded on the west by the Min Jiang fault zone, an east-vergent reverse fault. However, Holocene alluvial terraces in headwaters of the Min River are preserved across the fault in several places, indicating that displacement rates on the Min Jiang fault are <1 mm/yr. Active faulting only occurs along the eastern foot of the range (Huya fault) for a short distance (~60 km), despite 3 km of relief on the eastern range front. The relationship between these structures and the tilting observed in the Min Jiang basin is enigmatic; the faults do not appear to exert a strong control on the rates and pattern of deformation within the basin. A simple flexural model demonstrates that rates of tilting on the western flank of the Min Shan are too high to be simply attributed to an isostatic response to surficial loading and unloading of the lithosphere. Present-day horizontal shortening across the Min Shan is geodetically determined to be less than 2–3 mm/yr, suggesting that only a small part of the observed tilting can be attributed to horizontal shortening. Thus, tilting and concomitant differential rock uplift in the Min Shan appear to require an additional driving component. We suggest that Quaternary deformation along the western Min Shan may reflect the surface response to thickening of a weak lower crust at the margin of the Tibetan Plateau.

Keywords: neotectonics, Tibetan Plateau, mountain building, flexure, Sichuan Basin, lower crust.

INTRODUCTION

Since the recognition that widespread intracontinental deformation within central Asia is the result of the Cenozoic collision of India and Eurasia (Argand, 1924; Molnar and Tapponnier, 1975), there has been a long-standing debate centered on the degree to which crustal thickening within the Tibetan Plateau accommodates convergence between the two continents (cf. England and Houseman, 1986; Tapponnier et al., 1982). Although most workers agree that the present crustal thickness of nearly 70 km and the great elevation (Fielding et al., 1994) of the plateau are the result of the collision (Dewey and Burke, 1973; Harrison et al., 1992; Molnar, 1988), the amount, rates, and style of shortening within Tibet as well as its spatial and temporal distribution remain largely unknown (Burchfiel and Royden, 1991; Coward et al., 1988). Many of the models for Asian deformation predict markedly different kinematics in the region east and northeast of the Indian indenter (Avouac and Tapponnier, 1993; Cobbold and Davy, 1988; England and Molnar, 1990b); thus, one means of distinguishing between competing models is to determine the kinematics of deformation within this region of the plateau. Our first goal therefore is to document the distribution and rates of late Cenozoic deformation in the north-trending mountain range termed the Min Shan—a little-known but important segment of the eastern margin of the Tibetan Plateau north of the Sichuan Basin, in Sichuan Province, China.

Our second goal is to evaluate the processes driving deformation at the margin of the plateau. Along much of the eastern margin there is a lack of correlation between the surface expression of structures and topography (Burchfiel et al., 1995; Royden et al., 1997). Faults and folds are often oblique to, and commonly older than, the topographic margin. These observations—coupled with satellite geodesy (King et al., 1997; Chen et al., 2000) and increasing evidence for a weak lower crust beneath Tibet (Jin et al., 1994; Nelson et al., 1996; Masek et al., 1994a)—led Royden et al. (1997) to suggest that crustal thickening in eastern Tibet may be focused in the lower crust. In this model, rock and surface uplift may be due

*E-mail: ekirby@mit.edu.

GSA Bulletin; March 2000; v. 112; no. 3; p. 375–393; 11 figures; 3 tables.

to isostatic and dynamic responses to lower-crustal thickening and not directly related to horizontal shortening of the upper crust. Our mapping and field observations along the Min Shan suggest that it is difficult to account for the pattern of surface deformation inferred from tilted Quaternary sediments by displacement on recognized structures. Furthermore, rates of late Pleistocene tilting along the western flank of the range far exceed geodetically measured rates of horizontal shortening (King et al., 1997; Chen et al., 2000). Thus, our results suggest the presence of an additional driving force and are permissive of thickening driven by lower-crustal flow.

Our third goal, intimately linked to the other two goals, is to evaluate the morphologic evolution of the Min Shan and, in particular, to ascertain to what degree high mountain ranges along the eastern margin of the plateau may reflect an isostatic response to erosion at the margin. Topographically high mountain ranges commonly occur at the edges of continental plateaus (Fielding et al., 1994) and may be (1) primarily tectonic features related to the dynamics of shortening at the margin (Lyon-Caen and Molnar, 1983; Royden et al., 1997), (2) primarily isostatic features related to mass removal along the topographic front (Masek et al., 1994b; Molnar and England, 1990; Montgomery, 1994) or, (3) some combination of both mechanisms (Burbank, 1992). The lack of large-magnitude shortening across the eastern margin (Burchfiel et al., 1995) makes this an important region in which to test the hypothesis of isostatically generated topography. In this paper, we argue from a simple flexural model that the rates of observed surface deformation in the Min Shan require unreasonably high rates of mass removal by erosion to produce the topography isostatically and thus point to the importance of additional driving mechanisms.

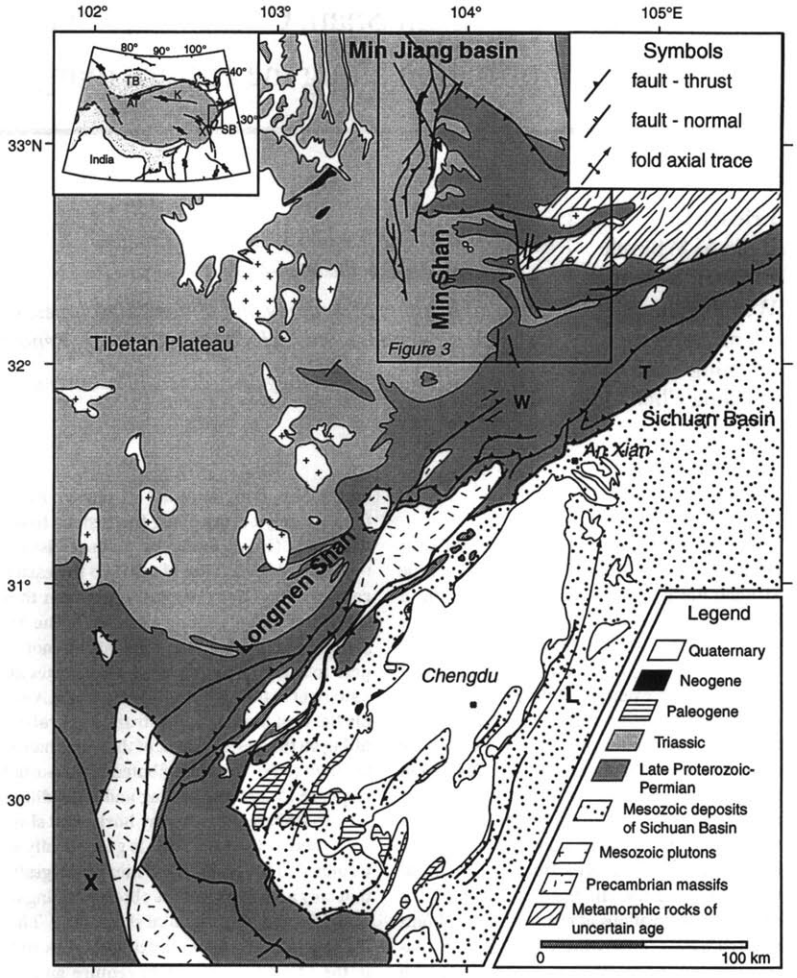

Figure 1. Simplified geologic map of the Longmen Shan region of the eastern Tibetan Plateau. Geology modified after Burchfiel et al. (1995), 1:200 000 geologic maps (Ministry of Geology and Mineral Resources, People's Republic of China, 1991), and our mapping. Inset shows location of the region relative to major tectonic elements of the Indo-Asian collision zone. Abbreviations: AT—Altyn Tagh fault, K—Kunlun fault, L—Longquan anticline, T—Tangwangzhai nappe, TB—Tarim basin, SB—Sichuan Basin, W—Wenchuan-Maowen fault zone, X—Xianshuihe fault.

BACKGROUND

In this section we summarize the salient parts of the late Cenozoic tectonics along the eastern margin of the Tibetan Plateau to set the background for our work in the Min Shan region. We follow Burchfiel et al. (1995) in using the term "Longmen Shan region" to refer to the eastern margin of the Tibetan Plateau along the edge of the Sichuan Basin between the Xianshuihe fault and the west Qinling Shan, and we use the term "Min Shan region" to refer to the margin of the plateau north of the Sichuan Basin (Fig. 1).

Active Tectonics of the Longmen Shan

The topographic margin of the Tibetan Plateau along the Longmen Shan is one of the most impressive continental escarpments in the world; from the Sichuan Basin at 500 to 700 m elevation, the land rises westward to peak elevations exceeding 6000 m over horizontal distances of 40–60 km. This topographic front led a number of workers to suggest that it was the locus of major active shortening (up to 20 mm/yr) between Tibet and south China (Avouac and Tapponnier, 1993; Ratschbacher et al., 1996). Recent results of GPS (Global Positioning System) space geodetic surveys indicate, however, that modern shortening rates across this margin must be less than 2–3 mm/yr and are within uncertainty of zero (King et al., 1997; Chen et al., 2000). Seismicity along this margin is generally restricted to small events ($M < 5$) that occur in a band paralleling the topographic margin (Editorial Board, State Seismological Bureau, 1989). The historic record of earthquakes in this region extends back over 1500 yr and documents a remarkable lack of significant ($M > 4$–5) events (Editorial Board, State Seismological Bureau, 1989), consistent with the slow shortening rates inferred from GPS.

Geologic evidence for active faulting in the northern Longmen Shan is equally scant and appears to be restricted to the Min Shan region (Burchfiel et al., 1995; Chen et al., 1994). Thrust

faults along the topographic front in the northern Longmen Shan (northeast of An Xian along the Tangwangzhai nappe; Fig. 1) are overlapped by Upper Triassic terrestrial clastic rocks, restricting the latest displacement along these faults to Mesozoic time (Burchfiel et al., 1995).

The absence of significant late Cenozoic shortening across the Longmen Shan is corroborated by a distinct lack of foreland sedimentation. Cenozoic deposits are restricted to the southwestern corner of the Sichuan Basin (Fig. 1) and are generally <500 m in thickness. Quaternary sediments in particular consist of a thin (<100 m) veneer in this region and appear to be ponded behind the Longquan anticline (Fig. 1). Although this anticline may be active, definitive evidence is lacking (Burchfiel et al., 1995). Elsewhere throughout the Sichuan Basin, modern sediments are routed to the East China Sea via tributaries of the Yangtze River. Thus, the Sichuan Basin does not appear to have been flexurally loaded during the Cenozoic (Royden et al., 1997). Indeed, in the northwestern corner of the basin (northeast of An Xian, Fig. 1), hogbacks of Mesozoic red beds ramp up toward the plateau, suggesting that the basin may have been flexurally upwarped during the late Cenozoic.

The slow modern velocity field, the lack of a Cenozoic foredeep, and the limited Cenozoic shortening across the Longmen Shan led Royden et al. (1997) to hypothesize that much of the development of this region of the plateau may be the result of eastward flow of weak lower crust from beneath the central plateau. Where this material impinges on the strong crust of the Sichuan Basin, it may focus crustal thickening (and consequent surface uplift) in the absence of significant upper-crustal shortening.

Tectonic Setting of the Min Shan

The Min Shan is a topographically high-standing mountain range that delineates the edge of the Tibetan Plateau for nearly 200 km north of the Sichuan Basin (Figs. 1 and 2A). The range is 40–50 km wide and contains peaks that reach elevations of 5600 m. The mean elevation of the plateau in this region is ~3500 m, and relief on the western flank of the range approaches 2 km (Fig. 2B). Although regional topographic gradients across this margin of the plateau are not as large as along the Sichuan Basin, the eastern flank of the Min Shan drops 3–4 km to the lowlands of the west Qinling orogen (<1000 m) over a lateral distance of 60–80 km.

Despite the impressive mountain front along the eastern Min Shan, active faults occur only along the central 60 km of the range front. Here the Huya fault juxtaposes Devonian–Triassic siliciclastic and carbonate rocks on the west with Proterozoic crystalline basement and cover sequences of the west Qinling orogen to the east (Fig. 3). The fault strikes just west of north and dips steeply (70°–85°) to the west. A series of earthquakes along the fault in 1976 demonstrate that active displacement across the fault is oblique reverse motion with a left-lateral component (Han and Xia, 1980; Jones et al., 1984). Hypocentral locations for these shocks are not well determined, but appear to be between 10 and 15 km deep (Jones et al., 1984), suggesting that the fault remains steep throughout much of the upper crust (Fig. 3).

The Min Shan is bounded along much of its western flank by another reverse fault, the Min Jiang fault zone. The Min Jiang fault zone consists of several strands of high-angle faults (Burchfiel et al., 1995; Chen et al., 1994), the easternmost of which is hereafter referred to as the Min Jiang fault. The Min Jiang fault cuts Quaternary deposits along the headwater reaches of the Min Jiang (jiang = river) and is clearly a recently active structure (Burchfiel et al., 1995; Chen et al., 1994; Tang et al., 1993; Zhao et al., 1994). However, geologic estimates of the magnitude, rates, and sense of displacement vary widely in the literature (cf. Chen et al., 1994; Zhao et al., 1994). Consequently, the significance of the Min Jiang fault in the active deformation field at the edge of the plateau is unknown.

Despite the presence of active faults on either flank of the Min Shan, recent geodetic surveys in the northern Longmen Shan region demonstrate that, within uncertainties of ~2–3 mm/yr, there is no active shortening across the range (King et al., 1997; Chen et al., 2000) (Fig. 2). However, as both the Min Jiang and Huya faults have steep (>60°) westward dips, horizontal shortening associated with active reverse faulting may be minor. It is important to note, however, that the geodetic data restrict any vertical component of deformation associated with shortening across the Min Shan to less than a few millimeters per year. With the exception of the 1976 earthquake sequence on the Huya fault, historic seismicity along the eastern Min Shan appears to be limited to one large (approximate magnitude of 7–8) event in 1879 (Editorial Board, State Seismological Bureau, 1989). Thus, the geodetic measurements are likely representative of the regional velocity field over the past 1000–2000 yr and are consistent with slow horizontal strain accumulation across the range.

Neogene–Quaternary deposits are preserved along the western flank of the Min Shan in the headwaters of the Min Jiang (hereafter referred to as the Min Jiang basin—Figs. 1 and 3). They represent one of the only significant exposures of upper Cenozoic sediment preserved in this region of the Tibetan Plateau. We mapped these deposits and their structural relationships at a scale of 1:100 000 over the course of three field seasons between 1996 and 1998 (Fig. 4). Because the older sediments are progressively more deformed, we are able to place constraints on the displacement across the Min Jiang fault, as well as to evaluate the late Cenozoic deformation field within the Min Shan range itself.

STRATIGRAPHY OF THE MIN JIANG BASIN

Pre-Cenozoic Rocks of the Min Shan

Paleozoic–Mesozoic rocks in the Min Shan region comprise a thick (>4000 m) section of platformal, shallow-water siliciclastic rocks and reef-bearing limestones. We follow Burchfiel et al. (1995) in referring to this region as the Xue Shan platform. In the northern Min Shan, the platformal rocks are continuous to the east with late Proterozoic–Silurian rocks that rest unconformably on metamorphic rocks shown as Precambrian on published Chinese geologic maps (Fig. 3). However, to the west of the Min Jiang fault zone, Carboniferous and Permian rocks thin to nearly half their thickness on the platform. The overlying Triassic rocks change from shallow-water limestones to thick deposits of deep-water flysch characteristic of the Songpan-Garze basin. Thus, the Min Jiang fault zone marked an important paleogeographic boundary in the Paleozoic and early Mesozoic and may have been a structural boundary at this time (Burchfiel et al., 1995).

Pliocene Deposits

The oldest Cenozoic deposits in the study area are a series of small, discontinuous lenses of Tertiary conglomerates. The deposits are restricted to elongate exposures preserved along strands of the Min Jiang fault system (Tp; Figs. 2, 4) and are mapped as late Neogene (Pliocene) on Chinese geologic maps (Ministry of Geology and Mineral Resources, People's Republic of China, 1991). Near Kakagou (Fig. 4), well-indurated, coarse conglomerate is faulted against Triassic limestone. The conglomerate is weathered to a deep red color that is suggestive of its relative antiquity. However, the absolute age of these deposits is unknown, owing to the lack of datable material and/or fossils. Likewise, the original extent of these deposits cannot be confidently reconstructed. Their present geometry along the Min Jiang fault system, however, implies that they may have been restricted basins ponded during initiation of the fault system (Chen et al., 1994).

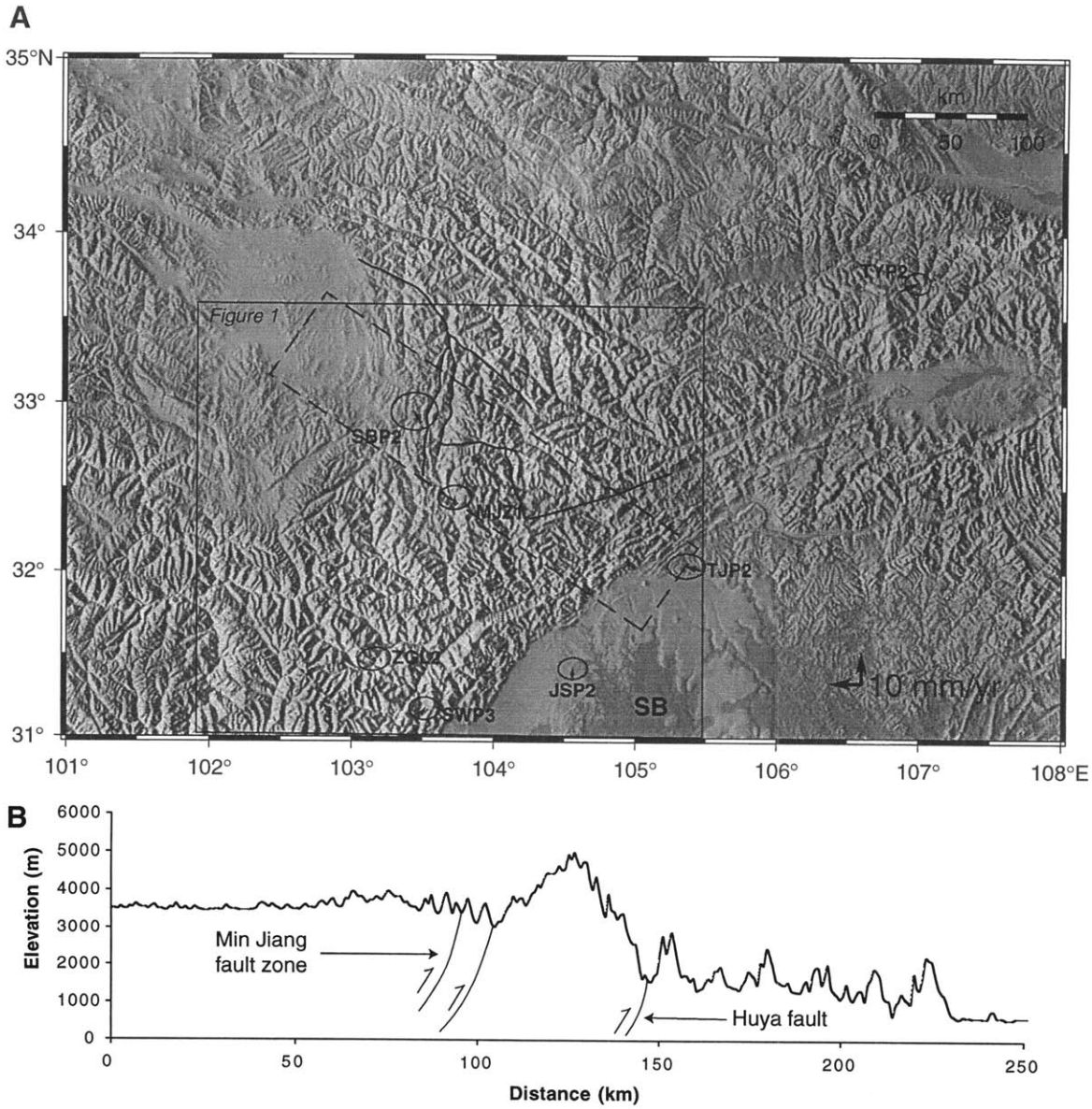

Figure 2. (A) Regional topography (GTOPO30; nominal resolution 1 km) and GPS velocities of the northern Longmen Shan region (Chen et al., 2000). Station names and coordinates can be found in King et al. (1997). Uncertainty ellipses are plotted at 95% confidence intervals. Major structures in the Min Shan are shown for reference to Figure 1 (box). SB—Sichuan Basin. Dashed rectangle shows region of topography used in flexural model (Fig. 10). (B) Schematic cross section depicting position of the Min Shan at the margin of the Tibetan Plateau and its relationship to the Min Jiang and Huya faults. Topography taken from a single profile near the northwest-southeast centerline of the dashed rectangle in A.

Quaternary Deposits

Quaternary deposits in the Min Jiang basin can be subdivided into two broad categories: middle Pleistocene–upper Pleistocene alluvial conglomerates and upper Pleistocene–Holocene alluvium related to the current Min Jiang drainage (Figs. 4 and 5). We designate relative ages with subscripts ranging from 1 to 4 (oldest to youngest). We caution, however, that these relative-age designations are restricted to this basin and should not be confused with similarly designated deposits elsewhere in China (similar labels are commonly used to represent absolute age on Chinese geologic maps) (Ministry of Geology and Mineral Resources, People's Republic of China, 1991).

Middle Pleistocene conglomerates (Q_1 in Fig. 4) form most of the deposits within the Min

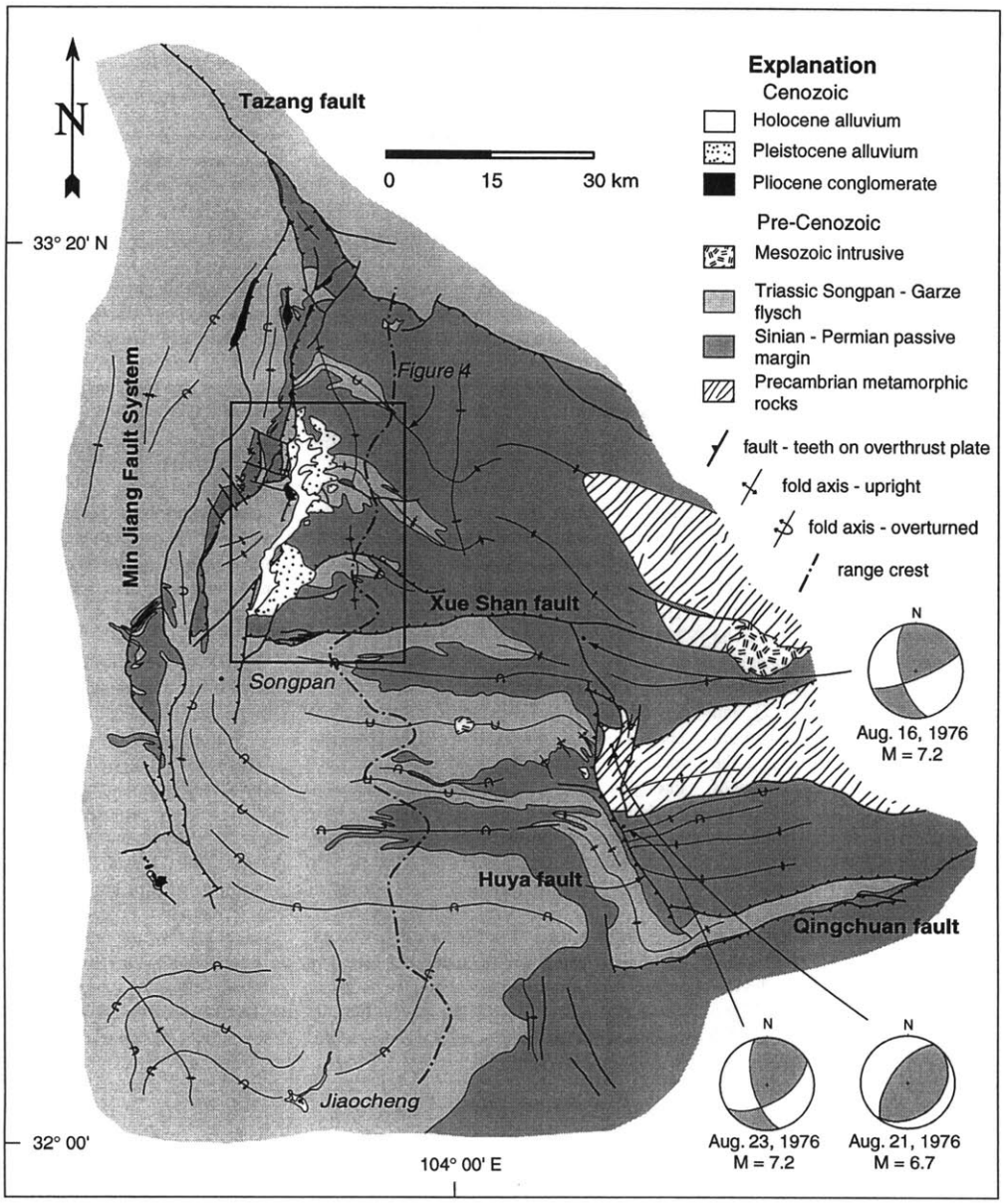

Figure 3. Geologic map of the Min Shan and surrounding region depicting major structures bounding the Min Shan and their relationship to Quaternary sediments in the Min Jiang basin. Dash-dot line represents the approximate trace of the high topography along the range crest. Epicenters and focal mechanisms of the 1976 Songpan earthquake swarm adapted from Jones et al. (1984). Map was compiled from 1:200 000 geologic maps (Ministry of Geology and Mineral Resources, People's Republic of China, 1991) and our work. Location of Figure 4 shown in box.

Jiang basin (Guanyin Shan Formation) (Chen et al., 1994). Q_1 deposits are bounded on the west by the Min Jiang fault. They are composed of a series of west-dipping coarse-gravel and boulder conglomerates, interbedded near their base with 10–20 cm beds of fine sand, silt, and reworked loess. Q_1 deposits are locally well indurated and are often exposed in 10–30 m high cliffs. Clasts within the Q_1 conglomerates range from 5 to 30 cm in diameter and are well rounded and well sorted. Clast composition is primarily limestone (>90%), with minor sandstone and siltstone material. The conglomerates are clast supported and contain a weak to moderate crystalline calcareous cement.

Figure 4. Geologic map of the Min Jiang basin depicting the relationships between the Min Jiang fault and Quaternary sedimentary deposits along the west flank of the Min Shan. Note the lack of faults east of the basin proper. Topographic base was originally 1:100 000. Inset is an equal-area, lower-hemisphere projection of poles to bedding in Q_1 conglomerate showing its uniform west-northwest dip.

Q_1 conglomerates were deposited on a bedrock surface of low relief in westward-thickening wedges. Maximum preserved thickness reconstructed from the mapped geometries is nearly 200 m at the western margin of the deposits. Clast compositions are similar to Mississippian–Permian limestones exposed in the Min Shan and distinct from the turbiditic flysch of the Triassic to the west (Chen et al., 1994). Clast imbrication within the deposits indicates a component of west-directed transport during deposition. The alluvial character of the deposits, their geometry, clast composition, and transport directions all suggest that Q_1 conglomerates were derived from the Min Shan range, and we interpret them as remnant alluvial fans draped along the west flank of the range.

These alluvial fans are now dipping west between 12° and 16° (Figs. 4 and 6A) and have been deeply eroded by the modern streams draining the Min Shan. In the northern end of the basin, near the town of Gonganin, Q_1 alluvial fans are deeply dissected into high remnant hills and mesas (Fig. 6B). Streams draining this part of the Min Shan have incised through the Q_1 and 40–80 m into the underlying Paleozoic carbonates. Thus, total incision along tributaries to the Min Jiang exceeds 200 m since abandonment of the alluvial fans. The conglomerates were deposited on a bedrock surface that currently dips west at a slightly steeper angle than the Q_1 beds (15°–18°) and is preserved along ridge crests east of the mapped extent of Q_1 deposits (Figs. 4 and 6C). The age of this unconformity is unknown.

Q_1 conglomerates are overlain at one locality east of Zhangla (Fig. 4) by 10 m of slightly less indurated gravel. The gravels are separated by a 1–2-m-thick loess bed and have a slight (2°–5°) angular discordance across this bed. The loess has a well-developed reddish weathering profile that extends into the upper 1 m of the Q_1 conglomerates beneath it. Small 0.5–1 cm clay nodules occur at the contact of the loess and the Q_1 conglomerates. We interpret the gravels above this horizon to be a younger, but related, deposit that we have mapped as $Q_{1\text{-}2}$. The angular unconformity and paleosol indicate that this horizon marks an important local hiatus in deposition. Bedding in the $Q_{1\text{-}2}$ gravels above the unconformity locally dips moderately to the east (Fig. 4), similar to the Q_1 gravels below. Both units are folded on the western limb of an open syncline (Fig. 4) and thus predate much of the folding.

Other deposits of probable $Q_{1\text{-}2}$ age are preserved throughout the southern and western parts of the Min Jiang basin. The deposits are generally moderately well indurated gravels, which are slightly reddish in color with a clay-rich matrix. We correlate them with the $Q_{1\text{-}2}$ east of Zhangla primarily on the character of the deposit and the degree of induration. We recognize the uncertainties in such a correlation, but rely on it in the absence of material available for absolute dating. It is possible that deposits mapped as $Q_{1\text{-}2}$ span a relatively large time between the deposition of Q_1 and alluvial terraces of Q_2 age.

$Q_{1\text{-}2}$ deposits are also exposed immediately beneath the Min Jiang fault along the southwestern edge of the Min Jiang basin, west of the town of Zhangla (Fig. 4). They consist of two types of intercalated deposits: rounded alluvial gravels similar to those described above and angular breccias set in a red clay matrix. The gravels strike to the northwest and dip northeast. The breccias typically consist of clasts similar to the Triassic limestone west of the Min Jiang fault. They are interpreted as colluvial material shed off the hanging wall of the fault. The presence of locally derived talus within these deposits suggests that the former western margin of the basin was near its present-day position. A thin veneer of loess and colluvium (Fig. 4) covers $Q_{1\text{-}2}$ deposits throughout most of the southern Min Jiang basin.

Similar alluvial deposits crop out over a wide region in the northwest corner of the Min Jiang basin (west of Gonganin, Fig. 4). Gravels here are moderately well indurated and consist of 10–20 cm cobbles set in a reddish clay matrix. They are interfingered with breccia deposits similar to those exposed in the southwest. Exposure in this part of the basin is generally poor, but where we find exposures of the gravels, they dip moderately to steeply west and are locally folded beneath the Min Jiang fault.

Late Quaternary Alluvial Terraces

Fluvial terraces preserved along the Min Jiang from the headwater region near Gonganin to the town of Songpan (Fig. 2) consist of deposits of late Pleistocene–Holocene age. Between Gonganin and Chuanjiusu, two levels of fill terraces are inset into the older Pleistocene deposits (Chen et al., 1994). The higher terrace (Q_2) is preserved in discontinuous exposures only within the Min Jiang basin, whereas the lower terrace (Q_3) is continuous between the headwater regions and the town of Songpan.

The Q_2 terrace consists of ~40 m of gravel and is best exposed in the northern part of the basin. In this region, Q_2 gravels have only a moderately well developed weathering horizon with a clay-rich matrix confined to the upper 1 m of the deposit. Terrace surfaces preserved along the eastern bank of the Min Jiang dip 2°–3°W and appear to represent tributary fans draining into the Min Jiang. Elsewhere in the northern basin, terrace surfaces are not preserved, but discontinuous exposures of similar alluvium suggest that they were once present along much of the river (Fig. 4).

The Q_2 terrace is also exposed along the western side of the Min Jiang in the southern part of the basin (Fig. 4). Here it consists of ~30 m of alluvial gravel and has a colluvial wedge composed primarily of reworked loess draped atop it. The colluvial wedge contains rare boulders of Triassic limestone and of older Pleistocene conglomerate. The terrace is cut by the Min Jiang fault west of the town of Zhangla and provides an important relative timing constraint on the youngest displacement along the fault (discussed subsequently).

The Q_3 terrace along the Min Jiang is continuous between Gonganin and Songpan (Fig. 4). Within the Min Jiang basin, the terrace consists of 15–35 m of coarse-gravel fill inset into the older deposits (Fig. 6A). The terrace has no appreciable soil development and is overlain by alluvial fans whose sources were the main tributaries in the basin. In the center of the basin, this terrace is locally a strath bench inset into a large landslide that fills much of the valley near the Gamet monastery (Fig. 4). The Q_3 terrace locally onlaps the Min Jiang fault and thus places an upper bound on the timing of displacement across the fault (discussed subsequently).

Despite the continuity of the Q_3 terrace across the southern margin of the Min Jiang basin, the nature of the terrace changes south of Chuanjiusu. Terraces within the Min Jiang basin are entirely alluvial fill, whereas south of the basin margin, the Q_3 terrace is a strath terrace whose tread ranges from 5 to 10 m above the modern channel. The Q_3 terrace along this reach generally has a cap of alluvial gravels that ranges from 5 to 15 m in thickness and is overlain by tributary alluvial fans. South of Songpan, the terrace is not present, but tributary alluvial fans are ubiquitous, and their distal parts are generally truncated by recent incision of the Min Jiang. These fans are probably contemporaneous with alluvial fans preserved atop the Q_3 terrace.

Modern alluvium is confined to the bed of the Min Jiang and its tributaries, consists of gravel- to boulder-sized clasts of carbonate, and is mapped as Q_4 (Fig. 4).

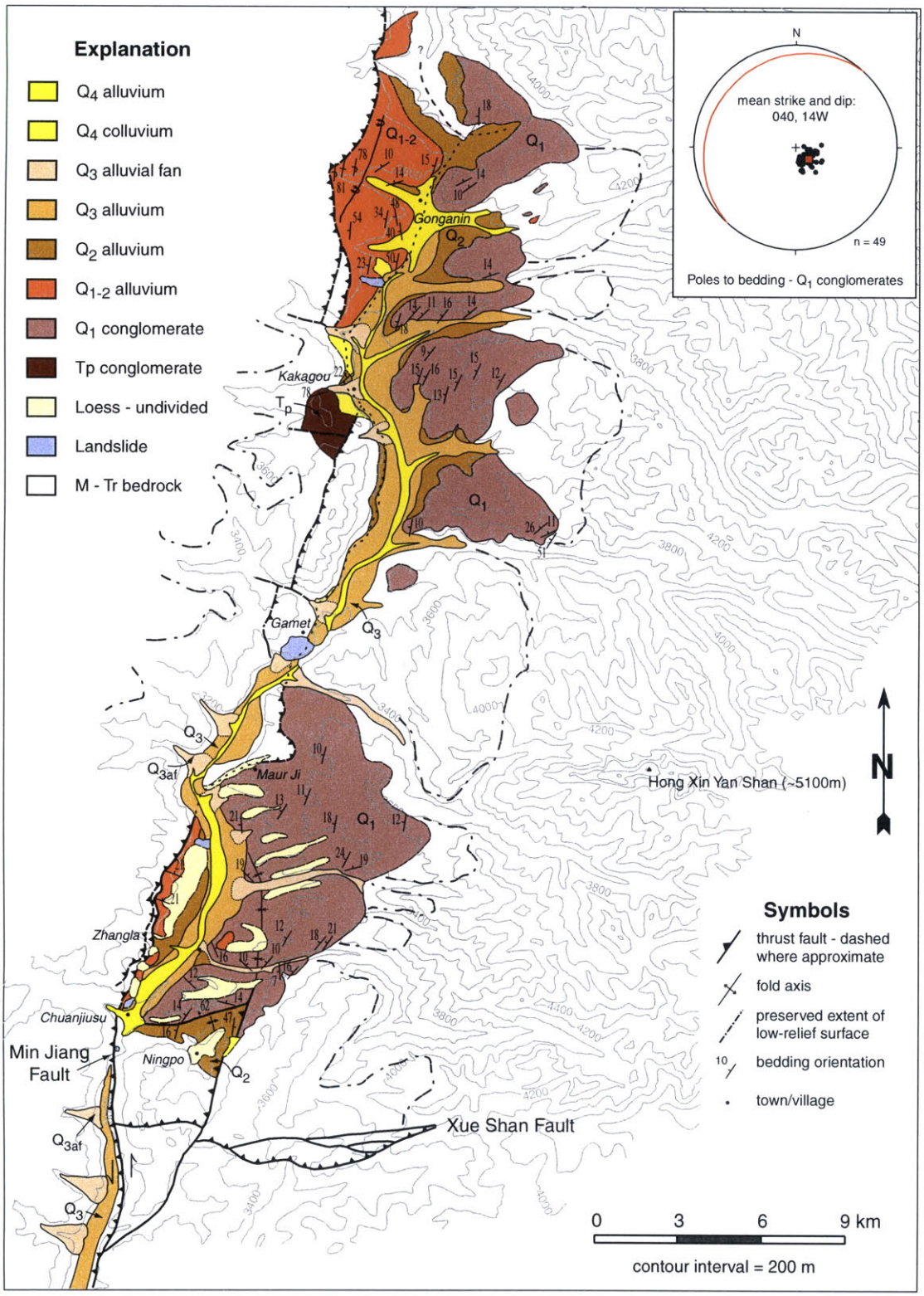
Explanation
Q4 alluvium
Q4 colluvium
Q3 alluvial fan
Q3 alluvium
Q2 alluvium
Q1-2 alluvium
Q1 conglomerate
Tp conglomerate
Loess - undivided
Landslide
M - Tr bedrock
N
mean strike and dip:
040, 14W
n = 49
Poles to bedding - Q1 conglomerates
Gonganin
Kakagou
Garnet
Maur Ji
Zhangla
Chuanjiusu
Ningpo
Min Jiang
Fault
Xue Shan Fault
Hong Xin Yan Shan (~5100m)
Symbols
thrust fault - dashed
where approximate
fold axis
preserved extent of
low-relief surface
bedding orientation
town/village
0 3 6 9 km
contour interval = 200 m

CHRONOLOGY OF THE MIN JIANG BASIN DEPOSITS

In order to assess the absolute age of the deposits within the Min Jiang basin we collected samples for ^{14}C and photon-stimulated luminescence (PSL) dating. The latter technique can be a sensitive means for dating the burial time of detrital grains of sediment (e.g., Aitken, 1998). The particular approach employed here (IRSL, or infrared-stimulated luminescence) produces a signal from fine, silt-sized feldspars. The technique relies on an assumption that the natural luminescence of detrital grains was zeroed by exposure to sunlight prior to final deposition. Although the insolation histories are unknown, we selected samples from facies most likely to represent depositional settings favorable to luminescence resetting (e.g., eolian silt, laminated lacustrine silt). Furthermore, the IRSL method is extremely sensitive to daylight; as little as a few minutes insolation can remove >90% of the IRSL signature (Aitken, 1998). IRSL sampling and analytical techniques are presented in the Appendix.

^{14}C Chronology: Q_2 and Q_3 Terraces

Detrital charcoal from fine-sand beds near the top of the Q_3 terrace north of Zhangla (Fig. 4) provides age constraints for the timing of displacement on the Min Jiang fault. Analytical data and ages are reported in Table 1. Sample EK 97-9 (angular fragment of charcoal 1–2 cm in diameter) was collected from a fine-sand layer interbedded with gravel ~1 m below the surface of the Q_3 terrace and gave a calibrated age of 8129–8420 yr B.P. (2σ). Sample EK 97–8 (multiple detrital charcoal fragments <1 mm in diameter) was collected from a similar sandy lens within the terrace gravels (~0.5 km south of 97–9) and yielded an age of 6670–6944 yr B.P. (2σ). We also collected a single sample of charcoal-rich soil (EK 97–10) from a fine-grained alluvial fan atop the terrace at Zhangla (Fig. 4). Conventional ^{14}C analysis on the bulk organic fraction gave an average age of 2742–2993 yr B.P. (2σ) that places a minimum bound on the age of the terrace. We obtained a fourth sample (EK 97–26) of wood from within a colluvial and landslide deposit draped atop the Q_3 terrace just west of the town of Chuanjiusu (Fig. 4). This sample yielded a conventional ^{14}C age of 14 118–15 720 yr B.P. (2σ), suggesting that some of the Q_3 terrace gravels were deposited in the latest Pleistocene. Although it is possible that this wood may be recycled to some degree, we find it unlikely that woody material would remain intact for many thousands of years at the surface, and we interpret this age as the approximate time of burial of wood within the slide deposit. Taken as a whole, ^{14}C chronology suggests that the Q_3 terrace gravels range in age from >14 000 yr to 6600 yr B.P.

TABLE 1. RADIOCARBON ANALYSES OF CHARCOAL SAMPLES

Sample number	Stratigraphic unit	$\delta^{13}C$ (‰)	^{14}C age (yr B.P. ± 1σ)	^{14}C age (corrected)* (yr B.P. ± 1σ)	Calendric age range (yr B.P. ± 2σ)
EK 97-10†	Q_4 fan	–25.7	2730 ± 75	2810 ± 77	2742–2993
EK 97-8§	Q_3 terrace	–23.4	5945 ± 55	6120 ± 57	6670–6944
EK 97-9§	Q_3 terrace	–12.5	7525 ± 55	7750 ± 57	8129–8420
EK 97-26†	Q_3 colluvium	–22.1	12560 ± 180	12940 ± 185	14118–15720
EK 96-1§	Q_2 alluvium	–25.9	22780 ± 340	23460 ± 350	N.D.

Note: Samples are listed in stratigraphic order (see Fig. 5 for relative stratigraphic sample locations). Reported ^{14}C ages use Libby's half life (5568 yr) and are referenced to the year A.D. 1950. Analytical uncertainties are 1σ and reflect the total uncertainty in the measurement. Calendric ages calibrated using the University of Washington CALIB program (Stuiver and Reimer, 1993). N.D.—not determined.

*The corrected age is the due to the 3% difference between the Libby half life of ^{14}C (5568 yr) and the actual half life (5735 yr).

†Conventional ^{14}C measurement performed at Geochron Laboratories, Cambridge, Massachusetts. Sample 97-10 consists of a charcoal-rich organic soil horizon. The clay/organic fraction was isolated by ultrasound dispersion, filtered to remove rootlets, and treated with dilute HCl to remove carbonate. Sample 97-26 consists of wood. It was washed, split into small pieces, treated with HCl to remove carbonate, and with NaOH to remove humic acids.

§AMS measurement performed by G. Burr at the University of Arizona AMS facility.

Although we were unable to obtain datable material from the Q_2 terrace proper, relationships with alluvial sediments of late Pleistocene age near Ningpo (Fig. 4) suggest that the terraces probably date to the late Pleistocene. We obtained detrital charcoal fragments from east-dipping sands and silts north of the town of Ningpo (Fig. 4). The sediments interfinger with coarse gravels near the modern Min Jiang, and we interpret them as fine-grained alluvial-fan deposits transitional with Q_2 fluvial terraces. Although this correlation is somewhat tentative, the unconsolidated nature of the sediments and the presence of a thin (<5 m) loess cap are consistent with relationships observed on well-preserved Q_2 terraces along the western side of the Min Jiang. Sample EK 96-1 yielded a ^{14}C age of 22 780 ± 340 yr B.P. (1σ), which implies that Q_2 deposits date to the late Pleistocene.

IRSL Chronology: Q_1 Deposits

We also collected three samples for luminescence dating (IRSL method). Two of these samples were collected from loess and silt interbedded with the Q_1 conglomerates and place important bounds on the age of these deposits. A third sample, collected from young lacustrine sediments along the Min Jiang (north of Jiaocheng; Fig. 3), allowed us to test the IRSL multialiquot zeroing assumption. This assumption states that all grains were exposed to daylight for more than tens of minutes prior to final deposition. Analytical techniques for all three samples are presented in the Appendix, dosimetry data are presented in Table 2, and luminescence data are presented in Table 3.

All IRSL experiments employed a two-temperature preheating protocol (Table 3). Separate batches of aliquots (discs, each having ~0.5 mg of grains on an Al substrate) were given different heat treatments as reported in Table 3. The rationale for this protocol is that statistical agreement of the paired equivalent dose (D_E) values is expected to indicate that a thermally stable IRSL signature has been isolated. In this case, the weighted mean D_E value is used in the age calculation (Table 3).

Examples of the IRSL data are shown in Figure 7. Dose-response curves (center) illustrate the reproducibility of individual data points (one for each aliquot). The IRSL signatures (after preheating) for all samples were not large and evinced relatively large scatter. For sample TIBT 98-2 (EK 98-5) and the 170 °C experiment of sample TIBT 98-4 (EK 98-9), short-shine normalization (Ollerhead et al., 1994) did not reduce the scatter significantly, but for the other samples, normalization improved the precision of the extrapolated D_E values. A weighted mean of the plateau segments in Figure 7A was used in age calculation, though the apparent (at 1σ) decline in D_E value with higher preheating is not understood.

Sample EK98-5 (TIBT 98-2) was collected from laminated lacustrine sediments along the Min Jiang, ~50 km south of the Min Jiang basin. Lacustrine sediments are interbedded with tributary alluvial fans along the river, which are correlative with fans of Q_3 age in the headwater reaches (Fig. 4). The resulting apparent age of 14.2 ± 1.7 ka (Table 3) broadly agrees with ^{14}C ages up to ~15 ka for Q_3 terrace gravels in the headwaters of the Min Jiang and lends a measure of confidence to our IRSL results. Silts within the lacustrine deposits appear to have been effectively zeroed by sunlight during transport and residence in the water column.

Two samples were collected from the Q_1 deposits (Fig. 5). Sample EK 98–9 (TIBT 98-4) was collected from fine silts and reworked loess near the base of Q_1 (~15 m above the basal contact with bedrock). The sample yielded an IRSL age of 254 ± 35 ka. A second sample (EK 98-6 / TIBT 98-3) collected from the 1-m-thick loess paleosol atop Q_1 conglomerates near Zhangla

TABLE 2. DOSIMETRY DATA FOR IRSL SAMPLES FROM THE MIN JIANG BASIN

Sample (TIBT)	Water*	K_2O (wt%) (±0.05)	C_t§ ($ks^{-1}\cdot cm^{-2}$)	C_{th}§ ($ks^{-1}\cdot cm^{-2}$)	Th (ppm)	U (ppm)	*b* value# $pGy\cdot m^2$	Dose rate** (Gy/k.y.)
98-2	0.10 ± 0.05	2.13	0.712 ± 0.010	0.403 ± 0.037	10.84 ± 0.98	2.46 ± 0.30	0.923 ± 0.091	3.82 ± 0.23
		2.18†	0.674 ± 0.010	0.285 ± 0.020	7.68 ± 0.70	3.03 ± 0.20		
98-3	0.18 ± 0.03	2.43	0.8540 ± 0.0098	0.495 ± 0.036	13.32 ± 0.97	2.81 ± 0.29	1.0 ± 0.1	4.28 ± 0.16
		2.85	0.836 ± 0.010	0.469 ± 0.033	12.6 ± 1.0	2.87 ± 0.20		
98-4	0.10 ± 0.05	1.05	0.4858 ± 0.0079	0.164 ± 0.022	4.41 ± 0.59	2.51 ± 0.18	1.0 ± 0.1	2.83 ± 0.19
		2.26†	0.710 ± 0.048	0.323 ± 0.042	8.7 ± 1.2	3.03 ± 0.20		

*Estimated average historic ratio of weight of water/weight of dry sample, based on measurements of moist collected samples and laboratory saturated samples (3 samples per IRSL sample). Uncertainties here and elsewhere are ±1σ.

†From top to bottom, estimated uncertainty in these values is ±0.09 and ±0.25.

§Total and thorium count rates from finely powdered samples for thick-source-alpha-particle-counting (TSAC) method (Huntley and Wintle, 1981). $C_u = C_t - C_{th}$. Equations for the use of these count-rate values in the calculation of dose rate are given by Berger (1988). A second row of data corresponds to the average values from sediment surrounding the IRSL sample at a radius of 12–23 cm. These data are used to calculate the γ dose-rate component.

#Alpha effectiveness factor (Huntley et al., 1988; Berger, 1988). Values of 1.0 are estimated (from this and other projects).

**Calculated with the conversion factors and equations given by Berger (1988), and includes a cosmic ray component varying from 0.04 to 0.14 with estimated average depth, from the data of Prescott and Hutton (1988). Note that the dose rates are typical of most sediments (2–4 Gy/k.y.).

TABLE 3. IRSL DATA AND AGES FOR LUMINESCENCE SAMPLES

Sample (TIBT)	Preheat*	D_E† (Gy)	Time§ (s)	Age (ka)
98-2	135 °C/2d	61.3 ± 4.1	1–40	
	155 °C/2d	49.3 ± 3.4	1–40	
	Weighted mean D_E =	54.2 ± 5.9		14.2 ± 1.7
98-3	150 °C/2d	710 ± 180	20–60	
	170 °C/2d	640 ± 160	1–35	
	Weighted mean D_E =	670 ± 120		157 ± 28
98-4	140 °C/2d	730 ± 130	1–15	
	160 °C/2d	710 ± 130	1–15	
	Weighted mean D_E =	719 ± 92		254 ± 35

Note: The polymineralic 4–11 μm size fraction was used for all IRSL measurements. IRSL was detected at the 420 ± 20 nm spectral region (bandpass 390–470 nm at 1% cut). All bleaching was for 3 hr with >780 nm solar spectrum passed (based on the bleaching protocol introduced by Huntley and Clague, 1996). Applying the heat treatment after bleaching corrects for any possible thermal-transfer effect (Ollerhead et al., 1994), an apparently negligible effect with these samples.

*The chosen prereadout annealing. For all samples, the weighted mean D_E is used for age calculation (see text).

†Weighted mean equivalent dose plus average error over time interval in next column. A weighted-saturating-exponential regression and error model (Berger et al., 1987) was employed for all samples. For some samples, interaliquot scatter was minimized by short-shine normalization (to natural signals) (Ollerhead et al., 1994).

§The readout (LED-on) time interval for which D_E is calculated (e.g., Fig. 7).

(Fig. 4) yielded a luminescence age of 157 ± 28 ka. Without independent age determinations, the IRSL results must be taken as a best approximation of the depositional age. However, we note that both of our age determinations fall within known periods of loess deposition in north-central China (Kukla, 1987). Together, these samples indicate that most of the sedimentation in the Min Jiang basin took place in a short time period between ca. 250 ka and 160 ka.

Chen et al. (1994) reported two thermoluminescence (TL) ages of 158 ± 12 ka and 830 ± 69 ka for samples from the Guyian Shan Formation (mapped as Q_1; Fig. 4). The first sample was taken "from the base of the loess" covering the formation and therefore may be correlative with the paleosol between Q_1 and Q_{1-2} (157 ± 28 ka). Their second sample was taken "50 m down in the Guyian Shan Formation." Chen et al. (1994) provided no information about the material in the horizon sampled, except that formation "is composed of thick beds (1–3 m) of conglomerate interbedded with thin (10–30 cm) beds of sandstone." Considering the likelihood of rapid (poor TL-zeroing) deposition in these types of deposits and the general question of the upper limit of TL dating techniques (Berger, 1995; Prescott and Robertson, 1997), we cannot assess the accuracy of the older TL age, except that it is likely an overestimate. Our ages are also significantly younger than ages typically assigned to "Q_1" deposits throughout southwestern China (ca. 1.6–0.6 Ma) (Ministry of Geology and Mineral Resources, People's Republic of China, 1991), which suggests caution in interpreting absolute age from regional correlation of terrestrial Quaternary deposits in western China.

Our results further suggest that periods of deposition were tied to glacial-interglacial cycles. The onset of Q_1 deposition occurred shortly prior to ca. 250 ka and appears to coincide with oxygen isotope stage 8 (Imbrie et al., 1984). Loess deposition between Q_1 and Q_{1-2} (ca. 160 ka) coincides with the stage 6 termination (Imbrie et al., 1984), and this loess may be correlative with the L_2 loess of the Upper Lishi Formation in well-studied sections on the Loess Plateau (Kukla, 1987). Aggradation of Q_2 fluvial terraces is not well dated in the Min Jiang basin, but may date to ca. 22 ka (e.g., ^{14}C from Ningpo sediments), near the time of the last glacial maximum (Imbrie et al., 1984). Aggradation of the Q_3 terrace occurred between ca. 15 ka and ca. 6–7 ka, coincident with isotope stage 2. Thus, fill-terrace development along the headwater reaches of the Min Jiang was apparently coincident with the last glacial period. Incision of the Min Jiang into the Q_3 terrace gravels appears to postdate 6 ka. These results are striking in their correlation to late Pleistocene climatic oscillations (Imbrie et al., 1984) and suggest that late Quaternary terrestrial deposition in the Min Jiang basin was closely coupled to changing sediment and water flux during glacial-interglacial cycles.

QUATERNARY FAULTING IN THE MIN SHAN

Quaternary deposits within the Min Jiang basin are variably deformed (Fig. 4) and place important constraints on the kinematics and rates of Quaternary deformation in the Min Shan. We first consider the recent and active displacement along the Min Jiang fault and then examine several important structures within and east of the range.

Min Jiang Fault

The Min Jiang fault zone consists of several strands of high-angle reverse faults that strike approximately due north and parallel the western

side of the Min Shan for nearly 100 km. The easternmost strand bounds the western margin of the Min Jiang basin and juxtaposes Triassic limestone and flysch with terrace deposits along the Min Jiang river (Chen et al., 1994; Tang et al., 1993; Zhao et al., 1994). Although many of these authors consider the fault to be active, recent GPS results from a station west of the fault zone (station SBP2; Fig. 2) suggest that short-term displacement rates are less than several millimeters per year and within uncertainty of zero (Chen et al., 2000; King et al., 1997). In addition to uncertainty regarding the Holocene slip rates of the fault, previous workers disagreed on the sense of displacement. All have agreed that there is a strong component of shortening across the fault, but the strike-parallel component has been interpreted as both dextral and sinistral (cf. Chen et al., 1994; Zhao et al., 1994). We mapped the easternmost segment of the fault (herein referred to as the Min Jiang fault, sensu stricto) from north of Gonganin (Fig. 4) to the town of Songpan (Fig. 3).

The southern part of the Min Jiang fault follows the eastern side of the Min Jiang valley between the towns of Chuanjiusu and Songpan (Figs. 3 and 4). The fault, although not well exposed, offsets tributary drainages and gullies along the eastern valley wall. Seven of nine tributary gullies along this stretch of the fault appear to be deflected in a manner consistent with a component of left-lateral displacement along this segment of the fault (Fig. 6D). We were unable to map the fault south beyond Songpan, although a series of northwest-striking folds in the Triassic appears to be continuous across the projection of the Min Jiang fault (Fig. 3). Thus, we infer that the displacement on the fault diminishes along strike to the south or is transferred to distributed shortening.

Along the southern part of the Min Jiang basin, a north-striking, west-dipping splay of the Min Jiang fault (herein named the Ningpo fault after a nearby village and monastery) juxtaposes fine-grained sands and gravels in its hanging wall (Q_2 in Fig. 4) with the Q_1 conglomerates to the east. Gravels west of this fault are warped into an asymmetric anticline with a north-trending axial trace (Fig. 4). The Ningpo fault can be followed as a discrete break between the Q_1 and Q_2 deposits for ~1 km to the north, whereupon the trace of the fault transfers into the axial trace of an open syncline (Fig. 4) within the Q_1 gravels. The geometry of the folding within both the Q_1 and Q_2 deposits suggests that the fault has a component of west-side-up, reverse displacement, akin to the Min Jiang fault. It is noteworthy that this is the only part of the basin where a fault coincides with the eastern basin margin.

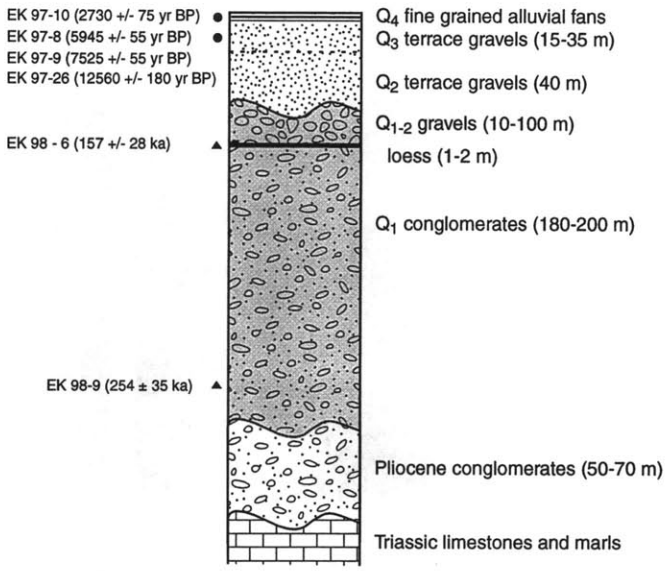

Figure 5. Schematic composite stratigraphic column of Tertiary–Quaternary sediments of the Min Jiang basin. Coarse pattern represents cobble to boulder conglomerates along Min Jiang fault (white) and Q_1 alluvial-fan conglomerates (gray). Loess interlayer is shown as heavy black line. Fluvial-terrace gravels of modern Min Jiang drainage (Q_2 and Q_3; fine-dot pattern) are overlain by Q_4 alluvial fans (ruled pattern). Approximate sample locations are shown along the left side of the column (radiocarbon—circles, IRSL—triangles).

The Ningpo fault is joined by an east-trending fault east of Chuanjiusu (Fig. 4). This fault dips ~60°N and is marked by a 10–20-cm-wide gouge zone within the Q_2 sediments in the valley bottom. The separation on the fault appears to be north side up, and the fault may have a right-lateral component. The fault appears to transfer displacement between the Min Jiang and Ningpo faults, some of which may be accommodated by folding of Q_2 sediments west of the Ningpo fault.

The Min Jiang fault itself is best exposed in a small drainage west of the town of Zhangla, in the southern end of the Min Jiang basin (Fig. 4). Here the fault dips 55°–65°W and places brecciated Triassic limestone above Q_2 terrace gravels. A 1–3-cm-wide zone of clay-rich red gouge marks the fault zone. The Q_2 terrace is inset along this segment of the Min Jiang valley into older Q_{1-2} gravels. These deposits are mixed alluvial gravels and breccias of angular limestone clasts derived from the Triassic in the hanging wall of the Min Jiang fault.

Approximately 4 km north of Zhangla, the Q_{1-2} gravels pinch out, and the fault places limestone directly over the Q_1 conglomerate. The fault itself is not well exposed along this stretch, but its mapped trace suggests that it dips moderately to the west (Fig. 4). From this point north, there is little evidence for recent displacements along the Min Jiang fault. We infer that the trace of the fault parallels the linear range front between Gamet and Kakagou (Fig. 4); however, exposure is poor along the steep forested slopes. On the western side of the ~4000 m ridge between Gamet and Kakagou, an east-dipping splay of the fault juxtaposes the Triassic with Pliocene conglomerates (Chen et al., 1994), indicating that this strand of the fault zone is relatively young. However, we were unable to find any scarps or morphologic evidence that this splay is active at present. The Triassic limestone between the two strands is interpreted as a pop-up block within the Min Jiang fault zone (Fig. 4).

North of Kakagou, a second strand of the Min Jiang fault zone bounds the western edge of the Min Jiang basin (Fig. 4). This fault is well exposed in the drainage west of Gonganin, dips ~45°W, and places Triassic limestones above Q_{1-2} alluvium. The Q_{1-2} gravels are exposed over ~15 km^2 along the western side of the Min Jiang valley headwaters. Gravels within this subbasin generally dip moderately west and are locally folded into an overturned footwall syncline beneath the western fault strand. They appear to be juxtaposed with Q_1

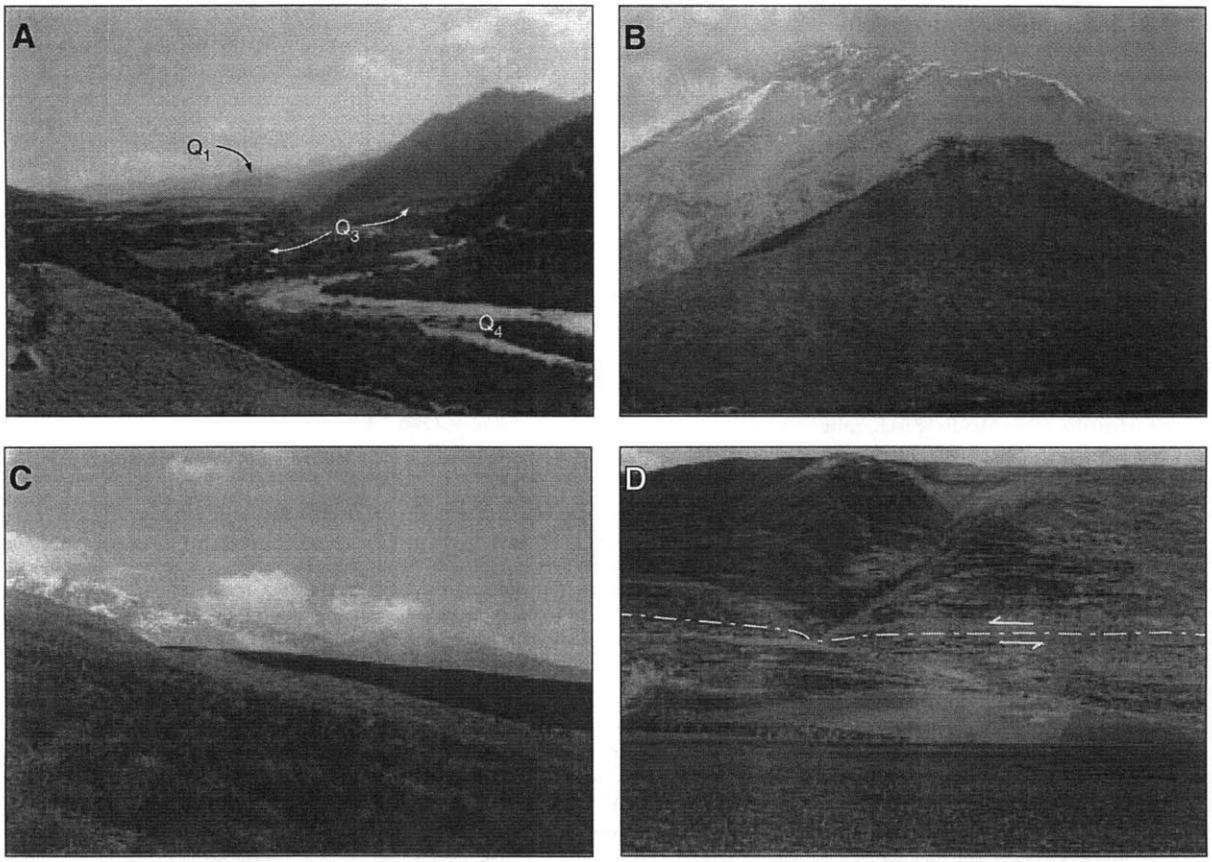

Figure 6. Field photographs of sediments within the Min Jiang basin (A–C) and of the Min Jiang fault (D, E). (A) Looking north at the central Min Jiang basin. West-dipping ridges in the background are composed of Q_1 conglomerates dipping ~14°. Alluvial sediments (late Pleistocene-Holocene) of the Min Jiang river (Q_3, Q_4) fill the valley in the near midground. (B) View looking north-northeast at remnant Q_1 (mesalike hill in midground) in the northern Min Jiang basin. Hill is ~170 m high. Ridge in background is composed of west-dipping Triassic limestones. (C) Tilted bedrock surface beneath basin extends along ridge tops toward crest of range. Photograph is looking south along the eastern edge of the Q_1 conglomerates. Snow-capped peak is Hong Xin Yan Shan (~ 5100 m). (D) Shutter ridge along the southern Min Jiang fault indicative of a component of left-lateral displacement. Trace of fault shown in white. The terraced fields at the base of the ridge are on a young alluvial fan built across the fault trace. View is to the east. (E) View to the southeast of high erosion surface west of the Min Jiang fault (highlighted by arrow). Min Jiang fault runs along base of ridges (dashed white line). The flat, linear ridges in the foreground at left are Q_2 terraces preserved in the headwaters of the Min Jiang.

conglomerates exposed on high hilltops east of the Min Jiang. However, the contact is obscured by modern alluvium. We infer from the mapped geometries that the eastern strand of the Min Jiang fault forms the eastern boundary of this subbasin. The exposure in the steep forested hillslopes north of the drainage divide is poor, and consequently the northern extent of this structure is uncertain. However, the western strand of the Min Jiang fault clearly continues to the north, where it juxtaposes Triassic limestones and Pliocene gravels (Fig. 4). Our interpretation of these geometries is that much of the displacement on the eastern Min Jiang fault transfers to the western strand across the subbasin of Q_{1-2} gravels.

Long-Term Displacement on the Min Jiang Fault

The morphology of the Tibetan Plateau to the west of the Min Jiang fault places loose bounds on the total displacement across the fault. Preserved remnants of a low-relief erosion-surface cap ridge crests west of the Min Jiang fault (Figs. 4 and 6D). This surface is ~200–300 m above the modern valley of the Min Jiang. Although bedrock surfaces are continuously evolving elements in an active landscape, the low relief and partial preservation of the surface suggest that erosion rates on the surface proper are probably low. We interpret the surface as the western continuation of the low-relief surface that floors the Min Jiang basin. This correlation must be considered tentative, but, if correct, implies a net throw on the Min Jiang fault of between ~350 and ~750 m. Thus, the Min Jiang fault does not appear to have a significant amount of displacement across it in the late Cenozoic.

Timing of this displacement is, however, uncertain. The age of the erosion surface in the Min Shan is essentially unknown. Our mapping indicates that it must be older than the Q_1 conglomerates (ca. 250 ka), but its relationship to the Pliocene(?) deposits is unclear. Regionally, much of the surface of the northeastern Tibetan Plateau is morphologically similar: a low-relief surface cut on vertically foliated Triassic flysch. However, the few Tertiary sediments that exist are not well dated. Consequently, all we can determine is that reverse-sense displacement on the Min Jiang fault appears to be late Cenozoic, and the initiation of movement likely predates the deposition of Q_1. If we assume that the Pliocene basins along the fault zone mark the onset of displacement, long-term slip rates must be significantly less than 1 mm/yr. We conclude that shortening across the Min Jiang fault is likely to have been relatively minor during the Quaternary.

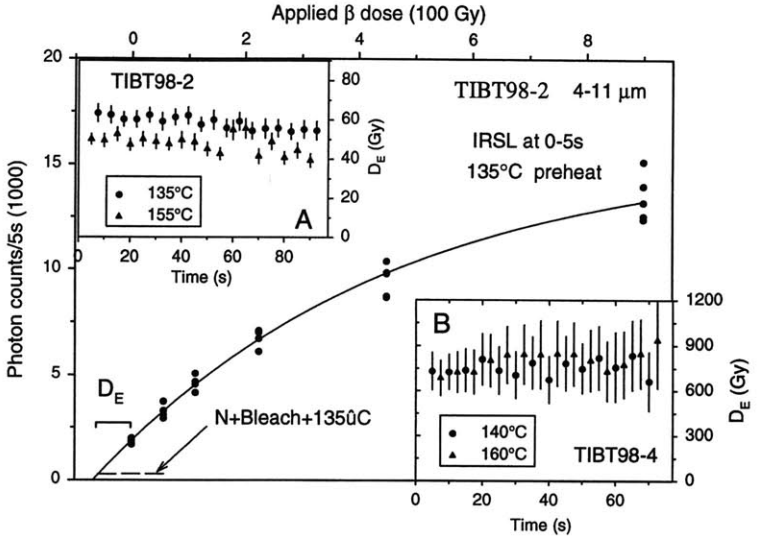

Figure 7. Illustrative luminescence (IRSL) dose-response curve (center) and plots of equivalent-dose (D_E) vs. readout time (inserts A and B). A weighted-saturating-exponential regression model was used for all samples. Error bars on the D_E plots are ±1σ. Equivalent-dose data for 155 °C (inset A) and 160 °C (inset B) are shifted by +2.5 s for clarity of plotting.

Terrace Profiles and Recent Displacements Along the Min Jiang Fault

The modern Min Jiang and associated Q_3 (Holocene) terrace cross the Min Jiang fault in three places within the study area (Fig. 4). In each locality there are no visible breaks or offsets in the terraces. Although this continuity suggests that there has been little displacement on the fault in Holocene time, we surveyed the modern channel and terrace profiles to assess whether low rates of motion on the fault were manifested in changes in the gradient of the channel system and/or terraces (e.g., Pazzaglia et al., 1998). Details of the surveying procedure are given in the Appendix.

The modern channel and Q_3 terrace surface onlap the fault just southwest of the town of Maur Ji (Fig. 4). The terrace gravels are unusually well indurated here, and the channel is fairly narrow. However, there are several cold springs and associated tufa mounds that mark the trace of the fault, and we infer that the competence of the gravels in this locality reflects the local groundwater flux. The terrace surface does not appear to be deformed within the resolution of our survey (~2 m; see Appendix). The terrace surface is nearer to the modern channel along this reach of the Min Jiang (Fig. 8), however, and we interpret this proximity as reflecting the increased stream gradient as the river flows over resistant limestone. Approximately 5 km north, the fault crosses back to the western side of the Min Jiang and is buried beneath a large landslide mass just south of the Gamet monastery (Fig. 4). This slide mass is composed of angular, shattered blocks of Triassic limestone, and onlap relationships between Q_3 terraces on either side of the slide mass indicate that the slide predates the terrace. Both of these relationships suggest that the Min Jiang fault has had little displacement along it during Holocene time.

South of Chuanjiusu, the fault crosses the river for a third time and is also obscured by a small landslide. There is a small strath terrace beveled into the toe of the slide, which appears to be continuous with the Q_3 terrace. Previous workers suggested that the Q_3 terraces were unusually high along this reach of the Min Jiang, a fact they attributed to recent displacement on the adjoining Xue Shan fault (Chen et al., 1994; Tang et al., 1993); our survey fails to confirm this conclusion. The Q_3 terrace is continuous between Chuanjiusu and Songpan (Fig. 8). Several large alluvial fans onlap the terrace surface near the mouths of larger tributary streams. Although there is significant relief (up to 80 m) on the fan surfaces, they do not represent warping of the main terrace tread.

Mapped relationships between the Min Jiang fault and terraces along the Min Jiang indicate that the youngest displacement on the fault is bracketed between deposition of the Q_2 gravels and the Q_3 terrace. There does not appear to have been significant displacement on the fault during the past ~7000 yr. Given the uncertainties of our sur-

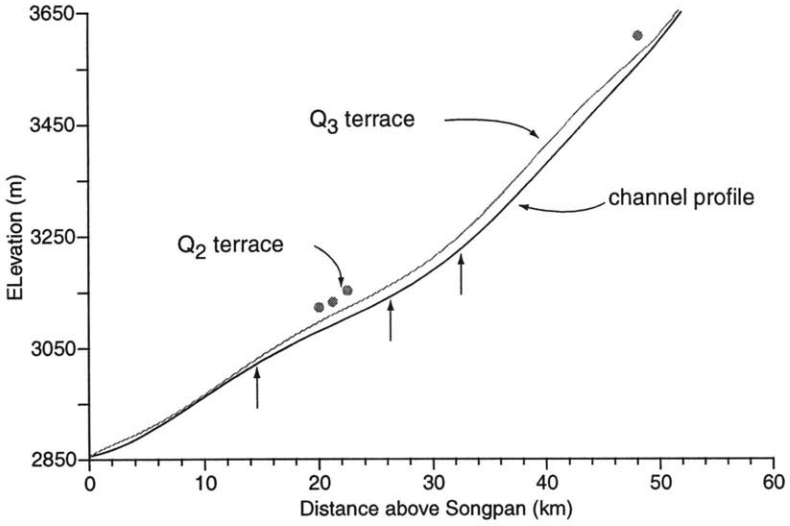

Figure 8. Longitudinal profile of the Min Jiang (black) and Q_3 terrace surface (gray) surveyed between Gonganin and Songpan. Gray dots represent discontinuous Q_2 terrace surfaces. Arrows show the intersection between the trace of the Min Jiang fault and the river channel. Note the smooth transition of the Q_3 terrace across the northern two intersections. Downstream of the final intersection, the channel steepens and the terrace undergoes a transition to a bedrock strath bench ~1–3 m above the river. This change may reflect slight differential rock uplift between the hanging wall and footwall of the Min Jiang fault.

vey (±2 m), there is no appreciable deformation of the Q_3 terrace, requiring Holocene displacement rates to have been less than ~1 mm/yr. This conclusion is consistent with the short-term rates observed in the geodetic data (King et al., 1997). However, the Min Jiang fault cuts Q_2 (late Pleistocene) gravels west of Zhangla (Fig. 4). These relationships are consistent with displacement occurring during moderate to large seismic events with long recurrence intervals (>7000 yr). In addition, the transition from alluvial to strath terraces south of Chuanjiusu coincides with the point where the valley of the Min Jiang is on the hanging-wall block and may reflect bedrock incision in response to slightly increased rates of rock uplift. Although this incision may be an indication of activity on the Min Jiang fault, a quantitative assessment of this hypothesis is beyond the scope of this paper.

Huya Fault

The structural position of the Huya fault along the eastern flank of the Min Shan (Fig. 3) and the historic seismic activity along it (Jones et al., 1984) suggest that this fault may play an important role in active deformation along the Min Shan. However, the mapped extent of the fault (Ministry of Geology and Mineral Resources, People s Republic of China, 1991) along the central ~60 km of the range (Fig. 3) suggests that displacement diminishes along strike or is transferred to distributed deformation. In order to assess these possibilities, we examined the Huya fault in reconnaissance fashion along much of its length. The central segment of the fault crops out along the Fu Jiang, where it dips steeply west (70°–90°) and juxtaposes Paleozoic limestones of the Xue Shan platform with metamorphic rocks mapped as Precambrian (Fig. 3). These geologic relationships (younger over older) are unusual for a reverse fault and suggest that the Huya fault may have a pre-Cenozoic ancestry. Along the valley of Fu Jiang, the fault cores a steep rugged canyon and is spatially associated with numerous rockfalls and landslides, the most recent of which are presumably the result of the 1976 earthquakes (Jones et al., 1984).

The Huya fault terminates to the north against the Xue Shan fault and to the south against the Qingchuan fault (Fig. 3). These relationships at the terminations of the Huya fault have important implications for the transfer of displacement along the eastern range front of the Min Shan. Although it is possible that the Huya fault is a blind structure along the range front north of the Xue Shan fault, the apparent continuity of Paleozoic and Mesozoic units across the range front (Fig. 3) suggests that the total amount of displacement must be relatively small. This geometric relationship at the north end of the Huya fault requires that displacement across it must decrease along strike to the north or be accommodated by distributed deformation between the Xue Shan and Tazang faults (Fig. 3).

A similar relationship exists at the southern end of the Huya fault where Triassic rocks west of the fault are folded around its southern termination and are continuous with Triassic rocks along the Qingchuan fault (Fig. 3). Although the Qingchuan fault makes a remarkably linear trace on satellite images (Fig. 2), geodetic results (Chen et al., 2000; King et al., 1997) suggest that active displacement on the Qingchuan fault is restricted to a few millimeters per year of right-lateral displacement. Our reconnaissance observations of undeformed Pleistocene terraces along the Fu Jiang (E. Kirby, unpublished data) suggest that shortening is negligible. Although the Qingchuan fault may represent a component of right-lateral shear northeast of the topographic margin of the plateau, it does not appear to absorb displacement along the Huya fault. Thus, displacement along the southern Huya fault is likely transferred to small, discontinuous structures of similar orientation in the southern Min Shan (Fig. 3).

Xue Shan Fault

The Xue Shan fault is an west-trending zone of faults that terminate against the Min Jiang fault north of the town of Songpan (Figs. 3 and 4). The fault extends beyond the modern topographic margin of the plateau into the foreland, where it carries Paleozoic rocks in both its hanging wall and footwall (Fig. 3). These geometries suggest, but do not require, relatively minor displacement across the fault. At its eastern end, the Xue Shan fault is intruded by a Mesozoic pluton, indicating that much of the displacement predates Mesozoic magmatism (Ministry of Geology and Mineral Resources, People's Republic of China, 1991). We were unable to verify proposed recent activity along the Xue Shan fault (Tang et al., 1993) near the crest of the range. Such displacement, if present, appears to be limited, and we interpret the Xue Shan fault as a Mesozoic structure that has played a minor, if any, role in Cenozoic deformation within the Min Shan.

RATES AND PATTERNS OF SURFACE DEFORMATION IN THE MIN SHAN

In spite of the apparently minor displacement along the Min Jiang and other faults west of the Min Shan, there is abundant evidence for tilting of Pleistocene–Holocene markers within the range. In this section we describe tilting recorded

in two places within the western Min Shan: (1) in young lacustrine sediments along the Min Jiang and (2) within the Min Jiang basin. In both localities, tilting is present over 10–20 km wavelengths and does not appear to be directly associated with exposed faults.

Recent Tilting in the Southern Min Shan

Recent tilting is recorded in the southwestern Min Shan in lacustrine sediments north of the Diexi landslide. The Diexi landslide is a large (~1 km^3) slide mass that dammed the Min Jiang drainage near the village of Jiaocheng (Fig. 3). This site is located near the epicenter of a moderate-sized earthquake in 1933 that initiated a rockslide obliterating the village of Diexi (Chen et al., 1994). The prehistoric slide, however, is preserved on both sides of the valley and appears to have dammed the entire Min Jiang. The surface of the slide is ~200 m above the current river level and preserves characteristic hummocky topography, draped with ~1 m of loess. Some large boulders are visible atop the slide mass.

Deposits of lacustrine sediments as thick as 30 m occur upstream from the landslide mass for nearly 25 km along the Min Jiang. These deposits are typically preserved beneath abandoned alluvial fans debauched from side-tributary drainages, although drapes of sediment can be seen high on a few hillslopes. We correlate these fans with the Q_3 tributary alluvial fans in the Min Jiang basin (Fig. 4). The lacustrine sediments are extremely fine-grained silts and muds, have a characteristic yellow color, and are generally laminated on a millimeter scale. The original thickness of many of the deposits does not appear to be preserved, and often overlying fan material has cut deep channels into the silts.

We surveyed the relative elevations of the preserved lake sediments along the valley for 21 km north of the slide (survey techniques are presented in the Appendix). The northernmost remnants of demonstrably lacustrine sediment range from 20 to 40 m above the elevation of the slide surface at Jiaocheng (Fig. 9). We referenced all elevations to the lowest point on the upstream side of the dam where we could discern the original surface of the slide. The edge of the remnant slide on the opposite valley wall is present at almost the same elevation (1–2 m higher), and we are confident that, although the original spillway could have been lower than our estimated position, it could not have been higher. Furthermore, we consistently surveyed the highest-preserved sediments; any subsequent erosion would serve to reduce this estimate. Although our inference of tilting relies on a few exposures of sediment at elevations higher than the slide, these elevations are minimum estimates of the original elevations, and our estimate of the degree of tilting is likewise a minimum.

We obtained a sample of the lacustrine sediments for IRSL dating (see Appendix for analytical procedures and Tables 2 and 3 for results). Sample EK 98-5 (TIBT 98-2) was collected from a 10 m face of wavy, laminated lacustrine muds ~19 km above the landslide. The sample gives an age of 14.2 ± 1.7 ka and is within error of our estimate for the age of Q_3 deposits upstream (6–13 ka). Given 20–40 m of tilting over a 21 km base line, this age implies tilting rates of 6.6×10^{-8} to 1.4×10^{-7} rad/yr. At the northern end of the former lake, this range translates to differential rock uplift rates of 1.4–2.8 mm/yr. These rates are fairly rapid given the apparent absence of geodetically detectable shortening across the range. The linear geometry of the deposit, unfortunately, allows us to resolve only the north-south component of the tilting; any east-west component remains unknown.

Pleistocene Tilting of Q_1 and Relief Development in the Min Shan

East-west tilting is recorded in the west-dipping Pleistocene Q_1 conglomerates east of the Min Jiang fault. Q_1 deposits are preserved over nearly 175 km^2 of the Min Jiang basin (Fig. 4). Over most of this region, the conglomerates strike 010° to 040° and dip ~14°NW (Fig. 4, inset). The only exception occurs at the southern end of the basin, where the gravels are gently folded. Throughout the rest of the basin, they are preserved on long west-sloping ridges between deeply incised tributary drainages (Fig. 6A). The present-day eastern extent of the basin is defined by the onlap of these conglomerates onto an ~15°–18°W-dipping bedrock surface of very low relief (Fig. 6C). This surface extends from beneath the conglomerates and continues to elevations exceeding 4200 m along the west flank of the Min Shan (Fig. 4).

Determining the magnitude of the tilting recorded in the Q_1 conglomerates depends largely on an estimate of the initial slope. Depositional slopes of terrestrial deposits can vary widely, depending on the nature of the transport process, sediment size, and fine sediment content (e.g., Blair and McPherson, 1994). However, three lines of evidence lead us to conclude that the depositional slope of the Q_1 conglomerates in the Min Jiang basin was fairly shallow. First, the deposits are alluvial in character. All exposures of the Q_1 conglomerates are clast-supported gravels interbedded with fine sands and silts. The finer-grained layers dip concordantly with the coarser gravels. We found no exposures within the Q_1 conglomerates of debris-flow deposits or of glacial till. Compilations of the slopes of modern alluvial fans in a wide range of environments indicate that depositional slopes on fans dominated by alluvial deposits rarely exceed 3°–4° (Blair and McPherson, 1994). Second, measurements of the surface slope on undeformed Q_2 terraces preserved in the tributary valleys east of Gonganin (Fig. 4) range from 1° to 3°. Although these may not be a direct analogue for the earlier deposits, the Q_2 terrace gravels are of similar grain size and composition and were likely deposited on a similar depositional slope. Third, we were able to estimate the paleoflow depth from preserved channel geometries, and we measured the median grain size at one locality within the

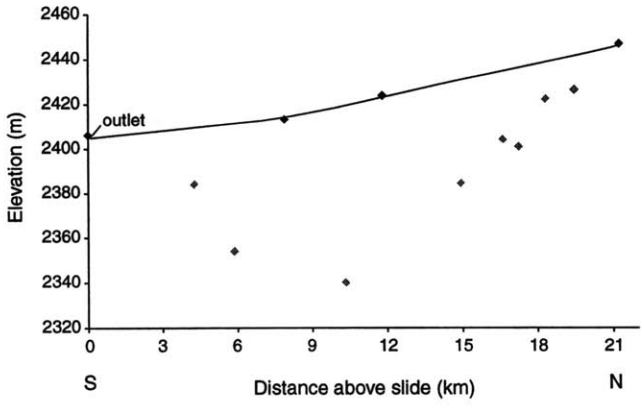

Figure 9. Survey results of lacustrine sediments associated with the Diexi landslide in the southern Min Shan (see Fig. 3 for location). Gray symbols represent localities where the deposits had been eroded. Black symbols represent the upper extent of deposits with no definitive evidence for subsequent erosion.

Q_1 conglomerates. This approach yielded a paleoslope estimate of <1° (Paola and Mohrig, 1996). Although a single measurement may not be a reliable indicator of the regional dip, taken with the other lines of evidence, it suggests that the Q_1 conglomerates were deposited with a shallow initial slope. In the discussion that follows, we make a conservative estimate that the initial slope was ~4°. This estimate is at the high end of the range of likely depositional slopes and thus represents a maximum value.

Given the present mean dip of the Q_1 conglomerates (~14°NW; Fig. 4), the analysis above indicates that the Q_1 has been tilted by at least 10°. The spatial extent over which it occurred indicates that down-to-the-northwest tilting represents a significant component of Quaternary deformation along western flank of the Min Shan. Our mapping demonstrates that there are no faults exposed between the eastern edge of the basin and the crest of the Min Shan. Young faults cut the Q_1 conglomerates only in the southernmost end of the basin (Ningpo fault; Fig. 4). North and east of this region, the conglomerates dip uniformly to the west-northwest. Preserved remnants of the subbasin erosion surface extend nearly to the crest of the Min Shan (Fig. 6C) and suggest that the western part of the range behaved as a relatively coherent block during late Quaternary deformation.

Simple geometric considerations suggest that tilting of the Q_1 conglomerates can account for most of the modern relief between the Min Shan and the plateau to the west. Q_1 gravels are preserved as far as 6 km east of the Min Jiang fault; the erosion surface upon which they were deposited is preserved as far as 9 km east of the fault. Tilting of 10° over these horizontal base lines (3–6 km for the Q_1 and 7–9 km for the subbasin surface) leads to differential rock uplift of 500–1000 m at the eastern edge of the Q_1 gravels and 1200–1500 m at the eastern edge of the subbasin surface. Projecting this tilting to the crest of the Min Shan (some 12–15 km east of the Min Jiang fault) would result in 2000–2500 m of differential rock uplift. Modern relief between the range crest and the Min Jiang valley ranges from 1600 to 2200 m, and it is clear that most, if not all, of it could have developed as a result of Pleistocene tilting. Paleoflow indicators and clast composition suggest that Q_1 deposits were derived from the Min Shan; clearly, there must have been some initial topographic gradient east of the basin. However, the lack of observed structures between the basin and the crest of the range makes a compelling argument that the much of the modern topography developed during Pleistocene tilting along the western flank of the range.

Inferred rates of tilting within the Min Shan are remarkably rapid. Tilting of 10° in 250 k.y. requires rates on the order of 7×10^{-7} rad/yr. Differential rock uplift rates depend upon the base line chosen, but for the three positions we have already discussed the eastern extent of Q_1, the eastern extent of the subbasin surface, and the crest of the range—rates range from 2.0 to 4.1 mm/yr, 4.8–6.2 mm/yr, and 8.3–10.3 mm/yr, respectively. We stress that these values only reflect differential rock uplift. Inferred mean incision rates of tributary streams through the Q_1 and the underlying bedrock approach ~1.5 mm/yr (e.g., ~200 m in ~160 k.y.). The lack of information regarding the lowering rate of hillslopes and ridge crests in the Q_1 deposits and the lack of denudation rates east of the preserved basin margin prevent us from obtaining a quantitative estimate of surface uplift in the Min Shan (England and Molnar, 1990a). However, the preservation of the bedrock surface that floors the basin at elevations approaching the crest of the range leads us to infer that differential surface uplift was very likely positive along the west flank of the Min Shan during the late Pleistocene.

FLEXURAL ISOSTATIC CONTRIBUTION TO TILTING IN THE MIN JIANG BASIN

Some component of the down-to-the-northwest tilting observed in the Min Jiang basin could be attributed to a flexural isostatic response to denudation along the eastern flank of the range. Such a mechanism has been invoked for high mountain ranges flanking both the Tibetan Plateau and Andean Altiplano (Masek et al., 1994b; Molnar and England, 1990; Montgomery, 1994), as well as for high-standing continental escarpments (Kooi and Beaumont, 1994; Tucker and Slingerland, 1994). In order to assess the necessary conditions under which an isostatic response to erosional unloading could significantly influence the deformation observed in the Min Shan, we utilize a simple flexural model. We take two complementary approaches. We first consider the modern topographic relief as the residue from the removal of a distributed load from the lithosphere so that we can model the flexural response to erosional dissection of a plateau margin. Second, we model the effects of uniform erosional unloading of the eastern flank of the range and ask how much mass removal is required to produce the observed tilting (deflections) in the Min Jiang basin.

In our first model, the load removed from the lithosphere is calculated from the topographic relief in the landscape. We utilize a digital elevation model of the topography in eastern Tibet (90 m nominal resolution, data set described in Fielding et al., 1994) and extract the topographic relief along a 75-km-wide swath oriented perpendicular to the topographic margin of the plateau (see Fig. 2 for location). The swath width was chosen to enclose the entire upper drainage basin of the Fu Jiang, the major river draining the eastern Min Shan, and so provides a relatively complete picture of the relief structure of the landscape east of the Min Shan. We binned elevations across the swath and calculated local relief as the difference between the maximum elevation and all other elevations within a bin. This is functionally equivalent to fitting a surface to peak elevations and extracting the difference between that surface and the landscape (Montgomery, 1994). However, by measuring relief along the entire channel system, we obtain a volumetric estimate of local valley-bottom to ridge-top relief. Relief is averaged in each bin to obtain an estimate of the mean relief along the chosen swath. This quantity is imposed as a distributed surficial load removed from the lithosphere.

We model the lithospheric response to removal of this topographic load as that of a thin, uniformly rigid elastic plate overlying a viscous substrate (Turcotte and Schubert, 1982; equation 3.125). In the discussion that follows we use the term "flexural rigidity" interchangeably with the term "effective elastic thickness," T_e, where we assume a Young's modulus of 7×10^{10} Pa and Poisson's ratio of 0.25 (Turcotte and Schubert, 1982). The density contrast between the crust and mantle in our model is 600 kg/m^3 (ρ_{crust} = 2700 kg/m^3, ρ_{mantle} = 3300 kg/m^3). The effective elastic thickness and the lateral boundary conditions control the flexural response to the imposed load. End loads in our model are assumed to be zero. We place the load within a model domain that is long (>500 km) relative to the load and force the ends of the model domain to have zero deflection. The modeled deflection is then calculated over the original length of the swath. In this way, we avoid edge effects at the ends of our sampled topography.

The topography of the Min Shan region (Fig. 10) is characterized by a gradual increase in elevation from the Tibetan Plateau in the west to the Min Jiang fault and an abrupt rise in elevation between the Min Jiang fault and the crest of the range. Elevations then fall rapidly toward the foreland. Mean relief across this landscape varies from 200 to 500 m west of the Min Jiang fault, to nearly 2000 m along the eastern flank of the range. In order to facilitate interpretation of the potential isostatic response attributable to this relief, we impose the flexural response on an initially horizontal reference surface (Fig. 10) at the elevation of the Tibetan Plateau at the western end of our swath (~3500 m). We caution that we are not assuming an initial condition of the plateau prior to erosion. The horizontal line simply serves as a marker horizon on which to examine the effects of varying parameters. The imposed load is always the mean relief measured along the swath.

The lack of an independent estimate of the rigidity of the lithosphere in eastern Tibet forces us to model a range of possible values. Results are shown in Figure 10C and are strongly dependent on the modeled rigidity of the lithosphere. For elastic thickness ranging from 30 to 40 km, the potential isostatic response is distributed over a wide region of the eastern plateau. Although these models match the broad rise in topography between the Tibetan Plateau and the Min Jiang fault fairly well, they fail to reproduce the high topography of the Min Shan. Only for elastic thicknesses approaching 4–5 km do the model results produce a deflection of similar wavelength as the Min Shan. This result implies that in order for the deformation observed along the west flank of the Min Shan to be an isostatic response to erosional unloading, the crust of the eastern plateau would have to have extremely low rigidity (~4 to 8×10^{20} N·m; T_e = 4–5 km).

An additional constraint can be inferred from the amplitude of the modeled deflections. Even if the lithosphere of the Min Shan region is extremely weak ($T_e \approx 5$ km), the predicted amplitude of the deflection between the location of the Min Jiang fault and the crest of the range is on the order of 500 m (Fig. 10C). This result implies that even if all the present-day relief developed in the last 250 k.y., the isostatic response would not reproduce the observed tilting along the western flank of the Min Shan. We can, however, ask how much additional denudation would be required to generate a deflection of the observed amplitude (inferred to be 2000–2500 m at the crest of the range). Here we assume that all denudation is concentrated along the eastern flank of the Min Shan. Although this is not true in detail, it should allow us to approximate, to a first order, the amount of mass removal necessary to produce a deflection similar to the observed topography of the Min Shan.

The deflection of a point at the uneroded edge of a plateau is a strong function of load width up to the flexural wavelength (for T_e = 5 km, this wavelength is ~45 km; Fig. 11). Removal of a distributed load (of uniform thickness) from a region greater than or equal in width to this distance produces a deflection at the margin with a magnitude equal to ~0.48 of the removed thickness. Consequently, in order to produce a deflection with amplitude of 2–2.5 km, we would have to remove at least 4–5 km of material east of the crest of the range. It is important to note that this simple model also demonstrates that if denudation is focused in a narrow zone (i.e., less than the flexural wavelength) along the range front, the isostatic response is greatly reduced.

Our model results indicate that in order for the observed deformation and topography along the western flank of the Min Shan to be produced as an isostatic response to erosion, two conditions

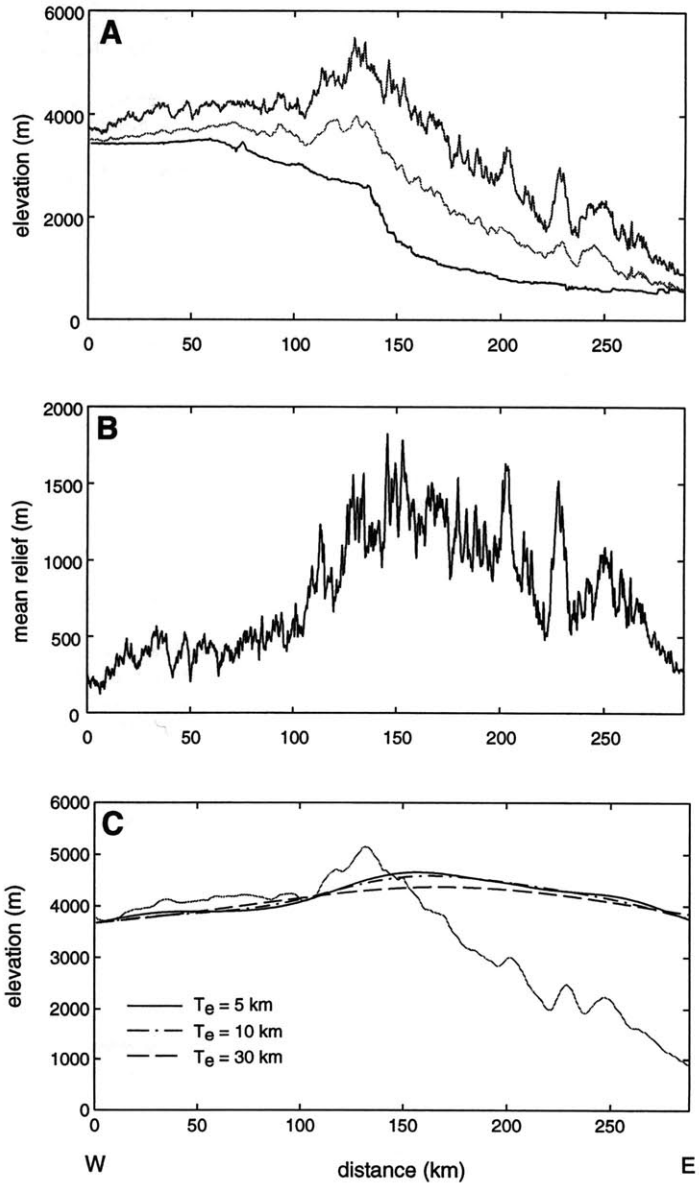

Figure 10. (A) Topographic swath profile across the Min Shan margin. Maximum, minimum (dark lines), and mean elevations (gray) are extracted from ~90 m bins (1 pixel), selected perpendicular to the swath. (B) Mean relief as a function of distance across the Min Shan. This function is used as a distributed line load removed from the lithosphere in our flexural model. (C) Modeled deflections for various T_e values for a reference surface calculated from removal of load in B. Reference surface is originally a horizontal surface at 3500 m. Gray line shows envelope of maximum topography for reference. Details of the calculation are discussed in the text.

must hold: (1) the crust must be extremely weak ($T_e \leq 5$ km), and (2) there must have been 4–5 km of denudation east of the range crest. Unfortunately, little is known about the strength of the lithosphere in this region of the plateau. Estimates of the elastic thickness of the lithosphere in southern Tibet range from 5 to 15 km (Masek et al., 1994a). However, these measurements are in a region of active extension and high heat flow. There is little geologic evidence for such high heat flow in the Min Shan region, and we find it unlikely that the lithosphere has such low rigidity.

Removal of 4–5 km of material in ~250 k.y. from the eastern range front would require denudation rates on the order of 15–20 mm/yr. Existing thermochronologic data from the region are sparse, but bear importantly on the long-term denudation rates along the range. Fission-track measurements in apatite taken from a few localities within the Min Shan (Arne et al., 1997) yield ages between 30 and 120 Ma. Kirby et al. (1999) obtained a cooling trajectory from a small Mesozoic granite at the eastern foot of the range (west of the Huya fault; Fig. 3). Potassium feldspars ($^{40}Ar/^{39}Ar$) and apatite (U-Th-He) from this sample record rapid cooling from temperatures of ~200 °C beginning at ca. 6 Ma. These authors argued that mean denudation rates over this period were probably between 1 and 2 mm/yr. If these denudation rates are representative of the late Quaternary (past ~250 k.y.), they suggest that erosion along the eastern range front was likely limited to 250–500 m. This is an order of magnitude smaller than rates required to produce the observed tilting along the western flank of the Min Shan and suggests that the isostatic component is probably limited to 100–200 m (assuming T_e = 5 km). Thus, the tilting in the Min Jiang basin (and the consequent topography) appears to be primarily a tectonic signature.

DISCUSSION: DYNAMICS OF MOUNTAIN BUILDING IN THE MIN SHAN

The most striking observation regarding the active faulting along the Min Shan is that the active faults bear little relationship to the topographic range front. Although the Huya fault is near the eastern foot of the range, it is discontinuous along strike. North and south of the Huya fault, the topographic margin does not coincide with recognized active faulting. Indeed, in the northern Min Shan (north of the Xue Shan fault), Proterozoic–Triassic rocks form a continuous section that extends from the crest of the range to the foreland (Fig. 3). A similarly intact section occurs south of the Huya fault (Fig. 3). These relationships preclude large-magnitude Cenozoic shortening across the range and are surprising given the profound variation in elevation (and presumably crustal thickness) from the plateau to the foreland. The lack of correlation between active faults and the topographic margin of the plateau is reminiscent of the relationships in the Longmen Shan region to the south (Burchfiel et al., 1995), which have been interpreted as a consequence of shortening focused in a weak middle and lower crust (Royden et al., 1997). The geology of the eastern Min Shan thus argues against a conventional mode of shortening at the plateau margin whereby crustal thickening is absorbed at the surface by large-magnitude thrust faults and is consistent with the hypothesis of Royden et al. (1997).

Late Quaternary deformation within the western Min Shan is similarly enigmatic. The Min Jiang fault, although active in the late Pleistocene, does not appear to have significant Holocene displacement along it. In addition, the sense of displacement across the Min Jiang fault (plateau side up) cannot account for the high topography of the Min Shan relative to the plateau. The slow shortening rates inferred for the Min Jiang fault are consistent with regional horizontal velocities determined by space geodesy. However, the evidence for rapid tilting within the range since late Pleistocene time indicates that significant vertical deformation is localized beneath the Min Shan itself. The absence of faults between the eastern margin of the Min Jiang basin and the crest of the range and the continuity of the subbasin erosion surface suggest that, if discrete structures exist within the Min Shan, they must end at depth beneath the range. Likewise, if the Huya fault extends north along the Min Shan, either as a blind structure or as a series of distributed faults, it could account for tilting along the west flank of the Min Shan. However, projection of 10° of tilt across a base line of 50 km (approximately the distance to the inferred trace of the Huya fault) implies that vertical displacement rates (over the past 250 k.y.) on the fault exceed 35 mm/yr. On a fault dipping 60°W, this projection implies horizontal shortening rates across the fault of nearly 20 mm/yr. These rates are at odds with both the record of historic seismicity (Editorial Board, State Seismological Bureau, 1989) and recent GPS measurements (Chen et al., 2000). Clearly, the Huya fault cannot be directly responsible for the observed tilting in the Min Jiang basin. We infer that late Quaternary tilting along the western flank of the Min Shan reflects deformation localized beneath the range itself, the nature of which remains somewhat enigmatic.

The discrepancy between geodetically observed rates of horizontal shortening (Chen et al., 2000; King et al., 1997) and the tilting rates we infer from our mapping and chronology is a second remarkable result of our work. Insofar as the geodetic measurements are representative of the time-averaged velocity field, they appear to restrict the rates of differential

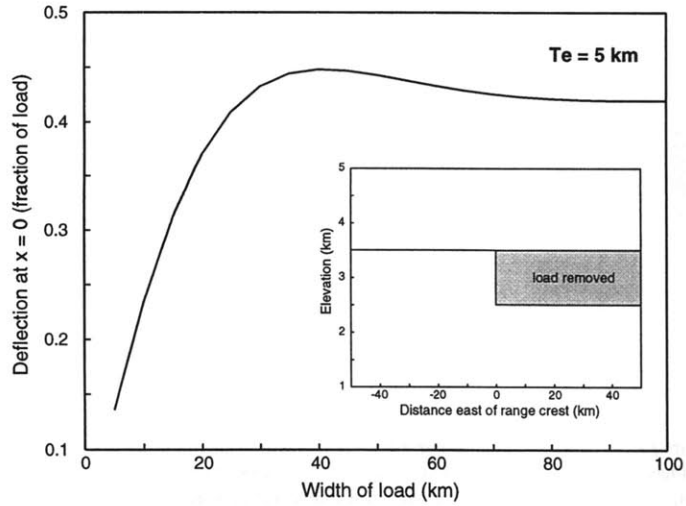

Figure 11. Deflection of an elastic plate as a function of the width of a distributed surface load. Inset shows a schematic representation of load geometry. Load is of constant thickness and variable width. Deflection is calculated at the inner edge of the load ($x = 0$) and roughly corresponds to the divide of a dissected plateau margin. Note that the greatest relief in the Min Shan occurs along the steep eastern range front, over a width of 50–100 km (see Fig. 10); thus (for $T_e \approx 5$ km), we expect deflections at the range crest to be between 0.4 and 0.45 of the load removed.

rock uplift that can be attributed to horizontal shortening to less than 2–3 mm/yr. Although the recurrence interval of seismic events beneath the Min Shan is not well known, the historic record of seismicity contains only four events of magnitude >6 (three of these occurred as part of a single sequence in 1976; Editorial Board, State Seismological Bureau, 1989; Fig. 2). As the record of earthquakes in this region of China extends back over 1500 yr, it seems likely that mean rates of horizontal shortening associated with seismic release are slow.

Although optical dating is still an immature discipline, there is a growing body of empirical evidence (Aitken, 1998; Berger, 1995) that suggests that the technique can resolve depositional ages within 20%–30% over the past 300–400 k.y. The correspondence between our IRSL age for the lacustrine sediments in the southwestern part of the range and ^{14}C ages on correlative terraces lends a measure of confidence to the technique. In addition, our age on the Q_{1-2} loess (ca. 160 ka) corresponds with a time period of documented loess deposition on the Loess Plateau (Kukla, 1987) and suggests that the technique is probably resolving depositional ages. Even if our age estimates are inaccurate by a factor of two, the inferred rates of tilting exceed those attributable to regional horizontal shortening. Although the resolution of this problem awaits further refinement of the Quaternary chronology and/or the establishment of a detailed geodetic survey across the range, we conclude that rapid tilting within the Min Shan is a significant component of the late Quaternary deformation field along this margin of the Tibetan Plateau.

Rapid Holocene tilting observed in lacustrine sediments in the southern Min Shan supports this inference and further highlights the discrepancy between vertical deformation rates inferred from the geology and the lack of significant shortening across the Min Shan. The age of the deposit (ca. 14 ka) indicates that tilting likely took place throughout the Holocene and may be active today. The lacustrine sediments are within 10 km of one GPS station (MJZ1; Fig. 2), which resolves no significant eastward motion relative to the foreland. As in the Min Jiang basin, we find it likely that distributed tilting is an important component of the recent deformation field in the southwestern Min Shan. As vertical velocities are difficult to measure by geodetic means, our work highlights the utility of geologic markers in reconstructing differential rock uplift across regionally significant length scales. In both localities along the Min Shan where geologic markers are present, we find evidence for substantial tilting. We can only speculate as to its importance elsewhere in this region of the plateau.

We have argued above that the observed late Quaternary tilting within the Min Shan cannot be directly attributed to either horizontal shortening or to an isostatic response to denudation at the plateau margin. Although both of these mechanisms undoubtedly contribute to the observed tilting in the Min Jiang basin, even in concert they do not appear to account for the rapid rates we infer from the geometry and age of the Q_1 deposits. Our results thus suggest the presence of an additional driving mechanism. The lack of evidence for large-magnitude Cenozoic shortening along the eastern range front of the Min Shan leads us to consider the possibility that much of the deformation may be driven by flow of a weak lower crust. If the hypothesis of Royden et al. (1997) is correct, lower-crustal material driven from beneath the central plateau may impinge on cold, unthickened crust at the plateau and localize crustal thickening. This scenario is especially true of regions of significant anisotropy (for example, the Sichuan Basin). The presence of pre-Cenozoic structures related to the Xue Shan platform (Min Jiang and Huya faults) may help localize crustal thickening and, to some degree, set the width of the mountain range. We suggest that the observed deformation (both faulting and distributed tilting) in the Min Shan may be a coupled upper-crustal response to thickening localized in the lower crust.

The nature of the coupling between lower-crustal flow and upper-crustal deformation remains somewhat enigmatic, as does the manner in which tilting along the western flank of the Min Shan is accommodated along the eastern range front. Tilting in the Min Jiang basin could represent the western limb of a range-scale antiform with a wavelength of between 50 and 100 km. Alternatively, west-side-up displacement on the Huya fault could be distributed on small discrete structures along the eastern range front between the Xue Shan and Tazang faults. In either case, the lack of significant horizontal shortening across the range appears to require that Quaternary deformation along this segment of the eastern margin of the Tibetan Plateau is driven from below.

ACKNOWLEDGMENTS

This work was supported by the Continental Dynamics program at the National Science Foundation (EAR-961460) and by NASA (NAG 5-6062). We thank B. King, L. Royden, C. Rubin, K. Karlstrom, and M. Clark for helpful discussions on various aspects of this work. B. King kindly helped prepare Figure 2, and L. Royden provided the algorithm for a band matrix inverse solution to the flexural equation. An informal review by C. Rubin and formal reviews by R. Arrowsmith, M. Roy, and F. Pazzaglia led to improvements in the manuscript. Finally, we thank the staff and drivers at the Chengdu Institute of Geology and Mineral Resources for making our work in China possible.

APPENDIX

Survey Techniques

We surveyed the relative elevations of channel profiles, stream terraces, and lacustrine sediments by using a hand-held altimeter (±1 m), clinometer (±0.5°), and laser range finder (±1 m). Uncertainties are quoted from manufacturer specifications. Survey locations were logged by using a hand-held GPS receiver. As the along-channel distance varies with the curvature of the channel, we approximated along-channel distance by using the vehicle odometer (±0.1 km) for the terrace and channel survey. We corrected for daily barometric changes by tracking barometric pressure with a data logger at a fixed location near the center of our survey base line and corrected for these changes over the time of the survey. We estimate that individual measurements are accurate to ~3 m, but that relative differences in elevation (i.e., terrace height above channel) are probably accurate to 1.5–2 m.

Sampling and Analytical Techniques—IRSL Dating

IRSL samples (Table 2 and Figure 5) were collected following the general guidelines found in Aitken (1998). The outer, desiccated face of each outcrop was removed (generally 10–20 cm) taking care to shield the outcrop from direct sunlight. Samples were collected in light-tight Gill Style sample tins and sealed with black tape to preserve moisture content and minimize sample disturbance. In most cases, it was possible to push the tins directly into the sediment, although in one case (TIBT 98–4), a block was carved from the outcrop with a knife. In all cases, the outer 2–3 mm of the block was removed under low-energy light conditions in the laboratory. At each outcrop, three small samples were collected for dosimetry measurements (Table 2). These were spaced over a 50–60 cm distance that bracketed the sample (the effective range of gamma radiation in typical sediment is ~30 cm). For the luminescence measurements, the polymineralic, noncarbonate, detrital, 4–11 μm-diameter size fraction was prepared. Laboratory preparation procedures are outlined elsewhere (Berger, 1990; Wintle and Huntley, 1980).

A luminescence age $t = D_E/D_R$, where D_E is the so-called "equivalent dose," or paleodose (units of Gy [gray], 1 Gy = 100 rads), and D_R is the effective dose rate (Gy/k.y.). D_E is a measure of the postdepositional absorbed ambient ionizing radiation and is derived from luminescence measurements. D_R is derived from independent measurements of U, Th, K, and water concentration. For U and Th measurements, the technique of thick-source alpha-particle counting (TSAC) (Huntley and Wintle, 1981) was applied to dried powders. K was determined by commercial atomic absorption spectrophotometry. Radioactive secular equilibrium is assumed; this assumption is apparently valid for many, although not all, alluvial and fluvial sediments (Olley et al., 1996). Of the available analytical techniques, TSAC can apparently provide a clue to the occurrence of such disequilibrium and, compared to neutron-activation techniques, can provide a more accurate dose-rate measurement for fluvial samples older than ~10 k.y. (Olley et al., 1996).

For IRSL measurements, the deep-blue luminescence near the known 410 nm emission from most K-rich feldspars was chosen for detection (Aitken, 1998). To convert the sample's fossil light to an absorbed-energy equivalent, calibrated laboratory beta (^{90}Sr–^{90}Y) and alpha (^{241}Am) sources were used. The signature was recorded with an automated, high-capacity Daybreak Nuclear Model 1150 reader using an EMI 9635Q photomultiplier tube. Dose-response curves and other data were processed with software produced by one of the authors (Berger; see Berger et al., 1987).

REFERENCES CITED

Aitken, M. J., 1998, An introduction to optical dating: New York, Oxford University Press, 267 p.

Argand, E., 1924, La tectonique de l'Asia: Proceedings, 13th International Geological Congress, Brussels, p. 171–372.

Arne, D., Worley, B., Wilson, C., Chen, S., Foster, D., Luo, Z., Liu, S., and Dirks, P., 1997, Differential exhumation in response to episodic thrusting along the eastern margin of the Tibetan Plateau: Tectonophysics, v. 280, p. 239–256.

Avouac, J. P., and Tapponnier, P., 1993, Kinematic model of active deformation in central Asia: Geophysical Research Letters, v. 20, p. 895–898.

Berger, G. W., 1988, Dating Quaternary events by luminescence, *in* Easterbrook, D. J., ed., Dating Quaternary sediments: Geological Society of America Special Paper 227, p. 13–50.

Berger, G. W., 1990, Effectiveness of natural zeroing of the thermoluminescence in sediments: Journal of Geophysical Research, v. 95, p. 12375–12397.

Berger, G., 1995, Progress in luminescence dating methods for Quaternary sediments, *in* Rutter, N. W., and Catto, N. R., eds., Dating methods for Quaternary deposits: Geological Association of Canada, p. 81–104.

Berger, G. W., Lockhart, R. A., and Kuo, J., 1987, Regression and error analysis applied to the dose-response curves in thermoluminescence dating: Nuclear Tracks and Radiation Measurements, v. 13, p. 177–184.

Blair, T. C., and McPherson, J. G., 1994, Alluvial fans and their natural distinction from rivers based on morphology, hydraulic processes, sedimentary processes, and facies assemblages: Journal of Sedimentary Research, v. 64, p. 450–489.

Burbank, D. W., 1992, Causes of recent Himalayan uplift deduced from deposited patterns in the Ganges Basin: Nature, v. 357, p. 680–683.

Burchfiel, B. C., and Royden, L. H., 1991, Tectonics of Asia 50 years after the death of Emile Argand: Eclogae Geologicae Helvetiae, v. 84, p. 599–629.

Burchfiel, B. C., Chen, Z., Liu, Y., and Royden, L. H., 1995, Tectonics of the Longmen Shan and adjacent regions: International Geology Review, v. 37, p. 661–735.

Chen, S. F., Wilson, C. J. L., Deng, Q. D., Zhao, X. L., and Luo, Z. L., 1994, Active faulting and block movement associated with large earthquakes in the Min Shan and Longmen mountains, northeastern Tibetan Plateau: Journal of Geophysical Research, v. 99, p. 24025–24038.

Chen, Z., Burchfiel, B. C., Liu, Y., King, R. W., Royden, L. H., Tang, W., Wang, E., Zhao, J., and Zhang, X., 2000, GPS measurements from eastern Tibet and their implications for India/Eurasia intracontinental deformation: Journal of Geophysical Research (in press).

Cobbold, P. R., and Davy, P., 1988, Indentation tectonics in nature and experiment: 2. Central Asia: University of Uppsala Geological Institute Bulletin 14, p. 143–162.

Coward, M. P., Kidd, W. S. F., Pan, Y., Shackelton, R. M., and Zhang, H., 1988, The structure of the 1985 Tibet Geotraverse, Lhasa to Golmud, *in* Chang, C., Shackleton, R. M., Dewey, J. F., and Yin, J., eds., The geological evolution of Tibet: Royal Society of London Philosophical Transactions, p. 307–336.

Dewey, J. F., and Burke, K. C. A., 1973, Tibetan, Variscan and Precambrian basement reactivation: Products of a continental collision: Journal of Geology, v. 81, p. 683–692.

Editorial Board, State Seismological Bureau, 1989, Lithospheric dynamics atlas of China: Beijing, China Cartographic Publishing House, p. 23.

England, P., and Houseman, G., 1986, Finite strain calculations of continental deformation: 2. Comparison with the India-Asia collision zone: Journal of Geophysical Research, v. 91, p. 3664–3676.

England, P., and Molnar, P., 1990a, Surface uplift, uplift of rocks, and exhumation of rocks: Geology, v. 18, p. 1173–1177.

England, P., and Molnar, P., 1990b, Right-lateral shear and rotation as the explanation for strike-slip faulting in eastern Tibet: Nature, v. 344, p. 140–142.

Fielding, E. J., Isacks, B. L., Barazangi, M., and Duncan, C., 1994, How flat is Tibet?: Geology, v. 22, p. 163–167.

Han, W., and Xia, D., 1980, The Songpan-Pingwu earthquakes and the movement of the Sichuan-Qinghai block (in Chinese): Earthquake Science Research, v. 1, p. 39–48.

Harrison, T. M., Copeland, P., Kidd, W. S. F., and Yin, A., 1992, Raising Tibet: Science, v. 255, p. 1663–1670.

Huntley, D. J., and Clague, J. J., 1996, Optical dating of tsunami-laid sands: Quaternary Research, v. 46, p. 127–140.

Huntley, D. J., and Wintle, A. G., 1981, The use of alpha scintillation counting for measuring Th-230 and Pa-231 contents of ocean sediments: Canadian Journal of Earth Sciences, v. 18, p. 419–432.

Huntley, D. J., Berger, G. W., and Bowman, S. G. E., 1988, Thermoluminescence responses to alpha and beta irradiations, and age determinations when the high-dose response is non-linear: Radiation Effects, v. 105, p. 279–284.

Imbrie, J., Hays, J. D., Martinson, D. G., McIntyre, A., Mix, A. C., Morley, J. J., Pisias, N. G., Prell, W. G., and Shackleton, N. J., 1984, The orbital theory of Pleistocene climate: Support from a revised chronology of the marine delta ^{18}O record, *in* Berger, A. L., Imbrie, J., Hays, J., Kukla, G., and Saltzman, B., eds., Milankovitch and climate, Part 1: Boston, Reidel Publishing Company, p. 169–305.

Jin, Y., McNutt, M. K., and Zhu, Y., 1994, Evidence from gravity and topography data for folding of Tibet: Nature, v. 371, p. 669–674.

Jones, L. M., Han, W., Hauksson, E., Jin, A., Zhang, Y., and Luo, Z., 1984, Focal mechanisms of the Songpan earthquakes of August 1976 in Sichuan, China: Journal of Geophysical Research, v. 89, p. 7697–7707.

King, R. W., Shen, F., Burchfiel, B. C., Royden, L. H., Wang, E., Chen, Z., Liu, Y., Zhang, X., Zhao, J., and Li, Y., 1997, Geodetic measurement of crustal motion in southwest China: Geology, v. 25, p. 179–182.

Kirby, E., Reiners, P., Farley, K., Krol, M., Liu, Y., Chen, Z., and Tang, W., 1999, Late Cenozoic uplift and landscape evolution of the eastern margin of the Tibetan Plateau: Inferences from $^{40/39}Ar$ and U-Th-He thermochronology: Geological Society of America Abstracts with Programs, v. 31, no. 7, p. A129.

Kooi, H., and Beaumont, C., 1994, Escarpment evolution on high-elevation rifted margins: Insights derived from a surface processes model that combines diffusion, advection, and reaction: Journal of Geophysical Research, v. 99, p. 12191–12209.

Kukla, G., 1987, Loess stratigraphy in China: Quaternary Science Reviews, v. 6, p. 191–219.

Lyon-Caen, H., and Molnar, P., 1983, Constraints on the structure of the Himalaya from an analysis of gravity anomalies and a flexural model of the lithosphere: Journal of Geophysical Research, v. 88, p. 8171–8191.

Masek, J. G., Isacks, B. L., and Fielding, E. J., 1994a, Rift flank uplift in Tibet: Evidence for a viscous lower crust: Tectonics, v. 13, p. 659–667.

Masek, J. G., Isacks, B. L., Gubbels, T. L., and Fielding, E. J., 1994b, Erosion and tectonics at the margins of continental plateaus: Journal of Geophysical Research, v. 99, p. 13941–13956.

Ministry of Geology and Mineral Resources, People's Republic of China, 1991, Regional geology of Sichuan Province: Beijing, Geological Publishing House, Geological Memoirs, ser. 1, no. 23, 728 p.

Molnar, P., 1988, A review of geophysical constraints on the deep structure of the Tibetan Plateau, the Himalaya and the Karakoram, and their tectonic implications, *in* Chang, C., Shackleton, R. M., Dewey, J. F., and Yin, J., eds., The geological evolution of Tibet: Royal Society of London Philosophical Transactions, p. 33–88.

Molnar, P., and England, P., 1990, Late Cenozoic uplift of mountain ranges and global climate change: Chicken or egg?: Nature, v. 346, p. 29–34.

Molnar, P., and Tapponnier, P., 1975, Cenozoic tectonics of Asia: Effects of a continental collision: Science, v. 189, p. 419–426.

Montgomery, D. R., 1994, Valley incision and the uplift of mountain peaks: Journal of Geophysical Research, v. 99, p. 13913–13921.

Nelson, K. D., Zhao, W., Brown, L. D., Kuo, J., Che, J., Liu, X., Klemperer, S. L., Makovsky, Y., Meissner, R., Mechie, J., Kind, R., Wenzel, F., Ni, J., Nabelek, J., Leshou, C., Tan, H., Wei, W., Jones, A. G., Booker, J., Unsworth, M., Kidd, W. S. F., Hauck, M., Alsdorf, D., Ross, A., Cogan, M., Wu, C., Sandvol, E., and Edwards, M., 1996, Partially molten middle crust beneath southern Tibet: Synthesis of project INDEPTH results: Science, v. 274, p. 1684–1688.

Ollerhead, J., Huntley, D. J., and Berger, G. W., 1994, Luminescence dating of the Buctouche Spit, New Brunswick: Canadian Journal of Earth Sciences, v. 31, p. 523–531.

Olley, J. M., Murray, A., and Roberts, R., 1996, The effects of disequilibria in the uranium and thorium decay chains on burial dose rates in fluvial sediments: Quaternary Science Reviews, v. 15, p. 751–760.

Paola, C., and Mohrig, D., 1996, Paleohydraulics revisited: Paleoslope estimation in coarse-grained braided rivers: Basin Research, v. 8, p. 243–254.

Pazzaglia, F. J., Gardner, T. W., and Merritts, D. J., 1998, Bedrock fluvial incision and longitudinal profile development over geologic time scales determined by fluvial terraces, *in* Tinkler, K. J., and Wohl, E. E., eds., Rivers over rock: Fluvial processes in bedrock channels: American Geophysical Union Geophysical Monograph 107, p. 207–235.

Prescott, J. R., and Hutton, J. T., 1988, Cosmic ray and gamma ray dosimetry for TL and ESR: Nuclear Tracks and Radiation Measurements, v. 14, p. 223–227.

Prescott, J. R., and Robertson, G. B., 1997, Sediment dating by luminescence: A review: Radiation Measurements, v. 27, p. 893–922.

Ratschbacher, L., Frisch, W., Chen, C., and Pan, G., 1996, Cenozoic deformation, rotation, and stress patterns in eastern Tibet and western Sichuan, China, *in* Yin, A., and Harrison, T. M., eds., The tectonic evolution of Asia: Cambridge, Cambridge University Press, p. 227–249.

Royden, L. H., Burchfiel, B. C., King, R. W., Chen, Z., Shen, F., and Liu, Y., 1997, Surface deformation and lower crustal flow in Eastern Tibet: Science, v. 276, p. 788–790.

Stuiver, M., and Reimer, P. J., 1993, Extended ^{14}C database and revised CALIB radiocarbon age calibration program: Radiocarbon, v. 35, p. 215–230.

Tang, R., Wen, D., Huang, Z., Wu, X., Lin, W., Chen, G., and Wu, G., 1993, The Quaternary activity characteristics of several major active fault zones in the Songpan-Longmenshan region: Earthquake Research in China, v. 7, p. 341–350.

Tapponnier, P., Peltzer, G., Le Dain, A. Y., Armijo, R., and Cobbold, P., 1982, Propagating extrusion tectonics in Asia: New insight from simple experiments with plasticine: Geology, v. 10, p. 611–616.

Tucker, G. E., and Slingerland, R. L., 1994, Erosional dynamics, flexural isostasy, and long-lived escarpments: A numerical modeling study: Journal of Geophysical Research, v. 99, p. 12229–12243.

Turcotte, D., and Schubert, G., 1982, Geodynamics: Applications of continuum physics to geological problems: New York, John Wiley and Sons, 450 p.

Wintle, A. G., and Huntley, D. J., 1980, Thermoluminescence dating of ocean sediments: Canadian Journal of Earth Sciences, v. 17, p. 348–360.

Zhao, X., Deng, Q., and Chen, S., 1994, Tectonic geomorphology of the Min Shan uplift in western Sichuan, southwestern China: Seismology and Geology, v. 16, no. 4, p. 429–439 (in Chinese with English abstract).

MANUSCRIPT RECEIVED BY THE SOCIETY AUGUST 20, 1999
REVISED MANUSCRIPT RECEIVED NOVEMBER 23, 1999
MANUSCRIPT ACCEPTED DECEMBER 7, 1999

Printed in U.S.A.

Chapter 3

Late Cenozoic Uplift and Landscape Evolution along the Eastern Margin of the Tibetan Plateau: Inferences from $^{40}Ar/^{39}Ar$ and (U-Th)/He Thermochronology

Abstract

High topography in central Asia is perhaps the most fundamental expression of the Cenozoic Indo-Asian collision, yet an understanding of the timing and rates of development of the Tibetan Plateau remains elusive. Here we investigate the Cenozoic thermal histories of rocks along the eastern margin of the plateau adjacent to the Sichuan Basin in an effort to determine when the steep topographic escarpment that characterizes this margin developed. Temperature-time paths inferred from $^{40}Ar/^{39}Ar$ thermochronology of biotite, multiple diffusion domain modeling of alkali feldspar ^{40}Ar release spectra, and (U-Th)/He thermochronology of apatite imply that the region underwent remarkably slow cooling (< 1 °C/m.y.) from the Early Jurassic until the Late Miocene. The regional extent and consistency of thermal histories during this time period suggest the presence of a stable thermal structure, and imply that regional denudation rates were very low (< 0.1 mm/yr for nominal continental geotherms). Beginning in the Late Miocene, samples from the topographic margin of the plateau experienced a pronounced cooling event (> 30–50 °C/m.y.) coincident with exhumation from inferred depths of 8-10 kilometers. Inferred denudation rates range from 1-2 mm/yr. Samples from the plateau surface continued to cool relatively slowly during this time period (~ 3 °C/m.y.), suggesting limited exhumation (1-2 km). We infer that the onset of rapid cooling reflects the erosional response to the development of regionally significant topographic gradients between the plateau and the stable Sichuan Basin. Thus, uplift of the Tibetan Plateau along its eastern margin appears to have initiated in the Late Miocene (ca. 11 Ma), and may have been diachronous along the margin.

Introduction

The question of when the Tibetan Plateau attained its current elevation, and how rapidly it did so, is at the forefront of debate over a wide range of first-order problems in continental tectonics. For example, the timing of plateau development places important constraints on the mechanism(s) by which convergence between India and Eurasia has been accommodated (Tapponnier et al., 1982; England and Houseman, 1986) while the rates of uplift of the plateau surface have major implications for the dynamics of plateau formation and the relative significance of deformational processes in the crust and mantle (England and Molnar, 1990). The development of high elevation in central Asia has been linked to the onset and intensification of the Asian monsoon (Molnar et al., 1993) and perhaps to the drawdown of atmospheric CO_2 via enhanced silicate weathering (Raymo et al., 1988). Thus, the elevation history of the Tibetan Plateau plays a central role in the continuing debate over large-scale linkages between tectonics and global climate change.

Despite the importance of the timing and rate of plateau development, there is little direct evidence for when and how rapidly uplift of the Tibetan plateau occurred (Molnar et al., 1993). Current estimates for when the plateau attained its current elevation are based on inferences regarding the initiation age of E-W extension in central and southern Tibet (Harrison et al., 1992; Coleman and Hodges, 1995) or bimodal, potassic volcanism in north-central Tibet (Turner et al., 1993; Turner et al., 1996). Both of these tectonic events are linked to a model for uplift of the plateau surface involving convective removal of a thickened continental lithosphere (Houseman et al., 1981; Molnar et al., 1993). Although simple geodynamic models linking surface uplift, potential energy increases in the lithosphere, extension and volcanism are conceptually compelling, a temporal and genetic link between extension, volcanism and surface uplift remains to be demonstrated. Even if this approach to dating plateau uplift was not so model-dependent, a paucity of relevant geochronological data limits our understanding of the temporal evolution extension and volcanism on the plateau. Furthermore, the cause of E-W extension on the high plateau is a matter of active debate; it may be related to a number of processes including: strain partitioning during oblique convergence (McCaffrey and Nabelek, 1998), spreading of the Himalayan arc (Seeber and Pecher,

1998), eastward extrusion of Tibet (Armijo et al., 1986), or thickening of crust with a depth-dependent rheology (Royden, 1996).

Rather than envisioning plateau uplift as a spatially and temporally uniform event, a second class of models holds that the plateau grew in lateral extent (primarily to the east) with continuing convergence between India and Eurasia (England and Houseman, 1986; England and Houseman, 1988; Royden, 1996). The deformational history of the Qiadam - Qilian Shan region of Qinghai Province seems to support the inference that shortening and crustal thickening has stepped northward with time (Meyer et al., 1998). However, this region is characterized by high mountain ranges and intermontane basins, and may have an uplift history quite independent of the plateau to the south. Although it has been recently suggested that portions of southern Tibet had already attained high elevations prior to the Indo-Asian collision (Murphy et al., 1997), there is virtually no information on how surface uplift of the plateau varied in space and time. In order to begin to comprehensively address this question, one must first determine when the present-day margins of the plateau developed.

In this contribution, we investigate the rates and patterns of Cenozoic denudation along the eastern margin of the Tibetan Plateau adjacent to the Sichuan Basin (Figure 1). The topographic margin of the plateau in this region is a 4-5 km high escarpment defined by short, consequent drainages eroding headward into an unincised plateau surface of low relief. Cenozoic shortening across this margin is restricted to a few tens of kilometers (Burchfiel et al., 1995), and the region thus affords a rare opportunity to examine directly the erosional response to uplift of the easternmost plateau. Thermal histories derived from $^{40}Ar/^{39}Ar$ (biotite and potassium feldspar) and (U-Th)/He (apatite) thermochronometry record slow cooling throughout the region from the Late Triassic until the mid-Late Miocene. Samples from the eastern foot of the escarpment experienced a pronounced Late Miocene cooling event that is not observed in samples from the interior of the plateau. We argue that this rapid cooling reflects the onset of rapid denudation along the topographic front of the plateau, and thus marks the initiation of significant regional elevation gradients between the plateau surface and the stable Sichuan Basin. Our results place the first direct bounds on the timing of uplift of the eastern Tibetan Plateau and indicate that the development of high elevation in

easternmost Tibet was restricted to the Late Miocene. Furthermore, our data suggest that the onset of denudation (and, by inference, uplift) may have been diachronous along the margin.

Morphology of the Eastern Margin

In contrast to the northern and southern margins of the Tibetan Plateau, the topographic expression of most of the eastern margin is irregular and diffuse. In southeastern Tibet, between the eastern syntaxis of the Himalaya and the Sichuan Basin, the plateau has no distinct topographic margin. Elevations decrease gradually from > 5000 m to < 1000 m over hundreds of kilometers (Figure 1a); this topographic gradient has been interpreted as the consequence of flow of weak lower crust from beneath the high plateau (Clark and Royden, 2000). In the Longmen Shan region, however, the topographic margin of the Tibetan Plateau is one of the world's most remarkable continental escarpments (Figure 1). Elevations rise from ~600 m in the southern Sichuan Basin to peaks exceeding 6500 m over a horizontal distance of less than 50 km. Regional topographic gradients typically exceed 10% along this mountain front and rival any other margin of the plateau. To the north, peak elevations decrease somewhat, but regional slopes remain steep, rising from ~700 m to nearly 5000 m in 30-40 km. At the northwest corner of the Sichuan Basin, the topographic front of the plateau turns north and transects the E-W trending Qinling Mountains. The margin is defined in this region by a high mountain range, the Min Shan, which marks the transition from plateau elevations of ca. 4000 m to elevations between 1000 –1500 m in the western Qinling Shan. Peak elevations in the Min Shan exceed 5500 m. North of the Min Shan, the topographic margin of the plateau is diffuse; plateau elevations gently grade into regional elevations near 1000 m.

The steep topographic escarpment adjacent to the Sichuan Basin has been deeply dissected by several major rivers; local valley – ridgetop relief in many places along the escarpment exceeds 3km (Figure 1). These rivers are short, steep bedrock channels that ultimately flow across the Sichuan Basin into the Chang Jiang (Yangtze River). Although some of the rivers to the west and southwest of the Sichuan Basin have their headwater regions in the central plateau, rivers draining the Longmen Shan escarpment

extend less than 200km westward. Along the northern portion of the margin, west of the Min Shan, rivers draining into the Sichuan Basin are actively eroding headward into the plateau surface and recent stream captures are evident in the drainage pattern and stream gradients (Kirby et al., 2000a). Along the southern portion of the margin drainage divides are set by a competition between rivers draining the eastern escarpment, and tributaries of the Dadu Jiang, a major south-flowing river to the west of the margin (Figure 1).

The surface of the plateau to the north and west of the escarpment stands at elevations between 3500 and 4000 m (Figure 1) and is characterized by extremely low local relief (200-300m). The landscape atop the plateau slopes gently to the west-northwest, and rivers draining this region flow generally northwest into the Huang He (Yellow River). Although some authors have recently proposed that the low relief of the central plateau is the consequence of backfilling of terrestrial basins behind active mountain ranges (Meyer et al., 1998), there is little evidence of this process in eastern Tibet. Large contiguous regions (> 10^5 km^2) of low relief are developed on pre-Cenozoic bedrock (Figure 1) and Cenozoic terrestrial sediments are rare and restricted to the vicinity of the Yellow River (People's Republic of China, 1991). The timing of development and subsequent evolution of this low-relief landscape is essentially unknown.

The eastern margin of the Tibetan Plateau adjacent to the Sichuan Basin thus appears to be an erosional escarpment formed in response to development of regional elevation gradients between the plateau surface and the Sichuan Basin. As the Sichuan Basin has remained relatively stable throughout the Cenozoic (Burchfiel et al., 1995), the evolution of relief along this escarpment can place important constraints on the timing of uplift of this region of the plateau. The primary goal of this paper is therefore to document the rates and pattern of denudation across the escarpment in an attempt to evaluate the timing of plateau development in this region.

Tectonic setting of the Longmen Shan region

The eastern margin of the Tibetan Plateau in the vicinity of the Sichuan Basin coincides with the Longmen Shan thrust belt, a feature developed along the western

margin of the Yangtze craton in Mesozoic time and reactivated in the Cenozoic (Dirks et al., 1994; Burchfiel et al., 1995). Although the focus of this paper is on the Cenozoic thermal evolution of rocks along the eastern margin, our results have important implications for the Mesozoic tectonic history of this region as well. In this section we briefly summarize salient aspects of the geology of the Longmen Shan region, discuss the Mesozoic tectonic history, and provide an overview of the Cenozoic tectonics. For a complete treatment of the geology of this complex region, see Burchfiel et al. (1995).

Geology of the Longmen Shan

For simplicity of discussion, we divide the geology of the Longmen Shan region into 4 distinct tectonostratigraphic packages (Figure 2). From oldest to youngest, these include: 1) crystalline basement rocks of the Yangtze craton, 2) Neoproterozoic – Permian platformal and passive margin sediments, 3) Triassic flysch of the Songpan-Garze terrane, and 4) Mesozoic – Cenozoic terrestrial sediments in the Sichuan Basin. These packages are juxtaposed across a series of structures with polyphase histories, collectively termed the Longmen Shan Thrust Belt (Dirks et al., 1994; Burchfiel et al., 1995). We describe each of these components and their structural relations below.

Crystalline rocks of the Yangtze craton are exposed in a belt of basement massifs adjacent to the southwest corner of the Sichuan Basin (Figure 2). The massifs consist of quartzofeldspathic gneisses and associated granitoids that are thought to be Precambrian in age (People's Republic of China, 1991). They are structurally overlain by a parautochthonous platformal and passive margin sequence, and thus assumed to represent the basement of the Yangtze craton. The sedimentary succession itself consists primarily of shallow water marine rocks of Neoproterozoic (Sinian) to Permian age. Permian carbonates generally grade into deep-water deposits of the Songpan-Garze terrane (Figure 2), a ~500,000 km^2 region of vertically dipping, isoclinally folded Triassic flysch and graywacke that may represent incomplete closure of a Paleotethyan ocean basin (Sengor et al., 1993).

All three of the above tectonostratigraphic packages were deformed during Mesozoic time as evidenced by a series of east-directed thrusts that place the Neoproterozoic – Triassic passive margin sequence atop the cratonal rocks (Chen and

Chen, 1987; Chen et al., 1994a; Dirks et al., 1994; Burchfiel et al., 1995; Chen and Wilson, 1996). The thrust belt trends northeast and merges with the E-W trending Qinling orogen (Mattauer et al., 1985) north of the Sichuan Basin. Northwest-trending folds within the Songpan-Garze wrap into parallelism with the western edge of the Longmen Shan thrust belt (Figure 2), and likely indicate that the thrust belt had a significant sinistral component during Mesozoic transpressional deformation (Dirks et al., 1994; Burchfiel et al., 1995).

Substantial metamorphism and plutonism accompanied Mesozoic deformation in the Longmen Shan region. Metamorphic grade of the passive margin sequence ranges from negligible to lower amphibolite grade and generally increases toward the hinterland (Dirks et al., 1994; Burchfiel et al., 1995). Metamorphism was accompanied by emplacement of a suite of Mesozoic plutons (generally granodiorite to monzonite) into the Triassic flysch northwest of the thrust belt (Roger et al., 1995b). These plutons are generally macroscopically undeformed, and crosscut isoclinal, upright folds within the flysch. Contact metamorphic mineral assemblages from the flysch adjacent to the plutons include andalusite and cordierite (Dirks et al., 1994), suggesting that the plutons were emplaced at pressures below of 2.5 - 3 kbar (Spear, 1993). Contact metamorphic minerals overgrow regional fabrics within the flysch, and, combined with the undeformed nature of the granitoids themselves, suggest that most of the plutons were emplaced late in the deformational history (Dirks et al., 1994).

The fourth tectonostratigraphic package in the region consists of terrestrial sediments east of the thrust belt. Triassic – Cretaceous sediments comprise westward thickening wedges of fluvial mudstones, sandstones, and conglomerates and were deposited in an flexural basin in front of the thrust belt (Chen et al., 1994a; Burchfiel et al., 1995). Total thickness of these deposits locally exceed 10 km (Burchfiel et al., 1995). Cenozoic sediment, however, is restricted to the southwest corner of the basin (Figure 2), and consist of a thin (< 500m) sequence of fluvial deposits of Paleogene – Quaternary age.

Mesozoic Tectonics of the Longmen Shan

Mesozoic deformation in the Longmen Shan thrust belt is reflected in major changes in depositional patterns along the western margin of the Sichuan Basin. Lower and Middle Triassic rocks atop the Yangtze craton are shallow-marine to non-marine in character. Rapid deposition of terrestrial deposits (up to several kilometers) began in the Late Triassic (Burchfiel et al., 1995). E-vergent thrust sheets in the Longmen Shan (Tangwangzhai nappe – Figure 2) carry Paleozoic passive margin rocks above uppermost Triassic and Lower Jurassic terrestrial sediments in the Sichuan Basin (Chen et al., 1994a). These faults are overlapped by Early and Middle Jurassic basin fill that narrowly restricts the timing of deformation along the thrust front (Burchfiel et al., 1995).

Within the Songpan-Garze terrane to the west, the Lower and Middle Triassic is characterized by deep-marine deposition, with a rapid influx of turbidites and flysch beginning in the Middle Triassic (Burchfiel et al., 1995). By Late Triassic time, the basin had shallowed, and coal-bearing clastics were deposited locally. The preservation of these shallow-water units suggests that the Mesozoic tectonism within the Songpan-Garze did not create high mountains subject to significant erosion (Burchfiel et al., 1995).

There is little direct evidence for late Middle Jurassic to Cretaceous deformation within the Longmen Shan region, although westward-thickening wedges of conglomerates of this age indicate continued subsidence along the foredeep (Burchfiel et al., 1995). Moreover, Arne et al. (1997) obtained Late Cretaceous $^{40}Ar/^{39}Ar$ ages (ca. 120-130 Ma) from muscovites in metamorphic rocks northwest of the Wenchuan-Maowen Fault. Although they interpreted these ages as reflecting differential cooling across this shear zone, the extent of Late Cretaceous deformation in the Longmen Shan remains unknown. Extensions of the thrust belt to the north and south did experience Late Mesozoic deformation (Zhang, 1992; Burchfiel et al., 1995).

Cenozoic Tectonics of the Longmen Shan

Despite the impressive topographic front along the Longmen Shan, shortening across this margin of the plateau appears to have been relatively minor during Cenozoic time. The lack of a Cenozoic foredeep along in the Sichuan Basin indicates that flexural loading of the basin was negligible during formation of the plateau (Burchfiel et al., 1995; Royden et al., 1997). In addition, space geodetic studies indicate that active

shortening across the Longmen Shan is less than a few mm/yr and within uncertainty of zero (King et al., 1997; Chen et al., 2000). Significant active deformation occurs along the Min Shan, a N-S trending range along the margin of the plateau north and west of the Sichuan Basin (Figure 2) (Tang et al., 1993; Chen et al., 1994b; Kirby et al., 2000b). Although structures along the eastern flank of the range are seismically active (Huya fault, Figure 2), focal mechanisms suggest that these structures are steeply dipping (Jones et al., 1984) and accommodate little shortening across the range. In addition, the apparent continuity of the Neoproterozoic-Permian sedimentary succession (Figure 2) indicates that net shortening across this margin of the plateau is rather limited (Kirby et al., 2000b).

Some Cenozoic deformation is present in the southern Longmen Shan, and this observation has important implications for the timing of tectonism along this margin of the plateau. In the southwestern Sichuan Basin, a series of NE-trending folds involve Cretaceous - Oligocene rocks, and are overlapped by flat-lying Neogene sediments (Figure 2). A belt of klippen composed of Paleozoic rocks was emplaced above folds in Upper Jurassic rocks that are continuous with the rocks below the Cenozoic section (Burchfiel et al., 1995). These relationships indicate that some shortening occurred after the Oligocene, but the absolute timing is unknown. However, lithologic affinities between the klippen and rocks in the thrust belt suggest that the magnitude of Cenozoic shortening in the southern Longmen Shan region is small and probably limited to a few tens of kilometers (Burchfiel et al., 1995).

Cenozoic deformation within the thrust belt to the west is unknown in magnitude and timing, although shortening appears to be relatively minor (Dirks et al., 1994; Burchfiel et al., 1995). Interestingly, a belt of normal faults occurs along the western margin of the Precambrian massifs (Burchfiel et al., 1995). These faults are characterized by low-grade mylonitic textures with kinematic indicators that suggest west side down displacement. These faults may be continuous with similar structures along the thrust belt to the southwest (Figure 2). $^{40}Ar/^{39}Ar$ cooling ages from micas within these mylonites ranged from the Cretaceous to the mid-Tertiary (ca. 25-30 Ma) (Hames and Burchfiel, 1993), and the authors interpreted the youngest of these ages as a best estimate of the timing of normal faulting.

Arne et al. (1997) interpreted fission-track age variations in zircon and apatite across the Longmen Shan thrust belt as indicating differential cooling in response to Cenozoic shortening and reactivation of Mesozoic structures. Zircon fission track ages west of the Wenchuan-Maowen fault range from 38 to 68 Ma, while a single sample east of the fault yielded an age of 110 Ma. Apatite fission-track ages are typically Late Miocene within the thrust belt and appear to be invariant across the Wenchuan-Maowen fault (Arne et al., 1997) (Figure 2). Apatites from Mesozoic terrestrial deposits in the Sichuan Basin yield fission-track ages between 93 and 189 Ma, in all cases near the depositional age of the sediments (Arne et al., 1997). In the Min Shan region, apatites yielded ages ranging from ca. 120 to 70 Ma. Track-length models from these three samples suggest an increase in cooling rates at ca. 20 Ma, that the authors interpret as the inception age of tectonism in this region of the plateau (Arne et al., 1997).

Thermal History of the Longmen Shan Region

In order to better resolve the Cenozoic thermal history of this region of the Tibetan Plateau, we utilized a variety of thermochronometers including $^{40}Ar/^{39}Ar$ in biotite and potassium feldspar, and (U-Th)/He in apatite. Details of the analytical procedures are presented in the appendix. Nominal closure temperatures in these systems span a temperature range from ca. 300-350° C (biotite) (Grove and Harrison, 1996) to ca. 70° C (apatite) (Farley, 2000), and multi-diffusion domain modeling of K-feldspar $^{40}Ar/^{39}Ar$ spectra (Lovera et al., 1989) permits exploration of much of the temperature interval in between. In order to test for possible spatial variations in the Cenozoic thermal history and to complement the data set of Arne et al. (1997), we collected samples from three regions of the plateau. Sample locations are given on Table 1 and shown on Figure 2. Two samples (93-3 and 93-1) are from Precambrian massifs (Pengguan and Baoxing massifs) along the topographic margin adjacent to the Sichuan Basin. One sample (97-14) is from a Mesozoic pluton along the eastern foot of the Min Shan (Figure 2), where the topographic margin of the plateau transects the west Qinling Mountains. Several samples (97-2, 97-4, 97-5, 97-6) were collected from Mesozoic plutons within the Songpan-Garze terrane west of the thrust belt. Samples from the last region were collected from the headwater regions of one of the primary drainages along

this margin, the Hei Shui He (Black Water River). We collected samples from the valley floors east of the drainage divide and from the low relief surface west of the divide. Together these samples span ~ 2 km of relief (Table 1).

Biotite $^{40}Ar/^{39}Ar$ Results

We obtained biotite separates from three granitoid plutons within the Songpan-Garze terrane. Samples EK 97-4 and 97-6 were collected from plutons in the headwaters of the Hei Shui He, while sample EK 97-14 was collected from a small (~3 km^2) stock at the eastern foot of the Min Shan (Figure 2). Incremental heating of these samples yielded relatively straightforward release spectra (Figure 3), but no statistically defined plateaux. Moreover, the highly radiogenic nature of the ^{40}Ar in the samples prevented their evaluation for possible excess ^{40}Ar contamination (Roddick et al., 1980). Our best estimates of the $^{40}Ar/^{39}Ar$ closure ages of these biotites are the ^{39}Ar weighted means of the dates for increments defining relatively flat portions of the spectra: ~194 Ma for 97-4, ~208 Ma for 97-6, and ~171 Ma for 97-14. Although provisional, these dates are consistent with emplacement ages determined for similar plutons in the Songpan-Garze terrane to the south (Roger et al., 1995b), and probably record rapid cooling of the plutons following emplacement.

Apatite (U-Th)/He Results

Apatite (U-Th)/He thermochronology is a recently redeveloped technique that provides age information in the low-temperature (< 100° C) range of thermochronologic systems (Zeitler et al., 1987; Lippolt et al., 1994; Wolf et al., 1996; House et al., 1997; Warnock et al., 1997; Wolf et al., 1997). Helium diffusion in most fluorapatite appears to be a thermally activated process with a nominal closure temperature (for a cooling rate of 10° C/m.y.) of ~70° C (Farley, 2000). Thus, the method has the potential to bridge the gap between surface temperatures and existing low-temperature thermochronometers (House et al., 1998). Details of the analytical procedures associated with age determination are presented in the Appendix. Data for apatites from samples in this study are presented in Table 1; sample locations and associated ages are presented in Figure 2.

The helium ages cluster in two distinct populations. Samples collected from the topographic margin of the plateau record Pliocene ages, while those from the interior of the plateau record Miocene ages. A sample collected from the Pengguan massif (93-3, ~900 m elevation), along the margin of the plateau adjacent to the Sichuan Basin, yielded a (U-Th)/He age of 4.6 ± 0.3 Ma, while a sample from the eastern foot of the Min Shan (97-14, ~1100 m elevation) yielded an age of 3.2 ± 0.5 Ma. It is worth noting that sample 93-3 was collected in close proximity to two apatite fission-track samples of Arne et al. (1997) and yields an age that is statistically indistinguishable from their results (see Figure 2).

Samples collected from the plateau yielded ages of 13.4 ± 0.8 Ma (97-2, ~1800 m elevation), 19.9 ±1.2 Ma (97-4, ~ 2000 m elevation), 20.6 ± 1.2 Ma (97-5b, ~4500 m elevation), and 8.2 ± 0.5 Ma (97-6, ~4300 m elevation). Although these samples span some 2 kilometers of relief, there does not appear to be a strong correlation of age with elevation. Given the limited number of samples and their geographic distribution, however, we can say little about the geometry and position of the partial retention zone for He over the time interval of interest (Wolf et al., 1998). An additional complication is introduced by the anomalously young age of one of the highest samples (97-6). At present, we cannot address whether there is substantial variation in apatite (U-Th)/He ages from the surface of the plateau. The variation in ages between the topographic margin of the plateau and the interior, however, appears to be a robust feature of the apatite data, and suggests that Late Cenozoic cooling may have been diachronous across the margin of the plateau. Similar variations in apatite fission-track ages are observed in the Longmen Shan (Arne et al., 1997) and to the south, along the Xianshuihe fault (Xu and Kamp, 2000).

K-feldspar $^{40}Ar/^{39}Ar$ Results

In order to resolve the thermal history of the Longmen Shan region between the Jurassic ages recorded in biotites and Miocene-Pliocene ages recorded in apatites, we analyzed potassium feldspars from 5 samples distributed across the plateau and modeled the results following the multiple diffusion domain (MDD) theory (Lovera et al., 1989; Lovera et al., 1991). Whether or not this model accurately represents radiogenic ^{40}Ar

diffusion in natural feldspars over geologic timescales is controversial (Parsons et al., 1988; Villa, 1994; Parsons et al., 1999). Persuasive as the mineralogical arguments against the MDD model may be, the fact remains that numerous applications of the method to samples from a variety of geologic settings have yielded sensible time-temperature paths that seem consistent with independent thermochronologic constraints (Arnaud et al., 1993; Leloup et al., 1993; Krol et al., 1996; Warnock and Zeitler, 1998). Our approach has been to proceed with the modeling exercise and ask, whenever possible, whether or not the modeled temperature-time path is consistent with the higher and lower-temperature constraints provided by the $^{40}Ar/^{39}Ar$ and (U-Th)/He data presented above.

The interpretation of the $^{40}Ar/^{39}Ar$ results in terms of the MDD model requires some assumption regarding the general form of the temperature-time path experienced by the samples (Lovera et al., 1989). We began with the simplest possible solution - monotonic cooling. Transient reheating would significantly alter the interpretation of the thermal history. However, we are confident that we can discount the possibility of Cenozoic reheating for a variety of reasons. First, there is no evidence for Cenozoic magmatism in this region of eastern Tibet; all dated plutons within the study area are Mesozoic in age (Roger et al., 1995b). The only recognized Cenozoic pluton is exposed in the Gongga Shan massif (Roger et al., 1995a), well to the south and west of the Sichuan Basin. Second, geothermal activity is very limited in this region of the plateau. Finally, preliminary analyses of fission-track length distributions in samples from the northern portion of the margin (Min Shan) suggest slow cooling during the late Mesozoic and early Cenozoic (Arne et al., 1997). Thus we feel that monotonic cooling is a reasonable first-order interpretation of the feldspar $^{40}Ar/^{39}Ar$ results. As discussed below, it appears to work in all cases but one.

Feldspars from the Longmen Shan region show differences in age and thermal history that appear to correspond with sample geographic distribution. We first discuss samples collected from the topographic margin (93-4, 97-14), one from the southern Longmen Shan (93-1), and then turn to samples from the interior of the plateau (97-4, 97-6).

Plateau margin. Measured age spectra for samples 93-4 and 97-14 are presented in figures 4a and 5a, respectively. Both samples are characterized by saddle-shaped release spectra that suggest the presence of excess argon in the low-temperature release steps. Duplicate isothermal heating increments (Harrison et al., 1994) permitted the isolation of Late Miocene components of gas released early in the experiments. The ages of subsequent steps increase monotonically to maxima of ~147 Ma (93-4) and ~61 Ma (97-14). Diffusion parameters (activation energy, E_a and frequency factor, D_0/r^2) calculated from the release of ^{39}Ar are presented in Figures 4b and 5b, and are typical of alkali feldspars (Lovera et al., 1997). The domain size distribution for each sample is shown on figures 4c and 5c.

Model temperature-time paths (inverted from the release spectra and kinetic parameters, see appendix) are shown in figures 4d and 5d. Both thermal histories are remarkably similar, and suggest that the samples underwent extremely slow cooling during the Cretaceous and Early Tertiary. The modeled cooling curve for 97-14 is poorly constrained by data at temperatures higher than ~240 °C, but a simple extrapolation of the nearly linear portion of the curve (between ~200 – 240 °C) to older ages is consistent with the nominal bulk closure temperature for ^{40}Ar in biotite (Grove and Harrison, 1996) having been achieved at ~171 Ma, the approximate age of biotite from this sample. Modeled cooling curves show a dramatic increase in cooling rates (~ 20–50 °C/m.y.) during the Late Miocene beginning at ca. 11 Ma for sample 93-4 and ca. 6 Ma for sample 97-14. For both samples, such an increase is compatible with Late Miocene (U-Th)/He apatite ages.

Plateau interior. In contrast to samples from the topographic margin, feldspars collected from Mesozoic plutons in the headwaters of the Hei Shui He (Figure 2) yielded minimum ages of ~50–70 Ma (Figures 6a and 7a, samples 97-4 and 97-6, respectively). Minor excess ^{39}Ar was apparent in the first 5-10% of the gas released. The measured ages increase monotonically from the minimum to ~195-210 Ma. The diffusion behavior of these samples was slightly more complex than that of samples from the topographic margin. For example, duplicate isothermal steps for sample 97-4 display a systematic offset resulting in two subparallel arrays on an Arrhenius diagram (Figure 6b). We attribute this behavior to a slight hystersis in the temperature cycling that appears to be a

consequence of our heating schedule for this sample (supplementary data table). Because the furnace had a greater amount of time to equilibrate during the second isothermal increment, we relied on these results to extract kinetic parameters.

Modeled thermal histories for these samples are also characterized by slow cooling during the Mesozoic and early Cenozoic (Figures 6d and 7d). Because these K-feldspars were more retentive of Ar than the plateau margin samples, their modeled temperature-time paths extend to higher temperatures and older ages, permitting a direct comparison of the results with the biotite $^{40}Ar/^{39}Ar$ data for 97-4 and 97-6 (Figures 6d and 7d, respectively). In both cases, the biotite data are consistent with the K-feldspar cooling models.

Southern Longmen Shan. Sample 93-1 was collected from the southern portion of the Baoxing massif, in the southern Longmen Shan region (Figure 2). Its release spectrum show evidence for considerable excess ^{40}Ar contamination of the low temperature steps and a remarkable monotonic increase in the apparent ages of higher temperature steps from ~65 Ma to ~550 Ma.

MDD modeling of the thermal history of this spectrum suggests relatively slow cooling between ~350 Ma and ~100 Ma (Figure 8d). Beyond this range, the model is poorly constrained. This result is surprising because independent evidence implies that the southern Longmen Shan had a complex tectonothermal history over much of the ~ 350 – 100 Ma interval. For example, the region was the locus of basaltic volcanism during the Permian (as evidenced by the Emei flood basalts) and of severe shortening during the Mesozoic (Chen et al., 1994a; Burchfiel et al., 1995). It may be that the assumption of monotonic cooling for the purpose of multidomain modeling is inappropriate over this time interval, and we unfortunately have no other geochronologic data that might corroborate the result. In any event, the absence of Cenozoic ages in the low-temperature portions of the release spectrum appear to indicate that the sample resided at relatively high levels in the crust prior to Cenozoic time.

Summary: cooling history of the Longmen Shan region

Thermal histories inferred from the combination of $^{40}Ar/^{39}Ar$ thermochronometry on biotite, (U-Th)/He thermochronometry on apatite, and alkali feldspar MDD modeling

provide a relatively complete picture of the low-temperature cooling history of rocks in the Longmen Shan region following Mesozoic tectonism. Despite differences in age and in structural setting, all samples are characterized by remarkably slow cooling (< 1°/m.y.) between the mid-Mesozoic and early Cenozoic (Figure 9, Table 2). However, samples from the modern topographic margin of the plateau (93-4, 97-14) record systematically younger ages than samples from the plateau interior (97-4, 97-6). These samples apparently closed to Ar diffusion in feldspar in the late Mesozoic and early Cenozoic, while those from the margin remained open to Ar loss until the Late Miocene and Pliocene. Samples from the margin record a profound increase in cooling rates beginning at ~11 Ma and ~6 Ma and continuing through apatite closure at ca. 3 - 4 Ma until the present day.

Rates and pattern of denudation

The regional extent and remarkably slow rate of cooling between the mid-Mesozoic and the Cenozoic suggests the establishment and persistence of an extremely stable thermal regime following Mesozoic tectonism. If we make the reasonable assumption that isotherms during this time were subhorizontal and that cooling reflects the motion of rocks through this thermal structure due to erosional denudation, we can translate cooling rates into estimates of denudation rate. For geotherms typical of stable continental regions (15 – 25°/km), cooling rates of < 1°/m.y. imply that denudation rates must have been extremely slow (< 0.1 mm/yr). These rates would have persisted over much of the region until the Late Miocene (Table 2, Figure 9).

Rapid Late Cenozoic cooling observed in samples from the margin of the plateau (Table 2) implies that denudation rates increased substantially in the Late Miocene. However, an estimate of their magnitude is complicated by the advection of heat during rapid denudation (Mancktelow and Grasemann, 1997). We can, nevertheless, estimate the depth of the sample prior to the onset of rapid cooling and obtain a mean denudation rate over the period of the rapid cooling event. Both samples from the topographic margin record the onset of rapid cooling at ~200°C, implying approximately 8-10 km of denudation during the Late Cenozoic. For sample 93-4 (Longmen Shan), this translates

into mean denudation rates on the order of 1 mm/yr, while for sample 97-14 (Min Shan) denudation rates appear to have been ~1-2 mm/yr.

Samples from the Songpan-Garze terrane, however, closed to Ar diffusion in feldspar between 50-60 Ma, consistent with a lesser degree of Late Cenozoic denudation. Indeed, the presence of (U-Th)/He apatite ages between 8-20 Ma suggests that Miocene-Recent denudation on the plateau has been limited to a few kilometers. Thus, the data suggest a pronounced gradient in Late Cenozoic denudation across the eastern margin of the plateau adjacent to the Sichuan Basin, with high rates focused in a narrow zone along the present topographic front. These results are broadly consistent with the amount and distribution of denudation inferred from apatite and zircon fission-track ages in the Longmen Shan region (Arne et al., 1997) and along the margin of the plateau south and west of the Xianshuihe fault (Xu and Kamp, 2000).

Our data also suggest that cooling rates may have increased slightly (~ 3-5 °/m.y.) in samples from the plateau at some time between feldspar and apatite closure (~60 – 20 Ma - Table 2 and Figure 9). However, the form of the cooling path during this interval is not constrained by our data. Denudation rates over this interval (for nominal geotherms) were likely on the order of 0.1 – 0.3 mm/yr. As cooling rates between apatite closure and surface temperatures appear to have been similar (Table 2), we infer that denudation rates were relatively slow during the Late Cenozoic. Importantly, we see no indication of the pronounced Late Miocene rapid cooling that affected samples along the margin.

Onset of Rapid Denudation

The apparent focusing of Late Cenozoic denudation along the present topographic margin of the plateau and subsequent exhumation of rocks from upper mid-crustal depths allows us to resolve the onset of rapid cooling fairly precisely: at ~11 Ma along the Longmen Shan segment and at ~6 Ma along the Min Shan. Evaluating whether or not these transitions also represent the onset of rapid denudation is problematic. For example, the advection of heat that accompanies an increase in denudation rate imparts a phase lag between the onset of rapid denudation and rapid cooling that complicates a direct interpretation of the onset of rapid cooling (House and Hodges, 1994; Stuwe et al., 1994; Mancktelow and Grasemann, 1997). As packages of rock are translated toward the

surface along with isotherms, cooling is delayed until they pass through compressed isotherms near the surface. However, simple modeling of the advective/conductive transfer of heat in response to rapid denudation in extensional settings (Ruppel et al., 1988) suggests that this lag time is relatively short (1 - 2 m.y.) in the upper regions of the crust. Therefore, our estimates of the onset of rapid cooling in the Longmen Shan are probably a reasonable proxy for the onset of rapid denudation. Thus we reason that the variation in timing observed between the Longmen Shan and the Min Shan may be an indication of important diachroneity between different regions of the modern plateau margin. However, a definitive test of this possibility is beyond the scope of our current sample distribution.

Although our results are broadly consistent with the amount and distribution of Cenozoic denudation inferred by Arne et al (1997), our estimates of the timing of onset of rapid Late Cenozoic denudation differ substantially. Arne et al. (1997) modeled fission-track length distributions in 3 apatite samples collected in a transect across the Min Shan (Figure 2). Although their results suggest slow cooling from Mesozoic time followed by a rapid Late Cenozoic cooling event, they were only able to constrain this event to within the past 20 m.y. Our results refine this estimate and suggest that rapid cooling in the Min Shan was restricted to the past 5 - 6 m.y.

Tectonic Implications

Timing of uplift in eastern Tibet

The timing and rates of denudation across the eastern margin of the Tibetan Plateau have important implications for the development of topography in this region. As discussed above, regional topographic gradients between the plateau and the Sichuan Basin are among the highest observed anywhere on the continents. Given the structural position of the samples at the foot of this topographic escarpment, it is unlikely that the inferred slow denudation rates prior to the late Miocene could be maintained in the presence of such extreme topographic gradients. This scenario would require climatic conditions approaching those in present-day Antarctica (Brook et al., 1995), and is clearly not appropriate for Central Asia during the Miocene. Indeed, present-day incision rates along rivers draining this margin range from 1-2 mm/yr (Kirby et al., 2000a),

attesting to the erosive power of streams along the eastern front of the escarpment. Thus, we interpret the pronounced Late Miocene increase in cooling rates as marking the development of regionally significant elevation gradients between the surface of the plateau and its foreland.

Our results suggest that uplift of the eastern plateau (relative to the Sichuan Basin) began between 10 - 12 Ma in the Longmen Shan and between 5 - 7 Ma in the Min Shan. Given the uncertainties in the $^{40}Ar/^{39}Ar$ age determinations (see supplementary data) and those imparted by the advection of heat in response to rapid denudation, we cannot be certain of the significance of the difference in age between samples. If there were substantial variation in the onset of plateau development along its eastern margin, it would have profound implications for the dynamics of plateau formation. While we suspect this may be true, a definitive answer awaits a more comprehensive study. In any case, development of the plateau along the Sichuan Basin appears to have initiated in late Miocene time (ca. 11 Ma).

This age, coupled with our thermochronologic estimates for denudation on the surface of the plateau allow us to place first-order bounds on the rates of plateau formation. The present day elevation difference between the surface of the plateau and the basin is ~3 – 3.5 km. Our results imply that denudation rates on the plateau were on the order of 0.1 – 0.3 mm/yr during the Late Miocene - Recent. Thus, mean rock uplift rates (surface uplift + exhumation (England and Molnar, 1990)) over this period thus range from 0.4 – 0.6 mm/yr. If we assume that plateau formation was accomplished by isostatically compensated crustal thickening, mean thickening rates would have been on the order of 2.4 – 4.6 mm/yr (assuming a ratio of crust to mantle density ~ 5/6). Thus, our data are compatible with the hypothesis that the topography in eastern Tibet developed by crustal thickening (Royden et al., 1997). Inferred rates of mean rock uplift do not require (nor do they necessarily exclude) convective removal of thickened lithosphere (Molnar et al., 1993).

The absence of evidence for large magnitude Cenozoic shortening of the upper crust in eastern Tibet (Burchfiel et al., 1995; Wang et al., 1998; Kirby et al., 2000b) implies that deformation and crustal thickening may have been accomplished by ductile flow in a weak lower crust (Royden, 1996; Royden et al., 1997). A number of

geodynamic models of plateau development (England and Houseman, 1986), including those invoking lower crustal flow (Royden et al., 1997), suggest that the plateau should grow laterally with time. If the plateau has been growing east and northeast by the evacuation of lower crust from beneath the plateau, our results indicate that it did not reach the margin of the Sichuan Basin until ~11 Ma. Importantly, our results contradict the recent suggestion that the present configuration of the plateau margins was established by ca. 20 Ma (Xu and Kamp, 2000). Indeed, the variability (~5 m.y.) in the onset of rapid cooling along different sections of the eastern margin adjacent to and north of the Sichuan Basin that uplift of the plateau may have been quite heterogeneous in space and time.

The distribution of Cenozoic denudation across the eastern margin of the plateau also has important implications for the coupling between surface and tectonic processes along the margin. Our results indicate removal of ~ 8 - 10 km of material along the plateau margin since Late Miocene time, nearly twice the inferred rock uplift in the plateau to the west and southwest. In the Min Shan region, our results in conjunction with Cretaceous apatite fission track ages obtained by (Arne et al., 1997) indicate that substantial Late Cenozoic denudation was confined to a narrow (< 40 km) region along the eastern flank of the range (see Figure 2). This pattern of Cenozoic denudation appears to be present in the Longmen Shan, although the width is poorly constrained. However, in both the Longmen Shan and Min Shan regions the zone of deep exhumation appears to correspond to the present-day topographic margin, and to a zone of high gradients along modern rivers (Kirby et al., 2000a). This spatial correlation of long-term exhumation of mid-crustal rocks and steep river gradients may reflect the focusing of crustal flow (Beaumont et al., 1992; Willett, 1999) in response to erosional unloading along the topographic margin.

Timing of normal faulting in the Longmen Shan

Our results from the Pengguan Massif, adjacent to the Sichuan Basin, place additional constraints on the timing of normal faults developed within the Longmen Shan thrust belt. The massif is an elongate NE trending body of Precambrian gneisses and granitoids and is bound on the NW by a series of low-grade mylonite zones with top to

the NW sense of displacement (Burchfiel et al., 1995). Although it is possible that displacement on these fault systems is responsible for some of the rapid cooling observed between 11-0 Ma, we see no evidence for a 25-30 Ma event as suggested by Hames and Burchfiel (1993). Indeed, throughout the Longmen Shan, our data suggest that the early and mid-Miocene was characterized by regionally uniform slow cooling. Thus, if the faults have Cenozoic displacement, it appears to be restricted to the Late Miocene-Pliocene. Otherwise, normal-sense displacement may be Mesozoic in age. Clearly, the exact timing of displacement on these normal fault systems remains an important problem in this region.

Landscape evolution along the eastern margin

The thermal histories presented here have important implications for the long-term morphologic evolution of the eastern Tibetan Plateau adjacent to the Sichuan Basin. In particular, our data place preliminary bounds on 1) the 'age' of the present-day surface of the plateau and, 2) the evolution of the modern relief along the escarpment. As described above, large regions of the eastern plateau comprise a low-relief surface cut on vertically foliated Triassic flysch. Although this surface (and any 'erosion surface') is a dynamic landform, and is currently evolving as an erosional and depositional feature, we can define three useful temporal characteristics of such a surface: 1) the time at which the surface is reduced to low relief, 2) the duration of such relief, characterized by slow erosion rates, and 3) the time at which the surface begins to be significantly dissected. While our data are far from comprehensive, the thermal histories of samples from the surface (97-6) and 2 km below it (97-4) suggest that the low relief atop the eastern plateau today may have developed in the Mesozoic and been sustained since then by relatively slow erosion. Subsequent dissection of this surface in response to the development of regional topographic gradients between the plateau and the Sichuan Basin apparently initiated in the Late Miocene, and most of the local relief (which now exceeds 3 km) must have developed since that time.

Conclusions

Thermal histories derived from integrated $^{40}Ar/^{39}Ar$ and (U-Th)/He dating of samples along the eastern margin of the Tibetan Plateau place important constraints on the timing of development of high topography adjacent to the Sichuan Basin. The data suggest that this region of the plateau was characterized by extremely slow cooling (~1°C/m.y.) following Mesozoic tectonism and pluton emplacement. These cooling rates apparently persisted over much of the region until the Late Miocene, and suggest the presence of a remarkably stable thermal regime. We infer that mean erosion rates during this time period were concomitantly slow (< 0.1 mm/yr for nominal geothermal gradients between 10°C/km and 30°C/km). We conclude that the precipitous present-day topographic gradients between the plateau and the Sichuan Basin could not have existed prior to the Late Miocene. Initial development of a landscape characterized by low relief atop the present-day plateau may well date to this period of relative tectonic stability.

Rapid cooling observed in samples from the present-day margin of the plateau began in the Late Miocene and likely reflects rapid erosion focused along the developing topographic margin. The relatively deep exhumation of rocks (~ 8 - 10 km) along this margin provides a unique record of the onset of rapid cooling as recorded in $^{40}Ar/^{39}Ar$ and (U-Th)/He isotopic systems. Thus, the present-day topography of the plateau does not appear to have been present prior to ~11 Ma.

We caution, however, that this estimate may not apply to the plateau as a whole. Plateau uplift, if driven by crustal thickening, may be quite heterogeneous in space and time. A Late Miocene age for uplift of the eastern plateau falls near the high end of the range of estimates for rapid uplift inferred from extension (Harrison et al., 1992; Coleman and Hodges, 1995) and volcanism (Turner et al., 1993). However, the ~5 m.y. difference in age between the initiation of rapid cooling along sections the eastern margin suggests that significant variability may exist even at scales of hundreds of kilometers. Only when we develop similar estimates of the timing of plateau uplift along many of its other margins, will we be able to comprehensively assess the timing and mechanisms of plateau formation.

Appendix: Analytical Methods

$^{40}Ar/^{39}Ar$ techniques

Pure mineral separates were prepared from crushed material using standard heavy liquid and magnetic methods. In all cases, material was hand-picked to ensure sample homogeneity (>99%). Mineral separates were washed in distilled water, acteone and ethanol prior to packaging in Al foil for irradiation. Individual packets were loaded in aluminum disks, shielded with Cd foil, and irradiated in the core position of the research reactor at McMaster University, Ontario.

K and Ca production factors during irradiation were established by analyzing reagent grade K_2SO_4 and CaF_2 included in each package. Fast neutron flux was monitored using Fish Canyon sanidine (27.95 Ma) (Cebula et al., 1986) and MMhb-1 hornblende (520.4 Ma) (Samson and Alexander, 1987). Monitors were analyzed by total fusion of 1-5 crystals with an Ar-ion laser. Flux gradients are typically negligible within a disk, but the irradiation parameter, J, may vary by up to 2% along the length of a package (Hodges et al., 1994). We assigned the mean J calculated for a disk to all samples in that disk. We assume a conservative 2% uncertainty in J (at 2σ) for all samples in order to account for potential uncertainties in interpolation of J between monitor positions and in potential heterogeneities in monitor materials. Ages stated in the text and figures include this propagated uncertainty.

Resistance furnace gas extraction was accomplished using a double-vacuum assembly in the CLAIR facility at MIT. Details of the extraction line can be found in Hodges et al. (1994). Temperatures were continuously monitored using a Re-W thermocouple; this system provides approximately 5° C control on temperature over the course of a heating increment. All samples were allowed to equilibrate with the ambient furnace temperature (250° C) for 5 min prior to analysis.

Operational blanks for the resistance furnace extraction line are dominated by the furnace and are strongly temperature dependent. Furnace system blanks were measured as a function of temperature prior to sample analysis. Blank corrections were generally small; signal sizes were typically two to three orders of magnitude larger than the furnace system blank.

After corrections were made for interfering isotopes, mass discrimination, and blank, $^{39}Ar/^{40}Ar$ data were analyzed in a variety of ways. Data are available upon request (Table 3 - supplementary data). The model age for each increment of gas extraction was calculated assuming an initial $^{40}Ar/^{36}Ar$ value of 295.5 and is assigned a 2σ uncertainty that reflects propagated errors in all correction factors and the J parameter. Release spectra illustrate model ages for incremental heating analyses as a function of the amount of $^{39}Ar_K$ in each step. Age plateaux determined from the incremental release spectra are defined as the error-weighted mean age of contiguous steps that define 50% or more of the total $^{39}Ar_K$ released, and, are statistically

indistinguishable at the 2σ confidence level, exclusive of uncertainty in the J value. For the biotites in this study, none of the spectra define plateaus, and we use a weighted mean of selected contiguous steps as our best estimate of the bulk closure age of the sample. All uncertainties associated with the ages are reported at the two-sigma level and include the uncertainty in the J factor but not uncertainties in the ages of the flux monitors.

For the K-feldspar analyses, the heating schedule was varied in order to facilitate retrieval of kinetic information for each sample (Lovera et al., 1991). Heating schedules are presented along with $^{40}Ar/^{39}Ar$ data in the supplementary data table (available upon request from AGU). Activation energies for the samples were obtained by fitting an unweighted linear regression to the initial, low temperature diffusion data on Arrhenius diagrams. Domain size distributions were modeled from fits to the ^{39}Ar release data via $\log(r/r_o)$ plots (Lovera et al., 1989; Lovera et al., 1991; Lovera, 1992). The model does not consider gas evolved above the temperature for incongruent melting of K-feldspar (~1150 °C). For our samples, we were typically able to model between 60 and 80 % of the gas.

Excess argon is often present in the first few percent of gas released and may obscure age information in the low-temperature portion of the experiment (Harrison et al., 1993). Recent experiments have shown that, in many cases, this excess argon is associated with the decrepitation of Cl-rich fluid inclusions (Harrison et al., 1993; Harrison et al., 1994). In order to facilitate retrieval and interpretation of age information from the early portion of the gas release we subjected all samples to duplicate isothermal heating. In all cases, the first step at a given temperature increment yielded anomalously old ages, while the second step typically yielded younger ages, presumably permitting us to see through the effects of Cl-related excess argon and to obtain a geologically meaningful age. We are thus able to model the thermal history of the samples to fairly low temperature (in some cases as low as ~120° C).

Once the domain structure and diffusion parameters are obtained, their thermal histories were explored using an automated inversion model (Zeitler, 1993). The automated inversion model is based on the controlled random search algorithm (CRS), previously applied to modeling fission track data (Willett, 1997). The CRS algorithm is used to find thermal histories, that when fed into a finite-difference diffusion model, produce model age spectra (typically a set of 100) that match the observed spectrum derived from laboratory incremental heating. In describing the cooling history of our samples we used the mean temperature history for the 100 histories. In the advent of an episode of reheating, a unique solution for the thermal history is not possible. In contrast, solutions allowing only monotonic cooling tend to cluster tightly within the closure window for Ar diffusion in the K-feldspar.

(U-Th)/He techniques

Apatite was separated from crushed samples using standard magnetic and heavy liquid techniques at MIT. Mineral separates were hand picked to ensure sample homogeneity; apatites were selected on the basis of morphology, size, and the absence of visible defects and inclusions (helium associated with U and Th bearing silicate inclusions can produce anomalously old ages – (House et al., 1997; Spotila et al., 1998)). Samples typically consisted of 10-20 crystals of apatite between 60 and 90 μm in diameter. Helium was degassed in a high-vacuum furnace and measured on a quadrupole mass spectrometer in the Noble Gas Laboratory of the California Institute of Technology (see Wolf et al., 1996 for details of the extraction line). Analytical precision is typically 6-8% (2σ), based on reproducibility of intralaboratory standards (Wolf, 1997). Following Farley et al. (1996), measured He concentrations were corrected for alpha ejection. This was accomplished using a geometric factor, F_T, derived from the size and shape of crystals in each sample (Farley et al., 1996). F_T values ranged from 0.58 – 0.79. Estimated uncertainty in this parameter is ~4-6% (2σ), based on repeat measurements (Spotila et al., 1998). After helium extraction, samples were dissolved in HNO_3 and measured for U and Th contents by isotope dilution on an inductively coupled plasma mass spectrometer (ICP-MS) at Caltech. Typical analytical precision is ~2% (Spotila et al., 1998). Together, these individual uncertainties propagate to yield a 2σ uncertainty of ±10% for individual ages (Spotila et al., 1998). Based on replicate analyses, we adopt uncertainties (2σ) for our samples of 6% (Table 1). However, for samples with low helium yield (97-14 and 94-3) we adopt uncertainties of 15% (2σ).

Table Captions

Table 1: Analytical data from (U-Th)/He age determinations from apatites in the Longmen Shan region. See appendix for analytical procedures.

Table 2: Cooling rates inferred from thermochronological analyses in the Longmen Shan region. Nominal closure temperatures for biotite and apatite are taken, respectively, as ~350° C (Grove and Harrison, 1996) and ~75° C (Farley, 2000).

Figure Captions

Figure 1: Regional morphology of the eastern margin of the Tibetan Plateau adjacent to the Sichuan Basin. A) Index shaded relief image of the Indo-Asian collision zone. Box shows approximate location of the study area. B) Shaded relief image of the eastern margin. Note the deeply dissected, high-relief escarpment along the margin. Major rivers draining the escarpment are overlain in black and serve to illustrate the approximate location of the drainage divide. Locations of swath-averaged topographic profiles are shown as rectangular boxes. C and D) Swath-averaged topography across the eastern margin in the Min Shan and Longmen Shan regions, respectively. Topography was extracted in a 100km wide, rectangular swath and projected onto a vertical plane located at the midline of the swath. Shown are maximum, mean, and minimum elevations for each swath. Note the remarkably steep topographic front along the Sichuan Basin, and the somewhat more moderate front north of the basin.

Figure 2: Simplified geologic map of the Longmen Shan region of the eastern margin of the Tibetan Plateau. Geology modified after Burchfiel et al. (1995), 1:200,000 geologic maps (Ministry of Geology and Mineral Resources, P.R. China, 1991), and our own observations. Names of selected cities, major structures, and geographic regions are show for reference to the text. P = Pengguan Massif, B = Baoxing Massif. Large ellipses show the sample locations and (U-Th)/He apatite ages of this study. Shown for reference in small ellipses are apatite fission-track age determinations of Arne et al. (1997).

Figure 3: Biotite $^{40}Ar/^{39}Ar$ release spectra for samples from granitoid plutons in the region. Arrows show the range of steps used in the weighted mean age calculation.

Figure 4: A) $^{40}Ar/^{39}Ar$ release spectrum (open boxes) and mean of 100 modeled age spectra (solid line) for alkali feldspar collected from the Pengguan massif, adjacent to the Sichuan Basin. B) Arrhenius plot of log D/r^2 versus reciprocal temperature. Arrhenius data are calculated assuming plane slab diffusion geometry from measured ^{39}Ar release during incremental heating experiment. C) Plot of log (r/r_o) versus ^{39}Ar released (dashed line) and theoretical fit (solid line) from model. D) Model thermal history for sample 93-4 obtained from inverse modeling of the kinetic parameters and domain structure. Solid lines represent the mean (black) and bounds (gray) of 100 best-fit results. Dashed lines represent portions of the model thermal history outside the range of ages recorded in the feldspar. Also shown is the apatite (U-Th)/He age from nearby sample 93-3.

Figure 5: A) $^{40}Ar/^{39}Ar$ release spectrum (open boxes) and mean of 100 modeled age spectra (solid line) for alkali feldspar collected from the eastern flank of the Min Shan, north of the Sichuan Basin. B) Arrhenius plot of log D/r^2 versus reciprocal temperature. Arrhenius data are calculated assuming plane slab diffusion geometry from measured ^{39}Ar release during incremental heating experiment. C) Plot of log (r/r_o) versus ^{39}Ar released (dashed line) and theoretical fit (solid line) from model. D) Model thermal history for sample 97-14 obtained from inverse modeling of the kinetic parameters and domain structure. The range of 100 best-fit results is represented by the gray region, while the mean of these is shown in black. Light gray regions represent portions of the model thermal history outside the range of ages recorded in the feldspar. Also shown is the (U-Th)/He age of coexisting apatite. Inset box shows the thermal history expanded to include coexisting biotite. Note that the biotite age is consistent with the projection of the slow cooling portion of the history.

Figure 6: A) $^{40}Ar/^{39}Ar$ release spectrum (open boxes) and mean of 100 modeled age spectra (solid line) for alkali feldspar collected from a granitoid pluton at ~2000m, in the headwater reaches of the Hei Shui He. B) Arrhenius plot of log D/r^2 versus reciprocal

temperature. Arrhenius data are calculated assuming plane slab diffusion geometry from measured ^{39}Ar release during incremental heating experiment. C) Plot of log (r/r_o) versus ^{39}Ar released (dashed line) and theoretical fit (solid line) from model. D) Model thermal history for sample 97-4 obtained from inverse modeling of the kinetic parameters and domain structure. The range of 100 best-fit results is represented by the gray region, while the mean of these is shown in black. Light gray regions represent portions of the model thermal history outside the range of ages recorded in the feldspar. Also shown are the ages of coexisting apatite ((U-Th)/He) and biotite ($^{40}Ar/^{39}Ar$).

Figure 7: A) $^{40}Ar/^{39}Ar$ release spectrum (open boxes) and mean of 100 modeled age spectra (solid line) for alkali feldspar collected from a granitoid pluton at ~4000m, in the headwaters of the Hei Shui He. B) Arrhenius plot of log D/r^2 versus reciprocal temperature. Arrhenius data are calculated assuming plane slab diffusion geometry from measured ^{39}Ar release during incremental heating experiment. C) Plot of log (r/r_o) versus ^{39}Ar released (dashed line) and theoretical fit (solid line) from model. Note that the data for the last ~50% of the gas were released above the incongruent melting temperature for alkali feldspar and thus contain no volume diffusion information. D) Model thermal history for sample 97-6 obtained from inverse modeling of the kinetic parameters and domain structure. The range of 100 best-fit results is represented by the gray region, while the mean of these is shown in black. Light gray regions represent portions of the model thermal history outside the range of ages recorded in the feldspar. Also shown are the ages of coexisting apatite ((U-Th)/He) and biotite ($^{40}Ar/^{39}Ar$).

Figure 8: A) $^{40}Ar/^{39}Ar$ release spectrum (open boxes) and mean of 100 modeled age spectra (solid line) for alkali feldspar collected from the Baoxing massif, southern Longmen shan. B) Arrhenius plot of log D/r^2 versus reciprocal temperature. Arrhenius data are calculated assuming plane slab diffusion geometry from measured ^{39}Ar release during incremental heating experiment. C) Plot of log (r/r_o) versus ^{39}Ar released (dashed line) and theoretical fit (solid line) from model. D) Model thermal history for sample 93-1 obtained from inverse modeling of the kinetic parameters and domain structure. The range of 100 best-fit results is represented by the gray region, while the mean of these is

shown in black. Light gray regions represent portions of the model thermal history outside the range of ages recorded in the feldspar.

Figure 9: Composite thermal histories for samples from the Longmen Shan region. Biotite ages are represented by rectangles, apatite ages by diamonds, and k-feldspar model thermal histories are shown as solid lines. Dashed lines show the inferred cooling paths between data points. Samples from the present-day topographic margin are shown in black and samples from the interior of the plateau in gray. Regional slow cooling during the Mesozoic and early Cenozoic implies long-term thermal stability. Rapid cooling of samples at the margin of the plateau initiates in the Late Miocene – Early Pliocene and is inferred to record the onset of rapid denudation during Cenozoic development of the plateau.

References Cited

Armijo, R., Tapponnier, P., Mercier, J.L., and Han, T., 1986, Quaternary extension in southern Tibet: Field observations and tectonic implications: Journal of Geophysical Research, v. 91, p. 13803-13872.

Arnaud, N.O., Brunet, M., Cantagrel, J.M., and Tapponnier, P., 1993, High cooling and denudation rates at Kongur Shan, Eastern Pamir (Xinjiang, China) revealed by 40Ar/39Ar alkali feldspar thermochronology: Tectonics, v. 12, p. 1335-1346.

Arne, D., Worley, B., Wilson, C., Chen, S., Foster, D., Luo, Z., Liu, S., and Dirks, P., 1997, Differential exhumation in response to episodic thrusting along the eastern margin of the Tibetan Plateau: Tectonophysics, v. 280, p. 239-256.

Beaumont, C., Fullsack, P., and Hamilton, J., 1992, Erosional control of active compressional orogens, *in* McClay, K.R., ed., Thrust Tectonics: London, Chapman and Hall, p. 1-18.

Brook, E.J., Brown, E.T., Kurz, M.D., Ackert, R.P., Raisbeck, G.M., and Yiou, F., 1995, Constraints on age, erosion, and uplift of Neogene glacial deposits in the Transantarctic Mountains determined from in situ cosmogenic 10Be and 26Al: Geology, v. 23, p. 1063-1066.

Burchfiel, B.C., Chen, Z., Liu, Y., and Royden, L.H., 1995, Tectonics of the Longmen Shan and adjacent regions: International Geology Review, v. 37, p. 661-735.

Cebula, G.T., Kunk, M.J., Mehnert, H.H., Naeser, C.W., Obradovitch, J.D., and Sutter, J.F., 1986, The Fish Canyon Tuff, a potential standard for the 40Ar-39Ar and fission-track methods: Terra Cognita, v. 6, p. 139-140.

Chen, S., Wilson, C.J.L., Luo, Z., and Deng, Q., 1994a, The evolution of the western Sichuan foreland basin, southwestern China: Journal of SE Asian Earth Science, v. 10, p. 159-168.

Chen, S.F., and Wilson, C.J.L., 1996, Emplacement of the Longmen Shan Thrust-Nappe Belt along the eastern margin of the Tibetan Plateau: Journal of Structural Geology, v. 18, p. 413-430.

Chen, S.F., Wilson, C.J.L., Deng, Q.D., Zhao, X.L., and Luo, Z.L., 1994b, Active faulting and block movement associated with large earthquakes in the Min Shan and Longmen mountains, northeastern Tibetan Plateau: Journal of Geophysical Research, v. 99, p. 24,025-24,038.

Chen, Z., Burchfiel, B.C., Liu, Y., King, R.W., Royden, L.H., Tang, W., Wang, E., Zhao, J., and Zhang, X., 2000, GPS measurements from eastern Tibet and their implications for India/Eurasia intracontinental deformation: Journal of Geophysical Research, v. 105, p. 16215-16227.

Chen, Z., and Chen, X., 1987, On the tectonic evolution of the western margin of the Yangzi block: Chengdu, Chengdu Inst. Geol. and Min. Res., 172 p.

Clark, M.K., and Royden, L.H., 2000, Topographic ooze: Building the eastern margin of Tibet by lower crustal flow: Geology, v. 28, p. 703-706.

Coleman, M., and Hodges, K., 1995, Evidence for Tibetan plateau uplift before 14 Myr ago from a new minimum age for east-west extension: Nature, v. 374, p. 49-52.

Dirks, P., Wilson, C.J.L., Chen, S., Lou, Z., and Liu, S., 1994, Tectonic evolution of the NE margin of the Tibetan Plateau: evidence from the central Longmen Mountains, Sichuan Province, China: Journal of SE Asian Earth Science, v. 9, p. 181-192.

England, P., and Houseman, G., 1986, Finite strain calculations of continental deformation 2. Comparison with the India-Asia collision zone: Journal of Geophysical Research, v. 91, p. 3664-3676.
England, P., and Molnar, P., 1990, Surface uplift, uplift of rocks, and exhumation of rocks: Geology, v. 18, p. 1173-1177.
England, P.C., and Houseman, G.A., 1988, The mechanics of the Tibetan Plateau, *in* Chang, C., Shackleton, R.M., Dewey, J.F., and Yin, J., eds., The Geological Evolution of Tibet, Volume 326 A, Philosophical Transactions of the Royal Society of London, p. 301-320.
Farley, K.A., 2000, Helium diffusion from apatite: General behavior as illustrated by Durango fluorapatite: Journal of Geophysical Research, v. 105, p. 2903-2914.
Farley, K.A., Wolf, R.A., and Silver, L.T., 1996, The effects of long alpha-stopping distances on (U-Th)/He ages: Geochimica et Cosmochimica Acta, v. 60, p. 4223-4229.
Grove, M., and Harrison, T.M., 1996, 40Ar* diffusion in Fe-rich biotite: American Mineralogist, v. 81, p. 940-951.
Hames, W.E., and Burchfiel, B.C., 1993, Laser 40Ar/39Ar dating of Cenozoic, greenschist-facies shear zones, Longmenshan, China: Geological Society of America Abstracts with Programs, v. 25, p. A118.
Harrison, T.M., Copeland, P., Kidd, W.S.F., and Yin, A., 1992, Raising Tibet: Science, v. 255, p. 1663-1670.
Harrison, T.M., Heizler, M.T., and Lovera, O.M., 1993, In vacuo crushing experiments and K-feldspar thermochronometry: Earth and Planetary Science Letters, v. 117, p. 169-180.
Harrison, T.M., Heizler, M.T., Lovera, O.M., Chen, W., and Grove, M., 1994, A chlorine disinfectant for excess argon released from K-feldspar during step heating: Earth and Planetary Science Letters, v. 123, p. 95-104.
Hodges, K.V., Hames, W.E., Olszewski, W., Burchfiel, B.C., Royden, L.H., and Chen, Z., 1994, Thermobarometric and 40Ar/39Ar geochronologic constraints on Eohimalayan metamorphism in the Dinggye area, southern Tibet: Contributions to Mineralogy and Petrology, v. 117, p. 151-163.
House, M.A., and Hodges, K.V., 1994, Limits on the tectonic significance of rapid cooling events in extensional settings: Insights from the Bitterroot metamorphic core complex, Idaho-Montana: Geology, v. 22, p. 1007-1010.
House, M.A., Wernicke, B.P., and Farley, K.A., 1998, Dating topography of the Sierra Nevada, California, using apatite (U-Th)/He ages: Nature, v. 396, p. 66-69.
House, M.A., Wernicke, B.P., Farley, K.A., and Dumitru, T.A., 1997, Cenozoic thermal evolution of the central Sierra Nevada, California, from (U-Th)/He thermochronometry: Earth and Planetary Science Letters, v. 151, p. 167-179.
Houseman, G.A., McKenzie, D.P., and Molnar, P., 1981, Convective instability of a thickened boundary layer and its relevance for the thermal evolution of continental convergent belts: Journal of Geophysical Research, v. 86, p. 6115-6132.
Jones, L.M., Han, W., Hauksson, E., Jin, A., Zhang, Y., and Luo, Z., 1984, Focal mechanisms of the Songpan earthquakes of August 1976 in Sichuan, China: Journal of Geophysical Research, v. 89, p. 7697-7707.

King, R.W., Shen, F., Burchfiel, B.C., Royden, L.H., Wang, E., Chen, Z., Liu, Y., Zhang, X., Zhao, J., and Li, Y., 1997, Geodetic measurement of crustal motion in southwest China: Geology, v. 25, p. 179-182.

Kirby, E., Whipple, K., Tang, W., Burchfiel, B.C., and Chen, Z., 2000a, Neotectonics along the eastern margin of the Tibetan Plateau: Inferences from bedrock river incision patterns, 15th Himalaya-Karakorum-Tibet Workshop: Chengdu, China.

Kirby, E., Whipple, K.X., Burchfiel, B.C., Tang, W., Berger, G., Sun, Z., and Chen, Z., 2000b, Neotectonics of the Min Shan, China: Implications for mechanisms driving Quaternary deformation along the eastern margin of the Tibetan Plateau: Geological Society of America Bulletin, v. 112, p. 375-393.

Krol, M.A., Zeitler, P.K., Poupeau, G., and Pecher, A., 1996, Temporal variations in the cooling and denudation history of the Hunza plutonic complex, Karakoram Batholith, revealed by 40Ar/39Ar thermochronology: Tectonics, v. 15, p. 403-415.

Leloup, P.H., Harrison, T.M., Ryerson, F.J., Chen, W., Li, O., Tapponnier, P., and Lacassin, R., 1993, Structural, petrological and thermal evolution of a Tertiary ductile strike-slip shear zone, Diancang Shan, Yunnan: Journal of Geophysical Research, v. 98, p. 6715-6743.

Lippolt, H.J., Leitz, M., Wernicke, R.S., and Hagedorn, B., 1994, (Uranium+thorium)/helium dating of apatite: experience with samples from different geochemical environments: Chemical Geology, v. 112, p. 179-191.

Lovera, O.M., 1992, Computer programs to model 40Ar/39Ar diffusion data from multidomain samples: Computers and Geosciences, v. 7, p. 789-813.

Lovera, O.M., Grove, M., Harrison, T.M., and Mahon, K.I., 1997, Systematic analysis of K-feldspar 40Ar/39Ar step-heating experiments, I: Significance of activation energy determinations: Geochimica et Cosmochimica Acta, v. 61, p. 3171-3192.

Lovera, O.M., Richter, F.M., and Harrison, T.M., 1989, The 40Ar/39Ar geothermometry for slowly cooled samples having a distribution of diffusion domain sizes: Journal of Geophysical Research, v. 94, p. 17917-17935.

Lovera, O.M., Richter, F.M., and Harrison, T.M., 1991, Diffusion domains determined by 39Ar released during step heating: Journal of Geophysical Research, v. 96, p. 2057-2069.

Mancktelow, N.S., and Grasemann, B., 1997, Time-dependent effects of heat advection and topography on cooling histories during erosion: Tectonophysics, v. 270, p. 167-195.

Mattauer, M., Matte, M., Malavieille, J., Tapponnier, P., Maluski, H., Xu, Z.Q., Lu, Y.L., and Tang, Y.Q., 1985, Tectonics of the Qinling Belt: Build-up and evolution of eastern Asia: Nature, v. 317, p. 496-500.

McCaffrey, R., and Nabelek, J., 1998, Role of oblique convergence in the active deformation of the Himalayas and southern Tibet plateau: Geology, v. 26, p. 691-694.

Meyer, B., Tapponnier, P., Bourjot, L., Metivier, F., Gaudemer, Y., Peltzer, G., Guo, S., and Chen, Z., 1998, Crustal thickening in Gansu-Qinghai, lithospheric mantle subduction, and oblique, strike-slip controlled growth of the Tibet plateau: Geophysical Journal International, v. 135, p. 1-47.

Molnar, P., England, P., and Martinod, J., 1993, Mantle dynamics, uplift of the Tibetan Plateau, and the Indian monsoon: Reviews of Geophysics, v. 31, p. 357-396.

Murphy, M.A., Yin, A., Harrison, T.M., Durr, S.B., Chen, Z., Ryerson, F.J., Kidd, W.S.F., Wang, X., and Zhou, X., 1997, Did the Indo-Asian collision alone create the Tibetan Plateau?: Geology, v. 25, p. 719-722.

Parsons, I., Brown, W.L., and Smith, J.V., 1999, 40Ar/39Ar thermochronology using alkali feldspars: real thermal history or mathematical mirage of microtexture?: Contributions to Mineralogy and Petrology, v. 136, p. 92-110.

Parsons, I., Rex, D.C., Guise, P., and Halliday, A.N., 1988, Argon-loss by alkali feldspars: Geochimica et Cosmochimica Acta, v. 52, p. 1097-1112.

People's Republic of China, M.o.G.a.M.R., Geological Memoirs, 1991, Regional Geology of Sichuan Province: Beijing, Geol. Publishing House, 728 p.

Raymo, M.E., Ruddiman, W.F., and Froelich, P.N., 1988, Influence of late Cenozoic mountain building on ocean geochemical cycles: Geology, v. 16, p. 649-653.

Roddick, J.C., Cliff, R.A., and Rex, D.C., 1980, The evolution of excess argon in Alpine biotites - a 40Ar/39Ar analysis: Earth and Planetary Science Letters, v. 48, p. 185-208.

Roger, F., Calassou, S., Lancelot, J., Malavieille, J., Mattauer, M., Xu, Z., Hao, Z., and Hou, L., 1995a, Miocene emplacement and deformation of the Konga Shan granite (Xianshui He fault zone, west Sichuan, China): Geodynamic implications: Earth and Planetary Science Letters, v. 130, p. 201-216.

Roger, F., Calassou, S., Lancelot, J.R., Malavieille, J., and Mattauer, M., 1995b, Geochronology and isotope geochemistry of granitoids associated with the Songpan-Garze decollement (eastern Tibet): Terra Abstracts, v. 7, p. 351-352.

Royden, L., 1996, Coupling and decoupling of crust and mantle in convergent orogens: Implications for strain partitioning in the crust: Journal of Geophysical Research, v. 101, p. 17,679-17,705.

Royden, L.H., Burchfiel, B.C., King, R.W., Chen, Z., Shen, F., and Liu, Y., 1997, Surface deformation and lower crustal flow in Eastern Tibet: Science, v. 276, p. 788-790.

Ruppel, C., Royden, L., and Hodges, K., 1988, Thermal modeling of extensional tectonics: Application to pressure-temperature-time histories of metamorphic rocks: Tectonics, v. 7, p. 947-957.

Samson, S.D., and Alexander, E.C., 1987, Calibration of the interlaboratory 40Ar/39Ar dating standard, MMhb-1: Chemical Geology, v. 66, p. 27-34.

Seeber, L., and Pecher, A., 1998, Strain partitioning along the Himalayan arc and the Nanga Parbat antiform: Geology, v. 26, p. 791-794.

Sengor, A.M.C., Cin, A., Rowley, D.B., and Nie, S.Y., 1993, Space-time patterns of magmatism along the Tethysides: Journal of Geology, v. 101, p. 51-84.

Spear, F.S., 1993, Metamorphic phase equilibria and pressure-temperature-time paths: Washington, D.C., Mineralogical Society of America, 799 p.

Spotila, J.A., Farley, K.A., and Sieh, K., 1998, Uplift and erosion of the San Bernardino Mountains associated with transpression along the San Andreas fault, California, as constrained by radiogenic helium thermochronometry: Tectonics, v. 17, p. 360-378.

Stuwe, K., White, L., and Brown, R., 1994, The influence of eroding topography on steady-state isotherms. Application to fission track analysis: Earth and Planetary Science Letters, v. 124, p. 63-74.

Tang, R., Wen, D., Huang, Z., Wu, X., Lin, W., Chen, G., and Wu, G., 1993, The Quaternary activity characteristics of several major active fault zones in the Songpan-Longmenshan region: Earthquake Research in China, v. 7, p. 341-350.

Tapponnier, P., Peltzer, G., Le Dain, A.Y., Armijo, R., and Cobbold, P., 1982, Propagating extrusion tectonics in Asia: New insight from simple experiments with plasticine: Geology, v. 10, p. 611-616.

Turner, S., Arnaud, N., Liu, J., Rogers, N., Hawkesworth, C., Harris, N., Kelley, S., van Calsteren, P., and Deng, W., 1996, Post-collisional, shoshonitic volcanism on the Tibetan Plateau: Implications for convective thinning of the lithosphere and the source of ocean island basalts: Journal of Petrology, v. 37, p. 45-71.

Turner, S., Hawkesworth, C., Liu, J., Rogers, N., Kelley, S., and van Calsteren, P., 1993, Timing of Tibetan uplift constrained by analysis of volcanic rocks: Nature, v. 364, p. 50-54.

Villa, I.M., 1994, Multipath Ar transport in K-feldspar deduced from isothermal heating experiments: Earth and Planetary Science Letters, v. 122, p. 393-401.

Wang, E., Burchfiel, B.C., Royden, L.H., Chen, L., Chen, J., Li, W., and Chen, Z., 1998, Late Cenozoic Xianshuihe-Xiaojiang, Red River, and Dali Fault Systems of Southwestern Sichuan and Central Yunnan, China: Boulder, Geologic Society of America, 108 p.

Warnock, A.C., and Zeitler, P.K., 1998, 40Ar/39Ar thermochronometry of K-feldspar from the KTB borehole, Germany: Earth and Planetary Science Letters, v. 158, p. 67-79.

Warnock, A.C., Zeitler, P.K., Wolf, R.A., and Bergman, S.C., 1997, An evaluation of low-temperature apatite U-Th/He thermochronometry: Geochimica et Cosmochimica Acta, v. 61, p. 5371-5377.

Willett, S.D., 1997, Inverse modeling of annealing of fission tracks in apatite; 1, A controlled random search method: American Journal of Science, v. 297, p. 939-969.

Willett, S.D., 1999, Orogeny and orography: the effects of erosion on the structure of mountain belts: Journal of Geophysical Research, v. 104, p. 28,957-28,981.

Wolf, R.A., 1997, The development of the (U-Th)/He thermochronometer: Pasadena, California Institute of Technology.

Wolf, R.A., Farley, K.A., and Kass, D.M., 1998, Modeling of the temperature sensitivity of the apatite (U-Th)/He thermochronometer: Chemical Geology, v. 148, p. 105-114.

Wolf, R.A., Farley, K.A., and Silver, L.T., 1996, Helium diffusion and low-temperature thermochronometry of apatite: Geochimica et Cosmochimica Acta, v. 60, p. 4231-4240.

Wolf, R.A., Farley, K.A., and Silver, L.T., 1997, Assessment of (U-Th)/He thermochronometry: The low-temperature history of the San Jancinto mountains, California: Geology, v. 25, p. 65-68.

Xu, G., and Kamp, P., 2000, Tectonics and denudation adjacent to the Xianshuihe Fault, eastern Tibetan Plateau: Constraints from fission track thermochronology: Journal of Geophysical Research, v. 105, p. 19231-19251.

Zeitler, P.K., 1993, Inversion of 40Ar/39Ar age spectra using the controlled-random-search method: EOS Trans. AGU (Supplement), v. 74, p. 650.

Zeitler, P.K., Herczeg, A.L., McDougall, I., and Honda, M., 1987, U-Th-He dating of apatite: A potential thermochronometer: Geochimica et Cosmochimica Acta, v. 51, p. 2865-2868.

Zhang, E., 1992, Geologic map of the Qinling-Dabie Mountains and adjacent regions (1:1,000,000): Beijing, Geological Publishing House.

Table 1: U-Th-He data

Sample	Location	Elevation (m)	He (ncc)/mg	U (ppm)	Th (ppm)	Raw age (Ma)	Ft*	Corrected age (Ma)	Average age (Ma)†
93-3	31.14°N, 103.49°E	1200	2.113	3.7	10.7	2.79	0.61	4.57	4.6 ± 0.7§
97-2(a)	32.31°N, 103.13°E	2400	44.877	30.3	9.5	11.33	0.793	14.29	13.4 ± 0.8
97-2(b)			21.427	18.9	5.7	8.69	0.694	12.53	
97-4	32.16°N, 102.93°E	2500	19.937	10.7	12.0	12.13	0.609	19.92	19.9 ± 1.2
97-5	32.20°N, 102.64°E	4400	15.302	6.8	12.7	12.82	0.623	20.57	20.6 ± 1.2
97-6(a)	32.16°N, 102.62° E	4300	9.149	11.3	19.2	4.75	0.643	7.39	8.2 ± 0.5
97-6(b)			11.016	11.1	16.4	6.06	0.676	8.97	
97-14	32.52°N, 104.13°E	1500	4.331	14.6	20.1	1.84	0.578	3.19	3.2 ± 0.5§

* Ft is a geometrical correction for alpha ejection (Farley et al., 1996).

† Average ages are mean ages of duplicate analyses (where appropriate). Uncertainties are based on reproducibility of laboratory standards and are taken as 6% (2σ).

§ For samples with low helium yields, we adopt a conservative 2σ uncertainty of 15%.

Table 2: Cooling rates in eastern Tibet

Location	Age range	Temperature	Cooling rate	Mineral system
Min Shan	170 – 6 Ma	350 – 200° C	~1 °/my	Biotite/feldspar
(97-14)	6 - 3 Ma	200 – 75° C	50 - 60 °/my	Feldspar/apatite
	3 – 0 Ma	75 – 20° C	~20°/my	
Longman Shan	150 – 11 Ma	240 – 190° C	~0.5 °/my	Feldspar
(93-3, 93-4)	11 - 4 Ma	190 – 75° C	15 – 20 °/my	Feldspar/apatite
	4- 0 Ma	75 – 20° C	~15°/my	
Songpan-Garze	195 – 50 Ma	350 – 190° C	~1 °/my	Biotite/feldspar
(97-4)	50 – 20 Ma	190 – 75° C	3 – 4 °/my	Feldspar/apatite
	20 – 0 Ma	75 – 20° C	~3°/my	
Songpan-Garze	210 – 60 Ma	350 – 250° C	~ 0.6 °/my	Biotite/feldspar
(97-6)	60 – 8 Ma	250 – 75° C	3 – 4 °/my	Feldspar/apatite
	8 – 0 Ma	75 – 20° C	~7°/my	

Supplementary table - Kirby et al.: Longmen Shan, $^{40}Ar/^{39}Ar$ data

Temperature (°C)	Duration (min)	$^{40}Ar/^{39}Ar$	$^{38}Ar/^{39}Ar$	$^{37}Ar/^{39}Ar$	$^{36}Ar/^{39}Ar$	$^{39}Ar_K$ (moles)	^{39}Ar Released (%)	$^{40}Ar^*$ (%)	Age (Ma)	± 2σ (Ma)†	± 2σ (Ma)§
EK 97-4: Biotite (wt: 0.0591 g; J=0.0029617 ± 1.725E-5)											
600	10	40.986	0.01951	0.21426	0.03586	1.44E-13	2.45	74.02	155.2	1.4	1.1
650	10	41.322	0.01439	0.07648	0.01326	5.16E-14	3.33	90.37	189.2	2.0	1.7
700	10	44.852	0.01691	0.03691	0.02330	1.56E-13	5.97	84.51	192.0	1.9	1.5
750	10	40.364	0.01394	0.01408	0.00681	4.43E-13	13.51	94.85	193.8	1.2	0.5
775	10	38.779	0.01234	0.00616	0.00158	5.24E-13	22.41	98.62	193.5	1.2	0.5
800	10	38.797	0.01233	0.00411	0.00091	5.52E-13	31.80	99.14	194.6	1.3	0.7
825	10	38.934	0.01240	0.00480	0.00074	4.90E-13	40.14	99.27	195.4	1.3	0.8
850	10	38.952	0.01250	0.00540	0.00073	3.85E-13	46.68	99.27	195.6	1.3	0.8
875	10	38.935	0.01255	0.00860	0.00082	2.74E-13	51.33	99.21	195.4	1.3	0.6
900	10	38.854	0.01379	0.00714	0.00041	1.68E-13	54.19	99.52	195.7	1.4	0.8
925	10	38.786	0.01269	0.02126	0.00070	2.01E-13	57.61	99.30	194.9	1.4	0.9
950	10	38.512	0.01223	0.02042	0.00099	2.11E-13	61.19	99.07	193.2	1.2	0.6
1000	10	38.108	0.01204	0.01578	0.00101	4.70E-13	69.19	99.04	191.2	1.2	0.6
1050	10	38.308	0.01314	0.02184	0.00093	6.60E-13	80.42	99.11	192.2	1.2	0.5
1075	10	38.847	0.01273	0.03707	0.00132	4.73E-13	88.46	98.83	194.4	1.2	0.4
1100	10	39.180	0.01262	0.08618	0.00116	3.47E-13	94.36	98.97	196.1	1.4	0.8
1150	10	39.277	0.01314	0.58034	0.00116	2.34E-13	98.34	99.06	196.9	1.1	0.4
1300	10	39.056	0.01242	0.72351	0.00116	9.78E-14	100.00	99.09	195.8	1.6	1.2
EK 97-6: Biotite (wt: 0.0531 g; J=0.0029461 ± 1.51842E-5)											
600	10	82.883	0.05983	0.32060	0.23658	4.24E-14	0.99	15.61	67.5	8.0	8.0
650	10	41.722	0.02092	0.22168	0.06037	4.70E-14	2.08	57.11	122.4	2.7	2.6
700	10	51.674	0.02265	0.12818	0.05235	7.16E-14	3.76	69.95	182.6	2.9	2.8
750	10	46.537	0.01666	0.03598	0.02273	1.41E-13	7.04	85.43	199.8	1.9	1.7
800	10	42.775	0.01360	0.02055	0.00507	3.10E-13	14.26	96.35	206.7	1.1	0.4
825	10	41.938	0.01287	0.01491	0.00246	2.80E-13	20.80	98.11	206.4	1.1	0.5
850	10	42.361	0.01329	0.01403	0.00229	2.32E-13	26.22	98.25	208.7	1.8	1.5
875	10	42.167	0.01348	0.01525	0.00260	2.06E-13	31.02	98.02	207.3	1.2	0.6
900	10	41.978	0.01349	0.01982	0.00264	1.87E-13	35.39	97.99	206.3	1.3	0.8
925	10	42.205	0.01351	0.03211	0.00284	1.74E-13	39.45	97.86	207.2	1.2	0.7
950	10	43.248	0.01393	0.05355	0.00396	1.77E-13	43.58	97.14	210.5	1.2	0.6
1000	10	43.388	0.01325	0.04137	0.00279	3.81E-13	52.46	97.95	212.8	1.2	0.5
1050	10	42.309	0.01289	0.04570	0.00138	5.20E-13	64.58	98.88	209.7	1.1	0.4

Supplementary table - Kirby et al.: $^{40}Ar/^{39}Ar$ data (continued)

Temperature (°C)	Duration (min)	$^{40}Ar/^{39}Ar$	$^{38}Ar/^{39}Ar$	$^{37}Ar/^{39}Ar$	$^{36}Ar/^{39}Ar$	$^{39}Ar_K$ (moles)	^{39}Ar Released (%)	$^{40}Ar^*$ (%)	Age (Ma)	± 2 σ (Ma)†	± 2 σ (Ma)§
1075	10	42.120	0.01277	0.05183	0.00113	4.41E-13	74.86	99.06	209.1	1.2	0.7
1100	10	41.988	0.01235	0.06569	0.00090	4.60E-13	85.57	99.22	208.8	1.3	0.7
1150	10	41.707	0.01215	0.21346	0.00070	5.00E-13	97.24	99.38	207.9	1.2	0.6
1300	10	41.209	0.01372	0.47378	0.00072	1.18E-13	100.00	99.40	205.6	1.3	0.9
				EK 97-14: Biotite (wt: 0.0252 g; J=0.0026131 ± 7.556E-5)							
700	10	53.894	0.07739	0.07323	0.14086	7.07E-15	0.46	22.80	57	44	44
800	10	55.337	0.03218	0.09162	0.08142	4.23E-14	2.38	56.54	141.8	6.0	4.6
825	10	45.525	0.03231	0.02828	0.05201	1.43E-14	3.03	66.22	137	11	10
850	10	51.005	0.02007	0.01583	0.03976	1.07E-13	7.89	76.96	176.2	5.4	2.4
875	10	40.915	0.01440	0.01015	0.00914	1.44E-13	14.42	93.39	171.7	5.0	1.4
900	10	39.244	0.01276	0.00802	0.00521	1.77E-13	22.45	96.07	169.5	4.9	1.4
925	10	39.027	0.01196	0.00631	0.00146	1.79E-13	30.56	98.88	173.3	4.9	1.2
950	10	39.261	0.01230	0.00672	0.00354	1.58E-13	37.71	97.32	171.6	5.0	1.6
975	10	39.471	0.01292	0.00197	0.00123	1.41E-13	44.12	99.06	175.5	5.0	1.2
1000	10	39.137	0.01186	0.00862	0.00116	1.31E-13	50.07	99.11	174.2	5.0	1.3
1050	10	39.012	0.01251	0.03380	0.00300	2.01E-13	59.18	97.72	171.3	4.8	1.0
1075	10	38.563	0.01379	0.01982	0.00415	6.69E-14	62.21	96.81	168.0	4.8	1.2
1100	10	37.251	0.01236	0.02296	0.00376	1.87E-13	70.71	97.01	162.8	4.6	1.1
1150	10	37.523	0.01230	0.06429	0.00146	1.81E-13	78.95	98.86	166.9	4.7	1.1
1200	10	39.810	0.01285	0.17648	0.00205	1.82E-13	87.21	98.51	176.0	4.9	0.9
1250	10	37.541	0.01241	0.26863	0.00401	1.38E-13	93.45	96.90	163.8	4.7	1.4
1300	10	31.445	0.01269	0.17321	0.00299	7.64E-14	96.92	97.23	138.7	4.1	1.3
1350	10	25.650	0.00991	0.03850	0.00254	6.79E-14	100.00	97.07	113.7	3.7	2.0
				93-1: K-feldspar (wt: 0.1238 g; J=0.017425 ± 2.04E-4)							
400	28	325.891	0.03075	0.06801	0.08362	4.34E-14	0.06	93.07	3507	67	64
400.1	34	28.075	0.01885	0.03384	0.03304	4.26E-14	0.12	62.29	534	63	62
450	28	39.471	0.01499	0.01823	0.01162	7.24E-14	0.22	93.60	977	28	27
450.1	34	8.768	0.01334	0.01300	0.00739	1.02E-13	0.36	76.92	224	14	14
500	28	61.133	0.01381	0.00573	0.00663	2.07E-13	0.64	99.88	1395	31	29
500.1	32	5.338	0.01329	0.01067	0.00279	2.14E-13	0.94	92.99	153	13	13
550	26	30.163	0.01378	0.01049	0.00316	4.08E-13	1.50	99.86	793	21	19
550.1	32	3.646	0.01164	0.01046	0.00147	4.49E-13	2.11	94.03	112.8	7.1	7.0
590	26	11.733	0.01277	0.01666	0.00138	6.18E-13	2.96	98.50	342.5	7.6	6.7
590.1	30	3.846	0.01225	0.02042	0.00076	6.25E-13	3.82	95.68	117.8	4.5	4.3

Supplementary table - Kirby et al.: $^{40}Ar/^{39}Ar$ data (continued)

Temperature (°C)	Duration (min)	$^{40}Ar/^{39}Ar$	$^{38}Ar/^{39}Ar$	$^{37}Ar/^{39}Ar$	$^{36}Ar/^{39}Ar$	$^{39}Ar_K$ (moles)	^{39}Ar Released (%)	$^{40}Ar^*$ (%)	Age (Ma)	± 2 σ (Ma)†	± 2 σ (Ma)§
620	26	6.851	0.01163	0.02290	0.00089	9.10E-13	5.07	98.57	212.2	3.5	2.5
620.1	30	3.015	0.01242	0.01519	0.00046	8.79E-13	6.28	97.02	91.4	2.2	1.9
650	26	4.499	0.01242	0.01266	0.00061	1.10E-12	7.79	97.19	134.9	3.7	3.3
650.1	30	2.511	0.01262	0.00995	0.00065	9.38E-13	9.08	94.07	74.3	2.3	2.2
670	24	3.330	0.01305	0.00931	0.00228	7.89E-13	10.16	81.57	84.7	3.0	2.9
670.1	28	2.235	0.01256	0.00761	0.00081	7.86E-13	11.24	92.48	64.7	2.1	2.0
690	24	4.005	0.01266	0.00738	0.00057	1.16E-12	12.83	95.95	119.2	3.4	3.1
690.1	28	2.701	0.01242	0.00695	0.00040	1.11E-12	14.35	97.26	83.0	1.6	1.3
710	24	3.714	0.01222	0.00460	0.00047	8.32E-13	15.49	97.52	111.0	2.5	2.2
710.1	28	4.696	0.01217	0.00530	0.00042	1.40E-12	17.42	97.95	142.4	3.0	2.5
730	24	5.521	0.01241	0.00532	0.00029	1.67E-12	19.71	99.18	165.2	4.3	3.9
730.1	28	5.747	0.01235	0.00487	0.00036	1.54E-12	21.82	99.85	173.8	2.5	1.6
750	24	5.459	0.01261	0.00607	0.00035	1.31E-12	23.62	98.60	162.5	3.4	2.8
750.1	28	5.786	0.01229	0.00485	0.00033	1.16E-12	25.21	99.84	173.1	4.0	3.5
770	24	6.489	0.01248	0.00533	0.00039	1.14E-12	26.78	99.90	192.8	3.5	2.7
770.1	28	7.442	0.01236	0.00529	0.00048	7.62E-13	27.83	99.22	217.8	3.3	2.3
790	20	7.433	0.01249	0.00651	0.00046	8.57E-13	29.00	99.36	217.8	3.1	2.0
810	20	7.661	0.01333	0.00687	0.00050	6.67E-13	29.92	98.03	221.8	3.3	2.2
830	20	7.902	0.01240	0.00724	0.00064	8.55E-13	31.09	99.62	231.9	3.5	2.5
850	20	8.207	0.01259	0.00836	0.00080	1.32E-12	32.90	98.11	237.1	3.2	1.9
870	20	8.738	0.01258	0.00871	0.00094	1.38E-12	34.79	97.67	249.8	2.9	0.8
890	20	9.239	0.01264	0.00957	0.00122	1.43E-12	36.75	96.92	261.7	3.3	1.7
910	20	9.480	0.01263	0.00946	0.00123	1.63E-12	39.00	96.84	268.0	3.0	0.9
930	20	9.726	0.01264	0.01002	0.00140	1.87E-12	41.57	96.84	274.4	3.2	1.1
950	20	9.810	0.01265	0.00965	0.00142	1.90E-12	44.18	96.38	275.2	3.0	0.5
970	20	10.235	0.01262	0.00975	0.00126	1.84E-12	46.71	97.46	288.8	3.5	1.6
990	20	10.750	0.01274	0.00971	0.00112	2.01E-12	49.47	97.47	303.3	3.4	1.0
1010	20	11.064	0.01263	0.00979	0.00093	1.97E-12	52.18	98.40	314.0	3.6	1.1
1020	20	11.090	0.01254	0.00914	0.00076	1.67E-12	54.47	98.91	315.7	3.6	1.3
1030	20	11.431	0.01241	0.00885	0.00073	1.58E-12	56.64	99.95	327.6	4.5	2.7
1040	20	11.946	0.01247	0.00867	0.00053	1.70E-12	58.97	99.88	340.9	4.6	2.9
1050	20	12.000	0.01245	0.00844	0.00060	1.55E-12	61.11	99.87	342.7	4.8	3.1
1060	20	12.224	0.01230	0.00776	0.00054	1.36E-12	62.98	99.86	348.2	4.4	2.4
1070	20	12.725	0.01252	0.00660	0.00054	1.36E-12	64.84	99.69	360.4	4.5	2.3
1070.1	40	13.156	0.01258	0.00572	0.00053	2.23E-12	67.91	99.91	372.1	5.0	3.1
1070.2	80	14.028	0.01252	0.00463	0.00052	3.44E-12	72.63	99.93	394.6	4.8	2.3
1070.3	160	15.367	0.01253	0.00327	0.00050	1.78E-12	75.07	99.60	426.7	5.8	3.8
1070.4	300	16.759	0.01235	0.00194	0.00052	2.02E-12	77.83	99.92	462.1	4.8	0.8

Supplementary table - Kirby et al.: $^{40}Ar/^{39}Ar$ data (continued)

Temperature (°C)	Duration (min)	$^{40}Ar/^{39}Ar$	$^{38}Ar/^{39}Ar$	$^{37}Ar/^{39}Ar$	$^{36}Ar/^{39}Ar$	$^{39}Ar_K$ (moles)	^{39}Ar Released (%)	$^{40}Ar^*$ (%)	Age (Ma)	± 2 σ (Ma)†	± 2 σ (Ma)§
1070.5	450	17.941	0.01221	0.00145	0.00055	1.95E-12	80.51	99.93	490.7	5.5	2.3
1100	20	18.312	0.01259	0.00024	0.00000	3.26E-13	80.95	99.44	498	11	10
1100.1	40	18.352	0.01259	0.00089	0.00054	6.36E-13	81.83	99.73	499.5	6.3	3.8
1125	20	18.337	0.01254	0.00215	0.00056	5.20E-13	82.54	99.75	500.3	5.8	2.8
1125.1	40	18.480	0.01241	0.00146	0.00059	8.17E-13	83.66	99.86	501.8	5.9	3.0
1150	20	18.312	0.01249	0.00180	0.00053	7.40E-13	84.68	99.68	498.5	6.8	4.5
1175	20	17.904	0.01255	0.00222	0.00078	1.36E-12	86.54	99.57	488.1	5.2	1.4
1200	15	18.136	0.01256	0.00236	0.00078	2.29E-12	89.69	99.93	495.1	6.0	3.2
1225	15	18.272	0.01255	0.00120	0.00074	1.86E-12	92.23	99.59	496.9	6.2	3.5
1250	15	18.481	0.01245	0.00001	0.00059	1.62E-12	94.46	99.92	503.6	6.0	3.1
1275	15	19.374	0.01249	0.00001	0.00052	1.72E-12	96.83	99.93	524.8	6.6	3.9
1300	15	20.587	0.01223	0.00033	0.00044	1.28E-12	98.58	99.91	552.9	6.4	3.1
1350	15	20.253	0.01236	0.00042	0.00051	6.95E-13	99.54	99.96	546.0	6.7	3.9
1400	15	18.450	0.01276	0.00149	0.00080	3.38E-13	100.00	99.21	500.2	6.0	3.1
				93-4: K-feldspar (wt: 0.0871 g; J=0.0174248 ± 2.038626E-4)							
400	26	20.712	0.01777	0.00904	0.02464	8.75E-14	0.16	64.53	377.7	9.2	8.3
400.1	30	3.889	0.01649	0.01882	0.00816	6.18E-14	0.27	36.36	44	11	11
450	26	2.468	0.01292	0.01123	0.00459	9.95E-14	0.44	42.36	32.6	8.5	8.5
450.1	32	1.454	0.01415	0.01045	0.00305	1.08E-13	0.63	33.47	15.2	4.3	4.3
500	26	4.895	0.01338	0.00596	0.00186	3.12E-13	1.19	87.39	129.7	2.0	1.4
500.1	32	0.877	0.01369	0.01079	0.00099	2.45E-13	1.62	59.21	16.3	2.6	2.6
550	26	3.465	0.01264	0.00806	0.00120	6.20E-13	2.73	87.82	93.2	1.6	1.2
550.1	32	0.722	0.01309	0.00910	0.00082	4.17E-13	3.47	57.27	13.0	1.8	1.8
600	26	1.913	0.01255	0.00708	0.00079	7.81E-13	4.86	84.25	50.0	1.0	0.8
600.1	32	0.639	0.01294	0.00644	0.00055	5.38E-13	5.82	64.33	12.9	3.5	3.5
640	26	0.912	0.01247	0.00611	0.00067	8.45E-13	7.32	70.92	20.2	1.0	1.0
640.1	32	0.544	0.01282	0.00705	0.00038	6.69E-13	8.51	67.09	11.4	0.8	0.8
680	26	1.152	0.01286	0.00578	0.00179	1.05E-12	10.38	48.35	17.4	0.8	0.8
680.1	32	0.564	0.01255	0.00500	0.00048	9.27E-13	12.03	63.24	11.2	1.1	1.1
720	26	0.981	0.01247	0.00639	0.00030	2.10E-12	15.76	84.26	25.8	0.6	0.5
720.1	32	1.905	0.01249	0.00877	0.00034	2.11E-12	19.51	91.29	53.9	0.8	0.5
750	24	1.600	0.01268	0.01094	0.00024	1.53E-12	22.24	91.51	45.5	0.7	0.5
750.1	30	1.217	0.01242	0.01029	0.00022	1.25E-12	24.46	89.30	33.8	0.6	0.5
780	24	1.146	0.01246	0.01123	0.00020	8.74E-13	26.01	89.04	31.8	0.9	0.8
780.1	30	1.233	0.01301	0.01418	0.00022	6.81E-13	27.23	89.39	34.3	1.3	1.3
810	22	1.232	0.01214	0.01761	0.00014	7.36E-13	28.53	91.20	35.0	1.2	1.1
840	20	1.255	0.01236	0.02665	0.00023	9.89E-13	30.29	89.33	34.9	0.7	0.6
860	20	1.289	0.01235	0.02445	0.00027	9.28E-13	31.95	88.67	35.6	0.9	0.8

Supplementary table - Kirby et al.: $^{40}Ar/^{39}Ar$ data (continued)

Temperature (°C)	Duration (min)	$^{40}Ar/^{39}Ar$	$^{38}Ar/^{39}Ar$	$^{37}Ar/^{39}Ar$	$^{36}Ar/^{39}Ar$	$^{39}Ar_K$ (moles)	^{39}Ar Released (%)	$^{40}Ar^*$ (%)	Age (Ma)	± 2 σ (Ma)†	± 2 σ (Ma)§
880	20	1.355	0.01252	0.02284	0.00024	1.03E-12	33.77	89.90	37.9	0.7	0.5
900	20	1.533	0.01239	0.02291	0.00026	1.46E-12	36.37	90.74	43.2	0.7	0.5
920	20	1.670	0.01242	0.01808	0.00030	1.31E-12	38.69	90.72	47.0	0.8	0.6
940	20	1.921	0.01249	0.01722	0.00034	1.49E-12	41.34	91.28	54.3	0.8	0.5
960	20	2.045	0.01248	0.01496	0.00031	1.36E-12	43.76	92.37	58.4	0.9	0.6
980	20	2.306	0.01234	0.01444	0.00037	1.51E-12	46.44	92.42	65.8	0.9	0.5
1000	20	2.481	0.01250	0.01309	0.00036	1.75E-12	49.56	93.06	71.2	0.9	0.5
1020	20	2.572	0.01246	0.01123	0.00031	1.63E-12	52.46	93.87	74.4	1.0	0.5
1030	20	2.585	0.01236	0.00817	0.00035	1.26E-12	54.70	93.43	74.4	1.1	0.7
1040	20	2.801	0.01256	0.00762	0.00031	1.23E-12	56.88	94.36	81.2	1.1	0.7
1050	20	2.875	0.01246	0.00677	0.00031	9.11E-13	58.50	94.53	83.5	1.3	0.9
1060	20	3.211	0.01239	0.00712	0.00025	1.03E-12	60.34	95.63	94.0	1.3	0.7
1075	20	3.383	0.01243	0.00633	0.00029	1.07E-12	62.25	95.47	98.8	1.3	0.6
1075.1	40	3.452	0.01255	0.00504	0.00033	1.63E-12	65.14	95.23	100.5	1.2	0.5
1075.2	80	3.623	0.01253	0.00362	0.00032	2.16E-12	68.99	95.59	105.8	1.4	0.7
1075.3	160	3.901	0.01246	0.00265	0.00040	2.63E-12	73.67	95.22	113.2	1.4	0.4
1075.4	240	4.210	0.01248	0.00209	0.00045	2.41E-12	77.96	95.27	121.9	1.5	0.5
1075.5	300	4.490	0.01251	0.00190	0.00052	2.25E-12	81.97	95.09	129.5	1.5	0.5
1075.6	300	4.684	0.01230	0.00109	0.00081	4.65E-13	82.80	93.47	132.7	2.6	2.2
1075.7	400	4.817	0.01223	0.00166	0.00068	1.43E-12	85.35	94.46	137.7	1.7	0.6
1100	20	4.915	0.01408	0.02368	0.00001	6.33E-14	85.46	98.59	146.2	7.1	6.9
1125	20	4.838	0.00766	0.00005	0.00001	1.15E-13	85.66	98.57	144	12	12
1150	20	5.148	0.01262	0.00472	0.00023	2.29E-13	86.07	97.36	151.1	2.8	2.2
1175	15	5.202	0.01173	0.00412	0.00036	3.18E-13	86.63	96.69	151.6	2.1	1.2
1200	15	5.047	0.01233	0.00346	0.00050	8.30E-13	88.11	95.74	145.8	1.8	0.7
1300	15	5.147	0.01241	0.00073	0.00067	6.65E-12	99.93	94.85	147.2	1.7	0.4
1400	15	20.839	0.01442	0.05764	0.00280	4.04E-14	100.00	95.73	538	26	26
				EK 97-4: K-feldspar (wt: 0.0482 g; J=0.002965 ± 7.20E-6)							
400	18	365.470	0.06393	0.34365	0.30444	5.60E-15	0.10	75.37	1077	38	38
400.1	36	130.050	0.09855	0.00202	0.11416	9.44E-16	0.12	74.02	453	236	236
450	18	78.988	0.00007	0.00295	0.11782	6.48E-16	0.13	55.85	222	178	178
450.1	36	48.301	0.01582	0.23736	0.05554	3.30E-15	0.19	65.92	163	31	31
500	17	53.403	0.06912	0.00085	0.05683	2.25E-15	0.23	68.43	186	46	46
500.1	34	59.642	0.04732	0.00024	0.02564	7.93E-15	0.38	87.18	258.7	7.5	7.5
550	17	28.880	0.00001	0.45589	0.01322	6.58E-15	0.50	86.36	129	10	10
550.1	34	29.908	0.01664	0.07304	0.00387	2.30E-14	0.93	95.97	147	14	14
600	16	13.366	0.01330	0.00015	0.00531	1.25E-14	1.16	87.76	61.7	3.7	3.7
600.1	32	15.517	0.00998	0.06196	0.00415	5.03E-14	2.08	91.69	74.6	1.2	1.2

Supplementary table - Kirby et al.: $^{40}Ar/^{39}Ar$ data (continued)

Temperature (°C)	Duration (min)	$^{40}Ar/^{39}Ar$	$^{38}Ar/^{39}Ar$	$^{37}Ar/^{39}Ar$	$^{36}Ar/^{39}Ar$	$^{39}Ar_K$ (moles)	^{39}Ar Released (%)	$^{40}Ar^*$ (%)	Age (Ma)	± 2 σ (Ma)†	± 2 σ (Ma)§
650	15	8.811	0.01647	0.00014	0.00006	1.40E-14	2.34	99.04	46.1	5.9	5.9
650.1	30	13.159	0.01301	0.06102	0.00176	1.20E-13	4.56	95.56	66.1	0.7	0.7
700	15	9.678	0.01122	0.08613	0.00218	4.55E-14	5.40	92.70	47.4	1.1	1.1
700.1	30	11.013	0.01216	0.08336	0.00123	2.25E-13	9.54	96.15	55.8	1.0	1.0
750	15	12.542	0.01407	0.04496	0.00296	6.33E-14	10.71	92.52	61.0	1.3	1.2
750.1	30	14.903	0.01319	0.08616	0.00291	2.24E-13	14.84	93.81	73.3	0.3	0.3
800	15	15.349	0.01246	0.07892	0.00081	5.90E-14	15.93	98.03	78.8	0.7	0.7
800.1	30	17.070	0.01280	0.04868	0.00089	2.14E-13	19.87	98.09	87.4	0.6	0.6
850	15	19.140	0.01569	0.25586	0.00171	2.89E-14	20.41	97.10	96.8	2.2	2.1
900	15	20.089	0.01225	0.06795	0.00128	1.40E-13	22.99	97.80	102.1	0.5	0.4
950	15	21.075	0.01257	0.09282	0.00118	2.72E-13	28.00	98.06	107.3	0.5	0.4
990	15	23.353	0.01249	0.06242	0.00060	2.23E-13	32.11	98.97	119.6	0.8	0.7
1030	15	25.245	0.01124	0.01719	0.00136	2.09E-13	35.96	98.14	127.9	0.7	0.6
1075	15	28.166	0.01266	0.00277	0.00167	2.28E-13	40.17	98.01	141.9	0.8	0.7
1075.1	30	30.702	0.01258	0.04035	0.00187	3.34E-13	46.32	97.99	154.2	0.7	0.6
1075.2	60	33.259	0.01234	0.02309	0.00245	3.55E-13	52.86	97.63	165.8	0.7	0.6
1075.3	120	35.331	0.01246	0.03525	0.00219	3.85E-13	59.96	97.98	176.3	0.8	0.7
1075.4	180	37.379	0.01226	0.04426	0.00064	3.07E-13	65.61	99.32	188.4	1.0	0.9
1100	15	38.734	0.02028	0.64628	0.00063	7.94E-15	65.75	99.46	195.2	4.3	4.3
1100.1	30	37.610	0.01007	0.19009	0.00059	3.65E-14	66.43	99.40	189.6	2.8	2.8
1100.2	60	37.652	0.01323	0.09316	0.00232	8.38E-14	67.97	98.02	187.4	2.6	2.5
1100.3	120	38.557	0.01275	0.03763	0.00111	1.53E-13	70.80	98.98	193.4	1.5	1.4
1125	10	37.416	0.03647	0.00047	0.00250	4.17E-15	70.87	97.85	186	61	61
1150	10	38.876	0.01015	0.04418	0.00009	6.91E-15	71.00	99.77	196.3	9.7	9.7
1175	10	40.582	0.01840	0.39876	0.00004	1.43E-14	71.26	99.87	204.8	6.1	6.1
1200	10	42.913	0.01983	0.18162	0.00217	2.77E-14	71.77	98.38	212.8	3.1	3.0
1300	10	47.174	0.01273	0.04608	0.00163	4.23E-13	79.58	98.85	233.7	0.8	0.5
1350	10	40.027	0.01216	0.01998	0.00071	1.11E-12	100.00	99.31	201.0	0.5	0.3
				EK 97-6: K-feldspar (wt: 0.0362 g; J=0.002963 ± 1.2224E-5)							
400	20	133.238	0.08955	1.38203	0.23859	2.71E-15	0.06	47.13	308	99	99
400.1	36	117.171	0.17717	20.79943	0.62493	1.05E-15	0.09	-56.57	0	371	371
450	20	62.047	-0.00001	0.00173	0.16414	1.15E-15	0.11	21.71	71	62	62
450.1	36	119.826	0.06790	0.00059	0.08243	3.35E-15	0.19	79.62	449	20	20
500	20	99.576	0.44844	0.00082	0.05600	2.44E-15	0.25	83.32	397	36	36
500.1	36	179.738	0.02682	0.00029	0.03712	6.79E-15	0.40	93.86	731	16	16
550	20	215.913	0.02479	0.14954	0.04111	1.59E-14	0.77	94.35	852.1	9.1	8.7
550.1	34	74.654	0.01621	0.00009	0.01607	2.25E-14	1.29	93.55	339.3	4.8	4.6
600	20	78.701	0.01738	0.17796	0.01341	2.07E-14	1.77	94.89	360.7	4.8	4.6

Supplementary table - Kirby et al.: $^{40}Ar/^{39}Ar$ data (continued)

Temperature (°C)	Duration (min)	$^{40}Ar/^{39}Ar$	$^{38}Ar/^{39}Ar$	$^{37}Ar/^{39}Ar$	$^{36}Ar/^{39}Ar$	$^{39}Ar_K$ (moles)	^{39}Ar Released (%)	$^{40}Ar^*$ (%)	Age (Ma)	± 2 σ (Ma)†	± 2 σ (Ma)§
600.1	34	43.667	0.01159	0.03851	0.00905	3.92E-14	2.67	93.73	206.5	2.3	2.2
650	20	47.100	0.01232	0.39593	0.01227	2.23E-14	3.18	92.22	218.5	4.3	4.3
650.1	34	32.681	0.00578	0.00006	0.00842	3.12E-14	3.90	92.18	154	17	17
700	20	39.357	0.01428	0.30325	0.01278	2.73E-14	4.53	90.29	180.7	4.3	4.3
700.1	34	21.402	0.01521	0.00005	0.00691	4.13E-14	5.48	90.14	100.3	1.3	1.3
750	20	24.728	0.01774	0.17173	0.01730	2.41E-14	6.04	79.11	101.7	2.7	2.7
750.1	34	17.163	0.01427	0.13495	0.00472	4.57E-14	7.09	91.53	82.1	1.7	1.7
800	20	18.467	0.01451	0.30064	0.00429	2.90E-14	7.76	92.89	89.5	1.3	1.2
800.1	34	16.205	0.01187	0.00004	0.00281	4.99E-14	8.91	94.47	80.1	1.4	1.4
850	20	18.758	0.01420	0.36255	0.00777	3.27E-14	9.66	87.55	85.8	2.4	2.4
850.1	34	17.050	0.01454	0.03843	0.00418	5.21E-14	10.87	92.39	82.3	2.0	1.9
900	18	19.666	0.01154	0.00008	0.00739	2.65E-14	11.48	88.56	90.8	2.7	2.7
900.1	30	18.669	0.01285	0.09670	0.00276	4.44E-14	12.50	95.30	92.7	2.2	2.2
950	18	22.425	0.01497	0.21285	0.00813	2.13E-14	12.99	89.06	103.8	3.3	3.3
990	18	24.170	0.01578	0.21196	0.00805	6.20E-14	14.42	89.94	112.7	2.6	2.6
1030	18	26.738	0.01374	0.07950	0.00516	8.37E-14	16.35	94.07	129.7	0.9	0.8
1075	18	33.401	0.01315	0.05932	0.00320	1.49E-13	19.77	96.98	165.3	1.3	1.1
1075.1	36	35.131	0.01296	0.02706	0.00407	3.30E-13	27.37	96.39	172.5	0.9	0.6
1075.2	72	34.080	0.01276	0.03357	0.00245	3.98E-13	36.55	97.69	169.7	0.9	0.6
1075.3	144	34.221	0.01274	0.02188	0.00156	3.60E-13	44.85	98.46	171.7	1.0	0.7
1100	18	34.883	0.01025	0.00009	0.00002	2.25E-14	45.36	99.79	177.1	8.5	8.4
1100.1	36	35.443	0.01186	0.01385	0.00159	7.09E-14	47.00	98.49	177.5	1.7	1.6
1100.2	72	35.772	0.01132	0.00001	0.00225	1.48E-13	50.41	97.96	178.3	1.0	0.7
1100.3	144	36.434	0.01269	0.00870	0.00269	2.42E-13	56.00	97.64	180.8	0.9	0.6
1125	18	36.574	0.01348	0.03977	0.00274	1.88E-14	56.43	97.61	181.4	6.7	6.7
1125.1	36	36.867	0.01086	0.00004	0.00196	5.58E-14	57.72	98.24	183.9	6.7	6.6
1125.2	72	37.636	0.01233	0.05143	0.00260	1.21E-13	60.50	97.79	186.8	1.5	1.3
1150	15	36.777	0.00346	0.00012	0.00114	1.72E-14	60.90	98.90	184.7	4.1	4.1
1175	15	37.996	0.01350	0.08996	0.00176	4.02E-14	61.83	98.47	189.7	2.9	2.8
1200	15	39.805	0.01358	0.07741	0.00311	9.01E-14	63.90	97.54	196.5	1.1	0.8
1225	15	39.757	0.01274	0.05437	0.00333	1.73E-13	67.89	97.37	195.9	1.3	1.1
1250	10	38.853	0.01300	0.07108	0.00299	1.20E-13	70.66	97.57	192.1	1.1	0.8
1300	10	37.283	0.01253	0.02117	0.00116	7.12E-13	87.07	98.90	187.1	0.9	0.5
1350	10	37.226	0.01247	0.01986	0.00089	5.61E-13	100.00	99.12	187.1	0.8	0.3
				EK 97-14: K-feldspar (wt: 0.0602 g; J=0.0026131 ± 7.556E-5)							
450	20	70.167	0.02676	0.00780	0.05749	1.15E-14	0.20	75.79	234.7	8.9	6.2
450.1	34	17.376	0.01570	0.02002	0.01984	2.35E-14	0.59	66.24	53.5	4.7	4.5
500	20	13.152	0.02221	0.00001	0.01493	1.79E-14	0.90	66.43	40.7	7.5	7.4

Supplementary table - Kirby et al.: $^{40}Ar/^{39}Ar$ data (continued)

Temperature (°C)	Duration (min)	$^{40}Ar/^{39}Ar$	$^{38}Ar/^{39}Ar$	$^{37}Ar/^{39}Ar$	$^{36}Ar/^{39}Ar$	$^{39}Ar_K$ (moles)	^{39}Ar Released (%)	$^{40}Ar^*$ (%)	Age (Ma)	± 2 σ (Ma)†	± 2 σ (Ma)§
500.1	36	7.738	0.01597	0.01689	0.00776	3.92E-14	1.56	70.33	25.5	2.6	2.5
550	20	5.065	0.01231	0.00001	0.00451	2.41E-14	1.97	73.60	17.5	2.6	2.6
550.1	36	7.630	0.01325	0.00765	0.00507	8.20E-14	3.36	80.30	28.6	1.8	1.6
600	20	6.608	0.01324	0.00053	0.00339	6.18E-14	4.41	84.78	26.2	4.5	4.5
600.1	30	4.044	0.01220	0.00734	0.00251	9.91E-14	6.08	81.54	15.5	1.3	1.2
650	20	5.056	0.01302	0.00034	0.00271	1.01E-13	7.80	84.06	19.9	1.4	1.3
650.1	30	2.534	0.01241	0.01023	0.00210	1.99E-13	11.17	75.39	9.0	0.6	0.5
700	20	2.775	0.01259	0.01401	0.00177	1.36E-13	13.47	81.03	10.6	0.7	0.6
700.1	30	1.790	0.01330	0.03103	0.00152	1.68E-13	16.33	74.77	6.3	1.1	1.0
750	20	5.160	0.01467	0.00861	0.01092	1.23E-13	18.41	37.40	9.1	1.1	1.0
750.1	30	2.281	0.01304	0.00416	0.00341	1.53E-13	21.00	55.67	6.0	1.5	1.5
800	20	1.634	0.01195	0.00166	0.00088	1.16E-13	22.96	83.71	6.4	0.7	0.7
800.1	30	1.614	0.01172	0.00467	0.00000	1.54E-13	25.57	99.69	7.6	1.0	1.0
850	20	2.352	0.01400	0.00758	0.00072	1.19E-13	27.58	90.85	10.1	0.8	0.7
850.1	30	2.653	0.01157	0.00471	0.00058	1.55E-13	30.20	93.41	11.7	0.6	0.5
900	20	3.487	0.01352	0.01710	0.00069	1.14E-13	32.13	94.06	15.4	0.5	0.2
940	20	3.152	0.01210	0.01126	0.00016	1.25E-13	34.25	98.33	14.6	0.7	0.6
980	20	3.657	0.01247	0.01623	0.00043	2.18E-13	37.93	96.41	16.5	0.5	0.2
1020	20	4.055	0.01205	0.04027	0.00023	2.48E-13	42.14	98.33	18.7	1.0	0.8
1050	20	4.217	0.01271	0.03166	0.00086	2.03E-13	45.58	93.92	18.6	0.7	0.4
1075	20	4.669	0.01268	0.02452	0.00083	2.12E-13	49.17	94.72	20.7	0.7	0.3
1075.1	40	5.631	0.01243	0.01179	0.00101	3.39E-13	54.91	94.65	25.0	0.8	0.2
1075.2	80	7.012	0.01273	0.01036	0.00140	4.12E-13	61.88	94.05	30.8	0.9	0.3
1075.3	150	7.849	0.01225	0.01213	0.00145	3.24E-13	67.37	94.48	34.6	1.0	0.1
1100	20	8.239	0.01417	0.00001	0.00092	1.85E-14	67.69	96.66	37.2	3.9	3.7
1100.1	40	9.358	0.01227	0.01377	0.00109	6.18E-14	68.73	96.53	42.1	1.7	1.2
1100.2	80	9.294	0.01137	0.01480	0.00188	1.16E-13	70.70	93.97	40.7	1.3	0.4
1100.3	120	10.254	0.01271	0.01248	0.00195	1.39E-13	73.06	94.34	45.0	1.3	0.4
1125	20	11.396	0.01162	0.01990	0.00003	1.65E-14	73.34	99.88	52.9	3.4	3.0
1125.1	40	10.995	0.01508	0.00326	0.00104	4.40E-14	74.09	97.17	49.7	2.8	2.4
1150	15	10.981	0.01698	0.00186	0.00005	1.09E-14	74.27	99.82	51.0	4.2	3.9
1175	15	11.094	0.01424	0.02444	0.00002	2.74E-14	74.74	99.92	51.5	2.5	2.1
1200	15	11.464	0.01417	0.02854	0.00001	4.68E-14	75.53	99.95	53.3	4.1	3.8
1225	15	12.008	0.01320	0.01460	0.00127	7.89E-14	76.87	96.84	54.0	2.4	1.8
1250	15	12.444	0.01294	0.01909	0.00265	1.27E-13	79.01	93.69	54.1	1.8	0.9
1300	15	12.607	0.01335	0.00875	0.00387	4.98E-13	87.45	90.90	53.2	1.5	0.2
1350	15	14.427	0.01302	0.00543	0.00422	7.41E-13	100.00	91.33	61.1	1.7	0.1

† Includes uncertainty in irradiation parameter, J

§ Excludes uncertainty in J

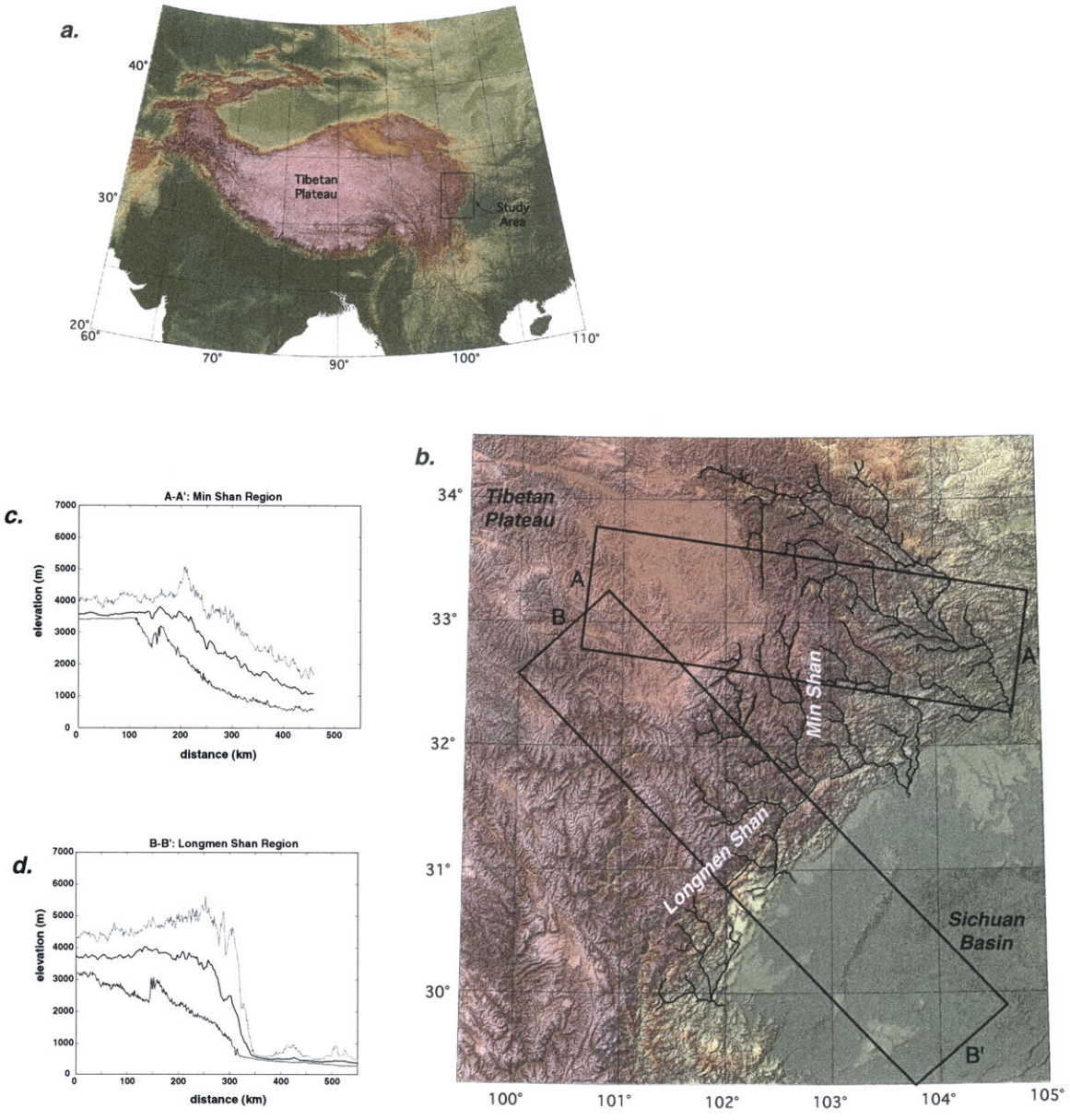
a.
40°
30°
20°
60°
70°
90°
100°
110°
Tibetan Plateau
Study Area
b.
34°
33°
32°
31°
30°
100°
101°
102°
103°
104°
105°
Tibetan Plateau
A
A'
B
B'
Min Shan
Longmen Shan
Sichuan Basin
c.
A-A': Min Shan Region
elevation (m)
distance (km)
d.
B-B': Longmen Shan Region
elevation (m)
distance (km)

Figure 1

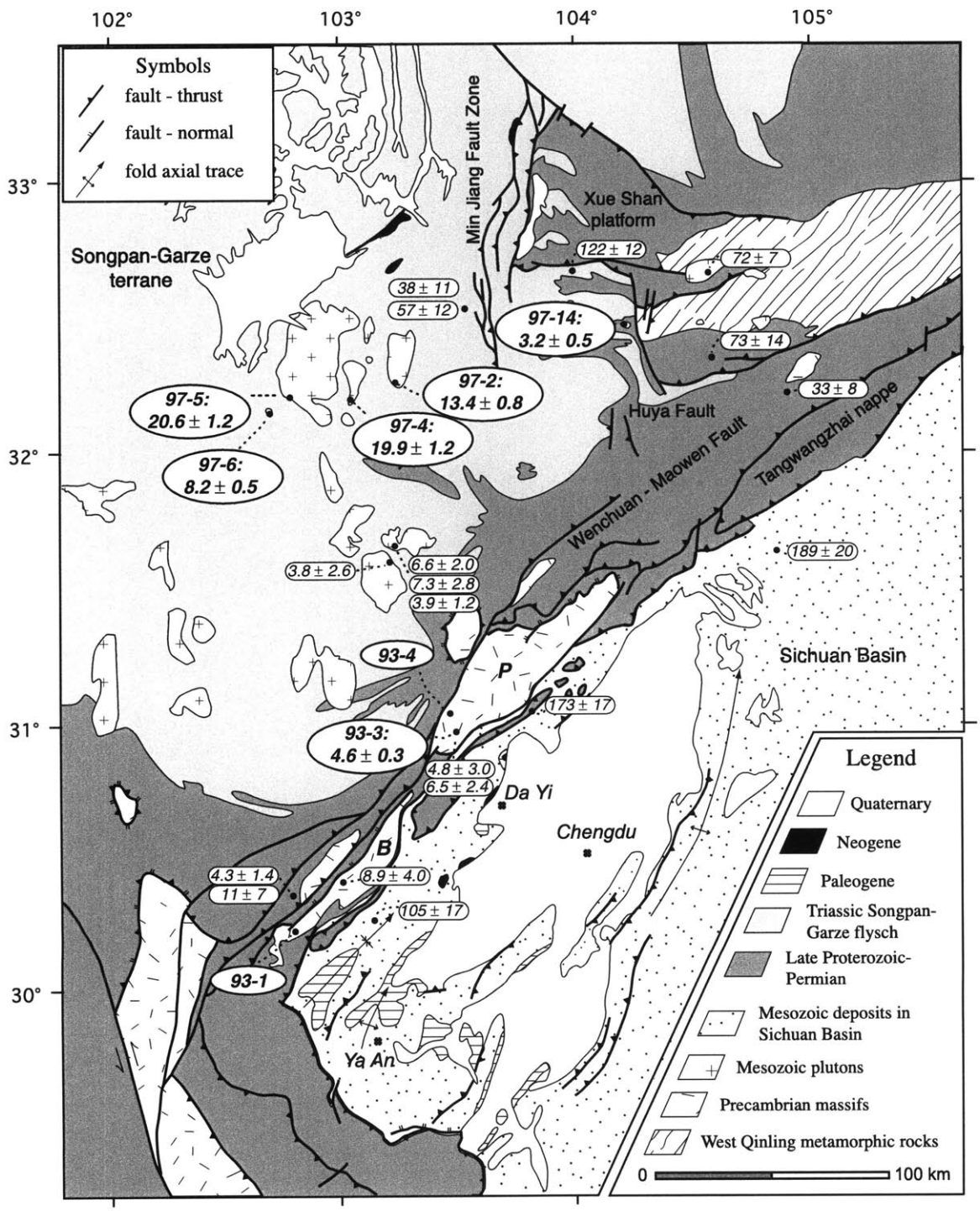
102°
103°
104°
105°
33°
32°
31°
30°
Symbols
fault - thrust
fault - normal
fold axial trace
Songpan-Garze terrane
Min Jiang Fault Zone
Xue Shan platform
Huya Fault
Wenchuan - Maowen Fault
Tangwangzhai nappe
Sichuan Basin
Da Yi
Chengdu
Ya An
P
B
122 ± 12
72 ± 7
38 ± 11
57 ± 12
97-14: 3.2 ± 0.5
73 ± 14
33 ± 8
97-2: 13.4 ± 0.8
97-5: 20.6 ± 1.2
97-4: 19.9 ± 1.2
97-6: 8.2 ± 0.5
189 ± 20
3.8 ± 2.6
6.6 ± 2.0
7.3 ± 2.8
3.9 ± 1.2
93-4
173 ± 17
93-3: 4.6 ± 0.3
4.8 ± 3.0
6.5 ± 2.4
4.3 ± 1.4
11 ± 7
8.9 ± 4.0
105 ± 17
93-1
Legend
Quaternary
Neogene
Paleogene
Triassic Songpan-Garze flysch
Late Proterozoic-Permian
Mesozoic deposits in Sichuan Basin
Mesozoic plutons
Precambrian massifs
West Qinling metamorphic rocks
0
100 km

Figure 2

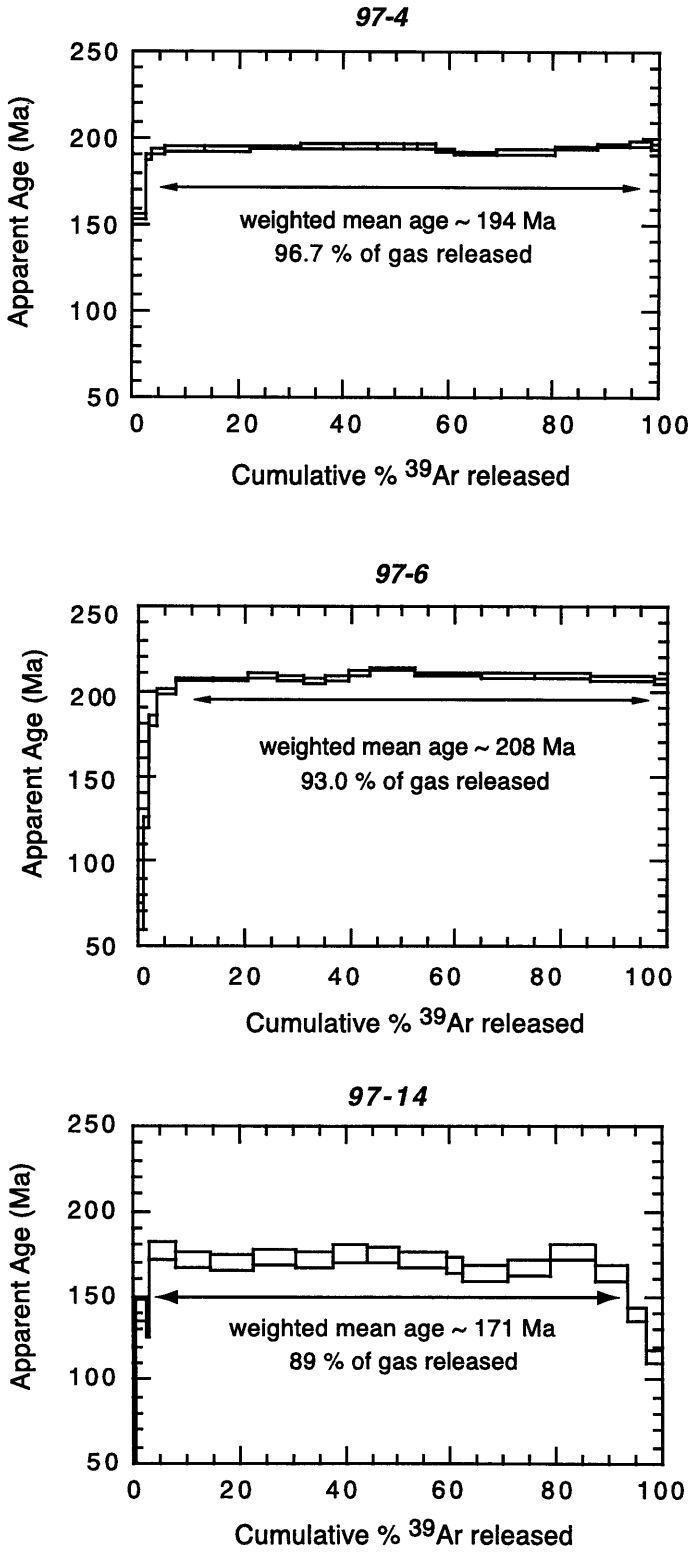
97-4
Apparent Age (Ma)
250
200
150
100
50
0
20
40
60
80
100
weighted mean age ~ 194 Ma
96.7 % of gas released
Cumulative % 39Ar released
97-6
Apparent Age (Ma)
250
200
150
100
50
0
20
40
60
80
100
weighted mean age ~ 208 Ma
93.0 % of gas released
Cumulative % 39Ar released
97-14
Apparent Age (Ma)
250
200
150
100
50
0
20
40
60
80
100
weighted mean age ~ 171 Ma
89 % of gas released
Cumulative % 39Ar released

Figure 3

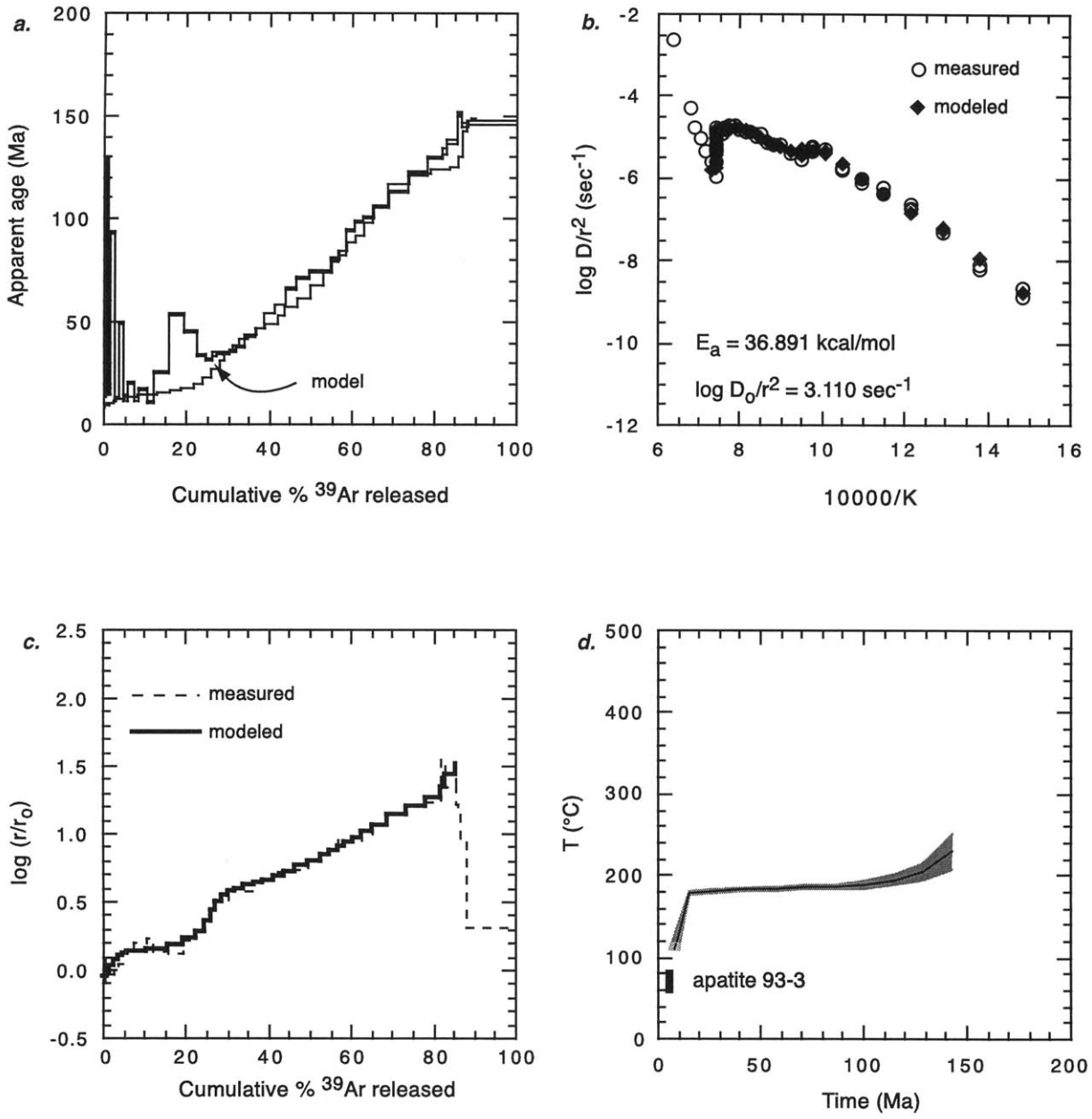
a.
Apparent age (Ma)
Cumulative % 39Ar released
model
b.
log D/r2 (sec-1)
10000/K
measured
modeled
Ea = 36.891 kcal/mol
log Do/r2 = 3.110 sec-1
c.
log (r/ro)
Cumulative % 39Ar released
measured
modeled
d.
T (°C)
Time (Ma)
apatite 93-3

Figure 4

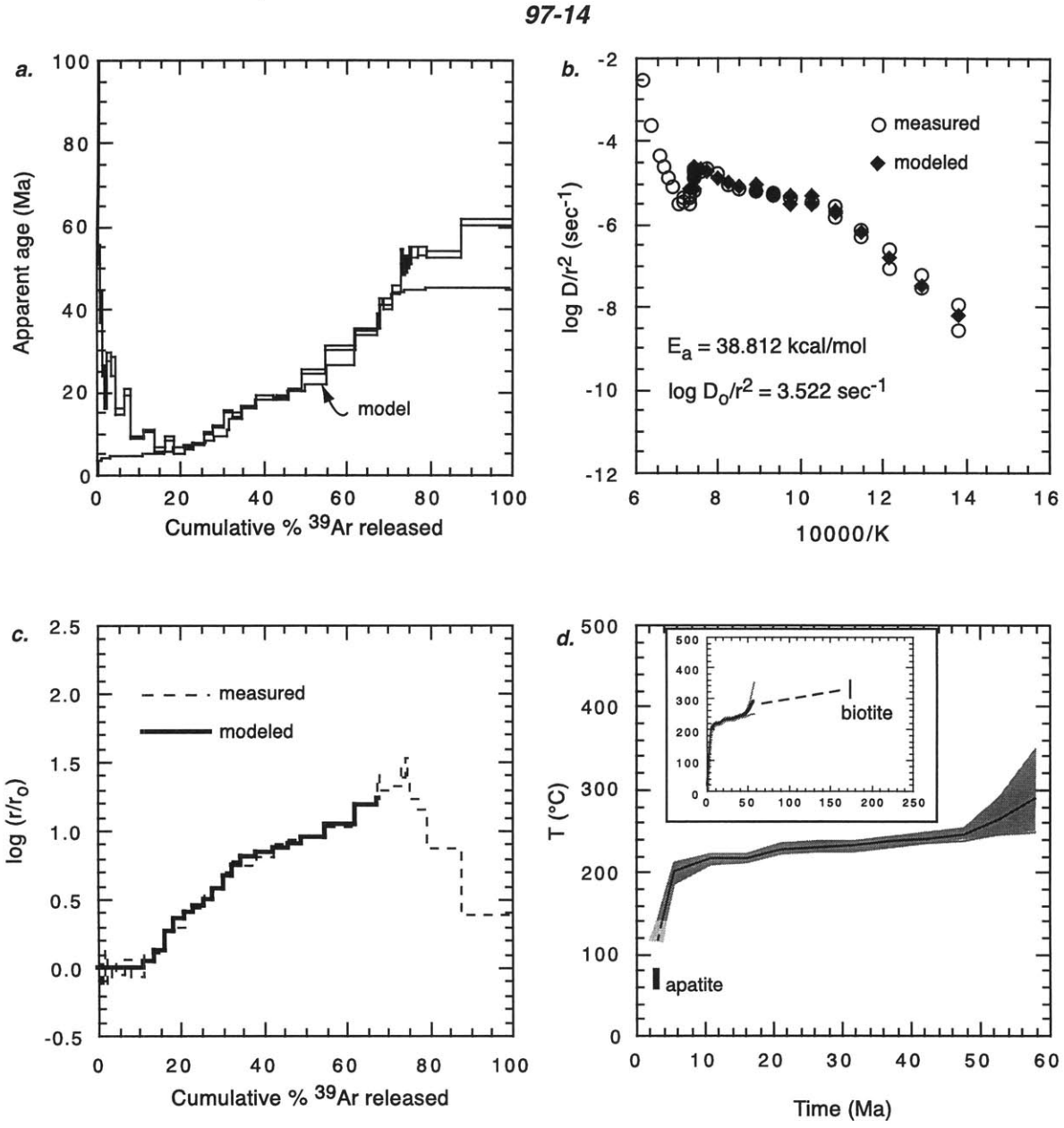
97-14
a.
Apparent age (Ma)
Cumulative % 39Ar released
model
b.
log D/r2 (sec-1)
10000/K
measured
modeled
Ea = 38.812 kcal/mol
log Do/r2 = 3.522 sec-1
c.
log (r/ro)
Cumulative % 39Ar released
measured
modeled
d.
T (°C)
Time (Ma)
biotite
apatite

Figure 5

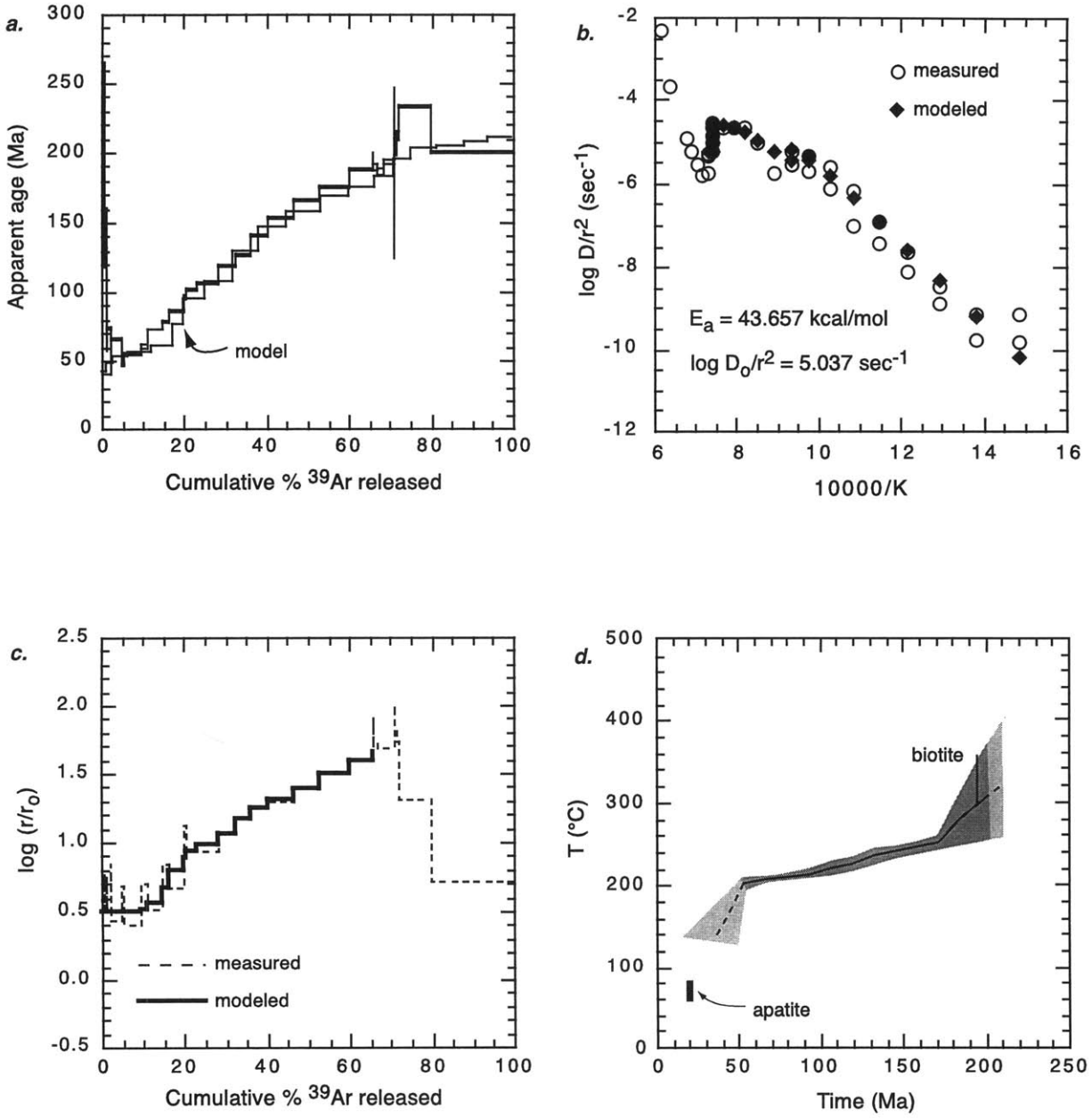
a.
Apparent age (Ma)
Cumulative % 39Ar released
model
b.
log D/r2 (sec-1)
10000/K
measured
modeled
Ea = 43.657 kcal/mol
log D0/r2 = 5.037 sec-1
c.
log (r/r0)
Cumulative % 39Ar released
measured
modeled
d.
T (°C)
Time (Ma)
biotite
apatite

Figure 6

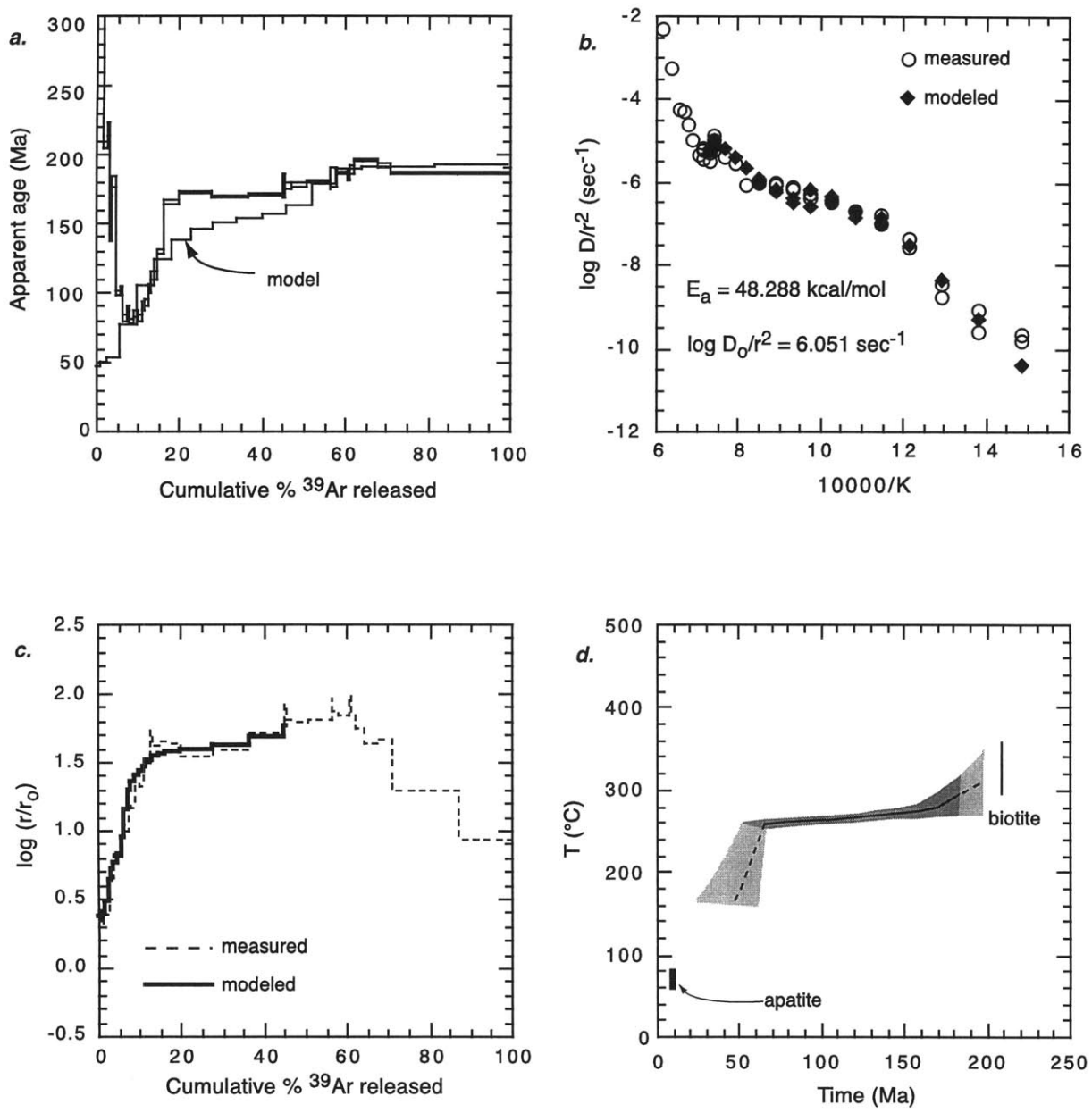
97-6
a.
Apparent age (Ma)
Cumulative % 39Ar released
model
b.
log D/r2 (sec-1)
10000/K
measured
modeled
Ea = 48.288 kcal/mol
log Do/r2 = 6.051 sec-1
c.
log (r/ro)
Cumulative % 39Ar released
measured
modeled
d.
T (°C)
Time (Ma)
biotite
apatite

Figure 7

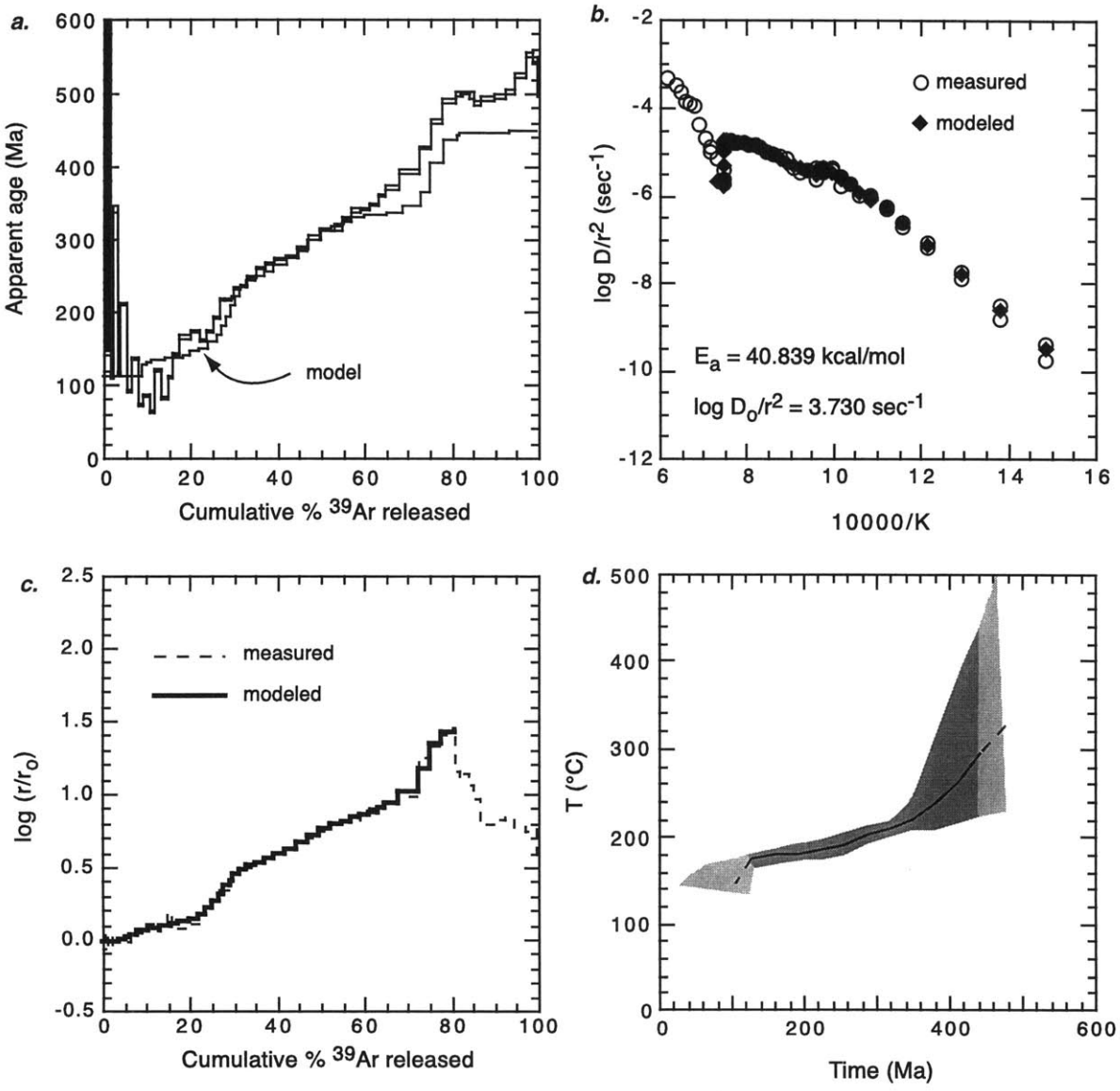
a.
Apparent age (Ma)
Cumulative % 39Ar released
model
b.
log D/r2 (sec-1)
10000/K
measured
modeled
Ea = 40.839 kcal/mol
log Do/r2 = 3.730 sec-1
c.
log (r/ro)
Cumulative % 39Ar released
measured
modeled
d.
T (°C)
Time (Ma)

Figure 8

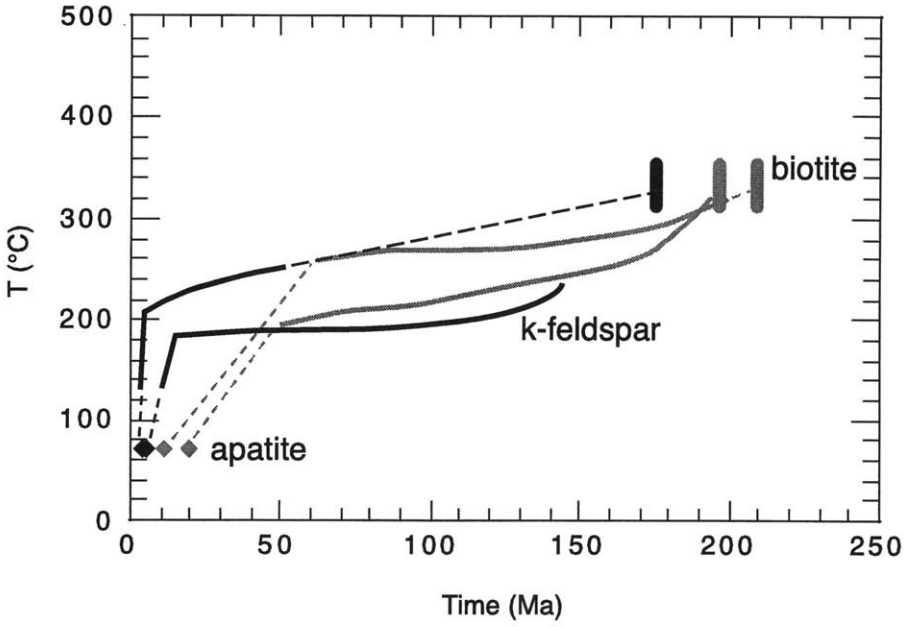
500
400
300
200
100
0
T (°C)
0
50
100
150
200
250
Time (Ma)
biotite
k-feldspar
apatite

Figure 9

Chapter 4

Distribution of active rock uplift along the eastern margin of the Tibetan Plateau: Inferences from bedrock river profiles

Abstract

The apparent lack of upper crustal shortening during Cenozoic development of the eastern Tibetan Plateau poses a fundamental geodynamic problem in that the distribution of crustal thickening may be decoupled from shortening structures observable at the surface. Here we investigate the controls on and the spatial distribution of bedrock channel gradients adjacent to the Sichuan Basin in an effort to assess the degree and nature of active deformation along this margin of the Tibetan Plateau. Analysis of river longitudinal profiles utilizing a channel steepness index (a measure of profile gradient normalized for drainage area) reveal a zone of steep channels adjacent to the topographic front of the plateau margin. Channel profiles are systematically less steep in their headwater reaches on the plateau and in their lower reaches east of the plateau margin; profile concavity provides a measure of the change in channel gradient as they cross this zone. Comparison of steepness indices to mapped lithologic variations reveals only limited influence of rock erodibility on channel gradient in this field area. Likewise, no systematic relationship between steepness indices and upstream drainage area is observed, suggesting that the influence of downstream changes in sediment flux on channel profiles is limited. We argue that the region of high profile steepness cannot be explained by orographic precipitation, base level changes, or a retreating topographic escarpment and must therefore reflect active rock uplift along the topographic front. The coincidence of the zone of high profile steepness with the topographically highest portion of the plateau margin suggests that rock uplift exerts a dominant control on channel gradients in this landscape, thus setting the distribution of topography. Furthermore, we suggest that the distribution of steep channel profiles provides an indication of spatial gradients in rock uplift rate across this margin of the plateau.

Motivation

Since the recognition that mass redistribution by surficial processes can profoundly influence the tectonic evolution of orogenic systems (Molnar and England, 1990; Beaumont et al., 1992; Hoffman and Grotzinger, 1993), intensive research over the past decade has focused on exploring the interrelationships between tectonic and surface processes. As rock uplift in active orogens is a consequence of the interplay between tectonic mass flux and erosionally driven denudation, the spatial distribution of rock uplift is a fundamental geodynamic quantity that can place important constraints on the geometry and distribution of active structures (e.g., Molnar, 1987) and on the localization of mass flux in an evolving orogen (Willett, 1999). However, active rock uplift can be a difficult quantity to measure, and is often inferred from the spatial distribution of deformation (e.g., Lave and Avouac, 2000), from distributed geodetic surveys (e.g., Jackson and Bilham, 1994), and from the distribution of thermochronologic ages (e.g., Zeitler, 1985).

Gradients of bedrock channels in tectonically active regions are set by a competition between local rock uplift and incision rate (Howard, 1994). Consequently, analysis of channel gradients and longitudinal profiles provides a promising means of exploring the spatial distribution of rock uplift (e.g., Hack, 1957; Hack, 1973; Snyder et al., 2000; Kirby and Whipple, in review). For example, in a pioneering analysis of transverse rivers crossing the Himalaya, Seeber and Gornitz (1983) argued that anomalously high gradients in the Higher Himalaya likely reflected rock uplift localized beneath the range crest, a prediction borne out, at least in the short-term, by recent geodetic and leveling surveys (Jackson and Bilham, 1994; Bilham et al., 1997). Bedrock channels are interesting in their own right as well. The bedrock channel network dictates critical relationships among relief, elevation, and denudation rate (Howard, 1994; Howard et al., 1994; Whipple et al., 1999) and conveys signals of tectonic and climatic change across landscapes, effectively setting landscape response time (Whipple and Tucker, 1999a). The rate of channel incision also sets the lower boundary condition for hillslopes and thus fundamentally controls denudation rates in the landscape. Thus, analysis of channel profile gradients and their distribution in a mountain landscape can provide important insights into the controls on the distribution of denudation.

In this paper we analyze downstream changes in channel profile gradient of rivers draining the eastern margin of the Tibetan Plateau in an effort to extract information about the spatial distribution of active rock uplift along this margin. Our efforts are motivated in large part by competing hypotheses for the evolution of the margin. The region has long been considered a locus of active shortening between the plateau and its foreland (e.g., Avouac and Tapponnier, 1993). However, recent geodetic (King et al., 1997; Chen et al., 2000) and geologic (Burchfiel et al., 1995) investigations indicate that there is little resolvable shortening across this margin. Royden and others (1997) proposed that much of the topography in eastern Tibet developed as a consequence of thickening by flow of lower crust with little attendant disruption of surface features. This model predicts, in a general way, that rock uplift may be decoupled from upper crustal shortening features. Consequently, analysis of channel profiles may provide an important means of identifying spatial gradients in rock uplift rate across this margin.

Approach and Scope

This paper develops a method for examining systematic changes in channel gradient across a landscape within the context of the detachment-limited unit stream power incision model (Howard et al., 1994). Our approach builds upon recent theoretical considerations of the dynamics of the stream-power incision model (Whipple and Tucker, 1999a), empirical evaluation of steady-state channel profiles under conditions of uniform lithology and uplift rate (Snyder et al., 2000), and analysis of channel response to spatial gradients in rock uplift rate (Kirby and Whipple, in review).

We examine channel gradients along rivers draining the eastern margin of the Tibetan Plateau adjacent to and north of the Sichuan Basin (Figure 1). All of these rivers are moderate size (< 200 km in length), steep bedrock channels (see below) whose headwaters rise at ~4000 m on the Tibetan Plateau. All eventually drain across the Sichuan Basin into the Yangtze River, and thus have experienced similar base level histories. Our analysis relies primarily on channel profiles extracted from a digital elevation model (see, Fielding et al., 1994), but is guided by field observations along select channels.

Our analysis reveals coherent spatial patterns in channel profile concavity and a channel steepness index (e.g., Snyder et al., 2000) across this margin of the plateau. We then evaluate a number of potential controls on this distribution of channel gradients, including lithology, base level change, escarpment retreat, orographic effects, sediment flux, and rock uplift. We use the spatial pattern of high steepness indices in combination with field observations of channel incision to argue that rock uplift exerts a dominant control on channel gradients in this landscape, and that we can utilize spatial changes in the channel steepness index as an indicator of spatial variations in active rock uplift along this margin of the plateau.

Background: Active Tectonics in Eastern Tibet

The eastern margin of the Tibetan Plateau adjacent to the Sichuan Basin is one of the world's most impressive continental escarpments. Elevations rise from ~500 m in the Sichuan Basin to peak elevations exceeding 6500 m over a distance of 40-60 km. Mean elevations on the plateau to the west range from 3500-4000 m (Figure 1). For ~200 km north of the Sichuan Basin, the topographic margin of the plateau trends north-south and coincides with a high mountain range, the Min Shan. Peak elevations in the range are ~5500 m and stand approximately 2 km above the plateau to the west and some 4km above the highlands of the West Qinling mountains to the east. North of ~34°N, the margin of the plateau ceases to be a readily discernable feature, and plateau elevations grade gently into regional elevations ~1000 m (Clark and Royden, 2000).

Despite the impressive topography along this margin of the plateau, recent space geodetic surveys indicate that active shortening between the plateau and its foreland is less than 2-3 mm/yr and is within uncertainty of zero (King et al., 1997; Chen et al., 2000). Furthermore, although the region was subject to severe upper-crustal shortening during the Mesozoic, very little shortening appears to have taken place during Cenozoic time (Burchfiel et al., 1995). Indeed, Cenozoic terrestrial sediments in the Sichuan Basin are restricted to a thin (<500 m) veneer in the southwestern corner of the basin (Burchfiel et al., 1995) and indicate that the basin underwent little flexural subsidence during development of the plateau (Royden et al., 1997). These observations led Royden et al. (1997) to suggest that plateau development and subsequent evolution were driven by

thickening in a weak lower crust that was rheologically decoupled from upper crustal deformation. This model predicts that the isostatic and dynamic response to such thickening would generate pronounced gradients in rock uplift across the margin of the plateau. Thus, the principal objective of this study is to examine whether such a signal is present in stream gradients.

We expect that gradients in rock uplift exist in the Min Shan region north of the Sichuan Basin (Figure 1). Tilting recorded in remnant Quaternary basins along the western flank of the range suggests that rapid rock uplift is localized beneath the range crest, in the apparent absence of significant horizontal shortening (Kirby et al., 2000). However, along the margin of the Sichuan Basin southeast of the range (Figure 1), frontal thrust faults are overlapped by Early Jurassic terrestrial sediments (Burchfiel et al., 1995) that restrict the timing of the most recent displacement on these structures to the Mesozoic. There are a series of discontinuous faults along the eastern flank of the Min Shan (Figure 1) (Chen et al., 1994b; Kirby et al., 2000), but their relationship to the high topography of the range is ambiguous (Kirby et al., 2000). Thus, stream profiles in this region may provide important insight into the extent to which active rock uplift in the Min Shan extends into the foreland to the east and southeast of the plateau margin.

A lack of Quaternary sediments in the plateau region south of the Min Shan prevents ready evaluation of deformation along the margin of the Sichuan Basin. However, there are several regionally extensive fault zones that are suspected of having some degree of Quaternary activity (Burchfiel et al., 1995). These include a series of frontal faults along the margin of the Sichaun Basin, collectively here termed the Guan Xian-An Xian fault system, a system of thrust faults that carry basement massifs in their hanging walls, termed the Yingxiu-Beichuan fault system (Chen et al., 1994a; Chen and Wilson, 1996), and the Wenchuan-Maowen fault zone (Burchfiel et al., 1995; Chen and Wilson, 1996) (Figure 1). The latter has a complex, polyphase history characterized by Mesozoic left-shear, transpressional thrusting, normal-sense (west-side down) displacement of unknown age, and late brittle displacement associated with sub-horizontal slickenlines (Burchfiel et al., 1995). Recent activity on these structures is debated (c.f., Chen et al., 1994b; Burchfiel et al., 1995). Consequently, stream profiles

may provide an indication as to the degree of activity on these structures and allow us to assess their potential role in influencing rock uplift along this margin.

Theoretical Framework

Incision by rivers into bedrock can be limited by the detachment of intact bedrock (e.g., Howard, 1994) or by the capacity of the channel to transport the sediment load (e.g., Willgoose, 1994; Tucker and Slingerland, 1996). In either case, incision is typically modeled as a power-law function of contributing drainage area (as a proxy for discharge) and local channel gradient (Howard and Kerby, 1983; Howard, 1994; Willgoose, 1994; Moglen and Bras, 1995). For the purposes of this discussion, we will examine the detachment-limited case (Howard et al., 1994), but we note that the analysis is readily applicable to transport-limited conditions. In studies where the transient response of channel profiles to temporal changes in climate, baselevel, or tectonics are a primary concern, the distinction between detachment-limited and transport-limited is more important (Whipple and Tucker, 1999b).

The evolution of a detachment-limited river profile is governed by the competition between rock uplift (relative to a fixed baselevel) and erosion rate, such that:

$$dz/dt = U(x,t) - KA^m S^n \qquad (1)$$

where dz/dt is the time rate of change of channel bed elevation, U is rock uplift rate, K is a dimensional coefficient of erosion, A is upstream drainage area, S is local channel gradient, and m and n are positive constants that reflect basin hydrology, hydraulic geometry, and erosion process (Howard et al., 1994; Whipple and Tucker, 1999a; Whipple et al., 2000a).

A number of researchers have recently argued that the incision rate in bedrock channels is a function of the ratio of sediment flux, q_s, to sediment carrying capacity, q_c (Sklar and Dietrich, 1997; Slingerland et al., 1997; Sklar and Dietrich, 1998). A simple way to represent this dependence is to write

$$K = K'f(q_s, q_c) \qquad (2)$$

where $f(q_s, q_c)$ is an unspecified function and K' is a dimensional coefficient that encapsulates the dependence of erosion rate on rock mass quality and erosion process

(Whipple and Tucker, 1999a). Sklar and Dietrich (1998) argue that sediment flux plays a dual role in influencing incision rates by: 1) accelerating erosion by increasing the number of tools in the flow ($q_s/q_c < 0.5$) and 2) inhibiting erosion by partial shielding of the bed from particle impact ($q_s/q_c > 0.5$). For the purposes of this analysis, we frame the problem with the simplest case where the influence of sediment flux is constant along the channel (i.e., $f(q_s, q_c) = 1$) and comment qualitatively on the influence of $f(q_s, q_c) < 1$ in the discussion (below).

Under steady-state conditions ($dz/dt = 0$), with uniform U and K and constant m and n, equation (1) can be solved to yield an expression for equilibrium channel gradient:

$$S_e = \left(U/K\right)^{\frac{1}{n}} A^{-\frac{m}{n}} \tag{3}$$

Thus, an equilibrium channel under conditions of uniform uplift and constant erosion coefficient should present a smooth longitudinal profile whose concavity is set by the ratio m/n and whose steepness is set by the coefficient $(U/K)^{1/n}$. In this contribution, we refer to the ratio m/n as the *intrinsic concavity* of the system to distinguish it from the observed concavity of channel profiles (see below). Note that this general form is equivalent to that for transport-limited channels at steady-state (Willgoose, 1994); the two regimes differ only in their transient response to changes in boundary conditions (e.g., Whipple and Tucker, 1999b).

Equation (3) resembles a power-law relation between channel gradient and drainage area often observed in natural landscapes (Flint, 1974; Tarboton et al., 1989; Moglen and Bras, 1995; Sklar and Dietrich, 1998; Snyder et al., 2000):

$$S = k_s A^{-\Theta} \tag{4}$$

We follow Snyder et al. (2000) in referring to the exponent (Θ) as the concavity index and the coefficient (k_s) as the steepness index. Both parameters are easily estimated from regression of channel gradient and drainage area (Seidl and Dietrich, 1992; Moglen and Bras, 1995; Snyder et al., 2000). Thus, under conditions of steady-state incision where U and K are uniform along the channel reach, analysis of channel profiles can yield important insights about the erosion process and the combined effects of uplift rate and erosivity via:

$$\Theta = \frac{m}{n} \tag{5a}$$

and

$$k_s = \left(U/K\right)^{\frac{1}{n}} \tag{5b}$$

The intrinsic concavity (m/n) of detachment-limited channels is thought to be independent of erosion process, is set by the relationships between drainage area and discharge and between discharge and channel width, and should fall in a narrow range of values between 0.35 and 0.6 (Whipple and Tucker, 1999a). Indeed, bedrock channel concavities measured under known conditions of uniform uplift rate and lithology yield estimates very near 0.45 (Whipple and Tucker, 1999a; Snyder et al., 2000; Kirby and Whipple, in review). Although the intrinsic concavity of transport-limited channels is not as well characterized, preliminary estimates of the concavity of transport-limited channels fall within the same range (0.3-0.6, Whipple and Tucker, 1999b).

A restricted range of the ratio m/n , however, does not necessarily imply that actual channel concavities (Θ) are likewise restricted. Any spatial variation in K (Moglen and Bras, 1995; Sklar and Dietrich, 1998) and/or U will impact actual channel concavity. For instance, if $f(q_s, q_c) < 1$, downstream changes in K may effect an increase in concavity where $f(q_s, q_c) < 0.5$ and a reduction in concavity where $0.5 < f(q_s, q_c) < 1$. In addition, in a recent study of channels in the Siwalik Hills crossing pronounced gradients in rock uplift rate (Lave and Avouac, 2000), Kirby and Whipple (in review) demonstrated that the concavity of steady-state river profiles was dependent on the position and direction of the channel relative to rock uplift gradients. Where uplift rate is increasing downstream, channels are convex upward ($\Theta < 0$) and where uplift rate is decreasing downstream, channels are highly concave ($\Theta \sim 0.8$-2.1). Channels parallel to uplift gradients have concavities within the range expected for uniform uplift ($\Theta \sim 0.45$). Thus, systematic regional differences in profile concavity can provide an important indication of differences in rock uplift rate, provided one can account for downstream changes in sediment flux and/or lithologic variability.

The coefficient k_s is in principal similar to the stream-gradient index (Hack, 1973), but allows for a more general evaluation of profile steepness independent of the form of the longitudinal profile. High values of k_s may reflect increased lithologic resistance (small K), decreased erosive power (e.g., Sklar and Dietrich, 1998), and/or increased uplift rate.

Relatively few field calibrations of the stream-power incision rule exist that allow estimation of model parameters. The slope exponent (n) has been argued to depend on the dominant erosion process and to vary between ~2/3 and ~5/3 (Whipple et al., 2000a). Howard and Kerby (1983) demonstrated that historic incision rates in rapidly eroding badlands were consistent with incision rate linearly proportional to bed shear stress (e.g. m ~1/3, n ~2/3). More recently, Kirby and Whipple (in review) demonstrated that the response of steady-state channel profiles to downstream changes in uplift rate was consistent with n between ~2/3 and ~1, while historic incision on the Ukak River in Alaska is best explained if n is significantly less than 1 (Whipple et al., 2000b). Estimates of the value of the erosion coefficient, K, are likewise limited, but appear to indicate that K may vary over ~4 orders of magnitude, depending primarily on lithology and regional climate (Stock and Montgomery, 1999). In addition, Snyder and others (2000) have presented evidence that K varies in concert with uplift rate in the King Range of northern California. Whether this reflects enhanced orographic precipitation, an increase in sediment flux, an increase in debris flow frequency, the presence of a significant critical shear stress for erosion, or some combination of these factors is not yet clear (Snyder et al., 1999).

As quantitative application of the stream power model is most readily accomplished under known boundary and initial conditions, where model parameters can be calibrated, we do not attempt a quantitative analysis here. Rather, our approach is to examine *relative* differences in channel profile concavity and steepness and ask whether there are discernable spatial patterns in Θ and k_s. If so, we can begin to assess whether these are associated with lithologic variability (Moglen and Bras, 1995; Tucker and Slingerland, 1996), with downstream changes in sediment flux (Sklar and Dietrich, 1998), with changes in boundary conditions (e.g. base level rise/fall), or with regional differences in rock uplift rate (Kirby and Whipple, in review).

Channel Bed Morphology and the Role of Sediment Flux

The demand placed on rivers in an tectonically active landscape to transport sediment supplied from upstream, coupled with the recognition that "mixed" bedrock channels are common in mountain belts around the world (Howard, 1998) has led a increasing number of workers to consider the role that sediment flux plays in influencing bedrock incision (Sklar and Dietrich, 1997; Slingerland et al., 1997; Sklar and Dietrich, 1998; Whipple and Tucker, 1999b). It is plausible, under the right circumstances, for the gradient of a bedrock river to be set by the need to transport the supplied sediment load and yet still be eroding at a rate equal to the rock uplift rate (Tucker and Slingerland, 1996; Whipple and Tucker, 1999b).

During the course of our field work in eastern Tibet, we had the opportunity to qualitatively observe most of the major rivers in the region. Throughout the Longmen Shan and Min Shan, rivers are typically confined by steep, bedrock walls and intermittently expose bedrock in the channel floor (Figure 2a). Discontinuous strath terraces abound in the region and provide qualitative evidence for recent incision. Many of the larger rivers, however, are mantled by a thin layer of cobble-boulder alluvium along the bed and have hydraulic morphologies (e.g. constrictional rapids near tributary fans) typical of step pool and boulder cascade channels (Montgomery and Buffington, 1997). Streambeds of smaller tributaries are often characterized by a lag of cobbles and boulders (Figure 2b and c). Thus many of the channels in the region are characteristic of "mixed" bedrock channels (Howard, 1998), but, as is the case with many of these channels, it is unclear whether this bed morphology reflects a long-term characteristic state, or whether the presence of sediment reflects the stochastic nature of sediment supply in response to storms, fires, or short-term climatic and land-use changes (Slingerland et al., 1997; Howard, 1998; Massong and Montgomery, 2000). In either case, it is clear that sediment flux could be an important influence on bedrock incision patterns in this landscape (e.g., Sklar and Dietrich, 1998).

The effect of sediment flux on stream profiles depends critically on the functional form of equation (2). However, if we accept the premise of Sklar and Dietrich (1998) that incision rate, in general, should reach a maximum at some intermediate ratio of q_s/q_c,

then we might expect that steady-state channel profiles would depart from a simple detachment-limited system in two significant ways. First, as erosion rates increase due to an increase in available tools, equilibrium channel gradients should decrease (see equation 3), imparting a high concavity to the upper portions of the channel network. Second, downstream reaches should display a relative increase in gradient (for a given area) as they are forced to steepen in order to maintain a constant erosion rate in the face of decreasing K as the bed is progressively protected from further erosion. The latter effect would reduce the concavity of the downstream reach relative to a detachment-limited model. Of course, systematic variations in grain size and sediment delivery from tributaries would impose additional complexities (Sklar and Dietrich, 1998).

Such changes in relative steepness of channel profiles may also result from a downstream transition between detachment-limited and transport-limited conditions. The nature and degree of this transition depend on the relative intrinsic concavities of the transport-limited and detachment-limited regimes (Whipple and Tucker, 1999b), as well as on the stochastic nature of sediment delivery (Tucker and Bras, 2000; Tucker et al., in review).

Distinguishing such influences on channel gradient from those imposed by spatial variations in rock uplift (e.g., Kirby and Whipple, in review) may be difficult. However, systematic variations due to sediment flux should be correlated directly with upstream drainage area or with tributary junctions(in the case of significant variation in the grain size of sediment delivered by tributaries, Sklar and Dietrich, 1998). Systematic variations in uplift should be geographically restricted, and show little dependence on upstream area.

Stream Profile Analysis

We examined 119 channels draining the eastern margin of the Tibetan Plateau between ~30°N and ~34°N (Figure 3). Topographic characteristics of the drainage basins are given in Table 1. The basins range in drainage area from ~20 km^2 to nearly 40,000 km^2. All channels ultimately drain across the Sichuan Basin and join the Yangtze River in SE Sichuan Province.

Channel elevations and upstream drainage areas were extracted from digital topographic data with a nominal resolution of 3 arc seconds (DTED data source, 3 arc second resolution, see Fielding and others (1994)). We removed spikes along the channel and smoothed the data using a moving average of 45 pixels. The window size was chosen to remove the high-frequency noise associated with the digital data, while retaining the general form of the profile. We calculated channel gradients over a constant vertical interval of 10m from the smoothed elevation data (e.g., Snyder et al., 2000). Regression of local channel gradient against upstream drainage area yielded estimates of the concavity and steepness indices (Θ and k_s, respectively). All regressions were limited to the fluvial channel, and excluded data from the hillslopes and colluvial channels (Tarboton et al., 1989; Montgomery and Foufoula-Georgiou, 1993; Snyder et al., 2000). Where we observed obvious breaks in the gradient-area scaling trends, we performed regressions on each segment independently.

In order to test the reliability of channel profiles extracted from the digital data, we conducted detailed surveys of 3 selected channels (Hei Shui He, Jin Jiang, and Fu Jiang – Figure 1) and reconnaissance surveys along several of others (Baishui Jiang, Min Jiang, Tsakahao He). We surveyed channel elevation using a differential GPS (Jin) or altimeter readings corrected for changes in barometric pressure over the course of the survey (Hei Shui and Fu). Both methods yielded channel profiles similar in form to those extracted from the digital data, including a steep knickzone along the upper reaches of the Fu (Figure 4). Thus, we are encouraged that the digital data appear adequate to capture the general form of longitudinal profiles in the region.

Glaciated drainage basins typically have profiles that display dramatically different concavities from fluvial basins (Brocklehurst and Whipple, 1999) and would complicate our analysis. Although glaciated regions occur in the headwaters of some channels near the drainage divide with the plateau, we only observed distinct glacial morphology of channel profiles in a few headwater reaches along the eastern margin of the plateau (Table 1). Field observations along several of these channels (Hei Shui He, Min Shan – Figure 1) revealed small terminal moraines between 4000-4500 m above mean sea level. For the purposes of this paper, drainages with obvious glacial morphology are excluded from consideration.

Results

Concavity

A cursory glance at the planform distribution of channels draining the Longmen Shan and Min Shan (Figure 1) reveals that there are 4 major drainage basins in the region. From south to north these include: 1) the Qing/Qingyi basin, 2) the Min Jiang and its major tributaries, the Hei Shui He and Tsakahao He, 3) the Fu/Jin system draining the eastern flank of the Min Shan, and 4) the Bailong/Baishui basins north of the Min Shan. We observe distinct differences in the concavity of channel profiles among these regions (Figures 5 and 6), and so discuss each independently.

Qing Jiang. The southern Longmen Shan is drained by the Qing Jiang and its major tributary, the Qingyi Jiang (Figure 1). These basins are relatively small, and the drainage divides are set by a competition with tributaries of the Dadu Jiang, a major N-S river to the west. The headwaters of the Qingyi rise in Triassic greywacke and flysch of the Songpan-Garze terrane, cross a basement massif composed of Precambrian crystalline gneisses and granitoids, and then flow through a series of klippen composed of a Paleozoic passive margin sequence (carbonates and shallow marine clastics) and Mesozoic terrestrial deposits. Despite these fault-bounded, lithologic variations, we observe generally smooth profiles (Figure 5a) with nearly uniform concavities (mean $\Theta \sim$ 0.45, Table 1, Figure 6), consistent with the expectation for detachment-limited steady-state profiles experiencing uniform uplift and rock resistance. An exception occurs along the lower reach of the Qing Jiang, which displays a somewhat higher concavity (~0.8, Table 1).

Min Jiang. Most of the central portion of the study area is drained by the Min Jiang and its tributaries, the Hei Shui He and Tsakahao He (Figure 1). The Min Jiang drains a large region of the plateau west of the Min Shan range, turns southwest and flows along the Wenchuan-Maowen fault zone, and then crosses the Pengguan Massif to debauch into the Sichuan Basin west of Chengdu (Figure 1). The Hei Shui and Tsakahao rivers rise on the plateau some 150km west of the Sichuan Basin and join the Min just west of the Pengguan Massif. Both of these rivers begin in Triassic flysch and

greywacke and cross a zone of greenschist grade metamorphics just west of the Wenchuan-Maowen fault (Dirks et al., 1994; Burchfiel et al., 1995).

Note that we did not analyze the middle reach of the Min Jiang itself, north of the junction with the Hei Shui He (Figure 1). A large landslide (>1 km^3) dammed the valley (at the junction of tributary 64, Figure 3) in the latest Pleistocene (Kirby et al., 2000), and is still present as a ~200 m step in the channel profile. Although the response of the Min to this local event is interesting in its own right, a detailed analysis of this problem is beyond the scope of this paper.

In general, tributaries of the Hei Shui He and Tsakahao He have concavities in the range of 0.4 – 0.5 (mean Θ of 0.42 and 0.43, respectively – Table 1). However, two important exceptions occur. First, the trunk streams of the Hei Shui He and Tsakahao He have relatively low concavities (Θ ~0.33 and 0.28, respectively – Table 1, Figure 6). Both rivers maintain steep gradients as they approach the Min Jiang (Figure 5b). In addition, the profile of the Min exhibits a pronounced increase in gradient as it approaches and crosses the Pengguan Massif (Figure 5). The second exception occurs along the western flank of the Min Shan, where tributaries of the Min Jiang exhibit concavities that range from 0.57 to 0.79 (Table 1, Figure 6).

Fu Jiang/Jin Jiang. North of the Sichuan Basin, rivers draining the eastern margin of the plateau have their headwaters along the crest of the Min Shan and exhibit generally high concavities (Figure 6; Table 1). A number of the profiles are characterized by a change from typical concavities (mean Θ ~0.52) along the upper ~20 km of the channel to high concavities (mean Θ ~0.78) along the lower reaches (Table 1; Figure 5c).

We include in this region a series of small channels draining the eastern flank of the Pengguan Massif (Figure 1). The massif is composed of Precambrian crystalline gneisses and granitoids separated from a series of Triassic mudstones by the Yingxiuwan-Beichuan fault zone (Figure 1). Channels in this region tend to have fairly complex profiles, characterized by moderately high concavities in the north and south. However, along the central portion of the massif, two channels display pronounced changes in concavity near the fault zone (Figure 6). Downstream of the fault, concavities are not well characterized due to a lack of data, and are not represented on Figure 6.

Bailong Jiang/Baishui Jiang. The Bailong and Baishui rivers, like those along the Min, have their headwaters on the Tibetan Plateau (Figure 1). The upper reaches of both these rivers have relatively low concavities west of the Min Shan, while their middle reaches exhibit either a uniform concavity (Θ ~0.45 - Bailong) or low concavity (Θ ~0.13 - Baishui) as they cross the topographic edge of the plateau north of the range (Figure 6). East of the topographic margin, however, both rivers transition to higher concavities with Θ values near ~0.75 (Figure 6).

In summary, we observe systematic regional patterns in profile concavity that appear to be spatially associated with the topographic front of the plateau margin. Small tributaries typically have concavities within the expected range for steady-state profiles experiencing uniform conditions. However, rivers that cross large regions of the margin tend to deviate from these values. Rivers that have their headwaters on the plateau and flow toward the topographic front tend to have low concavities, while those that rise in the Min Shan and flow toward the foreland region tend to have high concavities.

Steepness

In order to effect a meaningful comparison of mean river gradient among channels having different drainage areas and different concavities, we compared two different measures of channel steepness. First, we follow Sklar and Dietrich (1998) in normalizing by a representative area (A_r) in the center of the range of area data (here taken as 10^8 m^2) to obtain a representative slope (S_r), which describes the relative steepness of the profile reach:

$$S = S_r (A / A_r)^{-\Theta} \tag{6}$$

Given the wide range of drainage areas we considered, however, this technique was applicable to a limited number of channels (Table 1). Consequently, we also determined the regression intercept, k_s, for all channels using a fixed concavity (in this case, 0.4) (Snyder et al., 2000). Because the steepness index, k_s, (inferred from the regression intercept) covaries with the concavity of the channel, Θ, (inferred from the slope of the regression) (e.g., Sklar and Dietrich, 1998), this method also effectively removes the dependence on profile concavity (Figure 7a) and provides an alternative means of comparing channel steepness. A comparison of the two methods demonstrates that both

provide a similar gauge of relative differences in mean channel gradient among profiles (Figure 7b). Given this result, our argument that the intrinsic concavity of detachment-limited channels should be ~0.4 - 0.5, and the large number of channels in the region with concavities in this range (Table 1; Figure 6, Figure 7a), we utilize the latter method to compare steepness among channels.

In the case where profile concavity differs substantially from the reference value, the steepness of a channel inferred from the k_s value reflects only the mean gradient of the reach in question, and contains little information about the range of channel gradient across the reach (Figure 8). Consequently, for large rivers with concavities outside the expected range (e.g., Tsakahao He, Hei Shui He, Jin Jiang, Fu Jiang), we calculated k_s over intervals of gradient-area data between major tributaries to capture the downstream changes in steepness index implied by the concavity of the channels. For tributaries, the steepness index was calculated between the channel head and the junction with the trunk stream.

The resultant map of the steepness index, k_s, (Figure 9) illustrates that there are distinct spatial patterns in channel steepness across this margin of the plateau. A region of high-gradient channels (k_s ~90-100) exists near the margin of the Sichuan Basin (Figure 9) in the basin of the Qing Jiang and along the lower reaches of the Min Jiang. The zone of high-gradient channels continues north of the Sichuan Basin as a narrow region along the eastern flank of the Min Shan (k_s ~85-105, Figure 9). North of the Min Shan, the Baishui and Bailong maintain wide regions of increased gradient as they cross the plateau margin, although k_s values are somewhat lower (k_s ~60-80, Figure 9), similar to tributaries in the upper part of the Hei Shui and Tsakahao basins.

East and west of this zone of high channel gradients, channel profiles are systematically less steep (Figure 9). Rivers on the plateau, west of the Min Shan, have k_s values ~20-40, while those east of the range transition rapidly from high k_s values near the range crest to low values near the Sichuan Basin (Figure 9). Thus, the high concavity of channels draining the eastern flank of the Min Shan is a measure of this relatively rapid downstream transition to low gradients.

In a similar fashion, the low concavity of the Hei Shui He and Tsakahao He reflects an increase in steepness index as the rivers approach the edge of the plateau

(Figure 9). Tributaries near the headwaters of both rivers tend to have lower k_s values (~50-60) than those near the Min Jiang (~100-150). There are a few exceptions along the upper Hei Shui He (Figure 9); these may reflect a lithologic influence on channel gradient (discussed in detail below).

Importantly, the increase in steepness index near the topographic front appears to be independent of drainage area. The Min Jiang itself displays a pronounced increase in gradient as it nears the plateau margin (k_s ~100-140, Figure 9) that is apparent in the longitudinal profile (Figure 5b). The change in gradient occurs as the Min parallels the Wenchuan-Maowen fault zone (Figure 1) and may be related to displacement on this structure. In either case, the steepening of all channels relative to those farther west points to an external control on channel gradient that is independent of upstream drainage area (see below)

The pattern inferred from the stream gradients corresponds well with our field observations of channel morphology. For example, the lower reaches of the Min Jiang and Hei Shui He contain abundant evidence for recent incision in the form of discontinuous strath terraces (Figure 10a) and abandoned and incised tributary fans (Figure 10a). Local valley-bottom/ridgetop relief along these reaches ranges from 2-3 km. In contrast, there is little evidence for recent incision along the upper reaches of the Hei Shui where tributary fans are graded to river level (Figure 10b) and strath terraces are markedly absent. Local relief is relatively subdued, and ranges from 500 – 1000 m (Figure 10b). These observations qualitatively suggest that systematic differences in the steepness index (k_s) may be reflected by the distribution of incision across this margin of the plateau.

Controls on Profile Gradient

The zone of high stream gradients appears to coincide with the topographically highest portion of the plateau margin (Figure 1; Figure 9). Although this is perhaps not surprising, as bedrock channels dictate much of the relief structure of tectonically active landscapes (Whipple et al., 1999), it suggests that the controls on channel gradient in this landscape ultimately dictate the topography and the relief along the margin of the plateau. In what follows we discuss the following potential influences on channel gradients:

lithologic resistance, sediment flux, orographically induced variation in precipitation, changes in base level, escarpment retreat, and spatial variation in rock uplift. For each, we qualitatively assess whether the observed pattern of channel gradient can be explained by the process in question.

Lithology

It has been widely recognized that varying lithologic resistance to erosion can exert a strong control on channel gradient and landscape morphology (e.g., Hack, 1957; Hack, 1973; Moglen and Bras, 1995; Tucker and Slingerland, 1996). Recent calibration of a stream-power incision model in regions of widely varying lithology yields estimates of the erosion coefficient (K) that vary over ~4 orders of magnitude (Stock and Montgomery, 1999). Although differences in climate may account for some of this variation, it is clear that rock mass quality can significantly influence stream incision (Sklar and Dietrick, 1999; Stock and Montgomery, 1999). In order to assess the potential role of lithologic resistance in influencing channel gradients in eastern Tibet, we compare the spatial pattern of k_s values determined from the topographic data with mapped variations in lithology (Figure 11). The geology was digitized from Chinese geologic maps at a scale of 1:200,000 (map reference) and registered in a GIS database. In addition, we made qualitative observations regarding the competency of various lithologies (bedding planes, degree of jointing) during the course of our field investigations.

In general, we see little influence of varying lithology on channel profiles. In the great majority of cases, changes in profile gradient (manifest as changes in the slope-area arrays) do not correspond with mapped lithologic variations (Figure 11). For example, the two primary tributaries of the Qingyi Jiang, in the southern Longmen Shan (Figure 1), cross lithologies ranging from Triassic flysch to Precambrian gneisses and granites and yet show no discernable changes in gradient (Figure 5a, Figure 11).

Likewise, the increase in gradient along the lower reaches of the Min Jiang and its tributaries (Hei Shui He and Tsakahao He) begins well upstream of the crystalline rocks of the Pengguan Massif, and appears to be distributed across a zone some 30-50 km wide (Figure 11) west of the Wenchuan-Maowen fault. East of the fault, there is a pronounced

step in steepness index (Figure 11) that may be associated with the rocks of the Pengguan Massif or with displacement on the fault. In the field, we can discern little difference in rock competence between the headwater reaches of these rivers (Triassic flysch) and the downstream reaches (Silurian-Devonian metasediments). Both are pervasively jointed at the meter to decimeter scale and appear to offer little relative resistance to block extraction.

We do observe, however, a few channels where local changes in channel gradient coincide directly with lithologic changes. In general, these profiles are characterized by distinct convexities in the channel profile and corresponding steps in slope-area arrays (Figure 12). We discuss two of the most prominent, one of which occurs along the Fu Jiang in the eastern Min Shan and one which occurs in the upper Hei Shui He basin (highlighted on Figure 11 with arrows).

Perhaps the best example of lithologic control of channel gradient occurs along the trunk stream of the Fu Jiang along the eastern flank of the Min Shan. The profile of the Fu contains a prominent convex section some 40 km downstream of the headwaters (Figure 12a) that coincides exactly with a band of massively bedded, crystalline Pennsylvanian-Permian limestones (Figure 11). Steepness index (k_s) values along this reach are ~170, nearly three times that of the headwater region (Table 1). This stretch of channel runs in an extremely narrow gorge (in places <10 m) and is choked with massive boulders (10-15 m in diameter) and landslide debris that force the channel into steep cascades approaching 100m in height. Interestingly, the main tributary of the Fu Jiang crosses the same mapped lithology (~10km to the south), and displays no such steepening (Figure 11). Apparently subtle changes in the degree of competence of the rock can effect profound differences in channel gradient.

The second example of lithologic influences on channel gradient occurs along the trunk stream of the Hei Shui He, upstream of the confluence between the northern and western tributaries (Figure 1). Here the channel displays a pronounced increase in gradient as it crosses a Mesozoic pluton (Figure 11, 12b). The granite is characterized by a notable lack of jointing or foliation, and the channel is a narrow boulder cascade through this reach. Boulders range from 3-10m in diameter along this section of channel. The increase in gradient imparts a high concavity to this reach of channel, while upstream

of the granite, the concavity is quite low (Figure 6). Note that we chose regression intervals based on tributary junctions, not lithologic boundaries. Thus, the high concavity inferred from the regression extends for some distance downstream of the granite (Figure 12b). Several other steep tributaries in the region cross similar plutons, and we suspect that many of the high gradient reaches along these tributaries can be attributed to these plutons.

In summary, although variable lithologic resistance can exert a profound control on channel gradients, in this landscape lithologic effects appear to be limited to local channel reaches, and do not appear to account for the systematic regional patterns in channel gradient. This is likely a result of the well-jointed nature of most of the rocks along the eastern margin, and supports inferences that erosion by plucking and block extraction is an efficient mechanism of channel incision (e.g., Miller, 1991; Wohl, 1998; Whipple et al., 2000a).

Sediment Flux

Although the role of sediment flux in bedrock incision is still the subject of intensive research, it is clear that the availability of sediment could play a dual role in influencing bedrock incision and, thus, steady-state channel gradients (e.g., Sklar and Dietrich, 1998). As argued above, the competing roles of tool availability and bed protection might induce a relative increase in gradient as drainage area (and sediment load) increases. Although the increase in steepness index along the lower reaches of the Min Jiang and its tributaries could be interpreted as the result of this manner of response to increasing sediment load, we argue instead that the systematic patterns of channel gradient in eastern Tibet are not the result of downstream changes in sediment flux for two reasons.

First, there does not appear to be a consistent relationship between profile concavity and drainage area. While the Min Jiang and its tributaries begin to increase gradient between 10^8 and 10^9 m^2, those east of the Min Shan (Jin and Fu Jiang) continue to decrease in gradient at the same drainage area (Figure 13). We know of no simple mechanism by which sediment flux would act to produce such different patterns of downstream change in channel gradient. It appears, rather, that profile concavity is

geographically related to the region of high steepness index (k_s) along the topographic front of the plateau margin. Rivers that enter this region from the west (Hei Shui He/Tsakahao He) increase in steepness, while those rising along the Min Shan (Fu Jiang/Jin Jiang) decrease in steepness as they flow east.

Second, tributaries of the Min Jiang drainage system show similar spatial variations in steepness index. Tributaries near the headwaters of the drainage system have systematically lower k_s values than those near the topographic front (with the exception of those influenced by the distribution of Mesozoic granite plutons - Figure 11). This distribution of k_s values further argues that high channel steepness is not drainage area dependent and appears to geographically restricted to near the topographic front.

A complication arises from the fact that steepness indices of tributary streams along the lower reaches of the Tsakahao He, above its junction with the Min Jiang (Figure 1), are systematically higher than the trunk stream (Figure 9). This mismatch between tributary and trunk stream k_s values persists for various reference Θ values and does not appear reflect uncertainty in the intrinsic concavity (m/n). It is possible that the difference in steepness between the trunk and tributary streams reflects a reduced erosional efficacy of these tributaries, perhaps due to protection of the bed by large boulders (see Figure 2c). However, this effect does not explain the general increase in tributary k_s values from the plateau to near the topographic front (Figure 9). Thus, while sediment flux may play a role in setting gradients along the small tributaries, the general pattern of increasing steepness indices toward the topographic front appears to reflect an external control on channel gradients.

Orographic Precipiation

The topographic front along the Sichuan Basin coupled with the monsoonal climate of southwestern China induces a steep gradient in precipitation across this margin of the plateau (Fielding et al., 1994). Mean annual precipitation varies from ~2m/yr at the topographic front to slightly less than 1m/yr west of the drainage divide (Korzoun, 1977). A simple consideration of a stream-power incision rule, however, demonstrates that the increase in erosivity that might accompany greater precipitation along the front

would be accompanied by a reduction in channel gradient (e.g., Whipple et al., 1999) as the river is more effective at balancing rock uplift. Although orographic precipitation may establish a potentially important feedback between climate and long-term denudation (Willett, 1999), the high gradients along the topographic front appear to be maintained in the face of greater precipitation.

Base Level Fall

With the exception of a small region west of the Longquan anticline (Figure 11), the Sichuan Basin is a heavily dissected landscape. Rivers draining across the basin to join the Yangtze have incised meanders ~100-200 meters deep cut into Jurassic and Cretaceous mudstones that floor the basin. This incision appears to extend for some 500 km along the Yangtze River east from the Sichuan Basin (E. Kirby, unpublished data), and may represent a Quaternary base-level fall along the Yangtze and its tributaries (Zhao et al., 1997). The incision, however, does not extend west of the Longquan anticline (Figure 11), where the Min Jiang is actively aggrading on the Chengdu alluvial fan, and it appears that the anticline has effectively isolated the Min Jiang and its tributaries from this base level signal. Thus, recent base level changes cannot account for the steepening observed along the lower Min Jiang. Although base level fall could play an important role in influencing incision rates along the lower reaches of the rivers draining the Min Shan, we see no obvious sign of steepening in the lower reaches of channel profiles. Thus, if the signal is present, it appears to be have had a minor effect on channel gradients throughout the study area.

Escarpment Retreat

In a companion study of the Cenozoic thermal history of the Longmen Shan and Min Shan, Kirby et al. (in review) argued that the onset of rapid cooling in the Late Miocene marked the initial development of the plateau margin in this region. Given the absence of active upper crustal shortening along this margin (e.g., Chen et al., 2000), it is possible that the topography has been decaying since its initial development. The problem of escarpment retreat is fairly well studied (Gilchrist et al., 1994; Kooi and Beaumont, 1994; Tucker and Slingerland, 1994) along passive margins, and we might

expect that if the topographic margin had been retreating since the Miocene, channels would be steepest near the drainage divide, and equilibrated in their downstream reaches (Seidl et al., 1996; Weissel and Seidl, 1998). Such a pattern is inconsistent with the high gradients observed along the margin of the plateau adjacent to the Sichuan Basin. Although it is possible escarpment retreat could produce the pattern of stream gradients along the eastern flank of the Min Shan, independent evidence for rapid rock uplift within the range (Kirby et al., 2000) suggests that high stream gradients near the range crest are tectonically controlled.

Rock Uplift

Given the above arguments, we reason that the spatial distribution of high stream gradients along the topographic front of the plateau margin most likely reflects active rock uplift along the eastern margin of the plateau. As noted above, the correspondence between gradients of small tributaries of the Min Jiang along the front and the gradients of headwater reaches of rivers draining the eastern the Min Shan (Figure 13) suggests an external control on stream gradient, independent of lithology and drainage area (and, therefore, sediment flux). Geologic evidence for rapid rock uplift localized within the Min Shan (Kirby et al., 2000) points to a tectonic control on profile steepness.

Figure 14 schematically illustrates the spatial distribution of rock uplift that we infer from the distribution of profile steepness. Given the lack of well-constrained local calibration of the stream power incision model, we cannot determine rock uplift rates quantitatively (e.g., Kirby and Whipple, in review). Limited estimates of incision rates from fluvial terraces are presented in the next section. However, the spatial distribution of active rock uplift is in itself an important geodynamic quantity, particularly in a region with no resolvable upper crustal shortening.

Adjacent to the Sichuan Basin, the zone of high rock uplift appears to be distributed over a region ~50-70 km wide parallel to the margin, while north of the basin, high rock uplift is apparently localized within a narrow region along the eastern Min Shan. North of the range itself, the region of highest gradient becomes more diffuse, and the k_s values decrease somewhat (Figure 10). Rock uplift appears to be progressively

distributed over a wider region north of ~33°N. Note that we have no information regarding the extent of the region of high rock uplift west of the Qing Jiang headwaters.

In our interpretation, the relatively high concavity of channel profiles along the eastern flank of the Min Shan and the low concavity of the Min and Baishui systems reflect changing channel gradient in response to these spatial variations in rock uplift rate along the plateau margin (e.g., Kirby and Whipple, in review). The slight break in gradient-area arrays observed along tributaries of the Jin Jiang (e.g. Figure 5c) may reflect somewhat more uniform uplift rates in the central Min Shan, but in general the high concavity of these systems likely reflects rock uplift rates that are decreasing from the range toward the Sichuan Basin. Note that several N-S tributaries in the region east of the Min Shan have concavities very near 0.4 (e.g. channels # 95, 99, 104, 107 - Table 1), consistent with the presence of E-W gradients in rock uplift. In a similar fashion, the gradual increase in gradient (manifest as low concavity) along the Hei Shui He, Min Jiang, and Baishui Jiang apparently reflect a relative steepening of these channels as they cross into this region of high rock uplift along the topographic front.

The high concavity of small tributaries along the western flank of the Min Shan is consistent with this interpretation. In a study of remnant Pleistocene basins in the same region, Kirby et al. (2000) documented rapid, west-directed tilting along the western range flank. Rock uplift rates (relative to the plateau) inferred from the tilted basins range from ~2mm/yr at the foot of the range to ~8-10 mm/yr near the range crest. Thus, the high concavity of channels (Θ – 0.50 - 0.79) in this portion of the range (channels 52-55, Table 1, Figure 3) apparently reflects these gradients in rock uplift and lends additional strength to our argument that rock uplift rate exerts a first-order control on channel gradients in this landscape.

Incision Rates in the Min Shan

To this point, we have been concerned primarily with the interpretation of *relative* changes in channel gradient and their spatial distribution. Although a detailed investigation of the rates of channel incision throughout this landscape is far beyond the scope of this study, we attempt a preliminary assessment of incision rates utilizing well-preserved fluvial terraces along two rivers draining the eastern flank of the Min Shan.

We collected detrital charcoal from sandy lenses within gravel treads atop two strath terraces along the Jin Jiang (Figure 14), and we collected a sample of fine overbank silts for optically stimulated luminescence (OSL) dating (e.g., Aitken, 1998) from a strath terrace along the Fu Jiang (Figure 14). Radiocarbon analytical data is given in Table 2 and OSL data in Table 3 (for a detailed discussion of OSL sampling techniques and analytical procedures for this sample see Kirby et al., 2000).

For each sample locality, we assume that the age of the gravel tread atop the bedrock strath surface was abandoned shortly after deposition, such that the age provides a minimum estimate of incision rate. Incision rates are calculated using the relative height of the strath surface above the modern channel (i.e. incision through the gravel tread is assumed to be instantaneous). Incision rates vary from 1-3 mm/yr along the Jin Jiang to ~0.4 mm/yr along the Fu Jiang (Table 4).

Although the data are limited, the spatial distribution of incision rate is consistent with our inference of spatial gradients in rock uplift rate east of the Min Shan (Figure 14). For example, samples 97-13 and 98-3 are separated by only ~15 km, yet yield incision rates that vary by a factor of three (Table 4). Importantly, the higher incision rate (97-13) is located upstream of a major tributary (Figure 14) and has less than half the drainage area as the downstream locality. Thus, the higher incision rate cannot be associated with increasing discharge downstream, and likely reflects the rapidly increasing channel gradient toward the crest of the Min Shan. In so far as incision rates reflect the underlying rock uplift rates this relationship suggests that rock uplift also increases toward the Min Shan. Incision rates estimated along the Fu Jiang (sample 98-1; Figure 14) are somewhat lower and are consistent with decreasing rock uplift toward the foreland region east of the range.

Additional evidence for spatial gradients in rock uplift across the eastern Min Shan comes from the spatial distribution of terrace elevations (e.g., Merritts et al., 1994; Pazzaglia et al., 1998). Along a major tributary of the Jin, an active, high-flow strath terrace at the town of Zicheng (Figure 14) smoothly diverges to nearly 25 m above the channel bed ~10 km upstream (Figure 15). Although we were unable to obtain datable material from this terrace, the pattern of terrace divergence is consistent with increasing

rock uplift toward the Min Shan, and suggests that the age of terrace abandonment may be markedly diachronous in portions of this landscape (e.g., Weldon, 1986).

Discussion

Relationship of Stream Profiles to Active Faults

Although there is a general correspondence between the zone of highest rock uplift and active faults in the region (Figure 14), one of the most interesting results of this study is that we observe little direct influence of active faults on channel profiles. For example, in the eastern Min Shan, two tributaries of the upper Fu Jiang cross the Huya fault with no significant disruption of channel profiles (Figure 11, Figure 12). The Huya fault is a steeply west-dipping reverse fault (Chen et al., 1994b) and is known to be active from a series of seismic events in 1976 (Jones et al., 1984). Both channels are steeper to the west, in the hanging wall of the fault, but there is no discrete increase in stream gradient (see inset) as would be expected for a discrete increase in rock uplift rate across the fault. Rather, the increase in gradient appears to be distributed across a region some 20-30 km wide along the eastern flank of the Min Shan.

The Wenchuan-Maowen fault zone presents an interesting case. In a similar fashion to faults in the eastern Min Shan, channel steepness indices on either side of the Wenchuan-Maowen fault are remarkably similar (Figure 11) and may suggest similar long-term rates of rock uplift. However, the Min Jiang displays a pronounced increase in gradient as it crosses east of the fault zone. As noted above, we cannot readily separate the lithologic and tectonic contributions to this increase in gradient. As evidence for recent activity on this structure is equivocal (c.f., Chen et al., 1994b; Burchfiel et al., 1995), we can only suggest that the fault may be active. In either case, rock uplift appears to be highest east of the fault zone, near the topographic front of the margin.

We also observe distinct changes in channel steepness along the southeast side of the Pengguan massif. Streams draining the Pengguan Massif are quite steep west of the Yingxiuwan-Beichuan fault and maintain low gradients to the east (Figure 11). However, the fault also marks a pronounced lithologic transition from crystalline rocks to Triassic sediments, and the relative role of rock competence is unclear. Given the transition to depositional conditions in the adjacent Sichuan Basin, it seems likely that rock uplift

gradients in this region must be steep, and would be best accommodated by a discrete structure. Thus, we consider the Yingxiuwan-Beichuan fault a likely candidate to be active.

Deformation in the eastern Min Shan

The region of high rock uplift inferred from steepness indices in the Min Shan generally coincides with a series of high-angle, discontinuous faults along the eastern side of the range (Figure 14), of which the Huya is the most prominent. Although none of these structures link together, they apparently form a right-stepping, en echelon array that may accommodate some of the high rock uplift within the range. The northernmost mapped structure in the Min Shan, the Tazang fault, is a relatively continuous structure considered by Chinese workers to be active in the Pleistocene, possibly with left-lateral displacement (Tang et al., 1993). In our study, the Tazang fault appears to coincide with a transition to lower stream gradients and more subdued topography north of the Min Shan (Figure 14), and is inferred to mark a discontinuity in rock uplift. It is possible that left lateral displacement on the Tazang fault is transferred to shortening within and along the eastern flank of the Min Shan.

The lack of geodetically resolvable shortening across the Min Shan (King et al., 1997; Chen et al., 2000), however, suggests that strain accumulation in the upper crust is quite slow. Although the detailed paleoseismic histories of structures in the eastern Min Shan are unknown, the Chinese historic record suggests that recurrence intervals of large (>M 5) events in this region is fairly long (Editoral Board, 1989). Thus, the presence of active rock uplift within the Min Shan (see also, Kirby et al., 2000) poses a geodynamic problem in the manner by which rock uplift is accommodated along the eastern range flank. Indeed, the high concavity of channel profiles draining the eastern range flank suggest that the transition from high rock uplift within the range to low rock uplift at the margin of the Sichuan Basin is distributed over a zone some 20 – 40 km wide. Although the en echelon array of faults is spatially associated with this transition (Figure 14), the faults do not appear to mark an abrupt transition in rock uplift rates along the eastern range front. Thus, although strain localized on discrete structures clearly plays an important role in the distribution of active rock uplift in the Min Shan, a significant

portion of deformation may be accommodated by distributed tilting and/or pervasive shear of the crust.

Detachment Versus Transport Limited Conditions

The lack of a direct correlation between channel gradients and mapped lithologic changes and between channel gradients and active faults raises the possibility that many of these channels are transport-limited. That is, their gradients may be set by the need to transport sediment supplied from upstream (Tucker and Slingerland, 1996). Under these conditions, discrete variations in rock uplift and/or rock resistance may be smeared out along the channel, as the gradient responds to changing sediment input downstream. While we cannot confidently rule out this possibility, we note that geologic evidence for distributed rock uplift in the western (Kirby et al., 2000) and eastern Min Shan (Figure 15) suggests the presence of spatial gradients in rock uplift within the region. As changes in transport-limited channel gradient still reflect spatial variations in rock uplift, provided the systems are near steady-state (Willgoose, 1994), we conclude that our inference of spatial variations in rock uplift is robust. However, we do caution that the distribution of rock uplift portrayed in Figure 14 should be considered a schematic representation.

Tectonic Implications

Active rock uplift in the absence of significant upper crustal shortening is consistent with a model of deformation driven by thickening and flow within a weak lower crust (Royden et al., 1997). The coincidence of the zone of high inferred rock uplift with the topographic front of the plateau suggests that such thickening may be focused at the present topographic margin. Thus, the high topography along the margin may be a direct reflection of this process. Furthermore, the general association of active faults with the zone of highest inferred rock uplift corroborates the inference that active displacement on faults in this region is a relatively passive response to crustal thickening and that these structures do not directly control the distribution of rock uplift in this region (Royden et al., 1997). Indeed, the presence of spatial gradients in rock uplift rate east of the Min Shan suggests that deformation of the upper crust may be distributed over a region ~30-50 km wide. Enhanced resolution of these gradients would provide

important constraints on the nature of upper crustal deformation in response to lower crustal thickening. We see this as strong motivation for high-resolution geodetic studies across this range.

The distribution of rock uplift inferred from stream gradients also coincides roughly with the distribution of late Cenozoic denudation inferred from thermochronology (Kirby et al., in review). The zone of highest stream gradients along the margin of the plateau coincides with a region of late Miocene rapid cooling, while lower gradients on the plateau to the west coincide with older ages and slower cooling rates. The spatial association of high rock uplift and long-term denudation speaks to an interesting coupling between stream gradients and tectonic mass flux in this region. It is possible that material flux has been focused at the present-day margin of the plateau since the Late Miocene. If so, perhaps the anisotropy of the Sichuan Basin helps to maintain a steep topographic gradient (e.g., Clark and Royden, 2000) that in turn enhances fluvial erosion, localizing mass flux and rock uplift (e.g., Willett, 1999).

Conclusions

Analysis of stream profiles along the eastern margin of the Tibetan Plateau adjacent to and north of the Sichuan Basin reveals a systematic geographic distribution of channel steepness. Highest steepness indices (k_s) are spatially associated with the topographic margin of the plateau and occur in a zone ~50-60 km wide adjacent to the Sichuan Basin. North of the basin, steep channels are restricted to a 20-30 km wide band along the crest of the Min Shan. Channel profile concavity throughout the region appears to be directly related to this zone of high steepness index. Channels that flow from the plateau into the zone display low concavities that reflect a relative downstream increase in gradient. This steepening appears to be independent of channel drainage area. Channels that have their headwaters in the zone of high gradient display markedly higher concavities that reflect a relatively rapid downstream decrease in gradient. Small tributaries throughout much of the region have concavities within the range expected for channels experiencing uniform rock uplift and erosive power (Whipple and Tucker, 1999a). The region of high stream gradients is spatially associated with the highest topography along the plateau margin, reinforcing suggestions that the bedrock channel

network sets much of the relief structure of tectonically active landscapes (Whipple et al., 1999).

Throughout the study area we see little systematic correlation of stream gradient with lithologic variations. The effect of resistant lithology appears to be restricted to local increases in gradient associated with particularly massive, unjointed rocks. Likewise, we see no consistent relation between the channel steepness index (k_s) and drainage area, as might be expected if sediment flux were a controlling factor (e.g., Sklar and Dietrich, 1998). Thus, regional differences in channel steepness index point to an external control on channel gradient that we interpret as a region of active rock uplift along the plateau margin.

The presence of active rock uplift along this margin is remarkable, given the distinct lack of upper crustal shortening between the plateau and the Sichuan basin (Burchfiel et al., 1995; Chen et al., 2000). Although we observe a general association between active faults and the region of high stream gradients, mapped structures do not seem to exert a direct control on the distribution of rock uplift along this margin of the plateau. Indeed, in the eastern Min Shan, the high concavity of channels seems to indicate the presence of distributed spatial gradients in rock uplift rate. Distributed rock uplift in this region is consistent with preliminary determinations of incision rate from fluvial terraces, and suggests the possibility that rock uplift in this region may be a combined isostatic and dynamic response to flow in the lower crust (e.g., Royden et al., 1997).

Figure Captions

Figure 1. Topography of the eastern margin of the Tibetan Plateau adjacent to and north of the Sichuan Basin (inset shows location). Major channels draining the eastern margin are shown in black. Major faults are shown in red (W - Wenchuan–Maowen fault zone, G - Guanxian-Anxian fault zone, H – Huya fault, M – Min Jiang fault zone, Y – Yingxiuwan-Beichuan fault system), while those in gray (near Beichuan) are known to be Mesozoic in age. City abbreviations (in white)are as follows: B – Beichuan, C – Chengdu, L – Lushan, M – Maowen, P – Pingwu, T – Tianquan, W – Wenchuan, Y – Yingxiuwan, Z - Zicheng.

Figure 2. Photographs of channel bed morphology. A) Trunk stream of the Jin Jiang, approximately 50 km above Beichuan (Figure 1). Note bedrock exposed in channel bottom and along both banks. A thin veneer of cobbles and boulders mantles the high-flow channel bed (at right). Channel is approximately 5 m wide. B) Small tributary of Jin Jiang approximately 90 km above Beichuan. Channel is 3 m wide, and bed is mantled with cobbles and boulders throughout. C.) Tributary of Min Jiang, just upstream of Yingxiuwan (Y – Figure 1). Boulders up to 6 m in median diameter cover bed.

Figure 3. Index map of channels utilized in this study. Numbers are keyed to Table 1, and are located near the headwaters of the channel (with the exception of 80-88, along the front of the Pengguan Massif). The background is a shaded relief image of the region. Illumination is from the west-northwest. White squares highlight gaps in the digital elevation data (here filled with GTOPO30, 1 km resolution data).

Figure 4. Comparison of longitudinal profiles extracted from digital elevation model (gray) and field surveys (black).

Figure 5. Channel profiles and gradient-area data for selected channels in eastern Tibet. For each, raw elevation data along the channel profile is shown in gray, while the smoothed and despiked data is shown in black. Gradients were calculated on a 10m

vertical interval (see text for details) and are plotted against upstream area for each channel (inset figures). Linear regressions of slope-area data are shown as black lines, while regression with fixed concavity (Θ=0.4) are shown as dashed lines. Arrows above the longitudinal profiles designate the region of channel elevations represented by the regression. Channel profiles are representative of a.) typical concavity (Qingyi Jiang – channel #12, Figure 3), b.) low concavity (Hei Shui He/Min Jiang – channel # 35, Figure 3), and c.) high concavity (Fu Jiang – channel #101, Figure 3). Note that in (a), channel regression was truncated at margin of Sichuan Basin. Concavity index is slightly higher (~0.5) if regression includes all data. Also note in (c) how smoothed profile fits minima in a region of poor data quality. Key structures, geologic features and major tributary junctions are shown for reference to the longitudinal profiles.

Figure 6. Map of concavity indices (Θ) determined for channels in eastern Tibet. Background is shaded relief image of the region illuminated from the west-northwest. White squares represent regions of gaps in data coverage (as per Figure 3). The approximate position of the drainage divide is shown as a heavy dashed line.

Figure 7. Methods of normalizing channel gradient in eastern Tibet. A) Steepness index (k_s) calculated for a fixed concavity (Θ=0.4) plotted against the concavity of the profile (Θ). B) Comparison of representative slope (S_r) and steepness index(k_s) methods of determining relative channel steepness.

Figure 8. Gradient-area plot (data from Fu Jiang – channel # 101, Figure 3) showing the relationship of k_s values to the concavity of channel profiles. Note that high concavity of downstream reach reflects rapidly changing channel gradients between k_s values of ~100 and ~20, while the 'typical' concavity of the upstream reach has a k_s of ~130.

Figure 9. Map of steepness indices (k_s) determined for channels in eastern Tibet. Background as in Figure 3. Heavy dashed line represents the approximate position of the drainage divide.

Figure 10. Photographs of variations in channel incision and local relief along the Hei Shui He/Min Jiang drainage. A) Looking downstream along the lower Min Jiang (near Wenchuan – Figure 1). Strath terrace in midground is ~30 m above river level and is cut in Carboniferous limestone. Note impressive valley wall in background. Local relief along this stretch of river ranges from 3-4 km. B) Looking upstream along the upper reach of the Hei Shui He. Note alluviated bed and lack of bedrock outcrop in bed and banks. Rapid is formed from a constriction at the terminus of a tributary alluvial fan (at left in midground). Local relief is ~500m along this stretch.

Figure 11. Comparison of channel steepness to lithologic variability in eastern Tibet. Geology was digitized from 1:200,000 Chinese geologic maps (Ministry of Geology and Mineral Resources, 1991) and updated from Burchfiel et al. (1995) and Kirby et al. (2000). White arrows highlight regions of distinct lithologic control of channel gradients discussed in text. L – Longquan anticline. Heavy dashed line represents the position of the drainage divide.

Figure 12. Selected examples of lithologic influence on channel gradient. Data are presented as in Figure 5. Grey band represents extent of resistant bedrock. A.) Trunk stream of Fu Jiang. Knickzone corresponds with rib of Pennsylvanian-Permian limestone. Note that profile smoothly crosses Huya fault. B.) Trunk stream of Hei Shui He. Knickzone corresponds with Mesozoic pluton, and imparts a high concavity to the reach immediately downstream of granite.

Figure 13. Comparison of gradient-area relationships for three drainages considered representative of regional variations in concavity. Note that the Hei Shui He/Min Jiang system displays a systematic relative increase in gradient at ~10^8 m^2, while the Jin Jiang continues to decrease in gradient at the same drainage area suggesting that regional differences in concavity are not related to downstream changes in sediment flux (i.e. Sklar and Dietrich, 1998). Gradients in the headwater reaches of the Jin Jiang are similar to those along small tributaries of the lower Min Jiang, and suggest an tectonic control on channel gradient.

Figure 14. Schematic representation of the distribution of rock uplift inferred from channel profile steepness and its relationship to major structures in the region. Sample localities for incision rates are shown as black dots. The position of the drainage divide is shown for reference as a heavy dashed line. Abbreviations are as follows: Y-B – Yingxiuwan-Beichuan fault zone, H – Huya fault, M – Min Jiang fault zone, T – Tazang fault, W-M – Wenchuan-Maowen fault zone.

Figure 15. Surveyed elevations of continuous strath terrace along tributary of the Jin Jiang near Zicheng (channel #89, Figure 3). Divergence of terrace from channel bed is suggestive of increasing rock uplift toward the Min Shan range crest.

References Cited

Aitken, M.J., 1998, An Introduction to Optical Dating: New York, Oxford University Press, 267 p.

Avouac, J.P., and Tapponnier, P., 1993, Kinematic model of active deformation in Central Asia: Geophysical Research Letters, v. 20, p. 895-898.

Beaumont, C., Fullsack, P., and Hamilton, J., 1992, Erosional control of active compressional orogens, *in* McClay, K.R., ed., Thrust Tectonics: London, Chapman and Hall, p. 1-18.

Bilham, R., Larson, K., and Freymueller, J., 1997, GPS measurements of present-day convergence across the Nepal Himalaya: Nature, v. 386, p. 61-63.

Brocklehurst, S.H., and Whipple, K.X., 1999, Relief production on the eastern side of the Sierra Nevada, California: EOS, Trans. AGU, v. 80, p. F442.

Burchfiel, B.C., Chen, Z., Liu, Y., and Royden, L.H., 1995, Tectonics of the Longmen Shan and adjacent regions: International Geology Review, v. 37, p. 661-735.

Chen, S., Wilson, C.J.L., Luo, Z., and Deng, Q., 1994a, The evolution of the western Sichuan foreland basin, southwestern China: Journal of SE Asian Earth Science, v. 10; p. 159-168.

Chen, S.F., and Wilson, C.J.L., 1996, Emplacement of the Longmen Shan Thrust-Nappe Belt along the eastern margin of the Tibetan Plateau: Journal of Structural Geology, v. 18, p. 413-430.

Chen, S.F., Wilson, C.J.L., Deng, Q.D., Zhao, X.L., and Luo, Z.L., 1994b, Active faulting and block movement associated with large earthquakes in the Min Shan and Longmen mountains, northeastern Tibetan Plateau: Journal of Geophysical Research, v. 99, p. 24,025-24,038.

Chen, Z., Burchfiel, B.C., Liu, Y., King, R.W., Royden, L.H., Tang, W., Wang, E., Zhao, J., and Zhang, X., 2000, GPS measurements from eastern Tibet and their implications for India/Eurasia intracontinental deformation: Journal of Geophysical Research, v. 105, p. 16215-16227.

Clark, M.K., and Royden, L.H., 2000, Topographic ooze: Building the eastern margin of Tibet by lower crustal flow: Geology, v. 28, p. 703-706.

Dirks, P., Wilson, C.J.L., Chen, S., Lou, Z., and Liu, S., 1994, Tectonic evolution of the NE margin of the Tibetan Plateau: evidence from the central Longmen Mountains, Sichuan Province, China: Journal of SE Asian Earth Science, v. 9, p. 181-192.

Editoral Board, S.S.B., 1989, Lithospheric dynamics atlas of China: Beijing, China Cartographic Publishing House.

Fielding, E.J., Isacks, B.L., Barazangi, M., and Duncan, C., 1994, How flat is Tibet?: Geology, v. 22, p. 163-167.

Flint, J.J., 1974, Stream gradient as a function of order, magnitude, and discharge: Water Resources Research, v. 10, p. 969-973.

Gilchrist, A.R., Kooi, H., and Beaumont, C., 1994, Post-Gondwana geomorphic evolution of southwestern Africa: Implications for the controls on landscape development from observations and numerical experiments: Journal of Geophysical Research, v. 99, p. 12211-12228.

Hack, J.T., 1957, Studies of longitudinal stream profiles in Virginia and Maryland, U.S. Geological Survey Professional Paper 294-B, p. 45-97.

Hack, J.T., 1973, Stream profile analysis and stream-gradient index: J. Res. U.S. Geol. Surv., v. 1, p. 421-429.
Hoffman, P.F., and Grotzinger, J.P., 1993, Orographic precipitation, erosional unloading, and tectonic style: Geology, v. 21, p. 195-198.
Howard, A.D., 1994, A detachment-limited model of drainage basin evolution: Water Resources Research, v. 30, p. 2261-2285.
Howard, A.D., 1998, Long profile development of bedrock channels: Interaction of weathering, mass wasting, bed erosion, and sediment transport, *in* Tinkler, K.J., and Wohl, E.E., eds., Rivers Over Rock: Fluvial Processes in Bedrock Channels, Volume 107: Geophysical Monograph: Washington, D.C., American Geophysical Union.
Howard, A.D., and Kerby, G., 1983, Channel changes in badlands: Geological Society of America Bulletin, v. 94, p. 739-752.
Howard, A.D., Seidl, M.A., and Dietrich, W.E., 1994, Modeling fluvial erosion on regional to continental scales: Journal of Geophysical Research, v. 99, p. 13,971-13,986.
Jackson, M., and Bilham, R., 1994, Constraints on Himalayan deformation inferred from vertical velocity fields in Nepal and Tibet: Journal of Geophysical Research, v. 99, p. 13,897-13,912.
Jones, L.M., Han, W., Hauksson, E., Jin, A., Zhang, Y., and Luo, Z., 1984, Focal mechanisms of the Songpan earthquakes of August 1976 in Sichuan, China: Journal of Geophysical Research, v. 89, p. 7697-7707.
King, R.W., Shen, F., Burchfiel, B.C., Royden, L.H., Wang, E., Chen, Z., Liu, Y., Zhang, X., Zhao, J., and Li, Y., 1997, Geodetic measurement of crustal motion in southwest China: Geology, v. 25, p. 179-182.
Kirby, E., Reiners, P., Krol, M., Hodges, K., Whipple, K., Farley, K., Tang, W., and Chen, Z., in review, Late Cenozoic uplift and landscape evolution along the eastern margin of the Tibetan Plateau: Inferences from 40Ar/39Ar and (U-Th)/He thermochronology: Tectonics.
Kirby, E., and Whipple, K., in review, The effect of spatially variable rock uplift on river profile concavity: A new tool for neotectonic analysis of topography: Geology.
Kirby, E., Whipple, K.X., Burchfiel, B.C., Tang, W., Berger, G., Sun, Z., and Chen, Z., 2000, Neotectonics of the Min Shan, China: Implications for mechanisms driving Quaternary deformation along the eastern margin of the Tibetan Plateau: Geological Society of America Bulletin, v. 112, p. 375-393.
Kooi, H., and Beaumont, C., 1994, Escarpment evolution on high-elevation rifted margins: Insights derived from a surface processes model that combines diffusion, advection, and reaction: Journal of Geophysical Research, v. 99, p. 12,191-12,209.
Korzoun, V.I., 1977, Atlas of world water balance: Paris, UNESCO Press.
Lave, J., and Avouac, J.P., 2000, Active folding of fluvial terraces across the Siwalik Hills, Himalayas of central Nepal: Journal of Geophysical Research, v. 105, p. 5735-5770.
Massong, T.M., and Montgomery, D.R., 2000, Influence of sediment supply, lithology, and wood debris on the distribution of bedrock and alluvial channels: Geological Society of America Bulletin, v. 112, p. 591-599.

Merritts, D.J., Vincent, K.R., and Wohl, E.E., 1994, Long river profiles, tectonism, and eustasy: A guide to interpreting fluvial terraces: Journal of Geophysical Research, v. 99, p. 14031-14050.

Miller, J.R., 1991, The influence of bedrock geology on knickpoint development and channel-bed degradation along downcutting streams in south-central Indiana: Journal of Geology, v. 99, p. 591-605.

Moglen, G.E., and Bras, R.L., 1995, The effect of spatial heterogeneities on geomorphic expression in a model of basin evolution: Water Resources Research, v. 31, p. 2613-2623.

Molnar, P., 1987, Inversion of profiles of uplift rates for the geometry of dip-slip faults at depth, with examples from the Alps and Himalaya: Annales Geophysicae, v. 5B, p. 663-670.

Molnar, P., and England, P., 1990, Late Cenozoic uplift of mountain ranges and global climate change: chicken or egg?: Nature, v. 346, p. 29-34.

Montgomery, D.R., and Buffington, J.M., 1997, Channel-reach morphology in mountain drainage basins: Geological Society of America Bulletin, v. 109, p. 596-611.

Montgomery, D.R., and Foufoula-Georgiou, E., 1993, Channel network source representation using digital elevation models: Water Resources Research, v. 29, p. 1178-1191.

Pazzaglia, F.J., Gardner, T.W., and Merritts, D.J., 1998, Bedrock fluvial incision and longitudinal profile development over geologic time scales determined by fluvial terraces, *in* Tinkler, K.J., and Wohl, E.E., eds., Rivers Over Rock: Fluvial Processes in Bedrock Channels, Volume 107: Geophysical Monograph: Washington, D.C., American Geophysical Union.

Royden, L.H., Burchfiel, B.C., King, R.W., Chen, Z., Shen, F., and Liu, Y., 1997, Surface deformation and lower crustal flow in Eastern Tibet: Science, v. 276, p. 788-790.

Seeber, L., and Gornitz, V., 1983, River profiles along the Himalayan Arc as indicators of active tectonics: Tectonophysics, v. 92, p. 335-367.

Seidl, M.A., and Dietrich, W.E., 1992, The problem of channel erosion into bedrock: Catena Supplement, v. 23, p. 101-124.

Seidl, M.A., Weissel, J.K., and Pratson, L.F., 1996, The kinematics and pattern of escarpment retreat across the rifted continental margin of SE Australia: Basin Research, v. 12, p. 301-316.

Sklar, L., and Dietrich, W.E., 1997, The influence of downstream variations in sediment supply and transport capacity on bedrock channel longitudinal profiles: EOS, Trans. AGU, v. 78, p. F299.

Sklar, L., and Dietrich, W.E., 1998, River longitudinal profiles and bedrock incision models: Stream power and the influence of sediment supply, *in* Tinkler, K.J., and Wohl, E.E., eds., Rivers over rock: fluvial processes in bedrock channels: Geophysical Monograph 107: Washington, DC, American Geophysical Union, p. 237-260.

Sklar, L., and Dietrick, W.E., 1999, Relating rates of fluvial bedrock erosion to rock strength: An experimental study: EOS, Trans. AGU, v. 80, p. F448.

Slingerland, R., Willet, S.D., and Hennessey, H.L., 1997, A new fluvial bedrock erosion model based on the work-energy principle: EOS, Trans. AGU, v. 78, p. F299.

Snyder, N.P., Whipple, K.X., Tucker, G.E., and Merritts, D.J., 1999, Evidence for an equilibrium between main-trunk channel incision and tectonic uplift: Mendocino Triple Junction region, Northern California: GSA Abstracts with Programs, v. 31, p. A444.

Snyder, N.P., Whipple, K.X., Tucker, G.E., and Merritts, D.J., 2000, Landscape response to tectonic forcing: Digital elevation model analysis of stream profiles in the Mendocino triple junction region, northern California: Geological Society of America Bulletin, v. 112, p. 1250-1263.

Stock, J.D., and Montgomery, D.R., 1999, Geologic constraints on bedrock river incision using the stream power law: Journal of Geophysical Research, v. 104, p. 4983-4993.

Tang, R., Wen, D., Huang, Z., Wu, X., Lin, W., Chen, G., and Wu, G., 1993, The Quaternary activity characteristics of several major active fault zones in the Songpan-Longmenshan region: Earthquake Research in China, v. 7, p. 341-350.

Tarboton, D.G., Bras, R.L., and Rodriguez-Iturbe, I., 1989, Scaling and elevation in river networks: Water Resources Research, v. 25, p. 2037-2051.

Tucker, G.E., and Bras, R.L., 2000, A stochastic approach to modeling the role of rainfall variability in drainage basin evolution: Water Resources Research, v. 36, p. 1953-1964.

Tucker, G.E., Lancaster, S.T., Gasparini, N.M., and Bras, R.L., in review, The channel-hillslope integrated landscape development (CHILD) model, *in* Harmon, R.S., and Doe, W.W., eds., Landscape Erosion and Sedimentation Modeling, Kluwer Press.

Tucker, G.E., and Slingerland, R., 1996, Predicting sediment flux from fold and thrust belts: Basin Research, v. 8, p. 329-349.

Tucker, G.E., and Slingerland, R.L., 1994, Erosional dynamics, flexural isostacy, and long-lived escarpments: a numerical modeling study: Journal of Geophysical Research, v. 99, p. 12,229-12,243.

Weissel, J.K., and Seidl, M.A., 1998, Inland propagation of erosional escarpments and river profile evolution across the southeast Australian passive continental margin, *in* Tinkler, K.J., and Wohl, E.E., eds., Rivers Over Rock: Fluvial Processes in Bedrock Channels, Volume 107: Geophysical Monograph: Washington, D.C., American Geophysical Union.

Weldon, R.J., 1986, The late Cenozoic geology of Cajon Pass: Implications for tectonics and sedimentation along the San Andreas Fault [doctoral thesis]: Pasadena, Caltech.

Whipple, K.X., Hancock, G.S., and Anderson, R.S., 2000a, River incision into bedrock: Mechanics and relative efficacy of plucking, abrasion, and cavitation: Geologic Society of America Bulletin, v. 112, p. 490-503.

Whipple, K.X., Kirby, E., and Brocklehurst, S.H., 1999, Geomorphic limits to climate-induced increases in topographic relief: Nature, v. 401, p. 39-43.

Whipple, K.X., Snyder, N.P., and Dollenmayer, K., 2000b, Rates and processes of bedrock incision by the Upper Ukak River since the 1912 Novarupta ash flow in the Valley of Ten Thousand Smokes, Alaska: Geology, v. 28, p. 835-838.

Whipple, K.X., and Tucker, G.E., 1999a, Dynamics of the stream-power river incision model: Implications for height limits of mountain ranges, landscape response timescales, and research needs: Journal of Geophysical Research, v. 104, p. 17,661-17,674.

Whipple, K.X., and Tucker, G.E., 1999b, "Mixed" bedrock-alluvial channels: Detachment-limited or tansport-limited?: EOS, Trans. AGU, v. 80, p. F473.
Willett, S.D., 1999, Orogeny and orography: the effects of erosion on the structure of mountain belts: Journal of Geophysical Research, v. 104, p. 28,957-28,981.
Willgoose, G., 1994, A physical explanation for an observed-slope-elevation relationship for catchments with declining relief: Water Resources Research, v. 30, p. 151-159.
Wohl, E.E., 1998, Bedrock channel morphology in relation to erosional processes, *in* Tinkler, K.J., and Wohl, E.E., eds., Rivers Over Rock: Fluvial Processes in Bedrock Channels, Volume 107: Geophysical Monograph: Washington, D.C., American Geophysical Union.
Zeitler, P.K., 1985, Cooling history of the NW Himalaya, Pakistan: Tectonics, v. 4, p. 127-151.
Zhao, C., Xu, R., and Wang, S., 1997, The special long reversed river section in the Yangtze River reaches: Geology and Mineral Resources of South China, v. 3, p. 33-38.

Table 1 - Kirby et al.: Topographic parameters for rivers in the Longmen Shan region

Principal Channel	A_{min} (m^2)	A_{max} (m^2)	$\Theta \pm 2\sigma$	S_r ($A_r = 10^8$ m^2)	k_s ($\Theta = 0.4$)	Comments
Qing Jiang - upstream of Tianquan						
1	1×10^7	5×10^8	0.43 ± 0.04	0.063	97	
2	1×10^7	4×10^8	0.38 ± 0.03	0.052	89	
3	5×10^6	5×10^8	0.47 ± 0.03	0.086	142	
4	2×10^7	7×10^8	0.46 ± 0.04	0.061	102	
5	1×10^7	1×10^9	0.47 ± 0.03	0.044	64	
6	1×10^7	1×10^9	0.51 ± 0.04	0.058	97	
7	2×10^7	2×10^8	0.50 ± 0.05	0.052	95	
8	3×10^6	2×10^8	0.43 ± 0.03	0.058	92	
9	1×10^6	1×10^8	0.36 ± 0.03	0.032	48	
mean			***0.45 ± 0.05***		***92***	
Qingyi Jiang - upstream of Lushan						
10	1×10^7	5×10^8	0.43 ± 0.03	0.053	85	upper reach
10	8×10^8	3×10^9	$0.83 \pm 0.11^{\dagger}$	n.c.	92	lower reach
11	1×10^7	5×10^8	0.40 ± 0.03	0.048	77	
12	1×10^7	5×10^8	0.43 ± 0.03	0.059	104	
13	1×10^7	5×10^8	0.45 ± 0.03	0.068	100	
14	1×10^7	5×10^8	0.46 ± 0.03	0.057	101	
15	3×10^6	3×10^7	0.45 ± 0.09	n.c.	78	
mean			***0.44 ± 0.03***		***91***	
Yingxiuwan - upstream of Yingxiuwan						
	1×10^7	1×10^9	0.35 ± 0.02	0.068	117	glacial headwaters
16	2×10^8	2×10^9	0.47 ± 0.08	0.087	127	
	1×10^7	1×10^9	0.39 ± 0.02	0.088	129	glacial headwaters
mean			***0.40 ± 0.06***		***124***	
Unnamed tributary of Min Jiang - between Yingxiuwan and Wenchuan						
17	1×10^7	6×10^8	0.44 ± 0.02	0.059	100	
Tsakahao He - upstream of Wenchuan						
18	4×10^6	2×10^{10}	$0.28 \pm 0.02^{\dagger}$	0.035	68	includes Min Jiang
18	4×10^6	1×10^{10}	$0.31 \pm 0.03^{\dagger}$	0.040	63	above Wenchuan
18	4×10^6	4×10^8	0.34 ± 0.04	0.032	51	headwater reach
19	3×10^6	3×10^8	0.43 ± 0.04	0.042	64	
20	3×10^6	3×10^8	0.44 ± 0.02	0.043	76	
21	1×10^6	1×10^8	0.34 ± 0.03	0.048	71	
22	2×10^6	2×10^8	0.42 ± 0.06	0.052	78	
23	5×10^6	6×10^7	0.48 ± 0.04	n.c.	135	
24	6×10^6	7×10^7	0.57 ± 0.06	n.c.	115	
25	5×10^6	6×10^7	0.50 ± 0.04	n.c.	133	
26	6×10^6	2×10^8	0.48 ± 0.03	0.076	124	
27	1×10^6	3×10^7	0.35 ± 0.05	n.c.	51	upper reach
27	3×10^7	4×10^8	$0.21 \pm 0.05^{\dagger}$	0.063	92	lower reach
28	1×10^7	3×10^8	$0.43 \pm 0.05^{\dagger}$	0.082	132	stepped profile
29	1×10^7	5×10^7	0.59 ± 0.06	n.c.	149	
30	5×10^6	1×10^8	0.40 ± 0.05	0.062	99	
31	5×10^6	6×10^7	0.33 ± 0.03	n.c.	158	
32	3×10^6	3×10^8	0.29 ± 0.02	0.081	113	
mean			***0.43 ± 0.09***		***101***	
Heishui He - upstream of Maowen						
33	1×10^7	1×10^9	0.25 ± 0.07	0.020	30	upstream of granite
34	1.5×10^9	3×10^9	$2.50 \pm 0.56^{\dagger}$	n.c.	96	granite reach
35	4×10^6	3×10^{10}	$0.33 \pm 0.02^{\dagger}$	0.037	70	includes Min Jiang
35	4×10^6	1×10^{10}	$0.37 \pm 0.03^{\dagger}$	0.039	62	above Maowen
35	4×10^6	2×10^8	0.46 ± 0.03	0.034	59	headwater reach
36	1×10^7	7×10^8	0.48 ± 0.05	0.050	74	
37	1×10^8	5×10^9	$0.40 \pm 0.18^{\dagger}$	0.067	98	stepped profile
38	1×10^7	2×10^8	0.43 ± 0.05	0.052	86	
39	6×10^6	7×10^7	0.45 ± 0.08	n.c.	100	
40	2×10^6	1×10^8	0.39 ± 0.03	0.066	98	
41	8×10^6	1×10^8	0.34 ± 0.06	0.069	102	
42	2×10^7	1×10^9	0.36 ± 0.05	0.036	57	
43	5×10^6	1×10^8	0.50 ± 0.04	0.061	109	
44	1×10^7	1×10^8	0.41 ± 0.08	0.047	77	
45	1×10^7	1×10^8	0.41 ± 0.05	0.077	135	
46	5×10^6	1×10^9	0.36 ± 0.04	0.050	79	
47	5×10^7	1×10^9	$0.73 \pm 0.13^{\dagger}$	0.073	105	stepped profile
48	1×10^7	2×10^8	0.39 ± 0.05	0.076	112	
49	5×10^8	1×10^8	0.54 ± 0.03	0.037	74	southern Min Shan
50	2×10^6	3×10^8	0.57 ± 0.02	0.034	70	southern Min Shan
mean			***0.42 ± 0.08***		***84***	
mean (excludes 49,50)			***0.40 ± 0.07***		***86***	

Table 1 - Kirby et al. (continued)

Principal Channel	A_{min} (m^2)	A_{max} (m^2)	$\Theta \pm 2\sigma$	S_r ($A_r = 10^8$ m^2)	k_s ($\Theta = 0.4$)	Comments
Min Jiang - upstream of Maowen						
51	1×10^6	4.5×10^9	$0.36 \pm 0.02^{\dagger}$	0.025	40	fit above landslide
51	1×10^8	1×10^9	$0.40 \pm 0.02^{\dagger}$	0.023	37	upper reach
52	2×10^6	1×10^8	0.57 ± 0.05	n.c.	44	Zhangla basin
53	5.5×10^6	1×10^8	0.50 ± 0.08	n.c.	48	Zhangla basin
54	7×10^6	1×10^8	0.58 ± 0.06	n.c.	51	Zhangla basin
55	1×10^7	5×10^8	0.68 ± 0.13	0.020	52	Zhangla basin
56	1×10^7	1×10^8	0.79 ± 0.06	n.c.	44	
57	8×10^6	2×10^8	0.63 ± 0.04	0.032	75	
58	1×10^6	5×10^8	0.40 ± 0.02	0.056	92	
59	5×10^6	1×10^8	0.44 ± 0.07	n.c.	80	
60	1×10^8	5×10^7	0.32 ± 0.03	n.c.	59	
mean (52-60)			***0.54 ± 0.14***		***61***	
mean (52-57)			***0.62 ± 0.10***		***52***	
61	5×10^6	3×10^8	0.32 ± 0.06	0.019	30	
62	7×10^6	4×10^8	0.39 ± 0.06	0.024	39	
63	5×10^6	5×10^8	0.27 ± 0.09	0.014	23	
64	4×10^8	1.5×10^8	0.49 ± 0.08	0.040	67	upstream of convexity
64	1.5×10^8	6×10^8	$-0.37 \pm 0.17^{\dagger}$	n.c.	67	convex reach
mean (61-64)			***0.37 ± 0.09***		***40***	
Min Jiang - downstream of Maowen						
65	3×10^6	5×10^7	0.47 ± 0.04	n.c.	98	west of W-M fault
66	2×10^6	4×10^7	0.28 ± 0.05	n.c.	91	west of W-M fault
67	2×10^6	1×10^8	0.24 ± 0.03	0.096	115	west of W-M fault
68	5×10^6	8×10^7	0.53 ± 0.04	n.c.	150	west of W-M fault
69	5×10^6	7×10^7	0.52 ± 0.04	n.c.	140	west of W-M fault
70	1×10^7	2×10^8	0.59 ± 0.03	0.056	102	west of W-M fault
mean (65-70)			***0.43 ± 0.13***		***116***	
71	8×10^6	2×10^7	0.53 ± 0.11	n.c.	174	east of W-M fault
72	1×10^7	7×10^7	0.42 ± 0.05	n.c.	173	east of W-M fault
73	8×10^6	1×10^8	0.33 ± 0.06	0.096	137	east of W-M fault
74	4×10^7	2×10^8	$1.3 \pm 0.15^{\dagger}$	n.c.	129	east of W-M fault
75	5×10^6	1×10^8	0.63 ± 0.04	0.070	150	east of W-M fault
76	5×10^6	5×10^7	0.57 ± 0.06	n.c.	121	Pengguan Massif
77	5×10^6	5×10^7	0.58 ± 0.07	n.c.	122	Pengguan Massif
78	5×10^6	4×10^7	0.45 ± 0.08	n.c.	109	Pengguan Massif
79	1×10^6	4×10^7	0.29 ± 0.03	n.c.	136	Pengguan Massif
mean (71-79)			***0.48 ± 0.12***		***139***	
Pengguan Massif - eastern flank						
80	1×10^7	3×10^8	0.65 ± 0.03	0.055	95	
81	3×10^6	3×10^8	0.61 ± 0.02	0.056	109	
82	1×10^7	7×10^7	0.59 ± 0.05	n.c.	113	
83	1×10^7	1×10^8	0.58 ± 0.04	0.059	119	
84	3×10^6	2×10^7	0.62 ± 0.06	n.c.	111	upper reach
84	3×10^7	3.5×10^8	$0.03 \pm 0.08^{\dagger}$	0.084	134	lower reach
85	5×10^6	1×10^8	0.44 ± 0.05	0.057	95	upper reach
85	1×10^8	3.5×10^8	$0.18 \pm 0.11^{\dagger}$	0.075	135	lower reach
86	5×10^6	3×10^7	0.53 ± 0.07	n.c.	135	upper reach
86	3×10^7	2.5×10^8	$0.28 \pm 0.06^{\dagger}$	0.050	84	lower reach
87	1×10^7	1.5×10^8	0.96 ± 0.06	0.023	62	
88	3×10^7	2×10^8	0.74 ± 0.16	0.020	38	
mean			***0.64 ± 0.14***		***97***	
mean (1-4)			***0.57 ± 0.07***		***111***	
Jin Jiang - southern Min Shan						
89	8×10^6	4×10^9	0.56 ± 0.03	0.045	67	entire profile
89	8×10^6	1×10^8	0.53 ± 0.05	0.044	87	upper reach
89	2×10^8	4×10^9	0.76 ± 0.07	n.c.	58	middle reach
90	1×10^7	4×10^9	0.62 ± 0.02	0.046	71	entire profile
90	1×10^7	1×10^8	0.65 ± 0.04	0.047	98	upper reach
90	2×10^8	4×10^9	0.78 ± 0.08	n.c.	51	middle reach
91	3×10^6	4×10^9	0.60 ± 0.03	0.046	78	entire profile
91	5×10^6	2×10^8	0.39 ± 0.03	0.049	84	upper reach
92	3×10^6	1×10^8	0.56 ± 0.02	0.049	105	upper reach
92	1×10^8	4×10^9	0.78 ± 0.10	n.c.	55	middle reach
93	8×10^6	5×10^8	0.56 ± 0.03	0.044	70	
94	5×10^7	4×10^9	0.62 ± 0.08	0.037	57	survey branch
95	5×10^6	5×10^8	$0.41 \pm 0.07^{\dagger}$	0.025	39	
mean (entire reach)			***0.61 ± 0.05***		***72***	
mean (upper reach)			***0.52 ± 0.09***		***101***	
mean (lower reach)			***0.78 ± 0.05***		***53***	

Table 1 - Kirby et al. (continued)

Principal Channel	A_{min} (m^2)	A_{max} (m^2)	$\Theta \pm 2\sigma$	S_r ($A_r = 10^8$ m^2)	k_s ($\Theta = 0.4$)	Comments
Unnamed tributary of Fu Jiang - eastern Min Shan						
96	1×10^7	1.5×10^9	0.74 ± 0.05	0.025	41	
97	1×10^7	1×10^9	0.74 ± 0.04	0.026	48	
98	1×10^7	1×10^8	0.58 ± 0.05	0.012	29	
98	1×10^8	2×10^8	$-1.60 \pm 0.59^{\dagger}$	n.c.	43	convex reach
99	2×10^8	7×10^7	$0.41 \pm 0.04^{\dagger}$	0.022	39	
mean			***0.69 ± 0.08***		***39***	
Fu Jiang - central Min Shan						
100	5×10^8	3.5×10^8	0.42 ± 0.04	0.041	63	above knickzone
100	3.8×10^8	7×10^8	0.37 ± 0.29	0.105	171	knickzone
100	8×10^8	7×10^9	0.91 ± 0.16	n.c.	42	below knickzone
101	2×10^7	7×10^9	0.70 ± 0.03	0.086	86	entire profile
101	2×10^7	4×10^8	0.45 ± 0.05	0.102	131	upper reach
101	4×10^8	7×10^9	0.81 ± 0.11	n.c.	47	middle reach
102	2×10^7	1×10^8	0.83 ± 0.07	0.039	85	
103	1×10^7	2×10^8	0.48 ± 0.04	0.046	83	
104	1×10^7	5×10^7	1.50 ± 0.17	n.c.	58	upper reach
104	5×10^7	1×10^9	0.43 ± 0.13	0.025	36	lower reach
105	1×10^7	2×10^8	0.56 ± 0.04	0.043	79	
106	1×10^7	5×10^8	0.53 ± 0.05	0.035	61	above knickzone
106	6×10^8	2×10^9	1.40 ± 0.32	n.c.	102	below knickzone
107	1×10^8	5×10^7	0.38 ± 0.04	n.c.	84	upper reach
107	5×10^7	2×10^8	1.20 ± 0.10	0.030	62	lower reach
mean			***n.c.***		***n.c.***	
Baishui Jiang - northern Min Shan						
108	5×10^7	5×10^9	0.13 ± 0.04	0.018	58	upper reach
108	7×10^9	6×10^{10}	0.77 ± 0.34	n.c.	33	lower reach
109	5×10^8	2×10^9	0.32 ± 0.02	0.047	75	
110	1×10^7	7×10^8	0.61 ± 0.06	0.057	74	
111	1×10^7	6×10^8	0.67 ± 0.03	0.005	78	
112	8×10^8	7×10^7	0.40 ± 0.05	n.c.	101	upper reach
112	8×10^7	9×10^8	0.86 ± 0.07	0.046	49	lower reach
113	5×10^8	1×10^9	0.40 ± 0.02	0.037	59	
114	8×10^8	5×10^8	0.56 ± 0.03	0.045	81	
115	1×10^7	5×10^8	0.70 ± 0.04	0.045	69	
116	7×10^8	7×10^8	0.26 ± 0.04	0.017	33	
mean			***n.c.***		***n.c.***	
Bailong Jiang - northern Min Shan						
117	4×10^7	1×10^9	0.25 ± 0.05	0.020	38	upper reach
117	1×10^9	1×10^{10}	0.45 ± 0.10	n.c.	67	middle reach
117	1×10^{10}	4×10^{10}	$0.75 \pm 0.49^{\dagger}$	n.c.	41	lower reach
118	2×10^8	1×10^9	0.44 ± 0.03	0.041	63	
119	1×10^8	1.4×10^9	0.39 ± 0.05	n.c.	50	
mean			***0.38 ± 0.09***		***55***	

Note : A_{min} and A_{max} respectively refer to the minimum and maximum drainage areas considered in the regression.

† data excluded from mean where profile displayed distinct knickpoints or where systematic downstream changes in concavity occurred (e.g., eastern flank of the Pengguan Massif). See comments for details.

n.c. - not calculated. The relative steepness (S_r) was not calculated for profile reaches outside the range of A_r. Note that mean concavities were not calculated for the Fu and Baishui drainages due to a wide range of values.

Table 2: Radiocarbon analyses of charcoal samples

Sample number	$\delta^{13}C$ (%)	^{14}C age (yr B.P. $\pm$ 1σ)	^{14}C age (corrected)* (yr B.P. $\pm$ 1σ)	Calendric age range (yr B.P. $\pm$ 2σ)
97-13	-23.2	7015 $\pm$ 55	7225 $\pm$ 57	7680 - 8021
98-3	-25.2	10270 $\pm$ 70	10580 $\pm$ 72	11680 – 12478†

Note: Reported ^{14}C ages use Libby's half-life (5568 yr) and are referenced to the year A.D. 1950. Calendric ages were calibrated using the University of Washington CALIB program (Stuiver and Reimer, 1993). Samples were analyzed at the University of Arizona AMS facility by G. Burr.

* The corrected age results from the 3% difference between the Libby half-life and the actual half-life of ^{14}C (5735 yr).

† The large age range is the result of a ^{14}C plateau that overlapped with the Younger Dryas.

Table 3a: Dosimetry data for IRSL sample 98-1

Water*	K_2O (wt%)	C_t† (ks^{-1} cm^{-2})	C_{th}† (ks^{-1} cm^{-2})	Th (ppm)	U (ppm)	b value§ ($pGy\ m^2$)	Dose rate# (Gy/ka)
0.10±0.05	2.52±0.05	0.658±0.010	0.374±0.035	10.1±0.9	2.2±0.3	1.0±0.1	4.24±0.24
	2.72±0.10	0.705±0.022	0.412±0.027	11.0±1.0	2.3±0.1		

* Estimated average historic ratio of weight of water/weight of dry sample, based on measurements of moist collected sample and laboratory saturated samples (3 per IRSL sample). All uncertainties are stated at 1σ.

† Total and thorium count ratios from finely powdered samples for alpha-particle-counting (thick source method – Huntley and Wintle, 1981). Equations for the use of these count-rate values in calculation of dose rate are given by Berger (1988). The second row of data corresponds to the average values from sediment surrounding the IRSL sample at a radius of 20 cm.

§ Alpha effectiveness factor (Huntley et al., 1988; Berger, 1988).

Calculated with conversion factors and equations given by Berger (1988), and includes a cosmic ray component (for average estimated depth of 2.5m) from the data of Prescott and Hutton (1988). Note that the dose rate is typical for most sediments (2-4 Gy/k.y.).

Table 3b: IRSL data and age for sample 98-1

Preheat*	D_E† (Gy) ± 1σ	Time§ (s)	Age (ka) ± 2σ
140°C/2d	235±48	1-15	
160°C/2d	580±110	1-30	137±54

Note: The polymineralic 4-11 μm size fraction was used for the IRSL measurem,ent. IRSL was detected at the 420±20 nm spectral region (bandpass 390-470 nm at 1% cut). All bleaching was for 3hr with >780 nm solar spectrum passed (protocol of Huntley and Clague, 1986). Applying heat-treatment after bleaching corrects for any possible thermal transfer effect (e.g. Ollerhead et al., 1994).

* The chosen pre-readout annealing. Because the higher preheating led to a significantly higher D_E, only this value is used for age calculation.

† Weighted-mean equivalent dose plus average error (over time interval in next column) using model of Berger et al. (1987).

§ The readout (LED-on) time interval for which D_E is calculated.

Table 4: Incision rates in the eastern Min Shan

Sample	Location	River	Terrace Height* (m)	Age† (ka)	Incision Rate§ (mm/yr)
97-13	31.78°N, 104.10°E	Jin	25 ± 2	7.85 ± 1.7	3.2 ± 0.3
98-3	31.81°N, 104.19°E	Jin	13 ± 1	12.08 ± 4.0	1.1 ± 0.1
98-1	32.39°N, 104.59°E	Fu	58 ± 2	137 ± 54	0.4 ± 0.2

* Height relative to modern channel surveyed with a laser rangefinder (±1m) and clinometer (±0.25°).

† Uncertainties at 2σ.

§ Uncertainties estimated from range of combined uncertainty in terrace height and age.

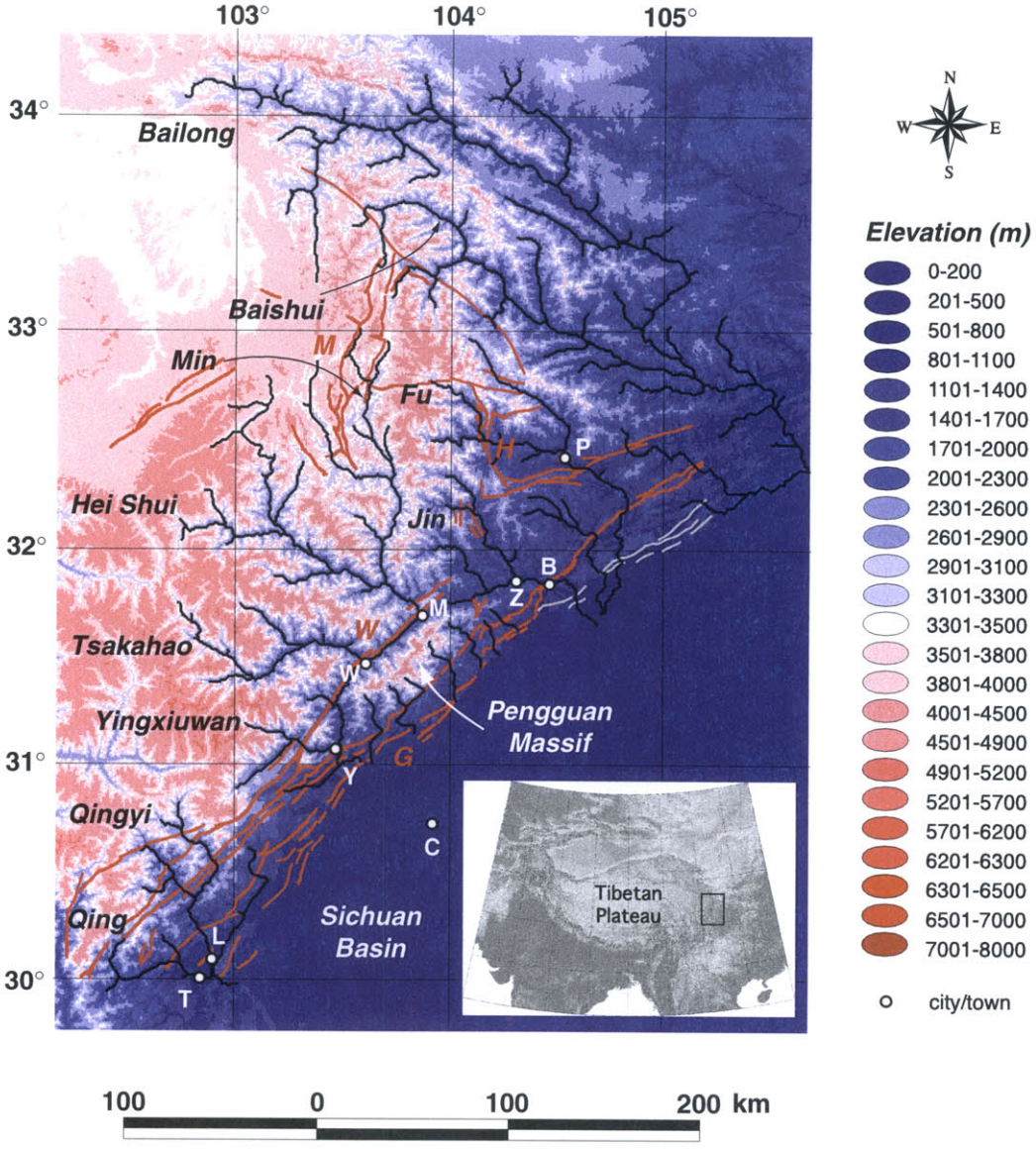
103°
104°
105°
34°
33°
32°
31°
30°
Bailong
Baishui
Min
Fu
Hei Shui
Jin
Tsakahao
Yingxiuwan
Pengguan
Massif
Qingyi
Qing
Sichuan
Basin
Tibetan
Plateau
P
B
Z
M
W
Y
C
L
T
M
H
Y
G
N
W
E
S
Elevation (m)
0-200
201-500
501-800
801-1100
1101-1400
1401-1700
1701-2000
2001-2300
2301-2600
2601-2900
2901-3100
3101-3300
3301-3500
3501-3800
3801-4000
4001-4500
4501-4900
4901-5200
5201-5700
5701-6200
6201-6300
6301-6500
6501-7000
7001-8000
city/town
100
0
100
200 km

Figure 1

a.

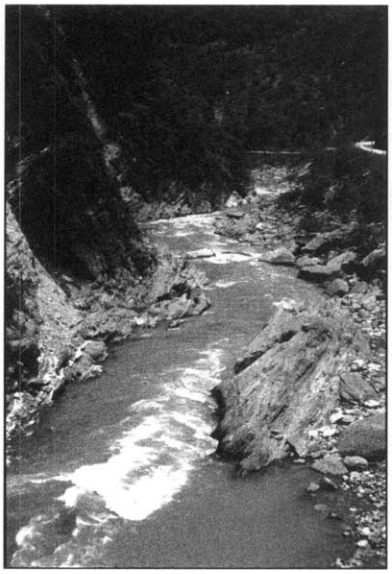

b.

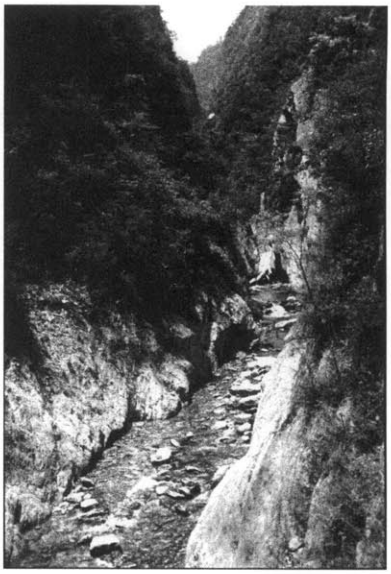

c.

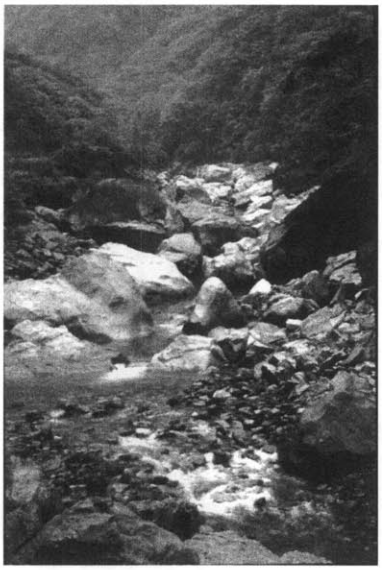

Figure 2

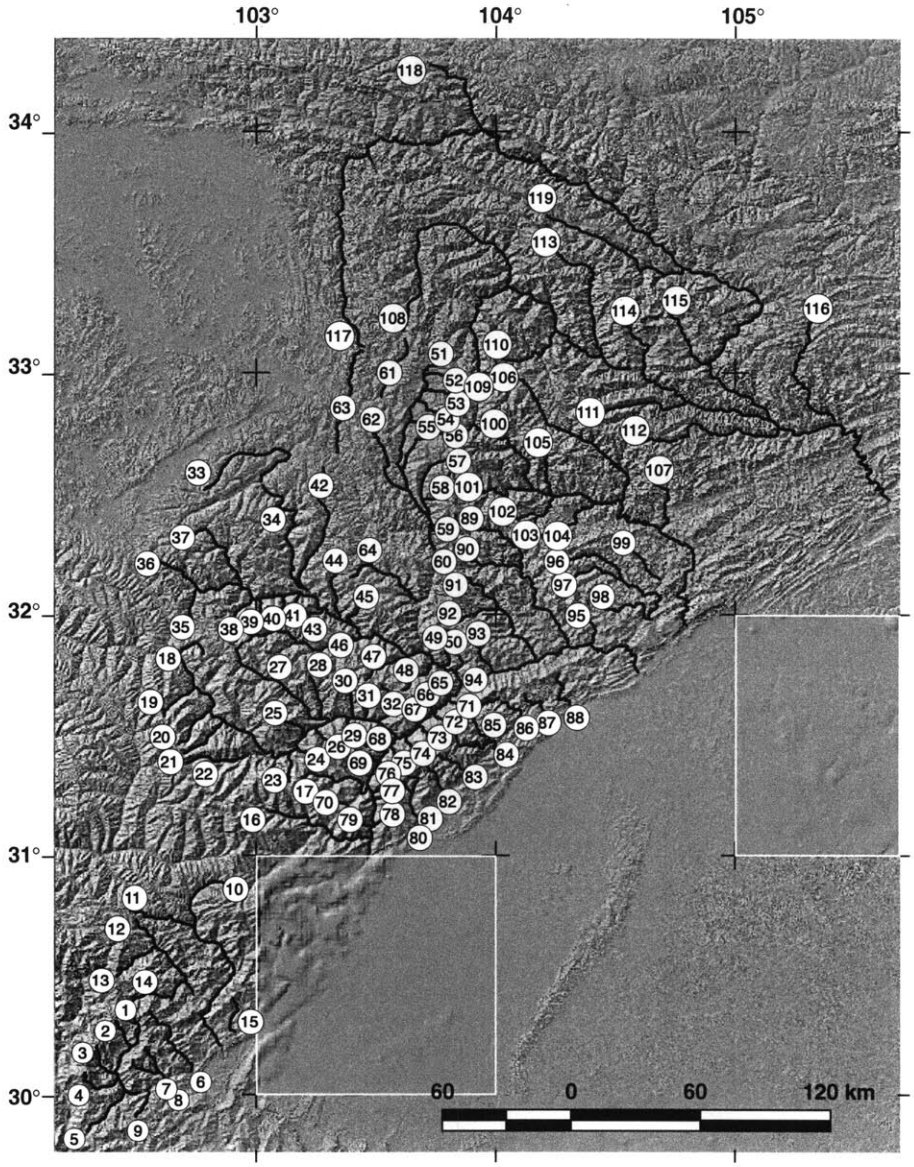

Figure 3

a.

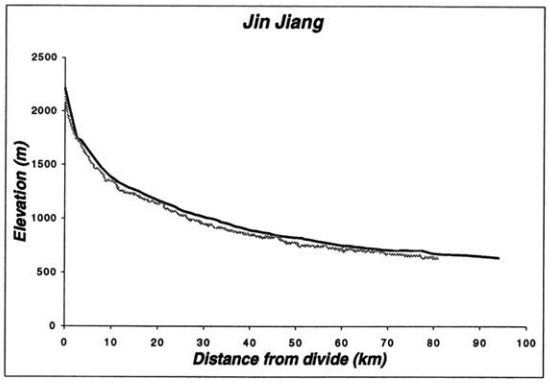
Jin Jiang
Elevation (m)
2500
2000
1500
1000
500
0
0 10 20 30 40 50 60 70 80 90 100
Distance from divide (km)

b.

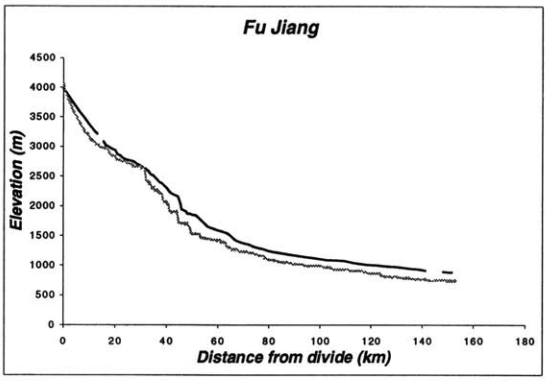
Fu Jiang
Elevation (m)
4500
4000
3500
3000
2500
2000
1500
1000
500
0
0 20 40 60 80 100 120 140 160 180
Distance from divide (km)

c.

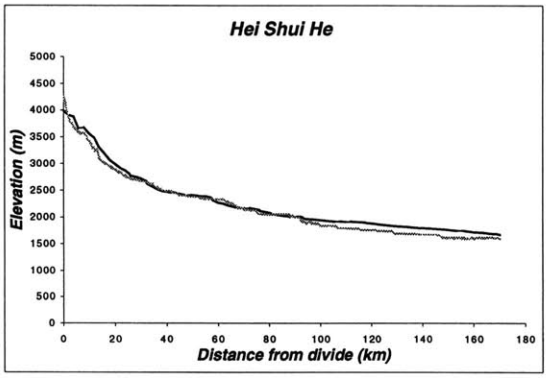
Hei Shui He
Elevation (m)
5000
4500
4000
3500
3000
2500
2000
1500
1000
500
0
0 20 40 60 80 100 120 140 160 180
Distance from divide (km)

Figure 4

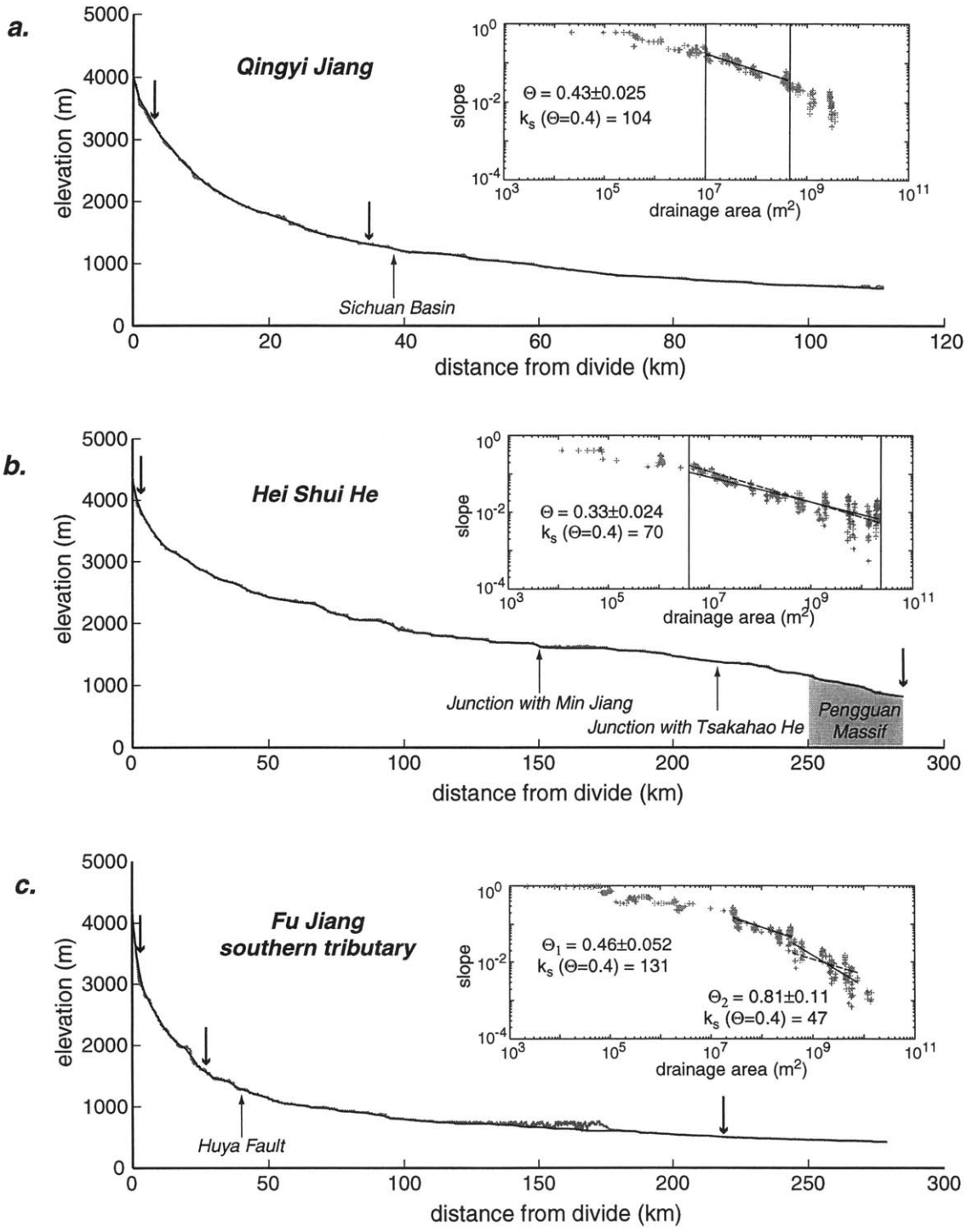
a.
Qingyi Jiang
Θ = 0.43±0.025
k_s (Θ=0.4) = 104
slope
drainage area (m²)
Sichuan Basin
elevation (m)
distance from divide (km)
b.
Hei Shui He
Θ = 0.33±0.024
k_s (Θ=0.4) = 70
slope
drainage area (m²)
Junction with Min Jiang
Junction with Tsakahao He
Pengguan Massif
elevation (m)
distance from divide (km)
c.
Fu Jiang
southern tributary
Θ1 = 0.46±0.052
k_s (Θ=0.4) = 131
Θ2 = 0.81±0.11
k_s (Θ=0.4) = 47
slope
drainage area (m²)
Huya Fault
elevation (m)
distance from divide (km)

Figure 5

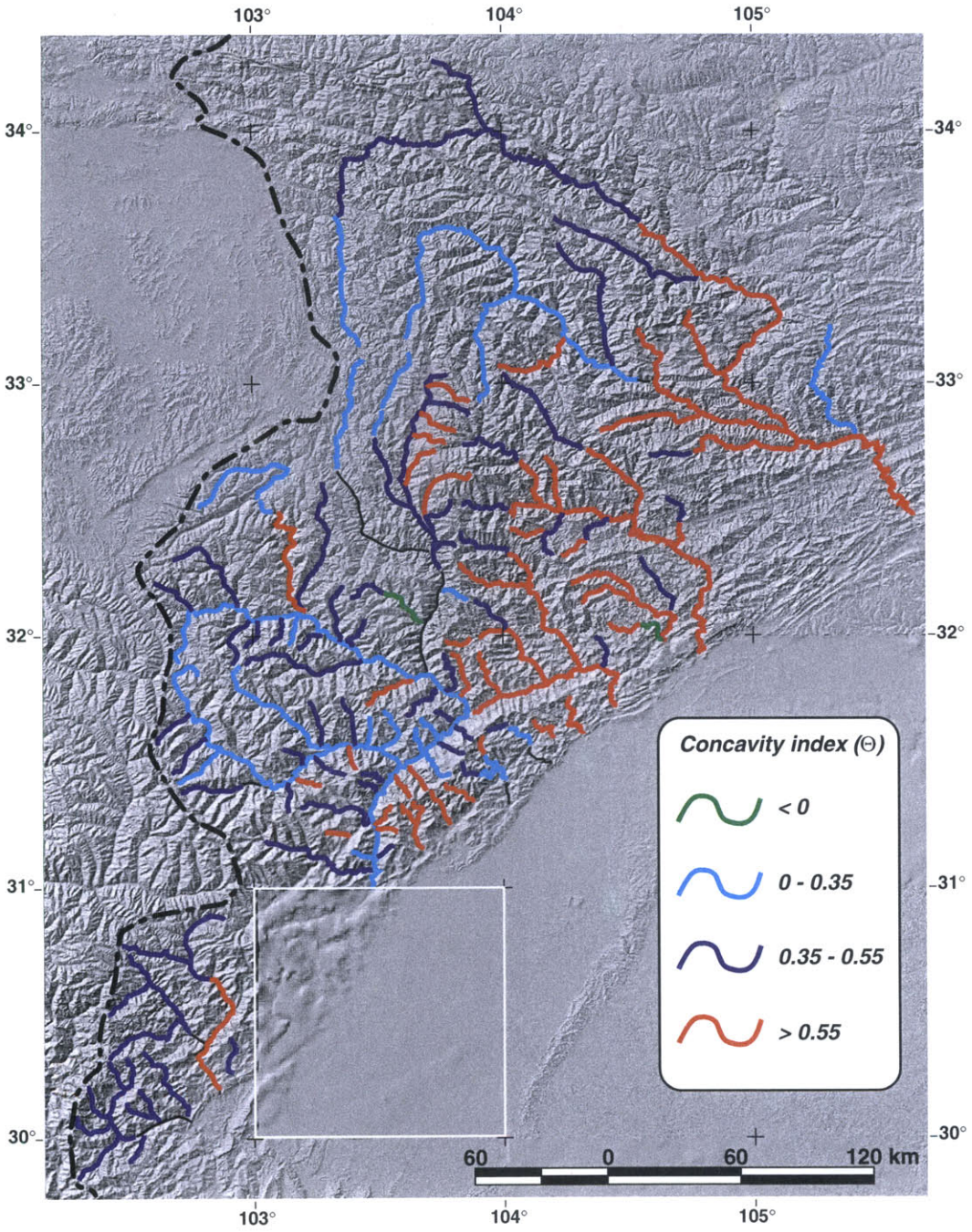
103°
104°
105°
34°
33°
32°
31°
30°
Concavity index (Θ)
< 0
0 - 0.35
0.35 - 0.55
> 0.55
60
0
60
120 km

Figure 6

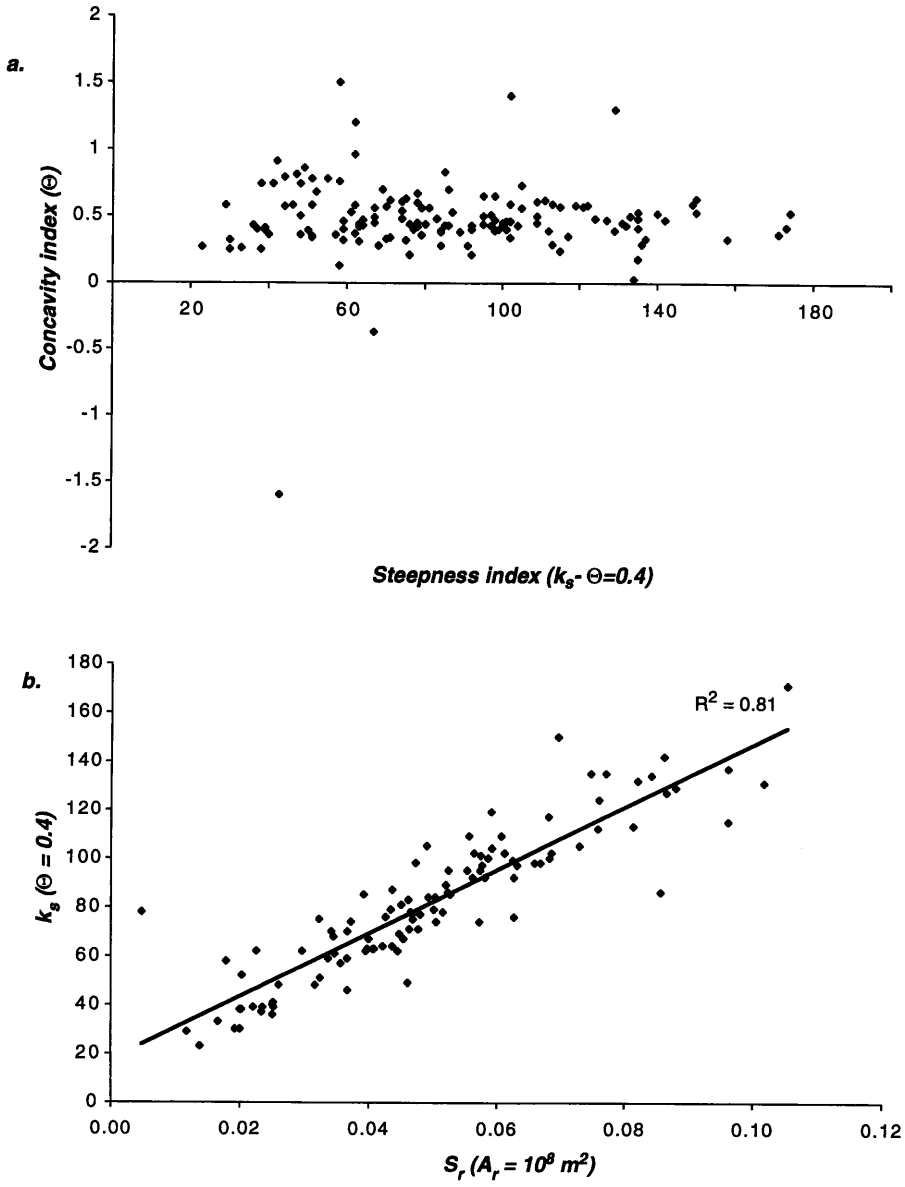
a.
Concavity index (Θ)
2
1.5
1
0.5
0
-0.5
-1
-1.5
-2
20
60
100
140
180
Steepness index (k_s- Θ=0.4)
b.
k_s (Θ = 0.4)
180
160
140
120
100
80
60
40
20
0
0.00
0.02
0.04
0.06
0.08
0.10
0.12
R^2 = 0.81
S_r (A_r = 10^9 m^2)

Figure 7

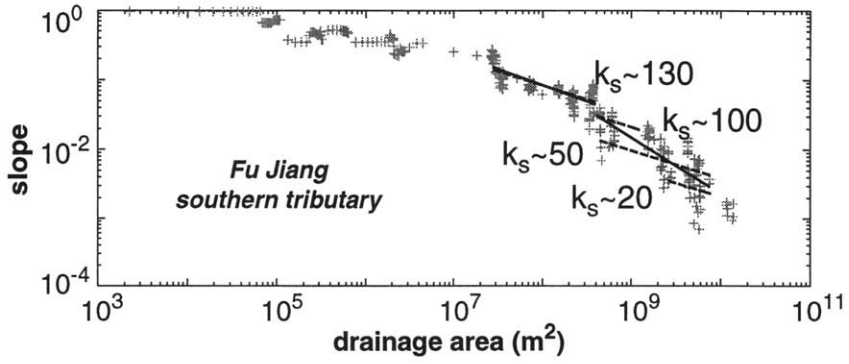
slope
drainage area (m²)
Fu Jiang
southern tributary
k_s~130
k_s~100
k_s~50
k_s~20

Figure 8

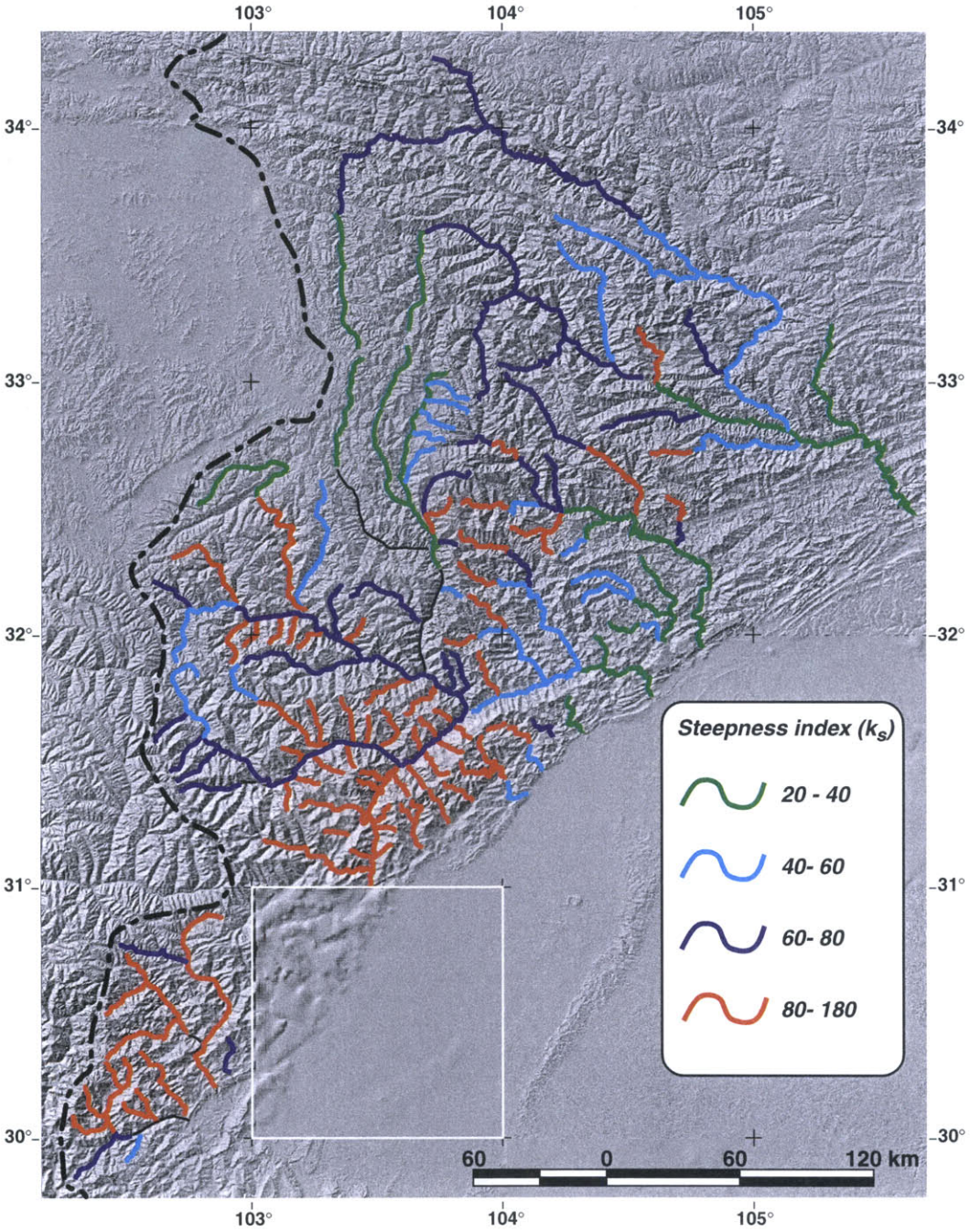
103°
104°
105°
34°
33°
32°
31°
30°
Steepness index (k_s)
20 - 40
40- 60
60- 80
80- 180
60
0
60
120 km

Figure 9

a.

b.

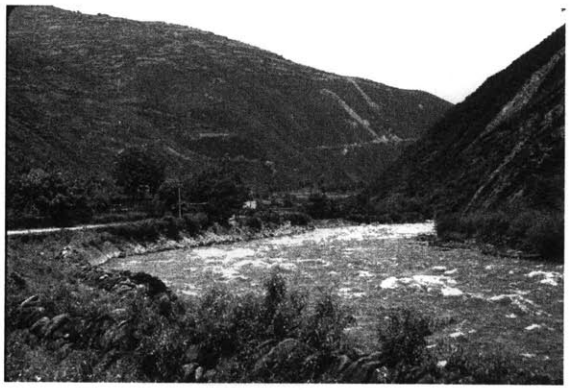

Figure 10

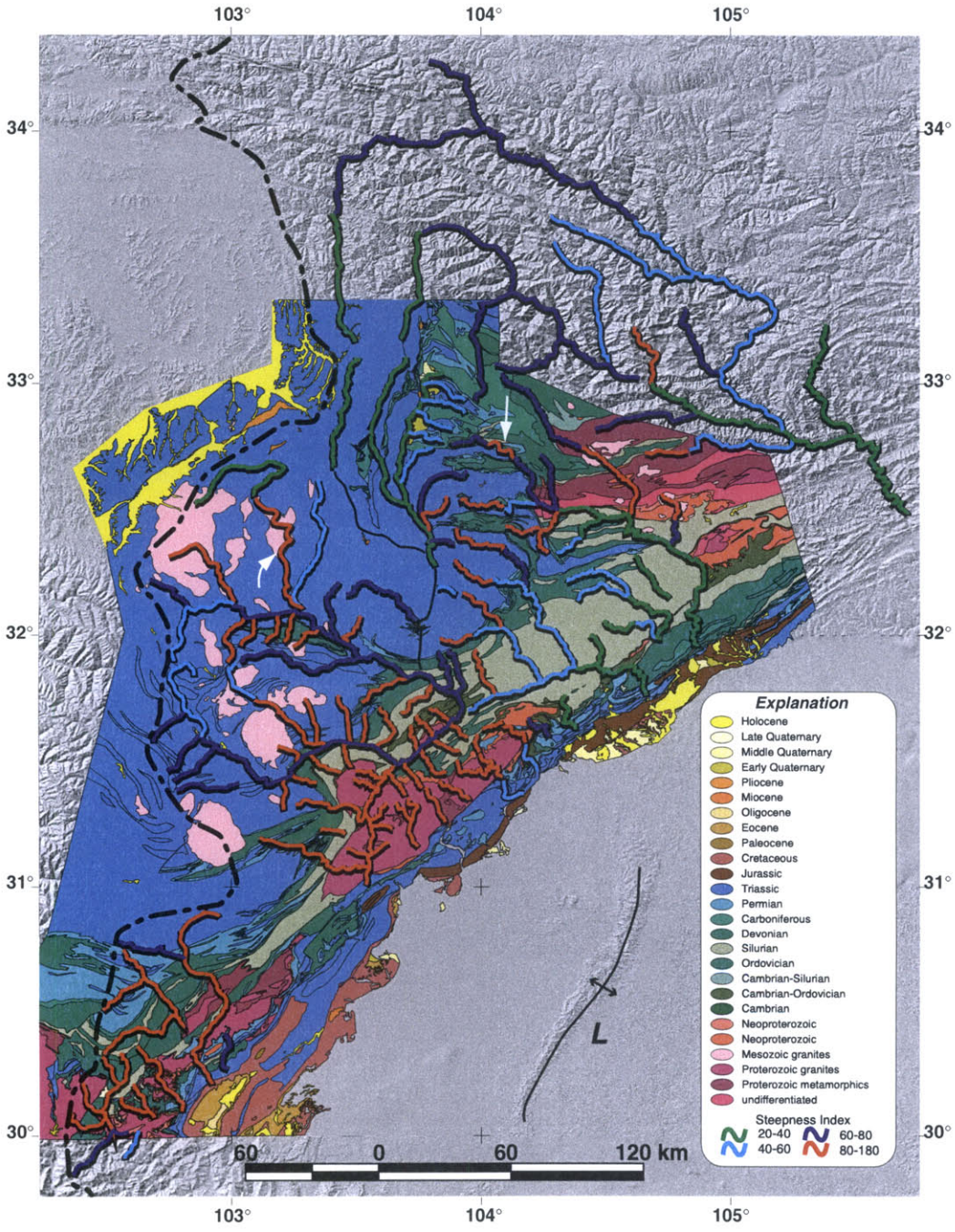
103°
104°
105°
34°
33°
32°
31°
30°
Explanation
Holocene
Late Quaternary
Middle Quaternary
Early Quaternary
Pliocene
Miocene
Oligocene
Eocene
Paleocene
Cretaceous
Jurassic
Triassic
Permian
Carboniferous
Devonian
Silurian
Ordovician
Cambrian-Silurian
Cambrian-Ordovician
Cambrian
Neoproterozoic
Neoproterozoic
Mesozoic granites
Proterozoic granites
Proterozoic metamorphics
undifferentiated
Steepness Index
20-40
40-60
60-80
80-180
L
60
0
60
120 km

Figure 11

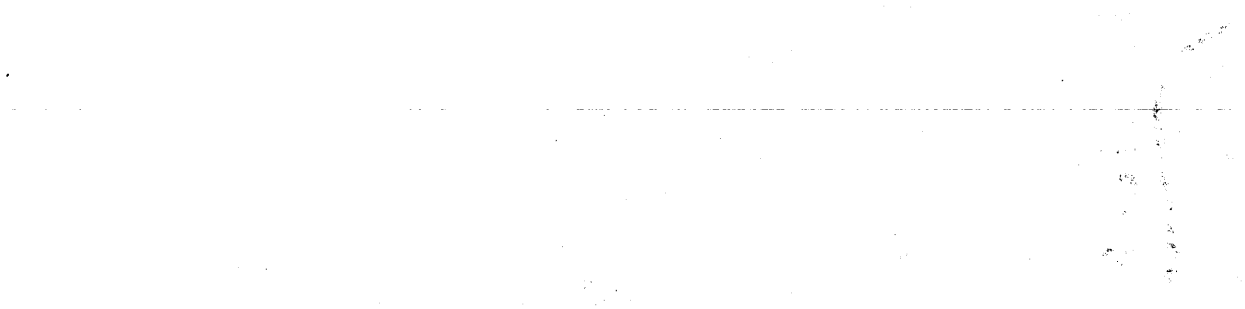

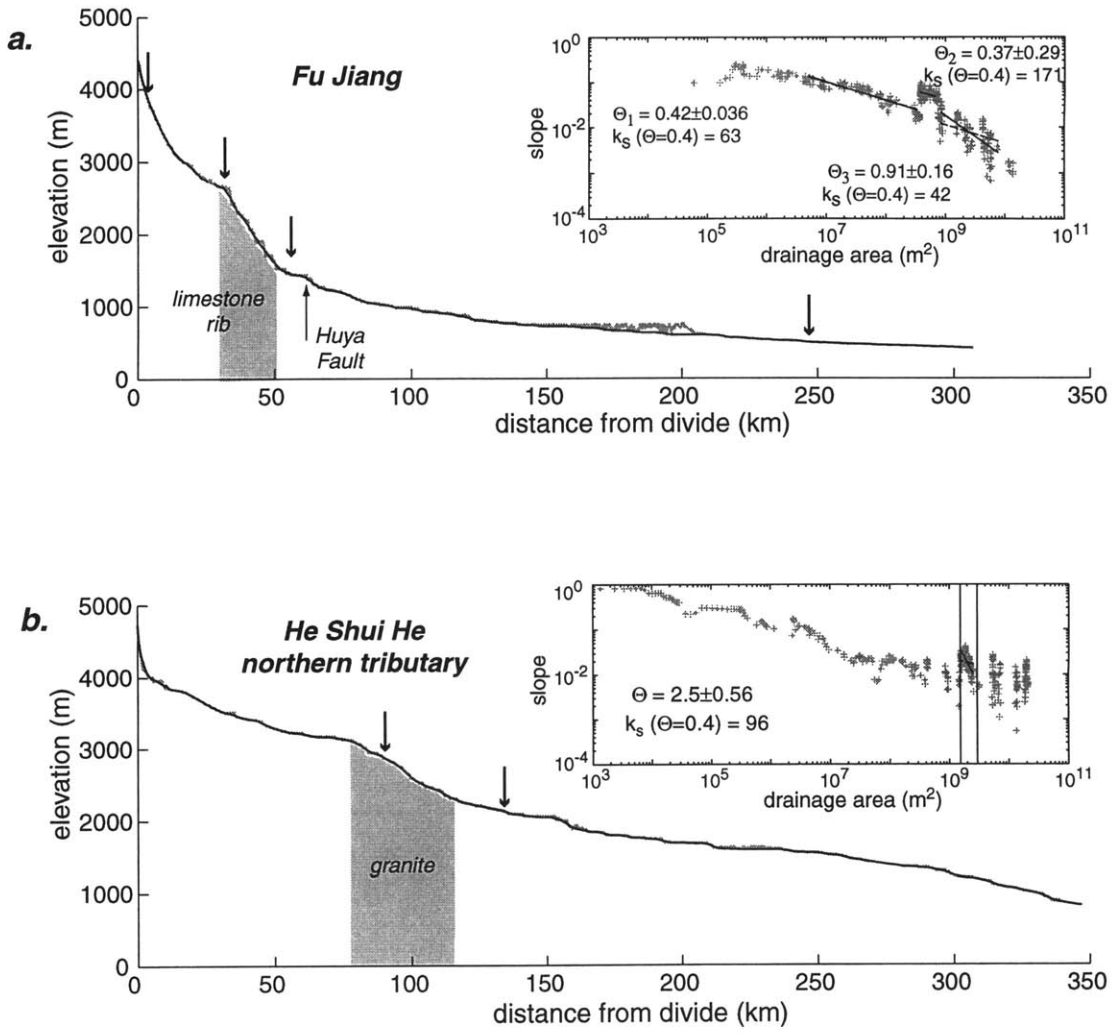
a.
Fu Jiang
elevation (m)
distance from divide (km)
limestone rib
Huya Fault
slope
drainage area (m²)
Θ1 = 0.42±0.036
ks (Θ=0.4) = 63
Θ2 = 0.37±0.29
ks (Θ=0.4) = 171
Θ3 = 0.91±0.16
ks (Θ=0.4) = 42
b.
He Shui He
northern tributary
granite
Θ = 2.5±0.56
ks (Θ=0.4) = 96

Figure 12

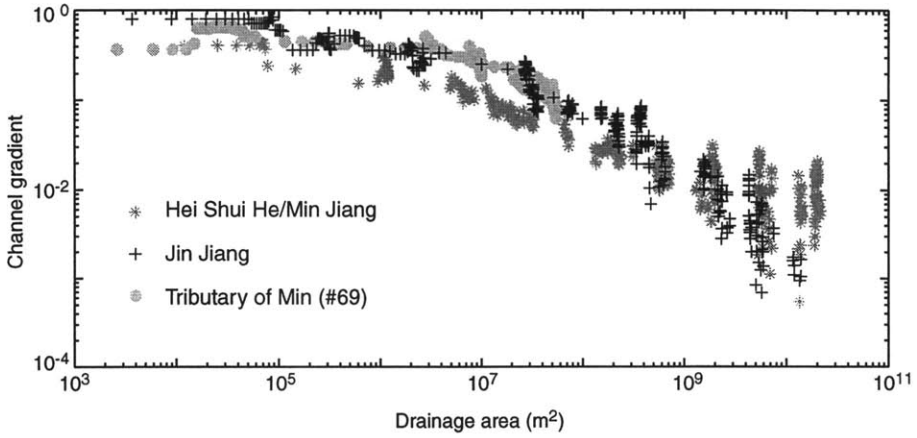
10 0
10-2
10-4
Channel gradient
Hei Shui He/Min Jiang
Jin Jiang
Tributary of Min (#69)
10^3
10^5
10^7
10^9
10^11
Drainage area (m^2)

Figure 13

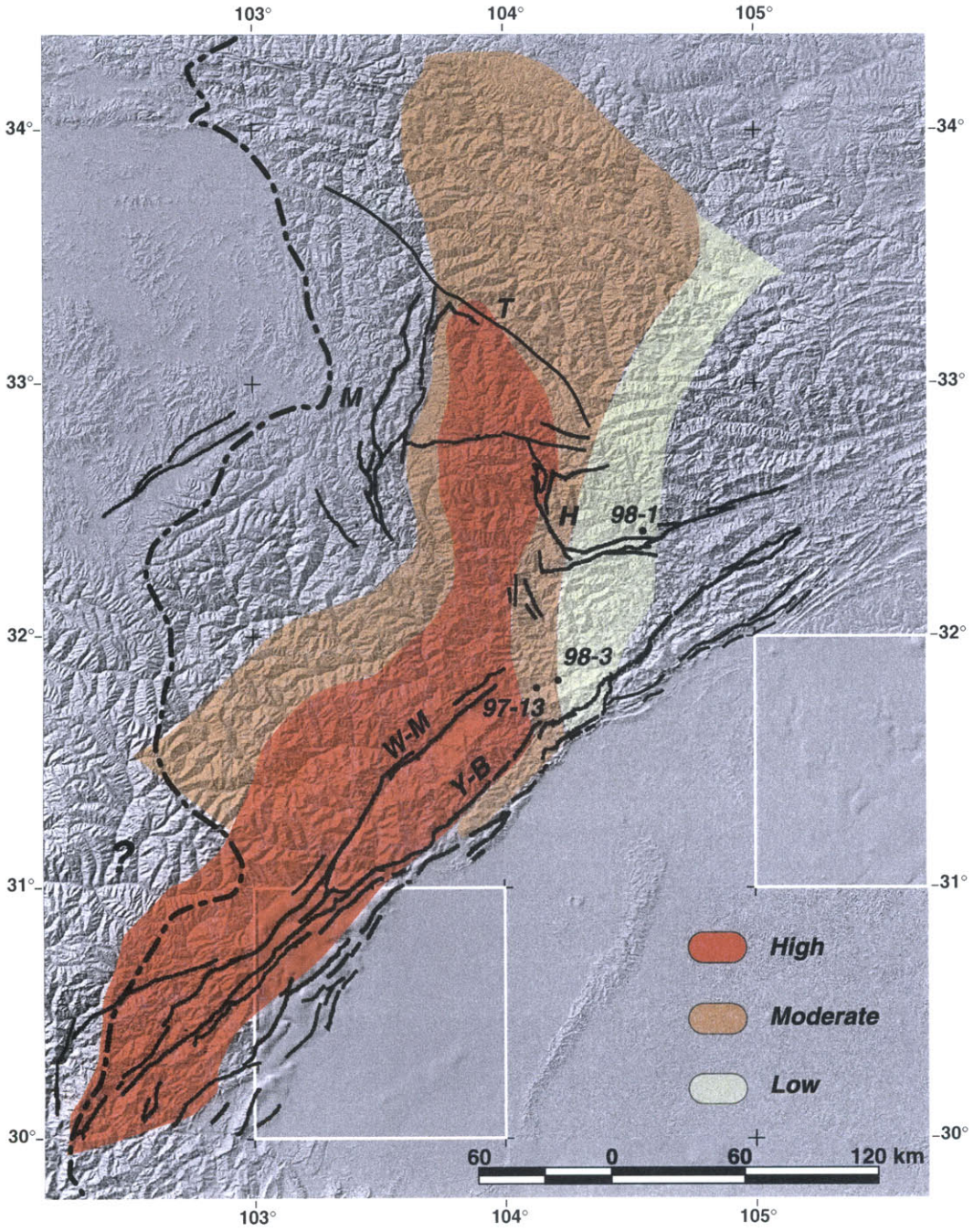
103°
104°
105°
34°
33°
32°
31°
30°
T
M
H
98-1
98-3
97-13
W-M
Y-B
?
High
Moderate
Low
60
0
60
120 km

Figure 14

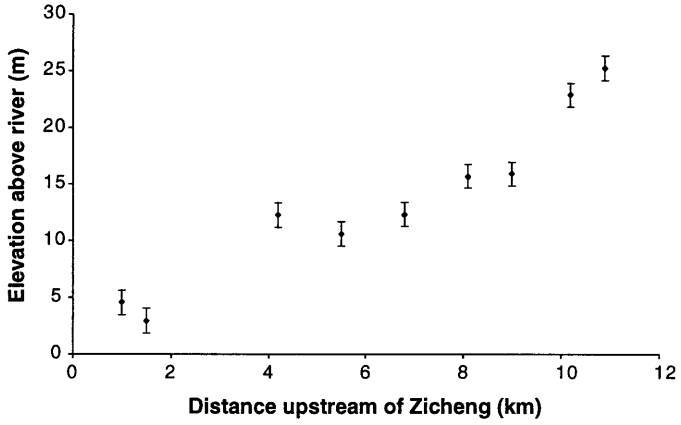
Elevation above river (m)
30
25
20
15
10
5
0
0
2
4
6
8
10
12
Distance upstream of Zicheng (km)

Figure 15

Chapter 5

The effect of spatially variable rock uplift on river profile concavity: A new tool for neotectonic analysis of topography

Abstract

Despite intensive research into the coupling between tectonics and surface processes, our ability to obtain quantitative information on the rates of tectonic processes from topography remains limited due primarily to a dearth of data with which to test and calibrate of process rate laws. Here we develop a simple theory for the impact of spatially variable rock uplift rate on the concavity of bedrock river profiles. Application of the analysis to the Siwalik Hills of central Nepal demonstrates that systematic differences in the concavity of channels in this region match the predictions of a stream power incision model and depend on the position and direction of the channel relative to gradients in the vertical component of deformation rate across a fault-bend fold. Furthermore, calibration of model parameters from channel profiles argued to be in steady-state with the current climatic and tectonic regime indicates that 1) the ratio of exponents on channel drainage area and slope (m/n) is ~0.46, consistent with theoretical predictions, 2) the slope exponent is consistent with incision either linearly proportional to shear-stress or unit stream power (n~0.66 or n~1, respectively), and 3) the coefficient of erosion is within the range of previously published estimates (mean $K = 4.3 \times 10^{-4}$ $m^{0.2}/yr$). Application of these model parameters to other channels in the Siwalik Hills yields estimates of spatially variable erosion rates that mimic expected variations in rock uplift rate across a fault-bend fold. Thus, the sensitivity of channel gradient to rock uplift rate in this landscape allows us to derive quantitative estimates of spatial variations in erosion rate directly from topographic data.

Introduction

A primary goal of tectonic geomorphology is to extract information regarding the patterns and rates of active deformation from topography. In tectonically active regions, the bedrock channel network dictates critical relationships between relief, elevation and denudation rate (Howard, 1994; Howard et al., 1994; Whipple et al., 1999) and, to first-order, controls the response time of the landscape to changes in boundary conditions (Whipple and Tucker, 1999). Consequently, analysis of the longitudinal profiles of channels provides a promising avenue of exploration of these relationships (Hack, 1957), and much recent research has focused on the quantitative description of bedrock channel forms and processes (e.g., Tinkler and Wohl, 1998). However, continued development of theoretical models for bedrock river incision is severely hampered by the sparse data available to calibrate model parameters that describe erosive efficiency (Howard and Kerby, 1983; Stock and Montgomery, 1999; Snyder et al., 2000; Whipple et al., 2000b).

In this paper, we develop a theory for the effect of spatially varying rock uplift rates on the concavity of bedrock river profiles within the context of the detachment-limited unit stream power incision model (Howard et al., 1994). Extension of this analysis to transport-limited conditions is readily accomplished, however, and the general approach outlined here is equally applicable to detachment-limited and transported-limited systems as the regimes are similar at steady-state (Willgoose, 1994). We demonstrate how analysis of stream profiles under conditions of non-uniform rock uplift allows for direct evaluation of model parameters. While our analysis emphasizes steady-state forms (erosion balancing rock uplift), transient conditions are easily addressed using numerical solution schemes.

We test our model in a region of known variation in uplift rate, the Siwalik Hills in central Nepal. Rock uplift rates across the Siwalik Hills anticline are well documented in a recent study of deformed Holocene terraces (Lave and Avouac, 2000), vary in a systematic way across the fold, and appear to be constant throughout the Holocene. The anticline is developed in a region of uniform lithology, and thus provides a nearly ideal location to examine the effects of spatially varying uplift rate on channel longitudinal profiles.

Detachment-limited Stream Power Model

Detachment-limited incision into bedrock is often modeled as a power-law function of contributing drainage area (a proxy for discharge) and channel gradient (Howard and Kerby, 1983; Howard, 1994; Moglen and Bras, 1995). A river profile evolution equation that reflects the competition between rock uplift and erosion can be written as:

$$dz/dt = U(x,t) - KA^m S^n \quad (1)$$

where dz/dt is the time rate of change of the river bed elevation, U is rock uplift rate relative to a fixed baselevel, A is upstream drainage area, S is local channel gradient, K is a dimensional coefficient of erosion, and m and n are positive constants related to basin hydrology, hydraulic geometry, and erosion process (Howard et al., 1994; Whipple and Tucker, 1999; Whipple et al., 2000a). Under steady-state conditions ($dz/dt = 0$), with uniform U, K and constant m and n, equation 1 can be solved to yield an expression for equilibrium channel gradient:

$$S_e = (U/K)^{\frac{1}{n}} A^{-\frac{m}{n}} \quad (2)$$

Equation 2 predicts a power-law relation between channel gradient and drainage area often observed in natural landscapes, of the form $S=k_s A^{-\Theta}$ (e.g., Tarboton et al., 1991; Moglen and Bras, 1995; Sklar and Dietrich, 1998; Snyder et al., 2000), where the coefficient, $(U/K)^{1/n}$ sets the channel steepness, k_s, and the ratio m/n is the intrinsic channel concavity, which equals the actual concavity (Θ) only under conditions of uniform K, U, m, and n.

Relatively few field constraints exist on appropriate values for K, n and m in various geologic, tectonic, and climatic regimes. Howard and Kerby (1983) demonstrated that historic incision rates in rapidly eroding badlands were adequately explained by a stream power model assuming incision rates linearly proportional to shear stress (i.e. m~1/3, n~2/3). Stock and Montgomery (1999) showed that, for a best-fit m and n (0.4 and 1, respectively), K varied over 4 orders of magnitude (10^{-3}-10^{-7} $m^{0.2}$/yr) depending on lithology and climate, while Snyder et al (2000) demonstrated that K may also vary in concert with uplift rate ($1 - 8 \times 10^{-5}$ $m^{0.2}$/yr). Recent studies of historic bedrock incision along the Ukak river in Alaska yield results constraining n to

significantly less than 1 ($n \sim 0.2 - 0.6$) and K (for m=0.4, n=1) to ~ 9 x 10^{-4} $m^{0.2}$/yr (Whipple et al., 2000b).

Although individual values of the exponents m and n are difficult to obtain from natural field experiments, the ratio of m/n is expected to be independent of erosion process (Whipple and Tucker, 1999) is more easily estimated (Seidl and Dietrich, 1992; Moglen and Bras, 1995). Theoretical considerations of the relationships between discharge and drainage area and between channel width and discharge suggest that the ratio m/n should fall in a narrow range between 0.35 and 0.6 (Whipple and Tucker, 1999), consistent with empirical data (Howard and Kerby, 1983). Equation 2 implies that the ratio m/n can be estimated directly from the concavity of the channel, if and only if the steady state assumption holds and U, K, m, and n are constant. Indeed, numerous estimates of channel concavity in a wide variety of landscapes yield values between 0.3 and 0.6 (Tarboton et al., 1991; Whipple and Tucker, 1999; Snyder et al., 2000), although some estimates have been reported outside the expected range (Seidl and Dietrich, 1992; Sklar and Dietrich, 1998). As pointed out by Whipple and Tucker (1999), a restricted range of the ratio m/n, however, does not necessarily imply that channel concavities are likewise limited. Any spatial variation in K and/or U will strongly influence channel concavity (Moglen and Bras, 1995; Sklar and Dietrich, 1998; Whipple and Tucker, 1999). Here we develop how spatial variations in rock uplift rate impact the concavity of detachment-limited channels. We do not explicitly consider the potential role of sediment flux in influencing incision rates (e.g., Sklar and Dietrich, 1998). If present, its effect will be subsumed in our estimates of model parameters.

Spatially Variable Rock Uplift Rate

For the sake of brevity, we restrict our analysis to a simple uplift function that yields a power-law gradient-area relationship:

$$U = U_0 x^{\alpha} \tag{3}$$

where U_0 is the rock uplift rate at the edge of the region of interest (taken here as the channel head) and α is a constant. Substituting equation (3) into equation (1), utilizing a well-known relation between streamwise distance and drainage area (Hack, 1957), where

$A=k_a x^h$, and solving under the assumption of steady-state yields an expression for equilibrium channel gradients of the form $S_e=k_s A^{-\Theta}$ where

$$k_s = \left(U_0/K\right)^{\frac{1}{n}} k_a^{-\frac{\alpha}{hn}} \tag{4}$$

and

$$\Theta = m/n - \alpha/hn \tag{5}$$

Note that because x is distance along the stream, the analysis is best applied to straight channels that run perpendicular to uplift rate gradients.

Equation (5) shows that profile concavity is a function not only of the ratio m/n, but also depends on the rates of change of uplift rate (α) and drainage area (h) with downstream distance and the slope exponent (n). Equation (5) predicts that channels in regions where rock uplift rate is increasing downstream ($\alpha>0$) should have low concavities (or may even be convex upward), while those flowing toward regions of decreasing uplift rate ($\alpha<0$) should have high concavities. When K is spatially uniform, equation (5) demonstrates that the slope exponent (n) can be directly estimated from the concavity of steady-state channels experiencing known variations in rock uplift rate.

Siwalik Hills Field Area

The Siwalik Hills are a set of low ranges in the sub-Himalaya developed in the hanging wall of the Main Frontal Thrust (MFT), the southernmost of a system of thrust faults in the Himalaya. The MFT disrupts Tertiary continental molasse of the Indo-Gangetic foredeep and currently marks the southern edge of active shortening in the Indo-Asian collision zone. Recent work on folded fluvial terraces along the Bagmati and Bakeya rivers (Lave and Avouac, 2000) (Figure 1) demonstrates that: 1) displacement on the MFT locally absorbs ~21 mm/yr of shortening between India and Asia, 2) fold geometry is consistent with a model of fold growth above a ramp in the MFT, and 3) incision rates vary systematically across the fold and appear to have been nearly steady throughout the Holocene. By accounting for changes in base level, sinuosity, and gradient, these authors argue that incision rates are equal to rock uplift rates across the anticline during the Holocene. Importantly, these authors demonstrate that changes in the

horizontal (advective) component of displacement has little effect on the incision rates along the low gradient fluvial systems they investigated (Lave and Avouac, 2000). Along the northern limb of the anticline, the vertical component of displacement increases in a nearly linear manner from ~5mm/yr north of the fold to >15mm/yr near the inferred trace of the MFT (Lave and Avouac, 2000). Rates then rapidly decrease to zero on the Indo-Gangetic plain. There also appears to be some variation in rock uplift rate along strike; maximum inferred rates are ~12mm/yr along the Bagmati River, and increase to ~17mm/yr along the Bakeya River (Lave and Avouac, 2000). The pronounced gradients in the vertical component of displacement and the nearly uniform lithology (fluvial sandstones and mudstones of the Middle and Lower Siwaliks) make this region an exceptional locale to study the influence of systematic variations in rock uplift rate on channel gradients.

Similar motivation led Hurtrez et al. (1999) to compare topographic characteristics of small drainage basins in the region against uplift rates derived from the local bedding orientation and the inferred ramp geometry. The authors examined a number of strike-parallel basins and found no significant correlation at length scales >600m. In contrast to their results, we show below that strike-perpendicular channels in the same region have dramatically different concavities that are readily explained by spatial variations in rock uplift rate.

Stream Profile Analysis

We examined 22 channels in the vicinity of the Bagmati and Bakeya rivers (Figure 1). Two of these channels (tributaries of the Bakeya and Bagmati, respectively) cross the anticline, spanning a range of rock uplift rates from ~5mm/yr to nearly 17mm/yr, and provide the primary motivation for this study. Of the remaining 20 channels, 13 have their headwaters along the crest of the anticline and flow toward regions of decreasing uplift rate, while 7 channels flow parallel to the strike of the fold, and should provide examples of channels experiencing a uniform uplift rate (Hurtrez et al., 1999). We did not examine the Bagmati and Bakeya rivers themselves, as they have been thoroughly studied and appear to respond to uplift primarily by channel narrowing (Lave and Avouac, 2000).

Channel elevations and upstream drainage areas were extracted from digital topographic data with a nominal resolution of 90m (DTED data source, described in Fielding et al., 1994). We removed spikes along the channel profiles, smoothed the data using a moving average of 10 pixels and then calculated channel gradients at 10m vertical intervals along the profile (e.g., Snyder et al., 2000) (Figure 2). Regression of gradients against upstream area yielded estimates of the concavity and steepness indices (Θ and k_s, respectively), while regression of drainage area against streamwise distance yielded estimates of h (Table 1). All regressions excluded data from hillslopes (Tarboton et al., 1991; Montgomery and Foufoula-Georgiou, 1993; Snyder et al., 2000) and from alluviated sections of the channels on either side of the anticline.

Qualitatively, the results of this analysis bear out predictions of the stream power incision model remarkably well. Basins oriented parallel to the strike of the anticline have concavities that range between 0.4 and 0.5 (mean of 0.46 – Table 1), in close agreement with theoretical predictions (Whipple and Tucker, 1999) and measurements (Snyder et al., 2000) of the concavity of equilibrium bedrock channels under conditions of uniform uplift and K. In contrast, concavity of basins oriented perpendicular to the fold depends in a systematic way on the position of the basin and the direction of flow relative to rock uplift gradients (Table 1). The two major tributaries in the center of the study area show convex-upward longitudinal profiles for some 7-9 km along the channels (Table 1, Figure 2). Stream gradients systematically increase downstream (Figure 2, insets) as these channels cross into regions of progressively higher rock uplift rate near the southern limb of the fold. Smaller basins that have their headwaters along the crest of the anticline display highly concave longitudinal profiles, with Θ values ranging from 0.7 to 2.1 (mean of 1.19 – Table 1), consistent with the fact that these channels cross regions of progressively decreasing rock uplift. Two exceptions to this pattern occur at the NW end of the study area (channels 1 and 2), where streams draining the southern limb of the anticline have concavities between 0.3 and 0.5. Both of these streams cross a wide region of the fold (Figure 1), and may indicate a different pattern of deformation in this area (see discussion).

Given that the position and magnitude of spatial gradients in rock uplift rate are best constrained on the back (northern) limb of the Siwalik Hills anticline (Lave and

Avouac, 2000), we first focus our analysis on the two tributaries of the Bagmati and Bakeya rivers that transect this region (Figure 1). Rock uplift rate along the north limb of the fold increases nearly linearly in a downstream direction (Lave and Avouac, 2000) (α=1 in equation 3), allowing us to determine the slope exponent (n) directly from the convexity of the channel profile (equation 5). We assume that the channels are in steady-state, that the ratio m/n is ~0.46 (the mean of strike-parallel basins) and we utilize the Hack exponent derived for each river (Table 1). We estimate that the slope exponent in a stream power incision model ranges from 0.6 to 0.9 (Table 2), consistent with incision rate nearly linear in basal shear stress (n~0.66) or in unit stream power (n~1) (Howard and Kerby, 1983; Whipple and Tucker, 1999). Our estimate of n is relatively insensitive to the choice of intrinsic concavity (m/n); varying m/n between 0.35 and 0.55 leads to a 0.08 variation in n. Given the range of our estimates between channels, we compare the performance of models using either n=2/3 or n=1.

As both of these incision models appear to be viable descriptions of channel gradient in the Siwalik Hills, we calculate the coefficient of erosion, K, for each (Table 2), utilizing equation (1). We account for the additional effective 'uplift' component imparted by the advective component of the displacement field (see appendix for details) and find that it is a relatively minor contribution (~3-5%) to the incision rate along the channels. The variation in maximum rock uplift rate between the Bagmati and Bakeya rivers imparts a degree of uncertainty into our estimates. To evaluate the range of variability, we calculate K for uplift patterns derived from each transect (Table 2). If erosion is linear in stream power (n~1), values of K range from 1.5 x 10^{-4} to 1.6 x 10^{-4} $m^{0.08}$/yr whereas if erosion is linear in shear stress (n~2/3), values of K range from 6.0 x 10^{-4} to 6.9 x 10^{-4} $m^{0.05}$/yr (Table 2). We take the mean of these values (for each choice of n) as a best estimate of the coefficient of erosion for this landscape (Table 2).

Modeling Erosion Rates

In order to illustrate the potential application of this analysis to neotectonic problems, we utilize the calibrated parameters in the stream power incision model to predict erosion rates along a number of the small channels draining the front and back limb of the Siwalik Hills anticline. Predicted erosion rates, for either n=2/3 or n=1, along

channels draining the northern and southern limbs of the anticline generally decrease downstream in a nearly linear fashion, while erosion rates along channels oriented parallel to strike are nearly constant (Table 1; Figure 3). Erosion rates calculated directly from slope-area data are similar to those calculated from best-fit regressions, although the scatter inherent in digital topographic data imparts a degree of variability to the former estimates (Table 1). Furthermore, the magnitudes of model erosion rates closely reproduce the expected range of rock uplift rates (Lave and Avouac, 2000), lending additional support to the inference of steady-state incision rates in this landscape.

Interpretation of erosion rate patterns in terms of variations in deformation along the anticline is complicated by uncertainty in the position of the channels relative to the fold axes. This is particularly true along the southern limb of the fold, where the vertical and horizontal components of displacement vary across a narrow (1-2 km) region (see appendix). However, given a priori knowledge of the geometry of the fault/fold system, modeled erosion rates in this landscape should, in principle, provide an indication of spatial variations in displacement rate. For example, erosion rates along two channels at the western end of the study area (Figure 1, Table 1) suggest significant variability in the pattern of rock uplift in this region. These channels lie between the MFT and a second strand of the frontal thrust system to the north (Lave and Avouac, 2000), and may indicate significant activity on this structure. This technique thus affords the opportunity to study along-strike variations in erosion rate above the MFT and to begin to assess the spatial variability of active shortening along the Himalayan foreland thrust system.

Discussion and Conclusions

Our analysis of stream gradients in the Siwalik Hills indicates that a stream power incision model provides a promising means of evaluating channel response to spatial variations in rock uplift rate. We find that the dependence of incision rate on channel gradient is consistent with erosion linearly proportional to either basal shear stress (n~2/3) or stream power (n~1). Both models provide an adequate description of incision rates, as one might expect for weakly consolidated substrate (Howard and Kerby, 1983). To facilitate comparison with published estimates of stream power incision parameters, we calculate K for values m=0.4, n=1 (Stock and Montgomery, 1999). The resultant

estimates yield a mean of ~4.3 x 10^{-4} $m^{0.2}$/yr (Table 2). Thus, although incision rates are high, the erosion coefficient is within the range of published estimates for weak, easily erodible rock in regions with abundant precipitation (Stock and Montgomery, 1999; Whipple et al., 2000b).

Our results further indicate that rock uplift rate exerts a strong control on channel gradient in the Siwalik Hills and that systematic differences in channel concavity reflect pronounced spatial variations in rock uplift rate across the fold. Interestingly, erosion rates derived from the calibrated stream power parameters along the southern limb of the anticline (Table 2) yield rock uplift rates remarkably consistent with those modeled by Hurtrez et al. (1999) from the local (hillslope) relief.

Finally, this study serves to illustrate the potential of extracting quantitative information on the spatial distribution of rock uplift directly from digital topographic data. Systematic variations in channel gradient and, particularly, concavity can highlight regions of underlying variation in rock uplift rate and place direct constraints on the geometry and distribution of active structures (e.g., Molnar, 1987). Of course, such analysis is subject to complications introduced by variations in lithology, by transient conditions, by glacial erosion (e.g., Brocklehurst and Whipple, 1999), and possibly by downstream variations in sediment flux and must be applied with caution. However, current application of the technique in eastern Tibet, the Higher Himalaya of central Nepal, and elsewhere along the Siwalik Hills anticline indicates that the approach is a powerful guide to understanding regional neotectonics.

Acknowledgements

We thank Simon Brocklehurst, Noah Snyder and Greg Tucker for discussions on various aspects of this study. Comments on an initial draft by Peter Molnar and Doug Burbank significantly clarified portions of the manuscript. Work was partially supported by NSF grants EAR-9614970 and EAR-9725723.

Appendix – Incision Model Calibration

In order to calibrate a stream power incision model along a channel experiencing a range of rock uplift rates above a developing fault-bend fold, we need to consider the total displacement field at each point along the channel. Consider a fault whose dip, relative to the horizontal, is given by Θ_d and with displacement rate D. The vertical component of deformation is given by:

$$V(x) = D\sin\Theta_d \tag{A1}$$

and the horizontal component by:

$$H(x) = D\cos\Theta_d \tag{A2a}$$

or

$$H(x) = V(x)\cos\Theta_d/\sin\Theta_d \tag{A2b}.$$

The horizontal component of displacement imparts an effective 'uplift' component that depends on the local gradient of the channel, S, such that:

$$H(x)_v = H(x)S = V(x)S/\tan\Theta_d \tag{A3}.$$

Note that S is positive if the channel flows in the same direction as the displacement vector and is negative if opposite. The effect will thus be to increase the 'uplift' rate on channels flowing in the direction of displacement and decrease 'uplift' rate on those opposed to it. The total effective vertical displacement felt by any point on the channel is simply the sum of these components:

$$V(x)_{eff} = V(x)\left(1 + S/\tan\Theta_d\right) \tag{A4}.$$

Thus, given a priori knowledge of the fault geometry, one can in principle extract the displacement rate, D, across a fault-bend fold from the steady-state erosion rate, ε:

$$D = \frac{\varepsilon}{(\sin\Theta_d + S\cos\Theta_d)} \tag{A5}.$$

Lave and Avouac (2000) documented a correspondence between bedding dip angles and rock uplift profiles inferred from deformed fluvial terraces along the Bagmati and Bakeya rivers, suggesting that a model of fault-bend folding adequately described the deformation field across the Siwalik anticline. Furthermore, these authors demonstrated that the horizontal component of displacement accounts for a negligible difference (<1%) in effective uplift rate felt by these low gradient channels. In order to model the distribution of deformation along the tributary streams in this study, we utilize the

geometry of bedding dip angles measured by Lave and Avouac (2000) and a displacement rate of 21 mm/yr (Figure A1). We also consider the effect of the horizontal component of displacement; although the tributaries we examine are somewhat steeper than the Bagmati and Bakeya rivers, the additional component of 'uplift' felt by these rivers is on the order of 3-5% (Figure A1). Note that in both deformation models, the effective vertical displacement increases linearly along the northern limb of the fold (Figure A1). Consequently, the additional component of displacement (equation A3) does not significantly change our estimate of the slope exponent n.

We calculate the erosion coefficient K as a function of downstream distance using equation (2). We combine the effective vertical displacement patterns described above (Figure A1) with drainage areas extracted from the digital topography and the local channel gradient. The difference in displacement patterns between the Bagmati and Bakeya rivers (Figure A1) presents the greatest source of uncertainty in our calculation. Given that the tributaries are located between these two transects (Figure 1), we calculate K for each displacement pattern and take the mean of these values (Table 2). Standard deviations are calculated for each estimate of K (Table 2), and these are incorporated into a Monte Carlo estimation of uncertainties on the global means. If horizontal advection and its influence on effective 'uplift rate' along the channel were ignored, the estimates of mean K shift by ~8%.

List of Figure Captions

Figure 1) Shaded relief image of the Siwalik Hills anticline in central Nepal. Channels examined in this study are shown as black lines and are keyed to Table 1. White dashed line represents the inferred trace of the Main Frontal Thrust.

Figure 2) Channel longitudinal profiles for tributaries of the Bagmati (a) and Bakeya (b) rivers. See Figure 1 for location. Black lines represent the elevation profiles obtained by smoothing the raw data (blue) within a 10 pixel sliding window. Red lines represent the elevations derived from the best-fit regression of gradient against drainage area (insets), while blue lines represent regressions forced with Θ=0.46.

Figure 3) Examples of erosion rate derived from the calibrated stream power incision model. Tributary 3 (squares) records decreasing erosion rates in a downstream direction, while tributary 15 (circles) yields nearly constant rates along the channel. Open symbols represent modeled rates for n=0.66; closed symbols represent rates for n=1. Linear regressions for each model shown as solid (n=1) and dashed (n=0.66) lines.

Figure A1) Vertical displacement patterns above the Main Frontal Thrust for the Bakeya (a) and Bagmati (b) transects. Rates were derived using bedding dip orientations from Lave and Avouac (2000). Open circles represent the vertical component of deformation derived for a constant shortening rate of 21 mm/yr. Filled circles represent the total effective vertical component derived from equation (A4) and utilized in calibration of the erosion coefficient K.

References Cited

Brocklehurst, S.H., and Whipple, K.X., 1999, Relief production on the eastern side of the Sierra Nevada, California: EOS Transactions with Abstracts, v. 80, p. F442.

Fielding, E.J., Isacks, B.L., Barazangi, M., and Duncan, C., 1994, How flat is Tibet?: Geology, v. 22, p. 163-167.

Hack, J.T., 1957, Studies of longitudinal stream profiles in Virginia and Maryland, U.S. Geological Survey Professional Paper 294-B, p. 45-97.

Howard, A.D., 1994, A detachment-limited model of drainage basin evolution: Water Resources Research, v. 30, p. 2261-2285.

Howard, A.D., and Kerby, G., 1983, Channel changes in badlands: Geological Society of America Bulletin, v. 94, p. 739-752.

Howard, A.D., Seidl, M.A., and Dietrich, W.E., 1994, Modeling fluvial erosion on regional to continental scales: Journal of Geophysical Research, v. 99, p. 13,971-13,986.

Hurtrez, J.-E., Lucazeau, F., Lave, J., and Avouac, J.-P., 1999, Investigation of the relationship between basin morphology, tectonic uplift, and denudation from the study of an active fold belt in the Siwalik Hills, central Nepal: Journal of Geophysical Research, v. 104, p. 12,779-12,796.

Lave, J., and Avouac, J.P., 2000, Active folding of fluvial terraces across the Siwalik Hills, Himalayas of central Nepal: Journal of Geophysical Research, v. 105, p. 5735-5770.

Moglen, G.E., and Bras, R.L., 1995, The effect of spatial heterogeneities on geomorphic expression in a model of basin evolution: Water Resources Research, v. 31, p. 2613-2623.

Molnar, P., 1987, Inversion of profiles of uplift rates for the geometry of dip-slip faults at depth, with examples from the Alps and Himalaya: Annales Geophysicae, v. 5B, p. 663-670.

Montgomery, D.R., and Foufoula-Georgiou, E., 1993, Channel network source representation using digital elevation models: Water Resources Research, v. 29, p. 1178-1191.

Seidl, M.A., and Dietrich, W.E., 1992, The problem of channel erosion into bedrock: Catena Supplement, v. 23, p. 101-124.

Sklar, L., and Dietrich, W.E., 1998, River longitudinal profiles and bedrock incision models: Stream power and the influence of sediment supply, *in* Tinkler, K.J., and Wohl, E.E., eds., Rivers over rock: fluvial processes in bedrock channels: Geophysical Monograph 107: Washington, DC, American Geophysical Union, p. 237-260.

Snyder, N.P., Whipple, K.X., Tucker, G.E., and Merritts, D.J., 2000, Landscape response to tectonic forcing: Digital elevation model analysis of stream profiles in the Mendocino triple junction region, northern California: Geological Society of America Bulletin, v. 112, p. 1250-1263.

Stock, J.D., and Montgomery, D.R., 1999, Geologic constraints on bedrock river incision using the stream power law: Journal of Geophysical Research, v. 104, p. 4983-4993.

Tarboton, D.G., Bras, R.L., and Rodriguez-Iturbe, I., 1991, On the extraction of channel networks from digital elevation data: Hydrological Processes, v. 5, p. 81-100.

Tinkler, K.J., and Wohl, E.E., 1998, Rivers Over Rock: Fluvial Processes in Bedrock Channels, Geophysical Monograph Series, Volume 107: Washington, DC, American Geophysical Union, p. 323.

Whipple, K.X., Hancock, G.S., and Anderson, R.S., 2000a, River incision into bedrock: Mechanics and relative efficacy of plucking, abrasion, and cavitation: Geologic Society of America Bulletin, v. 112, p. 490-503.

Whipple, K.X., Kirby, E., and Brocklehurst, S.H., 1999, Geomorphic limits to climate-induced increases in topographic relief: Nature, v. 401, p. 39-43.

Whipple, K.X., Snyder, N.P., and Dollenmayer, K., 2000b, Rates and processes of bedrock incision by the Upper Ukak River since the 1912 Novarupta ash flow in the Valley of Ten Thousand Smokes, Alaska: Geology, v. 28, p. 835-838.

Whipple, K.X., and Tucker, G.E., 1999, Dynamics of the stream-power river incision model: Implications for height limits of mountain ranges, landscape response timescales, and research needs: Journal of Geophysical Research, v. 104, p. 17,661-17,674.

Willgoose, G., 1994, A physical explanation for an observed-slope-elevation relationship for catchments with declining relief: Water Resources Research, v. 30, p. 151-159.

Table 1: Topographic characteristics of channels in the Siwalik Hills

Principal Channel	A_{min} (m^2)	A_{max} (m^2)	Θ ± (2σ)	k_s (Θ=0.46)	h ± (2σ)	Model E* *n* =0.66 (mm/yr)	Model E* *n* =1 (mm/yr)	Model E§ *n* =0.66 (mm/yr)	Model E§ *n* =1 (mm/yr)
Bakeya trib	9×10^6	5×10^7	-0.55 ± 0.32	59	1.68 ± 0.13				
Bagmati trib	3×10^6	3.5×10^7	-0.32 ± 0.12	55	1.46 ± 0.10				
1	1×10^6	1×10^7	0.30 ± 0.10†	60	1.26 ± 0.12	8-11 (0.80)	8-11 (0.81)	9-12 (0.45)	9-13 (0.45)
2	1×10^6	4×10^6	0.53 ± 0.20†	70	0.94 ± 0.03	[10.7]	[11.3]	[10.4]	[10.8]
3	2×10^6	5×10^6	1.30 ± 0.32	75	0.64 ± 0.05	12-7 (0.95)	11-8 (0.94)	13-6 (0.82)	15-5 (0.80)
4	1×10^6	3×10^6	1.10 ± 0.20	88	1.15 ± 0.23	9-6 (0.83)	9-5 (0.81)	13-5 (0.85)	15-3 (0.82)
5	5×10^5	3×10^6	1.00 ± 0.18	58	1.04 ± 0.05	13-6 (0.90)	14-5 (0.87)	13-7 (0.64)	16-6 (0.62)
6	1.5×10^6	3×10^6	2.10 ± 0.61	51	0.54 ± 0.04	12-7 (0.93)	14-5 (0.91)	13-3 (0.86)	15-2 (0.81)
7	2×10^6	1×10^7	1.30 ± 0.33	81	1.05 ± 0.10	10-4 (0.86)	11-3 (0.82)	13-7 (0.20)	15-6 (0.21)
8	1×10^6	4×10^6	1.10 ± 0.31	56	0.96 ± 0.07	15-9 (0.89)	18-9 (0.88)	11-3 (0.86)	11-2 (0.84)
9	2×10^6	7×10^6	0.99 ± 0.14	68	0.73 ± 0.04	12-8 (0.91)	14-7 (0.90)	12-3 (0.82)	13-2 (0.80)
10	5×10^5	4×10^6	1.20 ± 0.22	48	0.90 ± 0.03	15-7 (0.79)	18-6 (0.76)	10-4 (0.66)	10-3 (0.65)
11	1×10^6	8×10^6	0.74 ± 0.16	67	1.75 ± 0.25	12-9 (0.98)	13-9 (0.98)	11-7 (0.68)	12-6 (0.66)
12	1×10^6	4×10^6	1.40 ± 0.28	74	0.84 ± 0.20	8-5 (0.96)	8-4 (0.96)	11-8 (0.64)	12-7 (0.64)
13	9×10^5	5×10^6	0.87 ± 0.25	49	1.06 ± 0.16	10-7 (0.74)	10-6 (0.72)	11-6 (0.73)	11-5 (0.72)
14	4×10^5	5×10^6	0.50 ± 0.29	51	2.01 ± 0.54	[8.7]	[8.3]	[8.6]	[8.1]
15	5×10^5	1×10^7	0.47 ± 0.16	59	1.58 ± 0.10	[9.0]	[8.6]	[9.3]	[9.2]
16	1×10^6	7×10^6	0.48 ± 0.14	60	1.64 ± 0.17	[9.0]	[8.6]	[9.5]	[9.4]
17	6×10^5	2×10^6	0.51 ± 0.42	72	2.39 ± 0.70	[11.0]	[11.7]	[10.6]	[11.1]
18	1×10^6	1×10^7	0.44 ± 0.22	72	1.14 ± 0.05	[10.8]	[11.3]	[10.9]	[11.8]
19	7×10^5	2.5×10^6	0.34 ± 0.34	63	1.28 ± 0.09	[10.2]	[10.5]	[9.4]	[9.2]
20	1×10^6	1.5×10^7	0.51 ± 0.22	35	1.35 ± 0.07	[6.5]	[5.3]	[6.7]	[5.5]
mean (3-10)			***1.26 ± 0.37***	***66***					
mean (11-13)			***1.01 ± 0.31***	***63***					
mean (3-13)			***1.19 ± 0.38***	***65***					
mean (14-20)			***0.46 ± 0.14***	***59***					

* Erosion rate calculated using channel gradients inferred from Θ and k_s. Where rates vary along a channel, values represent rates at A_{min} and A_{max}, respectively. Correlation coefficient (R^2) shown in parentheses. Where rates are invariant along a channel, number in brackets represents the mean erosion rate.

§ Same as above, but calculated using channel gradient sampled at 10m intervals.

† Excluded from mean.

Table 2: Erosion coefficients calibrated for the Siwalik Hills

Principal Channel	n ($\alpha = 1$)	K ($m^{0.08}$/yr) (n=1, m/n=0.46)	K ($m^{0.06}$/yr) (n=0.66, m/n=0.46)	K ($m^{0.2}$/yr) (n=1, m/n=0.4)*
U(x) = 4 - 18 mm/yr				
Bakeya trib	0.59	1.64×10^{-4} ($\pm 2.54 \times 10^{-5}$)	6.85×10^{-4} ($\pm 1.50 \times 10^{-4}$)	4.68×10^{-4} ($\pm 7.76 \times 10^{-5}$)
Bagmati trib	0.88	1.54×10^{-4} ($\pm 2.95 \times 10^{-5}$)	6.39×10^{-4} ($\pm 1.73 \times 10^{-4}$)	4.27×10^{-4} ($\pm 8.91 \times 10^{-5}$)
U(x) = 6 - 12 mm/yr				
Bakeya trib	0.59	1.47×10^{-4} ($\pm 2.78 \times 10^{-5}$)	6.02×10^{-4} ($\pm 7.10 \times 10^{-5}$)	4.19×10^{-4} ($\pm 7.36 \times 10^{-5}$)
Bagmati trib	0.88	1.48×10^{-4} ($\pm 2.98 \times 10^{-5}$)	5.95×10^{-4} ($\pm 6.00 \times 10^{-5}$)	4.08×10^{-4} ($\pm 7.18 \times 10^{-5}$)
mean		1.54×10^{-4}	6.30×10^{-4}	4.32×10^{-4}
2σ		2.90×10^{-5}	1.27×10^{-4}	8.13×10^{-5}

Note: K was calculated for each point along the channel. Mean values and standard deviations (parentheses) are given. Uncertainties on the mean values reflect a Monte Carlo propagation of uncertainties.
* Calculated for direct comparison to published estimates (e.g. Stock and Montgomery, 1999)

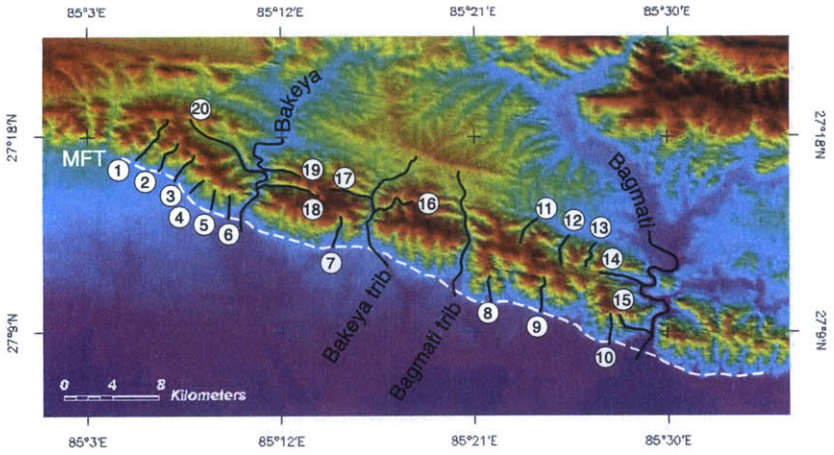
85°3'E
85°12'E
85°21'E
85°30'E
27°18'N
27°9'N
MFT
Bakeya
Bagmati
Bakeya trib
Bagmati trib
1
2
3
4
5
6
7
8
9
10
11
12
13
14
15
16
17
18
19
20
0 4 8 Kilometers

Figure 1

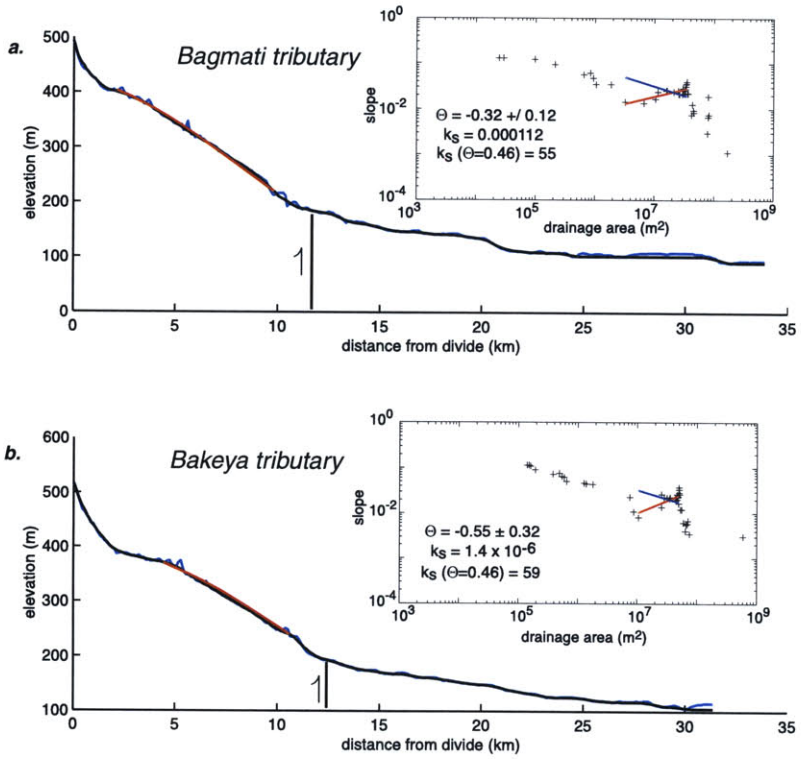
a.
Bagmati tributary
elevation (m)
distance from divide (km)
slope
drainage area (m²)
Θ = -0.32 +/ 0.12
kS = 0.000112
kS (Θ=0.46) = 55
b.
Bakeya tributary
elevation (m)
distance from divide (km)
slope
drainage area (m²)
Θ = -0.55 ± 0.32
kS = 1.4 x 10-6
kS (Θ=0.46) = 59

Figure 2

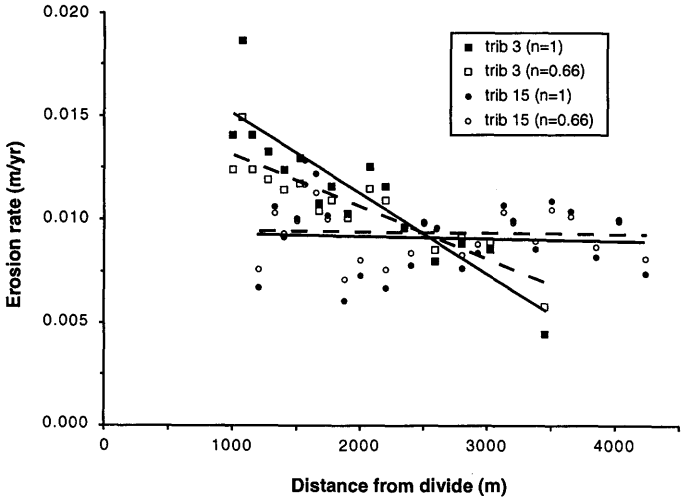
0.020
0.015
0.010
0.005
0.000
Erosion rate (m/yr)
0
1000
2000
3000
4000
Distance from divide (m)
trib 3 (n=1)
trib 3 (n=0.66)
trib 15 (n=1)
trib 15 (n=0.66)

Figure 3

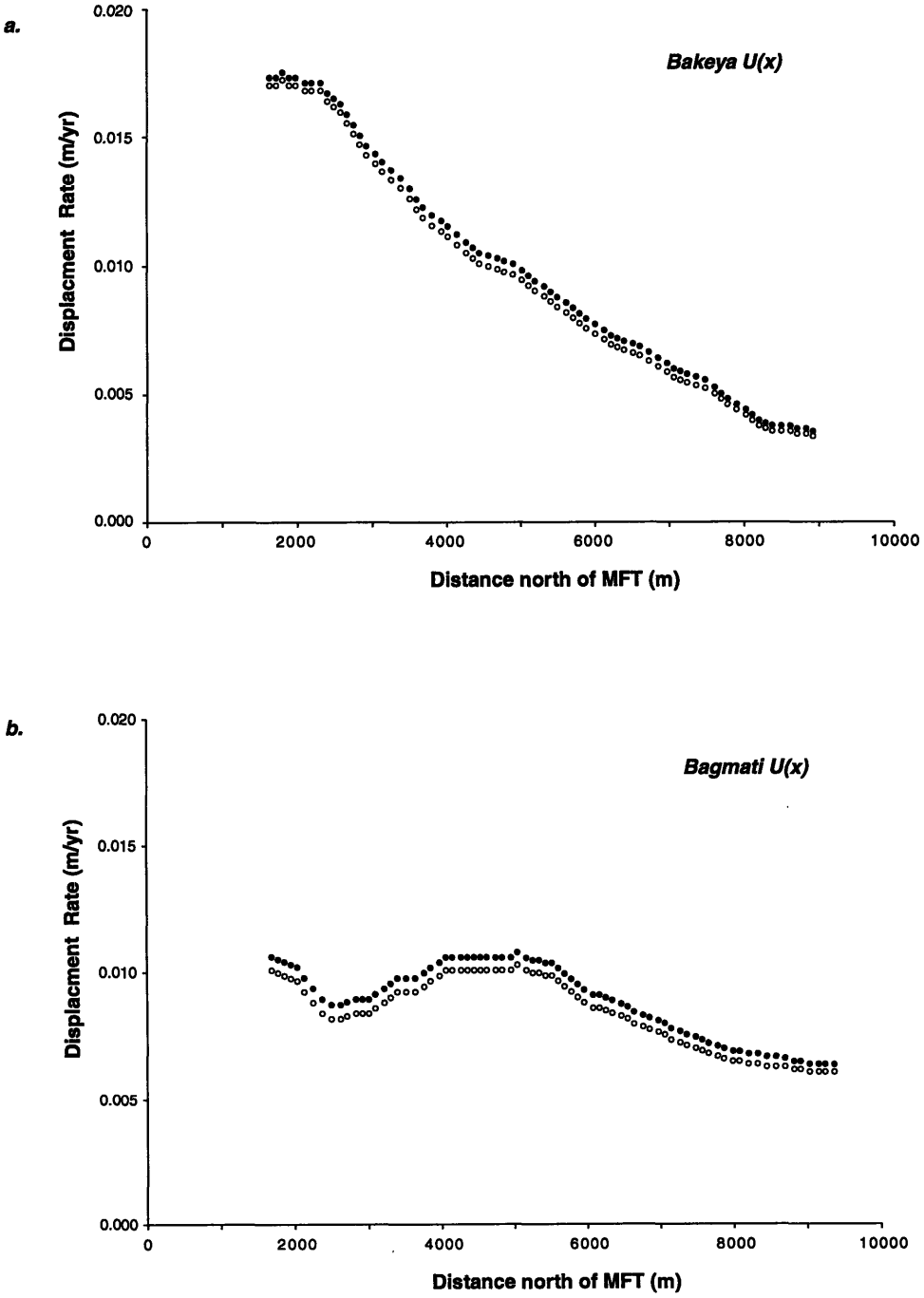
a.
Bakeya U(x)
Displacment Rate (m/yr)
0.020
0.015
0.010
0.005
0.000
0
2000
4000
6000
8000
10000
Distance north of MFT (m)
b.
Bagmati U(x)
Displacment Rate (m/yr)
0.020
0.015
0.010
0.005
0.000
0
2000
4000
6000
8000
10000
Distance north of MFT (m)

Figure A1

Chapter 6

Tectonic Synthesis

Introduction

The eastern margin of the Tibetan Plateau in the vicinity of the Sichuan Basin provides an interesting case study in the development of topography along the margins of orogenic plateaux. This chapter is a synthesis of the previous chapters and is intended to draw out the most significant insights gained from the combined results of this work, as well as to highlight some of the outstanding issues regarding the neotectonic and geomorphic evolution of the plateau margin.

The results of this study address three aspects of the evolution of the plateau margin that together bear important implications for the generation and maintenance of topography in eastern Tibet. These aspects include:

- Nature of active deformation along the margin
- Timing of initial development of the topographic margin
- Geodynamic significance of high topography along the margin

Nature of Active Deformation in Eastern Tibet

One of the most enigmatic aspects of the eastern margin of the plateau is the apparently minor contribution of upper crustal shortening to the present-day velocity field (King et al., 1997; Chen et al., 2000) between the plateau and the Sichuan Basin. Although these measurements provide short-term, interseismic estimates of the velocity field, they are probably representative of the velocity on geologic timescales for the following reasons: 1) velocities west of the margin are oriented northeast (relative to South China) and indicate a right-lateral shear between the central plateau and the Sichuan Basin (Chen et al., 2000); there is no indication that the slow velocities represent elastic strain accumulation at the margin, 2) seismicity along the plateau margin is relatively minor during the past ~1500 years (Editoral Board, 1989), consistent with slow seismic strain release, 3) historic seismicity on the Huya Fault (eastern Min Shan) is consistent with minor horizontal shortening (Jones et al., 1984), and 4) estimates of Cenozoic deformation in the southern Longmen Shan suggest that shortening is limited to a few tens of kilometers (Burchfiel et al., 1995). Thus, it appears reasonable to interpret

the geodetic results as broadly representative of the velocity field over geologic timescales.

Perhaps the primary result of these investigations is the recognition and documentation of Quaternary-Recent rock uplift along the margin of the plateau. Geologic evidence for recent rock uplift is found in tilted Pleistocene basins along the western flank of the Min Shan and in tilted lacustrine sediments along the Min Jiang north of Diexi (Chapter 2). In addition, analysis of the spatial variations in channel concavity and steepness across the region suggests that active rock uplift (relative to the Sichuan Basin) exerts a fundamental control on channel gradients and incision rates in this landscape (Chapter 4). The rates of rock uplift are locally high (up to 8-10 mm/yr), exceeding the maximum allowable shortening across the region (Chen et al., 2000), and indicate the presence of an additional driving mechanism.

One possible such mechanism may be the flexural isostatic response to erosion, as has been argued for the Himalaya and Andean margins (Masek et al., 1994). However, a simple flexural model (Chapter 2) demonstrates that in order to reproduce the tilting observed along the western Min Shan, two conditions must hold: 1) the flexural rigidity of the lithosphere must be quite weak and 2) erosion rates along the eastern range front must approach 15-20 mm/yr over a width of at least 40km. Estimates of Late Cenozoic denudation rates in this region (1-3 mm/yr, Chapter 3) are apparently too slow too produce the observed tilting. Thus, the tilting and rock uplift along the margin of the plateau appears to be a tectonic signal.

The presence of active rock uplift in the absence of significant shortening of the upper crust has important implications for the processes driving deformation along this margin of the plateau. Although a number of workers have argued that the dynamics of mantle flow beneath Tibet exerts a fundamental control on the elevation and uplift history of the plateau (e.g., Molnar et al., 1993), the spatial scale of active rock uplift along the eastern margin suggests that rock uplift is driven by crustal processes. Rock uplift appears to be focused along a narrow (40-60km wide) zone along the topographic front of the margin (Chapters 2, 4) and decreases toward the plateau, as well as toward the foreland. In addition, the spatial association of the region of highest rock uplift with the topographic edge of the plateau is consistent with geodynamic models for plateau

development where crustal thickening is focused at the foot of the topographic front (Molnar, 1988; Royden, 1996). However, the relatively minor shortening observed at the surface suggests that thickening may take place by flow within a weak mid-lower crust (Royden et al., 1997; Clark and Royden, 2000).

Miocene Development of the Plateau Margin

One of the great debates in Asian tectonics revolves around the elevation history of the plateau and its relationship to global climate. The time of development of high elevation of the plateau has generally been inferred from an apparent synchroneity between extension and volcanism in central Tibet and the onset of the Asian monsoon (e.g., Molnar et al., 1993). Although there is some evidence for diachroneity of crustal thickening in Tibet (Murphy et al., 1997; Meyer et al., 1998), little is known about the spatial and temporal distribution of surface uplift of the plateau. Our studies (Chapter 3) provide some of the best constraints yet for when the present-day topography of the eastern margin of the plateau began to develop.

Our inference of relatively low regional relief between the rocks now exposed on the plateau surface and the Sichuan Basin in the Early Cenozoic relies on the documentation of regionally extensive slow cooling following Mesozoic tectonism (Chapter 3). The implied stability of the regional thermal structure persists until the Late Miocene, at which time samples adjacent to the topographic front cool rapidly, presumably in response to rapid denudation along the developing margin. Samples from the plateau surface, however, do not record this rapid cooling event, and apparently continued to cool relatively slowly from the Miocene to the present. Thus, we conclude that high topography in this region was not present prior to the Late Miocene, and that subsequent denudation along the margin was focused at the topographic front.

Although this estimate in itself carries no information regarding the process by which the regional elevation gradients developed, in conjunction with the observations above, we can make some inferences regarding the evolution of the region. If the high elevation in eastern Tibet developed as the consequence of flow in the lower crust, the onset of rapid denudation adjacent to the Sichuan Basin probably marks the time at which this material flux reached the basin. While we know little about the denudation histories

of rocks on the plateau west of the margin, the absence of a rapid cooling event recorded in samples from the plateau (Chapter 3) suggests that the plateau did not develop as a steep topographic front migrating east with time. Rather the plateau may have maintained a low-gradient margin as it developed in relatively weak crust and the current regional topographic gradients may reflect crustal material ponding against the strong lithosphere of the Sichuan Basin (Clark and Royden, 2000).

Geodynamic Significance of High Topography Along the Margin

One of the primary goals of this thesis was to evaluate the controls on topographically high mountains that occur along the eastern margin of the plateau. Previous work had suggested that high topography characteristic of the margins of orogenic plateaux was largely an isostatic response to erosion and relief production along the margin (Wager, 1937; Masek et al., 1994; Montgomery, 1994). The combined results of our investigations have important implications for the processes setting the distribution of topographically high mountains adjacent to the Sichuan Basin.

There is a general coincidence between the highest topography and greatest local relief along the topographic front of the plateau margin with the region of highest stream steepness indices (Chapter 4). Given our arguments that stream gradients primarily reflect rock uplift in this landscape (Chapter 4), the spatial association with the highest topography suggests that the distribution of rock uplift exerts a primary control on the relief structure of the landscape at the margin of the plateau via its influence on channel gradient (e.g., Whipple et al., 1999). Furthermore, the relatively minor contribution of a flexural isostatic response to erosion to the observed rock uplift (Chapter 2 and above) suggests that most of the rock uplift is tectonically driven, and thus that the topography is fundamentally a filtered tectonic signal along the margin of the plateau.

The distribution of young cooling ages (Chapter 3, Arne et al., 1997) along the plateau margin appears to indicate that substantial Late Cenozoic denudation was focused at the topographic front (Chapter 3). Although the spatial distribution of long-term denudation is not well resolved by our sample distribution, the broad association of young cooling ages with the region of highest topography and highest stream steepness indices further suggests the possibility that high denudation rates have been maintained

via continued influx of crustal material. Thus, the topographic front of the plateau adjacent to the Sichuan Basin may be a quasi-steady feature where high denudation rates are maintained by high incision rates along steep channels which, in turn, help to localize strain and material flux at the topographic margin (e.g., Willett, 1999).

Outstanding Issues

Testing the ideas and hypotheses laid out above will yield further insight into two aspects of the evolution of this region: 1) the degree to which the spatial distribution of long-term denudation coincides with the distribution of active rock uplift, and 2) timing of initial relief development along the margin. Each of these issues has implications for the processes driving topographic development along the plateau margin. This section outlines the means by which these issues may be addressed.

One of the striking results of this work is the apparent coincidence between the spatial distribution of Late Cenozoic denudation and active rock uplift along the margin. However, gradients in cooling ages in the Longmen Shan region are inferred from a few, widely separated samples (Chapter 3). Likewise, although we infer the presence of spatial variations in active rock uplift from stream gradients (Chapter 4), the rates of river incision are only well-calibrated at a few localities. Enhanced resolution of gradients in long-term denudation and their relationship to structures would yield important constraints on the localization of mass flux along the margin, while an improved understanding of the rates of river incision and their spatial distribution would yield insight into the wavelength of upper crustal deformation in the region. If the spatial scale and rates of long-term denudation are comparable to those inferred from recent incision, they could provide a compelling case for a quasi-steady region of exhumation focused along the foot of the plateau margin.

The eastern Min Shan provides an important place to test this hypothesis. Significant Late Miocene-Recent denudation appears to have been confined to a narrow (<40 km wide) region along the eastern range front (see chapter 3) coincident with a region of high stream gradients (chapter 4). Fluvial terraces are widespread and yield preliminary incision rates consistent with the interpretation of high rock uplift rates in the range. I propose a three-pronged approach to investigating the distribution of rock uplift

across the eastern range front at varying temporal scales. 1) A transect of samples for (U-Th)/He thermochronology will be collected from the foreland to the crest of the range in order to investigate the spatial variability of cooling ages. Apatite is abundant in the crystalline rocks in the Qinling Shan (foreland region) and is present in the range within several small granite bodies and as detrital phases in the Songpan-Garze flysch (Chapter 3). In addition, we will collect a vertical transect of samples within the range in order to examine the distribution of cooling ages with elevation. 2) We will compare these results with the distribution of recent fluvial incision inferred from strath terraces. In particular, we will assess whether the region of high stream gradients coincides with greater incision rates. 3) We will also establish a geodetic survey aimed at measuring the rates of distributed tilting across the western Min Shan range. Together these diverse data sets should provide a picture of the rates and distribution of rock uplift since the development of the plateau margin in this region and will provide important constraints on the nature of upper crustal deformation in this region of the plateau.

The other outstanding issue revolves around the precision of our estimate for the initial development of the plateau margin. The Late Miocene age argued for in this thesis depends on young ages observed in feldspars and apatites from two samples adjacent to the topographic front. This estimate may be tested using the vertical distribution of cooling ages in a variety of mineral systems with different closure temperatures. In particular, an age elevation transect in the Pengguan Massif would yield a transect nearly 4000m in height. We predict that (U-Th)/He ages from apatites throughout this transect would be nearly invariant (a response to rapid cooling and denudation), but that titanites or zircons should yield a region of progressively older ages with increasing elevation. In conjunction with the Min Shan transect proposed above, we will begin to test the possibility that initial development of topography along this margin of the plateau was diachronous.

Similarly, a transect collected in the 2000-2500m of relief in the Mesozoic plutons in the headwaters of the Hei Shui would yield important information on the Late Cenozoic thermal history of this region and may allow an assessment of the apparent increase in cooling rates inferred between 50 and 20 Ma (Chapter 3). Together, all three transects will enhance our understanding of the timing and spatial distribution of cooling

rates and denudation in response to development of the topographic margin of the plateau.

References Cited

Arne, D., Worley, B., Wilson, C., Chen, S., Foster, D., Luo, Z., Liu, S., and Dirks, P., 1997, Differential exhumation in response to episodic thrusting along the eastern margin of the Tibetan Plateau: Tectonophysics, v. 280, p. 239-256.

Burchfiel, B.C., Chen, Z., Liu, Y., and Royden, L.H., 1995, Tectonics of the Longmen Shan and adjacent regions: International Geology Review, v. 37, p. 661-735.

Chen, Z., Burchfiel, B.C., Liu, Y., King, R.W., Royden, L.H., Tang, W., Wang, E., Zhao, J., and Zhang, X., 2000, GPS measurements from eastern Tibet and their implications for India/Eurasia intracontinental deformation: Journal of Geophysical Research, v. 105, p. 16215-16227.

Clark, M.K., and Royden, L.H., 2000, Topographic ooze: Building the eastern margin of Tibet by lower crustal flow: Geology, v. 28, p. 703-706.

Editoral Board, S.S.B., 1989, Lithospheric dynamics atlas of China: Beijing, China Cartographic Publishing House.

Jones, L.M., Han, W., Hauksson, E., Jin, A., Zhang, Y., and Luo, Z., 1984, Focal mechanisms of the Songpan earthquakes of August 1976 in Sichuan, China: Journal of Geophysical Research, v. 89, p. 7697-7707.

King, R.W., Shen, F., Burchfiel, B.C., Royden, L.H., Wang, E., Chen, Z., Liu, Y., Zhang, X., Zhao, J., and Li, Y., 1997, Geodetic measurement of crustal motion in southwest China: Geology, v. 25, p. 179-182.

Masek, J.G., Isacks, B.L., Gubbels, T.L., and Fielding, E.J., 1994, Erosion and tectonics at the margins of continental plateaus: Journal of Geophysical Research, v. 99, p. 13,941-13,956.

Meyer, B., Tapponnier, P., Bourjot, L., Metivier, F., Gaudemer, Y., Peltzer, G., Guo, S., and Chen, Z., 1998, Crustal thickening in Gansu-Qinghai, lithospheric mantle subduction, and oblique, strike-slip controlled growth of the Tibet plateau: Geophysical Journal International, v. 135, p. 1-47.

Molnar, P., 1988, A review of geophysical constraints on the deep structure of the Tibetan Plateau, the Himalaya and the Karakoram, and their tectonic implications, *in* Chang, C., Shackleton, R.M., Dewey, J.F., and Yin, J., eds., The Geological Evolution of Tibet, Volume 326 A, Philosophical Transactions of the Royal Society of London, p. 33-88.

Molnar, P., England, P., and Martinod, J., 1993, Mantle dynamics, uplift of the Tibetan Plateau, and the Indian monsoon: Reviews of Geophysics, v. 31, p. 357-396.

Montgomery, D.R., 1994, Valley incision and the uplift of mountain peaks: Journal of Geophysical Research, v. 99, p. 13,913-13,921.

Murphy, M.A., Yin, A., Harrison, T.M., Durr, S.B., Chen, Z., Ryerson, F.J., Kidd, W.S.F., Wang, X., and Zhou, X., 1997, Did the Indo-Asian collision alone create the Tibetan Plateau?: Geology, v. 25, p. 719-722.

Royden, L., 1996, Coupling and decoupling of crust and mantle in convergent orogens: Implications for strain partitioning in the crust: Journal of Geophysical Research, v. 101, p. 17,679-17,705.

Royden, L.H., Burchfiel, B.C., King, R.W., Chen, Z., Shen, F., and Liu, Y., 1997, Surface deformation and lower crustal flow in Eastern Tibet: Science, v. 276, p. 788-790.

Wager, L.R., 1937, The Arun river drainage pattern and the rise of the Himalaya: Geographical Journal, v. 89, p. 239-250.
Whipple, K.X., Kirby, E., and Brocklehurst, S.H., 1999, Geomorphic limits to climate-induced increases in topographic relief: Nature, v. 401, p. 39-43.
Willett, S.D., 1999, Orogeny and orography: the effects of erosion on the structure of mountain belts: Journal of Geophysical Research, v. 104, p. 28,957-28,981.